UNIVERSIDADE ESTADUAL DE CAMPINAS
INSTITUTO DE FíSICA GLEB WATAGHIN

Tese de Doutorado

Modelos de discos e outras estruturas
auto-gravitantes em Relatividade Geral

Aluno: Daniel Vogt – IFGW/UNICAMP
Orientador: Dr. Patricio Anibal Letelier Sotomayor – IMECC/UNICAMP
Co-orientador: Dr. Marcus A. M. de Aguiar – IFGW/UNICAMP

20 de Março de 2006

Banca Examinadora:
Dr. Patricio Anibal Letelier Sotomayor – IMECC/UNICAMP
Dr. George Emanuel Avraam Matsas – IFT/UNESP
Dr. Alberto Vazquez Saa – IMECC/UNICAMP
Dra. Kyoko Furuya – IFGW/UNICAMP
Dra. Carola Dobrigkeit Chinellato – IFGW/UNICAMP

Livros Grátis

Toda a nossa ciência, comparada com a realidade, é primitiva e infantil—e, no entanto, é a coisa mais preciosa que temos.

Albert Einstein

As teorias são redes, lançadas para capturar aquilo que denominamos "o mundo": para racionalizá-lo, explicá-lo, dominá-lo. Nossos esforços são no sentido de tornar as malhas da rede cada vez mais estreitas.

Karl Popper, *A Lógica da Pesquisa Científica*

Agradecimentos

Ao meu orientador Dr. Patricio Letelier, que me mostrou o caminho. Para mim foi um privilégio ter sido seu aluno de mestrado e doutorado.

À CAPES, pelo suporte financeiro.

Ao Dr. Rogério L. de Almeida, pessoa com vasta cultura geral, pelas nossas estimulantes conversas ao longo dos anos sobre os mais variados assuntos (alguns deles impublicáveis).

A Donald E. Knuth, criador do TEX, e a todos que desenvolveram o LATEX e seus inúmeros pacotes.

Zuletzt, aber nicht unwichtiger, möchte ich meinen Eltern danken. Ohne Ihre Unterstützung wäre ich nie so weit gekommen.

Resumo

Soluções exatas das equações do campo de Einstein que representam espaços-tempo com distribuições de matéria em forma de discos são construídas pelo método inverso (método das imagens). Estas soluções incluem discos estáticos finos de fluido perfeito com e sem halos, discos estáticos finos de fluido perfeito com carga elétrica e modelos de discos finos formados por poeira carregada. São estudadas ainda novas soluções em vários sistemas de coordenadas que representam discos estáticos grossos com espessura constante. Uma forma particular para a métrica isotrópica em coordenadas cilíndricas é usada para obter-se versões relativísticas de pares potencial-densidade Newtonianos comumente usados na Astronomia Galáctica. Um modelo relativístico simplificado, porém exato, de um núcleo ativo de galáxia também é apresentado. Finalmente, é feito um estudo de alguns pares-potencial densidade Newtonianos obtidos a partir da expansão multipolar do potencial Newtoniano que generalizam pares conhecidos.

Abstract

Exact solutions of Einstein field equations that represent space-times with disklike matter distributions are constructed using the inverse method (image method). These solutions include static thin perfect fluid disks with and without halos, static thin charged perfect fluid disks and models of thin charged dust disks. New solutions in various coordinate systems that represent static thick disks with constant thickness are also studied. A particular form of the isotropic metric in cylindrical coordinates is employed to obtain relativistic versions of Newtonian potential-density pairs commonly used in Galactic Astronomy. A simplified, although exact, relativistic model of an active galactic nuclei is also presented. Finally, some Newtonian potential-density pairs obtained from the Newtonian multipolar expansion that generalize known pairs are studied.

Conteúdo

Capítulo 1

Introdução

Grande parte dos objetos astronômicos apresenta distribuições de matéria
com simetria axial, com destaque para as formas discoidais encontradas por
exemplo, em certos tipos de galáxias e discos de acréscimo.

Quanto à morfologia, as galáxias podem ser classificadas como [1]: ga-
láxias elípticas (sistemas que contêm pouca poeira ou gases e cujo formato
é elipsoidal), galáxias lenticulares (possuem um proeminente disco que não
contém gás, poeira ou braços espirais, formam uma classe de transição entre
elípticas e espirais), galáxias espirais e galáxias irregulares (as que não se
encaixam nas classificações anteriores). As galáxias espirais, cujos exem-
plos típicos são a Via-láctea e Andrômeda, formam a classe mais numerosa.
Nossa galáxia é formada por um proeminente disco com gás, poeira e braços
espirais com cerca de 30 kpc de diâmetro (1pc=3,26 anos-luz) e cerca de 1,5
kpc de espessura. Apresenta ainda um núcleo e um halo galáctico quase-
esférico formado por concentrações de estrelas denominados aglomerados
globulares. Estas estrelas possuem propriedades bastante distintas das que
se encontram no disco.

Há ainda numerosas evidências observacionais de que a maioria das
galáxias hospedam em seus núcleos buracos negros gigantes com massas
que variam de milhões a alguns bilhões de massas solares e que acrescem
matéria ao redor dos mesmos. Alguns núcleos ativos de galáxias apresen-
tam ainda extensos jatos relativísticos de matéria que se estendem ao longo
do eixo de simetria. Um possível mecanismo para a produção destes jatos
envolve a interação, por meio de campos magnéticos, entre o buraco negro
central e o disco de acréscimo [2]. O acréscimo de matéria em forma de dis-
co por buracos negros massivos provavelmente também é o responsável pela
gigantesca quantidade de energia liberada pelos quasares, cuja luminosidade

típica equivale à de centenas de galáxias. Em geral, a teoria Newtoniana fornece uma boa descrição da dinâmica destes sistemas para distâncias maiores do que cerca de 100 raios de Schwarzschild no caso estático. Entretanto, nas proximidades de um buraco negro a não-linearidade e os efeitos rotacionais relativísticos não podem ser desprezados (ao contrário da gravitação Newtoniana, que não distingue campos estáticos de estacionários, na linguagem "gravito-eletromagnética" da Relatividade Geral a gravidade não apenas possui um componente elétrico, gerado pela massa, mas também um componente magnético originário de correntes carregadas de massa).

Estes breves comentários mostram que soluções exatas das equações de Einstein na forma de configurações discoidais de matéria (com ou sem buracos negros centrais) não possuem apenas interesse puramente teórico, mas podem ser bastante úteis para a astrofísica moderna. Ao longo dos anos um grande número destas soluções exatas têm sido estudadas. Soluções de discos estáticos finos finitos foram inicialmente estudadas por Bonnor e Sackfield [3], e Morgan e Morgan [4, 5]. No primeiro caso as soluções representavam discos feitos de poeira (sem pressão), enquanto Morgan e Morgan obtiveram uma classe de discos com pressão azimutal mas sem pressão radial, e mais tarde discos com matéria anisotrópica com pressão radial não-nula. Outras classes de soluções exatas de discos finos estáticos com ou sem pressão radial foram obtidas por diversos autores [6–10]. Também foram estudados discos finos com tensões radiais [11], campos magnéticos [12] e campos elétricos e magnéticos [13]. No caso estacionário, foram construídos modelos de discos finos como fontes da métrica de Kerr [14], com campos eletromagnéticos [15] e com e sem fluxo de calor na direção tangencial [16].

A estabilidade de discos sem pressão radial usualmente é justificada com duas interpretações: a existência de tensões de suporte ou que as partículas no disco movem-se sob a influência de seu próprio campo gravitacional de tal modo que haja igual número delas movendo-se tanto no sentido horário quanto no sentido anti-horário. Esta interpretação é conhecida como "modelo de contrarotação". Uma discussão detalhada deste modelo, incluindo outras condições sobre o movimento das partículas, e soluções de discos obtidas, é apresentada em [17–20].

A sobreposição de discos estáticos com um buraco negro de Schwarzschild foi primeiramente considerada por Lemos e Letelier [21–23]. Uma solução particularmente interessante estudada pelos autores consiste na sobreposição de um buraco negro com um disco anular obtido pela inversão do primeiro membro da família de discos de Morgan-Morgan. Para este sistema foram estudadas as linhas de campo gravitacional [24], movimento de partículas-teste [25], freqüências de oscilações epicíclicas e verticais [26] e generalizações

[27, 28]. Um passo adiante seria a inclusão de rotação, ou seja, a sobreposição de um buraco negro de Kerr com um disco estacionário. Infelizmente este problema não é simples e até o presente não foram encontradas soluções exatas explícitas para sistemas deste tipo (ver [29] para uma tentativa nesta direção).

Todos os modelos de discos mencionados acima foram obtidos pelo método inverso, isto é, a fonte de matéria é calculada a partir de uma dada métrica por meio das equações de Einstein. O método direto, no qual a fonte é dada e as equações de Einstein são resolvidas, tem sido usado por um grupo germânico para gerar classes de discos [30–36]. O procedimento consiste basicamente na solução de um problema de Riemann-Hilbert. Embora matematicamente não-triviais, estas soluções de discos possuem uma interpretação física direta. Uma revisão sobre este assunto é feita em [37].

A hipótese de discos infinitesimalmente finos é satisfatória numa primeira aproximação. Por exemplo, um disco galáctico típico possui um raio de cerca de uma ordem de grandeza maior que sua espessura. Em modelos mais realistas a espessura deve ser considerada e pode alterar significativamente certas propriedades do sistema, como sua estabilidade. González e Letelier [38] generalizaram o procedimento inverso até então usado para construir discos finos e apresentaram várias soluções de discos estáticos grossos.

Nesta tese usamos o método inverso para construir novos modelos de discos relativísticos estáticos, que incluem: discos finos de fluido perfeito com e sem halos em coordenadas isotrópicas, discos finos de fluido perfeito com carga elétrica em coordenadas isotrópicas, discos e estruturas sem simetria axial feitos de poeira carregada, uma generalização dos modelos de discos grossos apresentados em [38] e versões relativísticas dos pares potencial-densidade de Miyamoto-Nagai [39] e Satoh [40] usados como modelos Newtonianos de galáxias. Estudamos ainda a sobreposição de disco, buraco negro central e duas barras em coordenadas de Weyl como modelo relativístico simplificado de núcleos ativos de galáxias. O trabalho está dividido da seguinte forma: no Capítulo 2 fazemos um resumo dos conceitos de Relatividade Geral usados na tese, e no Capítulo 3 apresentamos algumas soluções exatas das equações de Einstein para várias métricas. Estas soluções formam a base para a construção dos discos citados. No Capítulo 4 discutimos em detalhe os métodos para gerar discos finos e grossos a partir de uma dada métrica. No Capítulo 5 comentamos brevemente o assunto e resultados de cada um dos artigos publicados ao longo do doutoramento e comentários finais. Esses artigos são reproduzidos nos Apêndices A a H.

Capítulo 2

Elementos de Relatividade Geral

Neste capítulo revisamos alguns conceitos de Relatividade Geral que serão usados adiante. Usamos unidades nas quais $c = G = 1$ e métricas com assinatura $(+, -, -, -)$. Neste capítulo e nos seguintes, os índices gregos assumem os valores $0, 1, 2, 3$; nas equações vírgula indica derivada comum e ponto e vírgula indica derivada covariante.

2.1 Equações geodésicas

Dada uma métrica com elemento de linha geral na forma:

$$\mathrm{d}s^2 = g_{\mu\nu}(x^\lambda)\mathrm{d}x^\mu\mathrm{d}x^\nu, \tag{2.1}$$

o movimento de uma partícula-teste num campo gravitacional descrito pela métrica Eq. (2.1) segue uma trajetória geodésica cujas equações de movimento são dadas por:

$$\ddot{x}^\mu + \Gamma^\mu{}_{\alpha\beta}\dot{x}^\alpha\dot{x}^\beta = 0, \tag{2.2}$$

onde os pontos indicam derivada em relação ao tempo próprio τ e os símbolos de Christoffel definem-se por:

$$\Gamma^\mu{}_{\alpha\beta} = \frac{1}{2}g^{\mu\lambda}\left(g_{\lambda\beta,\alpha} + g_{\alpha\lambda,\beta} - g_{\alpha\beta,\lambda}\right). \tag{2.3}$$

As equações geodésicas podem também ser obtidas a partir da Lagrangeana:

$$\mathcal{L} = \frac{1}{2}g_{\mu\nu}\frac{dx^\mu}{d\tau}\frac{dx^\nu}{d\tau}, \tag{2.4}$$

5

e das equações de Euler-Lagrange:

$$\frac{d}{d\tau}\left(\frac{\partial \mathcal{L}}{\partial \dot{x}^\mu}\right) - \frac{\partial \mathcal{L}}{\partial x^\mu} = 0. \tag{2.5}$$

Quando os coeficientes do tensor métrico independem de uma certa coordenada x^α, a correspondente equação de Lagrange fornece o momento generalizado conservado

$$\frac{\partial \mathcal{L}}{\partial \dot{x}^\alpha} = \text{cte}. \tag{2.6}$$

Obtém-se o limite Newtoniano das Eq. (2.2) considerando que as partículas movem-se lentamente e que os campos gravitacionais sejam fracos. A primeira condição implica $\dot{x}^i \ll \dot{t}$, onde $\dot{x}^i$ são os componentes espaciais da quadrivelocidade. A condição de campos fracos é descrita por:

$$g_{\mu\nu} = \eta_{\mu\nu} + h_{\mu\nu}, \tag{2.7}$$

onde $\eta_{\mu\nu}$ é a métrica de Minkowski e $|h_{\mu\nu}| \ll 1$. Com estas restrições, as Eq. (2.2) reduzem-se a:

$$\frac{d^2 x^i}{dt^2} = -\frac{1}{2}\frac{\partial h_{tt}}{\partial x^i}, \tag{2.8}$$

que quando comparada à equação Newtoniana de movimento num potencial gravitacional Φ fornece a relação $h_{tt} = 2\Phi$.

2.2 Formalismo de Tetradas

Em alguns problemas torna-se vantajoso a escolha de uma base de tetradas (*vierbeine*) constituída por quatro quadrivetores linearmente independentes e projetar as grandezas físicas convenientes nesta base. Um desenvolvimento detalhado deste formalismo pode ser encontrado em [41].

Em cada ponto do espaço-tempo definimos uma base de quatro vetores contravariantes $e_{(a)}{}^\mu$, onde os índices entre parênteses denotam os índices da tetrada e os índices sem parênteses referem-se aos índices do tensor. Associados aos vetores contravariantes temos os vetores covariantes: $e_{(a)\mu} = g_{\mu\nu}e_{(a)}{}^\nu$. Definimos ainda a inversa $e^{(b)}{}_\mu$ da matriz $[e_{(a)}{}^\mu]$ de modo que:

$$e_{(a)}{}^\mu e^{(b)}{}_\mu = \delta^{(b)}{}_{(a)} \quad \text{e} \quad e_{(a)}{}^\mu e^{(a)}{}_\nu = \delta^\mu{}_\nu. \tag{2.9}$$

Assumimos ainda que $e_{(a)}{}^\mu e_{(b)\mu} = \eta_{(a)(b)}$, onde $\eta_{(a)(b)}$ é a matriz diagonal com elementos diagonais $(1, -1, -1, -1)$. Com isto temos:

$$\eta_{(a)(b)} e^{(a)}{}_\mu = e_{(b)\mu}, \quad \eta^{(a)(b)} e_{(a)\mu} = e^{(b)}{}_\mu, \tag{2.10}$$

além da importante propriedade $e_{(a)\mu} e^{(a)}{}_\nu = g_{\mu\nu}$.

Dado um vetor ou tensor, projetamo-lo na base de tetradas para obtermos seus componentes de tetradas da seguinte maneira:

$$A_{(a)} = e_{(a)\mu} A^\mu = e_{(a)}{}^\mu A_\mu,$$
$$T_{(a)(b)} = e_{(a)\mu} e_{(b)\nu} T^{\mu\nu} = e_{(a)}{}^\mu e_{(b)}{}^\nu T_{\mu\nu}. \tag{2.11}$$

2.3 Tensor energia-momento de fluidos

O tensor energia-momento de matéria na ausência de forças externas e tensões internas é dado por:

$$M^{\mu\nu} = \rho u^\mu u^\nu, \tag{2.12}$$

onde ρ é definido como a densidade de energia da matéria. Havendo tensões internas adiciona-se à Eq. (2.12) um tensor de tensões simétrico $S^{\mu\nu}$, que deve ser ortogonal à quadrivelocidade: $S^{\mu\nu} u_\nu = 0$. No caso particular de um fluido perfeito com pressão isotrópica P, a forma mais simples para $S^{\mu\nu}$ consiste em tomar a combinação linear entre $g^{\mu\nu}$ e $u^\mu u^\nu$:

$$S^{\mu\nu} = P(\alpha u^\mu u^\nu + \beta g^{\mu\nu}). \tag{2.13}$$

A condição de ortogonalidade fornece $\beta = -\alpha$. Escolhendo-se $\alpha = 1$, obtém-se o tensor energia-momento $T^{\mu\nu}$ para um fluido perfeito:

$$T^{\mu\nu} = (P + \rho) u^\mu u^\nu - P g^{\mu\nu}. \tag{2.14}$$

Note-se que $T^t_t = \rho$ e $T^i_i = -P$, onde o índice i refere-se aos componentes espaciais.

Se o tensor energia-momento tiver componentes não-diagonais não-nulos, pode-se escrevê-lo na forma canônica em termos de seus autovalores e autovetores, resolvendo-se $T^\mu_\nu e^\nu = \lambda e^\mu$. Em alguns modelos de discos estudados nesta tese, o tensor energia-momento assume a forma:

$$T^\mu_\nu = \begin{pmatrix} T^t_t & 0 & 0 & 0 \\ 0 & T^r_r & T^r_z & 0 \\ 0 & T^z_r & T^z_z & 0 \\ 0 & 0 & 0 & T^\varphi_\varphi \end{pmatrix}. \tag{2.15}$$

Após a diagonalização, tem-se:

$$T^{\mu\nu} = \rho e_{(t)}{}^{\mu} e_{(t)}{}^{\nu} + P_{+} e_{(+)}{}^{\mu} e_{(+)}{}^{\nu} + P_{-} e_{(-)}{}^{\mu} e_{(-)}{}^{\nu} + P_{\varphi} e_{(\varphi)}{}^{\mu} e_{(\varphi)}{}^{\nu}, \quad (2.16)$$

onde $\{e_{(t)}{}^{\mu}, e_{(+)}{}^{\mu}, e_{(-)}{}^{\mu}, e_{(\varphi)}{}^{\mu}\}$ são os autovetores (base de tetradas), e

$$\begin{aligned}
\rho &= T_t^t, \qquad e_{(t)}{}^{\mu} = N_t(1,0,0,0), \\
\lambda_{\pm} &= \frac{(T_r^r + T_z^z)}{2} \pm \frac{1}{2}\sqrt{(T_r^r - T_z^z)^2 + 4T_z^r T_r^z}, \\
P_{\pm} &= -\lambda_{\pm}, \quad e_{(\pm)}{}^{\mu} = N_{\pm}\left(0, 1, \frac{\lambda_{\pm} - T_r^r}{T_z^r}, 0\right), \\
P_{\varphi} &= -T_{\varphi}^{\varphi}, \qquad e_{(\varphi)}{}^{\mu} = N_{\varphi}(0,0,0,1), \qquad\qquad (2.17)
\end{aligned}$$

onde $N_t, N_{\pm}, N_{\varphi}$ são fatores de normalização.

2.4   Equações de Einstein e Einstein-Maxwell

As equações de Einstein do campo gravitacional escrevem-se:

$$G_{\mu\nu} \equiv R_{\mu\nu} - \frac{1}{2}R g_{\mu\nu} = 8\pi T_{\mu\nu}, \qquad\qquad (2.18)$$

onde $G_{\mu\nu}$ é definido como o tensor de Einstein, $R_{\mu\nu}$ e R são, respectivamente, o tensor e o escalar de Ricci e $T_{\mu\nu}$ é o tensor energia-momento da matéria. O tensor de Ricci é obtido a partir do tensor de curvatura de Riemann:

$$R^{\rho}{}_{\mu\sigma\nu} = \Gamma^{\rho}{}_{\mu\nu,\sigma} - \Gamma^{\rho}{}_{\mu\sigma,\nu} + \Gamma^{\lambda}{}_{\mu\nu}\Gamma^{\rho}{}_{\lambda\sigma} - \Gamma^{\lambda}{}_{\mu\sigma}\Gamma^{\rho}{}_{\lambda\nu}, \qquad (2.19)$$

de acordo com $R_{\mu\nu} = R^{\rho}{}_{\mu\rho\nu}$, e o escalar de Ricci calcula-se a partir de $R = R^{\mu}{}_{\mu}$. Uma forma alternativa das Eq. (2.18) é:

$$R_{\mu\nu} = 8\pi\left(T_{\mu\nu} - \frac{1}{2}T g_{\mu\nu}\right), \text{ onde } T = T^{\mu}{}_{\mu}. \qquad (2.20)$$

No caso de espaços-tempo riemannianos, o tensor de curvatura satisfaz as seguintes identidades:

$$R^{\rho}{}_{\mu\sigma\nu} + R^{\rho}{}_{\sigma\nu\mu} + R^{\rho}{}_{\nu\mu\sigma} = 0 \quad \text{(identidade cíclica)}, \qquad (2.21)$$

$$R^{\rho}{}_{\mu\sigma\nu;\lambda} + R^{\rho}{}_{\mu\nu\lambda;\sigma} + R^{\rho}{}_{\mu\lambda\sigma;\nu} = 0 \quad \text{(identidade de Bianchi.)} \qquad (2.22)$$

Em conseqüência da identidade de Bianchi tem-se $G^{\mu}{}_{\nu;\mu} = 0$, o que implica nas equações $T^{\mu}{}_{\nu;\mu} = 0$, que determinam a dinâmica da matéria e

dos campos materiais. Vê-se assim como as equações para o movimento da matéria (fonte do campo gravitacional) estão automaticamente incluídas nas equações do campo gravitacional (ao contrário do que ocorre no eletromagnetismo).

A equação de Poisson pode ser obtida a partir do componente tt das Eq. (2.20), impondo as condições de baixas velocidades e campos fracos. O tensor energia-momento para um fluido perfeito Eq. (2.14) fornece $T_{tt} \approx \rho u_t u_t \approx \rho$ e $T = \rho - 3P$. Temos então:

$$R_{tt} \approx 4\pi(\rho + 3P). \tag{2.23}$$

Usando a Eq. (2.7) e a definição do tensor de Ricci, o componente R_{tt} reduz-se a:

$$R_{tt} \approx \frac{1}{2}\nabla^2 h_{tt}. \tag{2.24}$$

Comparando-se a Eq. (2.23) com a Eq. (2.24) e usando a relação $h_{tt} = 2\Phi$, obtemos a equação $\nabla^2\Phi = 4\pi(\rho + 3P)$. O termo entre parênteses pode ser denominado "densidade efetiva" Newtoniana ρ_N. Na matéria comum, a pressão (P/c^2 em unidades não geométricas) é muito menor do que a densidade de energia, assim temos $\rho_N \approx \rho$. Quando o fluido é anisotrópico, a "densidade efetiva" Newtoniana será dada por:

$$\rho_N = \rho + \sum_i P_i, \tag{2.25}$$

onde os P_i são as pressões ao longo das direções espaciais principais.

Na presença de campos eletromagnéticos, às equações para o campo gravitacional devem ser acrescentadas as equações de Maxwell escritas na forma manifestamente covariante:

$$F^{\mu\nu}{}_{;\mu} = 4\pi J^\nu, \tag{2.26a}$$

$$F_{\alpha\beta;\gamma} + F_{\gamma\alpha;\beta} + F_{\beta\gamma;\alpha} = 0, \tag{2.26b}$$

$$F_{\mu\nu} = A_{\nu,\mu} - A_{\mu,\nu}, \tag{2.26c}$$

onde $F_{\mu\nu}$ é o tensor campo eletromagnético, A_μ é o quadrivetor potencial e J^μ o quadrivetor densidade de corrente. No caso eletrostático, existe um sistema de coordenadas no qual o quadrivetor potencial pode ser expresso como $A_\mu = (\phi, 0, 0, 0)$, sendo ϕ o potencial elétrico. O tensor energia-momento do campo eletromagnético na ausência de cargas assume a forma:

$$T^{(\text{e.m.})}_{\mu\nu} = \frac{1}{4\pi}\left(F_\mu{}^\sigma F_{\sigma\nu} + \frac{1}{4}g_{\mu\nu}F_{\rho\sigma}F^{\rho\sigma}\right). \tag{2.27}$$

Na presença de cargas elétricas, o tensor energia-momento Eq. (2.27) não satisfaz a relação $T^{\mu\nu(\text{e.m.})}_{;\mu} = 0$; logo para satisfazê-la o termo à direita das equações de Einstein (2.18) deve conter a soma do tensor energia-momento do campo eletromagnético Eq. (2.27) e do tensor energia-momento das partículas portadoras de carga. No caso de matéria constituída por poeira carregada, o tensor energia-momento das partículas assume a forma $T^{\mu\nu(\text{mat.})} = \rho u^\mu u^\nu$.

Capítulo 3

Algumas Soluções Exatas em Relatividade Geral

Neste capítulo discutimos algumas soluções exatas das equações de Einstein em coordenadas de Weyl e coordenadas isotrópicas. Apresentamos algumas soluções para esferas de fluido em coordenadas isotrópicas e ainda discutiremos uma classe especial de métricas conformastáticas. Todas estas soluções serão usadas posteriormente para a construção de modelos de discos pelo método inverso. O livro de Stephani *et al* [42] é a referência secundária padrão para soluções exatas em Relatividade Geral.

3.1 Coordenadas esféricas canônicas

O elemento de linha em coordenadas esféricas canônicas $(t, \mathsf{r}, \theta, \varphi)$ é dado por:

$$\mathrm{d}s^2 = A(\mathsf{r})\mathrm{d}t^2 - B(\mathsf{r})\mathrm{d}\mathsf{r}^2 - \mathsf{r}^2(\mathrm{d}\theta^2 + \sin^2\theta\,\mathrm{d}\varphi^2). \tag{3.1}$$

Como referência, a solução de Schwarzschild é dada por:

$$A(\mathsf{r}) = 1 - \frac{2m}{\mathsf{r}}, \qquad B(\mathsf{r}) = \frac{1}{1 - \frac{2m}{\mathsf{r}}}. \tag{3.2}$$

A solução de Reissner-Nordström, que representa um buraco negro estático com massa m e carga elétrica Q escreve-se como:

$$A(\mathsf{r}) = 1 - \frac{2m}{\mathsf{r}} + \frac{Q^2}{\mathsf{r}^2}, \qquad B(\mathsf{r}) = \frac{1}{1 - \frac{2m}{\mathsf{r}} + \frac{Q^2}{\mathsf{r}^2}}. \tag{3.3}$$

O potencial elétrico ϕ expressa-se por $\phi = Q/\mathsf{r}$.

3.2 Coordenadas de Weyl

A métrica que descreve um espaço-tempo estático com simetria axial pode ser expressa de maneira geral como [43, 44]:

$$ds^2 = e^\Phi dt^2 - e^{-\Phi} \left[e^\Lambda (dr^2 + dz^2) + r^2 d\varphi^2 \right], \tag{3.4}$$

onde (t, r, z, φ) são coordenadas quase-cilíndricas e Φ e Λ são funções de r, z. As equações de Einstein (2.18) no vácuo para a métrica Eq. (3.4) reduzem-se a:

$$\nabla^2 \Phi = \Phi_{,rr} + \frac{\Phi_{,r}}{r} + \Phi_{,zz} = 0, \tag{3.5a}$$

$$\Lambda = \frac{1}{2} \int r \left[(\Phi_{,r}^2 - \Phi_{,z}^2) dr + 2\Phi_{,r}\Phi_{,z} dz \right]. \tag{3.5b}$$

A função Φ está relacionada com o potencial Newtoniano U por $\Phi = 2U$. Uma propriedade importante da métrica de Weyl é o fato de a Eq. (3.5a) ser a equação de Laplace em coordenadas cilíndricas, que por ser linear permite a sobreposição de soluções. A outra função métrica Λ é não-linear, porém usando-se a Eq. (3.5b) pode-se mostrar facilmente que:

$$\Lambda[\Phi_1 + \Phi_2] = \Lambda[\Phi_1] + \Lambda[\Phi_2] + 2\Lambda[\Phi_1, \Phi_2], \tag{3.6}$$

com

$$\Lambda[\Phi_1, \Phi_2] = \frac{1}{2} \int r \left[(\Phi_{1,r}\Phi_{2,r} - \Phi_{1,z}\Phi_{2,z}) dr + (\Phi_{1,r}\Phi_{2,z} + \Phi_{1,z}\Phi_{2,r}) dz \right], \tag{3.7}$$

onde Φ_1 e Φ_2 são soluções da Eq. (3.5a).

Algumas das soluções assintoticamente planas das Eq. (3.5a)–(3.5b) são listadas a seguir.

3.2.1 Solução de Chazy-Curzon

A solução para uma partícula com massa m na posição $z = z_0$ é dada por [45, 46]:

$$\Phi = -\frac{2m}{R}, \qquad \Lambda = -\frac{m^2 r^2}{R^4}, \tag{3.8}$$

onde $R = \sqrt{r^2 + (z - z_0)^2}$. Em alguns casos é conveniente expressar a função Φ na forma:

$$\Phi = \lim_{\alpha \to 0} \frac{m}{\alpha} \ln \left(\frac{z_0 - \alpha - z + \sqrt{r^2 + (z_0 - \alpha - z)^2}}{z_0 + \alpha - z + \sqrt{r^2 + (z_0 + \alpha - z)^2}} \right). \tag{3.9}$$

3.2.2 Solução para uma barra finita

Tomando-se o potencial Newtoniano para uma barra homogênea com densidade linear de massa λ e cujas extremidades possuem coordenadas $z = z_1$, $z = z_2$, $z_1 < z_2$, as funções métricas Φ e Λ escrevem-se:

$$\Phi = -2\lambda \ln\left(\frac{\mu_2}{\mu_1}\right), \tag{3.10}$$

$$\Lambda = 4\lambda^2 \ln\left[\frac{(r^2 + \mu_1\mu_2)^2}{(r^2 + \mu_1^2)(r^2 + \mu_2^2)}\right], \tag{3.11}$$

onde definimos $\mu_1 = z_1 - z + \sqrt{r^2 + (z_1 - z)^2}$ e $\mu_2 = z_2 - z + \sqrt{r^2 + (z_2 - z)^2}$. A função Eq. (3.11) obtém-se com o uso da relação Eq. (3.6):

$$\Lambda[\ln\mu_2 - \ln\mu_1] = \Lambda[\ln\mu_2] + \Lambda[\ln\mu_1] - 2\Lambda[\ln\mu_1, \ln\mu_2], \tag{3.12}$$

e dos resultados [7]:

$$\Lambda[\ln\mu_i] = \ln\left(\frac{\mu_i^2}{r^2 + \mu_i^2}\right), \qquad \Lambda[\ln\mu_1, \ln\mu_2] = \ln(\mu_1 - \mu_2). \tag{3.13}$$

3.2.3 Solução de Schwarzschild

A solução de Schwarzschild em coordenadas de Weyl pode ser expressa na forma [43]:

$$\Phi = \ln\left(\frac{R_1 + R_2 - 2m}{R_1 + R_2 + 2m}\right), \qquad \Lambda = \ln\left[\frac{(R_1 + R_2)^2 - 4m^2}{4R_1 R_2}\right], \tag{3.14}$$

onde $R_1 = \sqrt{r^2 + (m - z)^2}$ e $R_2 = \sqrt{r^2 + (m + z)^2}$. Esta solução pode ainda ser escrita em termos de $\mu_3 = m - z + \sqrt{r^2 + (m - z)^2}$ e $\mu_4 = -m - z + \sqrt{r^2 + (m + z)^2}$, usando-se as seguintes identidades [22]:

$$R_1 = \frac{\mu_3^2 + r^2}{2\mu_3}, \qquad m - z = \frac{\mu_3^2 - r^2}{2\mu_3},$$

$$R_2 = \frac{\mu_4^2 + r^2}{2\mu_4}, \qquad -m - z = \frac{\mu_4^2 - r^2}{2\mu_4}. \tag{3.15}$$

Assim,

$$\Phi = \ln\left(\frac{\mu_4}{\mu_3}\right), \qquad \Lambda = \ln\left[\frac{(r^2 + \mu_3\mu_4)^2}{(r^2 + \mu_3^2)(r^2 + \mu_4^2)}\right]. \tag{3.16}$$

Comparando-se as Eq. (3.16) com Eq. (3.10)–(3.11), observa-se que a solução de Schwarzschild em coordenadas de Weyl pode ser interpretada como uma barra centrada na origem com comprimento $2m$ e densidade linear $\lambda = 1/2$.

3.3 Coordenadas Isotrópicas

O elemento de linha em coordenadas isotrópicas com simetria esférica (t, r, θ, φ) pode ser expresso como:

$$\mathrm{d}s^2 = e^\nu \mathrm{d}t^2 - e^\lambda \left[\mathrm{d}r^2 + r^2(\mathrm{d}\theta^2 + \sin^2\theta \mathrm{d}\varphi^2) \right], \qquad (3.17)$$

onde ν e λ são funções de r. Aplicando-se a lei de transformação do tensor métrico de coordenadas esféricas canônicas para coordenadas esféricas isotrópicas, obtém-se a seguinte equação diferencial entre a coordenada radial isotrópica r e a coordenada radial canônica r:

$$\frac{\mathrm{d}\mathsf{r}}{\mathrm{d}r} = \frac{\mathsf{r}}{\sqrt{B(\mathsf{r})}r}. \qquad (3.18)$$

No caso da solução de Schwarzschild, a Eq. (3.18) fornece a relação:

$$\mathsf{r} = r \left(1 + \frac{m}{2r} \right)^2, \qquad (3.19)$$

o que permite obter a solução de Schwarzschild em coordenadas isotrópicas:

$$e^\nu = \frac{\left(1 - \frac{m}{2r} \right)^2}{\left(1 + \frac{m}{2r} \right)^2}, \qquad e^\lambda = \left(1 + \frac{m}{2r} \right)^4. \qquad (3.20)$$

Para a solução de Reissner-Nordström Eq. (3.3), a relação entre as coordenadas radiais é da forma:

$$\mathsf{r} = r \left(1 + \frac{m}{2r} \right)^2 - \frac{Q^2}{4r}, \qquad (3.21)$$

o que permite expressar a solução de Reissner-Nordström em coordenadas isotrópicas:

$$e^\nu = \frac{\left[1 - \frac{(m^2 - Q^2)}{4r^2} \right]^2}{\left(1 + \frac{m+Q}{2r} \right)^2 \left(1 + \frac{m-Q}{2r} \right)^2}, \quad e^\lambda = \left(1 + \frac{m+Q}{2r} \right)^2 \left(1 + \frac{m-Q}{2r} \right)^2,$$

$$(3.22)$$

com o potencial elétrico dado por:

$$\phi = \frac{Q}{r \left(1 + \frac{m}{2r} \right)^2 - \frac{Q^2}{4r}}. \qquad (3.23)$$

3.3.1 Esferas de fluido perfeito em coordenadas isotrópicas

Seja um fluido perfeito com tensor energia-momento dado pela Eq. (2.14). As equações de Einstein (2.18) para a métrica Eq. (3.17) reduzem-se a:

$$8\pi\rho = -\frac{1}{e^\lambda}\left(\lambda'' + \frac{\lambda'^2}{4} + \frac{2\lambda'}{r}\right), \tag{3.24a}$$

$$8\pi P = \frac{1}{2e^\lambda}\left(\lambda'' + \nu'' + \frac{\nu'^2}{2} + \frac{\lambda' + \nu'}{r}\right), \tag{3.24b}$$

$$8\pi P = \frac{1}{e^\lambda}\left(\frac{\lambda'^2}{4} + \frac{\lambda'\nu'}{2} + \frac{\lambda' + \nu'}{r}\right). \tag{3.24c}$$

Igualando-se Eq. (3.24b) e Eq. (3.24c) e definindo $w = e^{\nu/2}$, obtém-se a seguinte equação diferencial [47]:

$$w'' - \left(\lambda' + \frac{1}{r}\right)w' + \left(\frac{\lambda''}{2} - \frac{\lambda'^2}{4} - \frac{\lambda'}{2r}\right)w = 0. \tag{3.25}$$

Dada uma forma funcional para a função métrica λ, a Eq. (3.25) torna-se uma EDO linear de segunda ordem para w.

Tendo sido encontrada uma solução da Eq. (3.25), certas condições físicas devem ser impostas: a densidade e pressão devem ser funções não-negativas e monotonicamente decrescentes no interior da esfera de fluido, a velocidade de propagação do som $v_s^2 = dP/d\rho$ deve satisfazer $0 < v_s^2 \leq 1$. Além disso, na superfície da esfera de fluido, caracterizada pelo raio no qual a pressão P se anula, a solução interior deve ser ajustada à solução de Schwarzschild Eq. (3.20), impondo continuidade das funções métricas e^λ e e^ν e de suas derivadas primeiras em relação ao raio [47, 48].

Numerosas soluções para esferas de fluido em coordenadas isotrópicas foram apresentadas por Kuchowicz [48], inclusive as encontradas por Narlikar *et al* [47], originalmente publicadas num periódico pouco acessível. Discutiremos duas soluções simples que foram usadas para construir discos de fluido perfeito com halos (Apêndice A).

Solução de Buchdahl

Buchdahl [49] assumiu uma forma para as funções métricas semelhante à solução de Schwarzschild:

$$e^\nu = \frac{[1 - f(r)]^2}{[1 + f(r)]^2}, \qquad e^\lambda = [1 + f(r)]^4. \tag{3.26}$$

Com isto, a Eq. (3.25) reduz-se a:

$$ff'' - 3f'^2 - \frac{ff'}{r} = 0, \tag{3.27}$$

cuja solução é:

$$f = \frac{A}{\sqrt{1 + kr^2}}, \tag{3.28}$$

onde A e k são constantes. A densidade, pressão e equação de estado são dadas por:

$$\rho = \frac{3Ak}{2\pi \left(A + \sqrt{1 + kr^2}\right)^5}, \tag{3.29a}$$

$$P = \frac{kA^2}{2\pi \left(-A + \sqrt{1 + kr^2}\right) \left(A + \sqrt{1 + kr^2}\right)^5}, \tag{3.29b}$$

$$P = \frac{(2\pi)^{1/5} A}{3} \frac{\rho^{6/5}}{(3Ak)^{1/5} - 2A(2\pi\rho)^{1/5}}. \tag{3.29c}$$

Nota-se uma certa semelhança entre a Eq. (3.29c) e a equação politrópica Newtoniana $P = \kappa\rho^{6/5}$. Como a Eq. (3.29b) não possui raízes, a esfera de fluido de Buchdahl estende-se por todo o espaço.

Solução interior de Schwarzschild

A solução interior de Schwarzschild em coordenadas isotrópicas é obtida tomando-se:

$$\frac{\lambda''}{2} - \frac{\lambda'^2}{4} - \frac{\lambda'}{2r} = 0. \tag{3.30}$$

As soluções das Eq. (3.30) e Eq. (3.25) são, respectivamente,

$$e^\lambda = \frac{1}{(A_2 + A_1 r^2)^2}, \qquad e^\nu = \frac{(B_2 + B_1 r^2)^2}{(A_2 + A_1 r^2)^2}, \tag{3.31}$$

onde A_i e B_i são constantes. A densidade e pressão são dadas por:

$$\rho = \frac{3A_1 A_2}{2\pi}, \tag{3.32a}$$

$$P = \frac{A_2^2 B_1 + A_1^2 B_2 r^2 - 2A_1 A_2 (B_2 + B_1 r^2)}{2\pi (B_2 + B_1 r^2)}. \tag{3.32b}$$

As condições de continuidade das funções métricas Eq. (3.20) e Eq. (3.31) e de suas derivadas primeiras em relação ao raio no raio r_b tal que $P(r_b) = 0$ fornecem as expressões para as constantes:

$$A_1 = \frac{4m}{(m + 2r_b)^3}, \qquad\qquad A_2 = \frac{8r_b^3}{(m + 2r_b)^3},$$
$$B_1 = \frac{4m(4r_b - m)}{(m + 2r_b)^4}, \qquad\qquad B_2 = \frac{16r_b^3(r_b - m)}{(m + 2r_b)^4}. \tag{3.33}$$

3.4 Métricas conformastáticas

Esta classe de métricas constitui uma interessante solução das equações de Einstein-Maxwell. Consideremos a seguinte forma para a métrica:

$$\mathrm{d}s^2 = V^{-2}(x, y, z)\mathrm{d}t^2 - V^2(x, y, z)\left(\mathrm{d}x^2 + \mathrm{d}y^2 + \mathrm{d}z^2\right). \tag{3.34}$$

Substituindo a Eq. (3.34) nas equações de Einstein-Maxwell Eq. (2.18) e (2.26a)–(2.26c), com:

$$T_{\mu\nu} = T_{\mu\nu}^{\mathrm{mat.}} + T_{\mu\nu}^{\mathrm{e.m.}}, \tag{3.35}$$

onde $T_{\mu\nu}^{\mathrm{mat.}} = \rho u_\mu u_\nu$, $T_{\mu\nu}^{\mathrm{e.m.}}$ dado pela Eq. (2.27) e $J^\nu = \sigma\delta_t^\nu V$, estas são satisfeitas contanto que (a) V seja solução da equação de Poisson não-linear:

$$\nabla^2 V = -4\pi\rho V^3, \tag{3.36}$$

(b) a relação entre a função $V(x, y, z)$ e o potencial elétrico $\phi(x, y, z)$ seja da forma:

$$\phi = \pm\frac{1}{V} + \mathrm{const.}, \tag{3.37}$$

e (c) a relação entre a densidade de massa ρ e a densidade de carga σ seja $\rho = \pm\sigma$. Assim, esta solução descreve um espaço-tempo no qual matéria em forma de poeira possui densidade de massa igual à densidade de carga (nas unidades adotadas). Esta poeira encontra-se em equilíbrio pois a atração gravitacional é contrabalançada pela repulsão eletrostática. Em princípio, distribuições de matéria com forma arbitrária podem ser construídas (ver, por exemplo, [50–54] para algumas destas distribuições). Na ausência de matéria, a Eq. (3.36) reduz-se à equação de Laplace para V. A linearidade da equação de Laplace pode então ser usada para construir soluções que representam buracos negros extremos de Reissner-Nordström em posições arbitrárias em equilíbrio [55, 56].

17

Capítulo 4

Construção de Discos pelo Método Inverso

O objetivo deste capítulo é apresentar o método inverso usado para construir modelos de discos finos e grossos tanto na teoria Newtoniana quanto em Relatividade Geral. No caso de discos finos este procedimento é conhecido como método "deslocar, cortar e refletir" (Sec. 4.1) e é semelhante ao método das imagens usado comumente em eletrostática. A fim de obter discos com espessura arbitrária, é necessário modificar o procedimento adicionando um passo intermediário, o assim denominado método "deslocar, cortar, encher e refletir". Discutimos inicialmente o caso de discos infinitesimalmente finos. O formalismo para o tratamento de campos tensoriais como distribuições é brevemente apresentado na Sec. 4.2. Este formalismo permite o cálculo das propriedades da matéria que constitui o disco a partir do tensor métrico. Outras propriedades físicas de interesse para a análise dos discos são expostas na Sec. 4.3. Na Sec. 4.4 mostramos como adicionar espessura arbitrária aos discos. Alguns pares potencial-densidade Newtonianos usados na Astrononia Galáctica são apresentados na Sec. 4.5.

4.1   O método "deslocar, cortar e refletir"

Um procedimento simples para obter o potencial gravitacional de um disco foi introduzido por Kuzmin [57]. Consideremos o potencial:

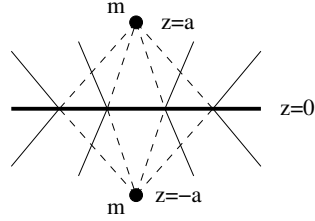$$\Phi = -\frac{Gm}{\sqrt{r^2 + (a + |z|)^2}}.$$

(4.1)

Figura 4.1: Interpretação do potencial Eq. (4.1). O potencial em $z > 0$ e $z < 0$ é o mesmo que seria gerado por uma massa pontual em $z = -a$ e $z = a$, respectivamente.
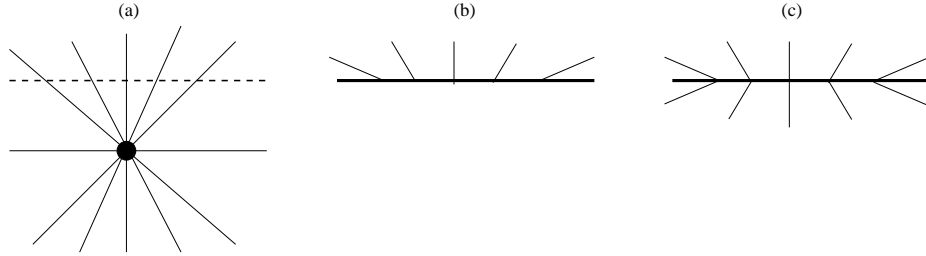
Figura 4.2: Ilustração do método "deslocar, cortar e refletir" para a construção de discos finos. (a) O espaço com a fonte ou singularidade é cortado pela superfície (linha tracejada). (b) A parte contendo a fonte é descartada. (c) O espaço sem a fonte é refletido usando a superfície.

Conforme mostra a Fig. 4.1, na região $z < 0$, Φ é idêntico ao potencial de uma massa pontual localizada em $(r, z) = (0, a)$ e em $z > 0$, Φ coincide com o potencial de uma massa pontual em $(r, z) = (0, -a)$. Logo Φ satisfaz a equação de Laplace exceto no plano $z = 0$. Aplicando o teorema de Gauss a um volume que contém um pequeno pedaço do plano $z = 0$ obtém-se a correspondente densidade superficial de massa:

$$\sigma_N = \frac{1}{2\pi G}\, \Phi_{,z}^+\big|_{z=0} = \frac{am}{2\pi(r^2 + a^2)^{3/2}}. \tag{4.2}$$

De maneira esquemática, pode-se descrever o procedimento de Kuzmin da seguinte forma (Fig. 4.2): escolhemos uma superfície (no caso, o plano $z = 0$) que divide o espaço em duas partes: uma sem singularidades ou fontes e outra com as singularidades. Descartamos em seguida a parte com as singularidades. Finalmente, fazemos uma inversão da parte não-singular usando a superfície. O resultado será um espaço com uma singularidade descrita por uma distribuição de Dirac com suporte na superfície. Este
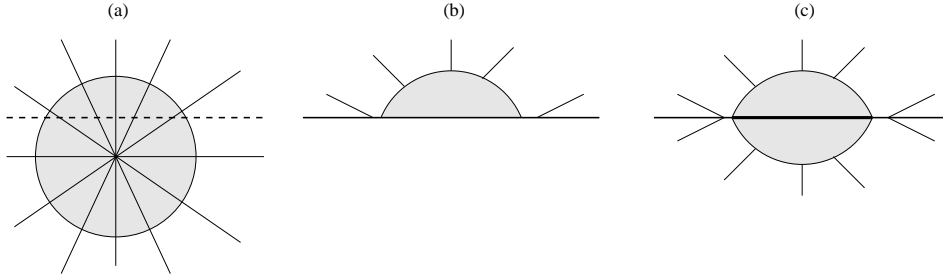
20

Figura 4.3: Ilustração do método "deslocar, cortar e refletir" para a construção de discos finos com halos. (a) A esfera de fluido é cortada pela superfície (linha tracejada). (b) A parte inferior que contém o centro da esfera é descartada. (c) O espaço com a calota é refletido usando a superfície.

procedimento é conhecido como método "deslocar, cortar e refletir". Matematicamente, consiste em aplicar a transformação $z \rightarrow |z| + a$, onde a é uma constante positiva, a um potencial gravitacional.

O mesmo procedimento também pode ser usado para gerar discos com halos (Fig. 4.3). Neste caso, uma esfera de fluido é cortada por um plano a uma distância do centro menor que o raio da esfera. A parte do espaço contendo o centro da esfera é descartada, e a outra parte é refletida usando a superfície. O resultado será um disco com um halo central. A parte do disco dentro do halo terá propriedades diferentes da parte externa ao halo. Se o método for aplicado a uma esfera de fluido perfeito em coordenadas isotrópicas (Sec. 3.3.1), o resultado será um disco de fluido perfeito com um halo central.

4.2   Distribuições em espaços-tempo curvos

A transformação matemática descrita na seção anterior aplicada a um elemento de linha em Relatividade Geral leva à necessidade de tratar campos tensoriais em termos da teoria de distribuições. A teoria geral de distribuições em espaços-tempo curvos com suporte em hipersuperfícies tridimensionais foi desenvolvida por Hamoui e Papapetrou [58], Lichnerowicz [59] e Taub [60]. Seguimos a exposição de Taub e particularizamos a teoria para o caso de discos.

O disco localizado no plano $z = 0$ divide a região Ω do espaço-tempo em duas metades Ω^+ e Ω^- onde $z > 0$ e $z < 0$, respectivamente. O tensor

métrico $g_{\mu\nu}$ é suposto ser contínuo através de $z = 0$, ou seja,

$$[g_{\mu\nu}] = g_{\mu\nu}|_{z=0^+} - g_{\mu\nu}|_{z=0^-} = 0. \tag{4.3}$$

Na vizinhança de $z = 0$ podemos expandir $g_{\mu\nu}$ em:

$$g_{\mu\nu}^{\pm} = g_{\mu\nu}^0 + z g_{\mu\nu,z}^{\pm} + \frac{1}{2} z^2 g_{\mu\nu,zz}^{\pm} + \dots, \tag{4.4}$$

onde os sinais $\pm$ referem-se à expansão acima e abaixo do disco, respectivamente. Desta maneira, pode-se caracterizar as descontinuidades na derivada primeira do tensor métrico pelo tensor $b_{\mu\nu}$, definido como:

$$b_{\mu\nu} \equiv [g_{\mu\nu,z}] = g_{\mu\nu,z}^+ \big|_{z=0} - g_{\mu\nu,z}^- \big|_{z=0}. \tag{4.5}$$

O tensor métrico é construído de forma a possuir simetria de reflexão em relação ao plano $z = 0$, o que significa $g_{\mu\nu}^-(r,z) = g_{\mu\nu}^+(r,-z)$. Esta relação implica que, quando $z \neq 0$, $g_{\mu\nu,z}^-(r,z) = -g_{\mu\nu,z}^+(r,-z)$. Assim, no limite apropriado quando $z \to 0$, a Eq. (4.5) pode ser escrita como:

$$b_{\mu\nu} = 2 g_{\mu\nu,z}|_{z=0}, \tag{4.6}$$

onde definimos $g_{\mu\nu,z}|_{z=0} = g_{\mu\nu,z}^+|_{z=0}$.

No sentido de distribuições podemos expressar os símbolos de Christoffel Eq. (2.3) como:

$$\Gamma^\alpha{}_{\beta\gamma} = (\Gamma^\alpha{}_{\beta\gamma})^D = \Gamma^{\alpha+}{}_{\beta\gamma}\theta + \Gamma^{\alpha-}{}_{\beta\gamma}(1-\theta), \tag{4.7}$$

onde θ é a função de Heaviside:

$$\theta = \begin{cases} 1, & z > 0 \\ 1/2, & z = 0 \\ 0, & z < 0 \end{cases}. \tag{4.8}$$

Derivando-se a Eq. (4.7), pode-se escrever:

$$\Gamma^\alpha{}_{\beta\gamma,\lambda} = (\Gamma^\alpha{}_{\beta\gamma,\lambda})^D + [\Gamma^\alpha{}_{\beta\gamma}]\delta^z_\lambda \delta(z), \tag{4.9}$$

onde $\delta(z)$ é a distribuição de Dirac com suporte em $z = 0$ e a descontinuidade dos símbolos de Christoffel em $z = 0$ é dada por:

$$[\Gamma^\alpha{}_{\beta\gamma}] \equiv \Gamma^{\alpha+}{}_{\beta\gamma} - \Gamma^{\alpha-}{}_{\beta\gamma} = \frac{1}{2}\left(\delta^z_\beta b^\alpha_\gamma + \delta^z_\gamma b^\alpha_\beta - g^{z\alpha} b_{\beta\gamma}\right). \tag{4.10}$$

Usando-se a definição do tensor de curvatura de Riemann Eq. (2.19), obtém-se para o tensor de Riemann distribucional:

$$R^\rho{}_{\mu\sigma\nu} = (R^\rho{}_{\mu\sigma\nu})^D + H^\rho{}_{\mu\sigma\nu}\delta(z), \tag{4.11}$$

onde:

$$\begin{aligned} H^\rho{}_{\mu\sigma\nu} &= [\Gamma^\rho{}_{\mu\nu}]\,\delta^z_\sigma - [\Gamma^\rho{}_{\mu\sigma}]\,\delta^z_\nu \\ &= \frac{1}{2}\left(\delta^z_\mu\delta^z_\sigma b^\rho_\nu - \delta^z_\mu\delta^z_\nu b^\rho_\sigma - g^{z\rho}\delta^z_\sigma b_{\mu\nu} + g^{z\rho}\delta^z_\nu b_{\mu\sigma}\right). \end{aligned} \tag{4.12}$$

Supondo que o tensor energia-momento possa ser expresso na forma:

$$T_{\mu\nu} = (T_{\mu\nu})^D + Q_{\mu\nu}\delta(z), \tag{4.13}$$

as equações de Einstein são equivalentes ao sistema:

$$R^\pm_{\mu\nu} - \frac{1}{2}g_{\mu\nu}R^\pm = 8\pi T^\pm_{\mu\nu}, \tag{4.14a}$$

$$H_{\mu\nu} - \frac{1}{2}g_{\mu\nu}H = 8\pi Q_{\mu\nu}, \tag{4.14b}$$

onde $H_{\mu\nu} = H^\rho{}_{\mu\rho\nu}$ e $H = H^\sigma{}_\sigma$. Assim, conhecendo-se a solução das Eq. (4.14a) nas regiões $\Omega^\pm$ fora do disco, pode-se calcular os componentes do tensor energia-momento da matéria do disco por meio das Eq. (4.14b). Usando a Eq. (4.12), obtemos:

$$Q^\mu_\nu = \frac{1}{16\pi}\left\{b^{z\mu}\delta^z_\nu - b^{zz}\delta^\mu_\nu + g^{z\mu}b^z_\nu - g^{zz}b^\mu_\nu + b^\rho_\rho\left(g^{zz}\delta^\mu_\nu - g^{z\mu}\delta^z_\nu\right)\right\}. \tag{4.15}$$

Para uma métrica estática geral na forma:

$$\mathrm{d}s^2 = g_{tt}(r,z)\mathrm{d}t^2 + g_{rr}(r,z)\mathrm{d}r^2 + g_{zz}(r,z)\mathrm{d}z^2 + g_{\varphi\varphi}(r,z)\mathrm{d}\varphi^2, \tag{4.16}$$

o tensor energia-momento Q^μ_ν será diagonal. Definindo a base ortonormal de tetradas:

$$e_{(t)}{}^\mu = \left(\frac{1}{\sqrt{g_{tt}}},0,0,0\right), \qquad e_{(r)}{}^\mu = \left(0,\frac{1}{\sqrt{-g_{rr}}},0,0\right),$$

$$e_{(z)}{}^\mu = \left(0,0,\frac{1}{\sqrt{-g_{zz}}},0\right), \qquad e_{(\varphi)}{}^\mu = \left(0,0,0,\frac{1}{\sqrt{-g_{\varphi\varphi}}},\right), \tag{4.17}$$

o tensor energia momento pode ser expresso como:

$$Q^{\mu\nu} = \sigma e_{(t)}{}^\mu e_{(t)}{}^\nu + P_r e_{(r)}{}^\mu e_{(r)}{}^\nu + P_z e_{(z)}{}^\mu e_{(z)}{}^\nu + P_\varphi e_{(\varphi)}{}^\mu e_{(\varphi)}{}^\nu, \tag{4.18}$$

onde a densidade superficial de energia, pressões (ou tensões) nas direções radial, direção do eixo z e azimutal são dados, respectivamente, por $\sigma = Q_t^t$, $P_r = -Q_r^r$, $P_z = -Q_z^z$ e $P_\varphi = -Q_\varphi^\varphi$. Devido ao termo $\sqrt{-g_{zz}}$ que divide a distribuição de Dirac, para obter as "verdadeiras" grandezas físicas acima elas devem ser multiplicadas por $\sqrt{-g_{zz}}$.

No caso da métrica de Weyl Eq. (3.4), usando as Eq. (4.6) e Eq. (4.15) obtemos as seguintes expressões para σ, P_φ, P_r e P_z (já multiplicadas por $\sqrt{-g_{zz}}$):

$$\sigma = \frac{1}{8\pi} e^{(\Phi - \Lambda)/2} \Phi_{,z} (2 - r\Phi_{,r}), \tag{4.19a}$$

$$P_\varphi = \frac{1}{8\pi} e^{(\Phi - \Lambda)/2} r\Phi_{,r} \Phi_{,z}, \tag{4.19b}$$

$$P_r = P_z = 0. \tag{4.19c}$$

Por não haver pressão na direção radial, a estabilidade dos discos gerados pela métrica de Weyl pode ser justificada pela hipótese de contrarotação, citada na Introdução. Neste caso define-se uma velocidade de contrarotação V das partículas no disco dada por [8]:

$$V^2 = \frac{P_\varphi}{\sigma} = \frac{r\Phi_{,r}}{2 - r\Phi_{,r}}. \tag{4.20}$$

Para a métrica em coordenadas isotrópicas cilíndricas:

$$\mathrm{d}s^2 = e^\nu \mathrm{d}t^2 - e^\lambda \left(\mathrm{d}r^2 + \mathrm{d}z^2 + r^2 \mathrm{d}\varphi^2 \right), \tag{4.21}$$

os componentes não-nulos do tensor energia-momento do disco são:

$$\sigma = -\frac{1}{4\pi} e^{-\lambda/2} \lambda_{,z} \tag{4.22a}$$

$$P_r = P_\varphi = \frac{1}{8\pi} e^{-\lambda/2} (\lambda_{,z} + \nu_{,z}) \tag{4.22b}$$

Vê-se que nestas coordenadas a isotropia entre os componentes radial e azimutal permite a construção de discos de fluido perfeito.

Os componentes do tensor energia-momento devem satisfazer certas desigualdades fisicamente razoáveis [61]. A condição fraca de energia é satisfeita se $\sigma \geq 0$, a condição dominante de energia impõe que $\sigma \geq |P_i|$, $i = r, z, \varphi$. Finalmente a condição forte de energia é satisfeita se $\rho_N = \sigma + P_r + P_z + P_\varphi \geq 0$, onde ρ_N é a "densidade efetiva" Newtoniana.

24

4.3 Outros parâmetros físicos dos discos

O estudo de órbitas geodésicas circulares no plano $z = 0$ permite obter informações importantes sobre as propriedades dos discos, sejam eles finos ou grossos. No caso da métrica geral Eq. (4.16), as equações geodésicas (2.2) fornecem a seguinte expressão para órbitas circulares:

$$\frac{\dot{\varphi}^2}{\dot{t}^2} = -\frac{g_{tt,r}}{g_{\varphi\varphi,r}}, \tag{4.23}$$

onde o ponto indica derivada em relação ao tempo próprio. Tomando a base ortonormal de tetradas Eq. (4.17) e o quadrivetor $v^\mu = (\dot{t}, 0, 0, \dot{\varphi})$, a projeção de v^μ sobre a base de tetradas fornece:

$$\mathsf{v}^{(t)} = \eta^{(t)(t)} e_{(t)\mu} v^\mu = \sqrt{g_{tt}} \dot{t}, \tag{4.24a}$$

$$\mathsf{v}^{(\varphi)} = \eta^{(\varphi)(\varphi)} e_{(\varphi)\mu} v^\mu = \sqrt{-g_{\varphi\varphi}} \dot{\varphi}. \tag{4.24b}$$

O quadrado da velocidade circular v_c medida por um observador no infinito será dada por:

$$v_c^2 = \left(\frac{\mathsf{v}^{(\varphi)}}{\mathsf{v}^{(t)}}\right)^2 = \frac{g_{\varphi\varphi} g_{tt,r}}{g_{tt} g_{\varphi\varphi,r}}, \tag{4.25}$$

onde usou-se a Eq. (4.23). Particularizando-se para as métricas de Weyl Eq. (3.4) e isotrópicas Eq. (4.21) obtém-se, respectivamente, as seguintes expressões para a velocidade circular:

$$v_c^2 = \frac{r\Phi_{,r}}{2 - r\Phi_{,r}}, \qquad v_c^2 = \frac{r^2 e^\lambda (e^\nu)_{,r}}{e^\nu (r^2 e^\lambda)_{,r}}, \tag{4.26}$$

lembrando que todas as quantidades são calculadas em $z = 0$. Outra grandeza física de interesse é o momento angular por unidade de massa $h = -g_{\varphi\varphi} \dot{\varphi}$ das partículas-teste em órbitas circulares. Substituindo a Eq. (4.23) na relação:

$$1 = g_{tt} \dot{t}^2 + g_{\varphi\varphi} \dot{\varphi}^2, \tag{4.27}$$

derivada a partir da Eq. (4.16), temos que o momento angular é expresso por:

$$h = -g_{\varphi\varphi} \sqrt{\frac{g_{tt,r}}{g_{tt,r} g_{\varphi\varphi} - g_{tt} g_{\varphi\varphi,r}}}. \tag{4.28}$$

Aplicando às métricas de Weyl Eq. (3.4) e isotrópicas Eq. (4.21) temos, respectivamente:

$$h = r^{3/2} e^{-\Phi/2} \sqrt{\frac{\Phi_{,r}}{2(1 - r\Phi_{,r})}}, \tag{4.29}$$

$$h = r^2 e^{\lambda} \sqrt{\frac{(e^{\nu})_{,r}}{e^{\nu}(r^2 e^{\lambda})_{,r} - r^2 e^{\lambda}(e^{\nu})_{,r}}}, \tag{4.30}$$

onde novamente todas as quantidades são calculadas em $z = 0$.

O momento angular permite estabelecer uma extensão relativística do critério de estabilidade de Rayleigh para um fluido em repouso num campo gravitacional [62]. Consideremos uma partícula que se move numa trajetória circular com raio $r_0 = $ cte. e com momento angular por unidade de massa $h_0 = r_0^2 \dot{\varphi}$. No referencial da partícula a força de atração gravitacional é equilibrada pela força centrífuga de módulo $F_c = h_0^2/r_0^3$. Suponhamos que a partícula seja deslocada ligeiramente para um raio $r > r_0$, com o momento angular permanecendo constante. O módulo da força centrífuga na nova posição passa a ser $F_c' = h_0^2/r^3$. Para que a partícula tenda a retornar à posição original, o valor de F_c' deve ser menor que o valor h^2/r^3 que equilibraria a força gravitacional. Assim devemos ter:

$$h^2(r) - h_0^2(r_0) > 0. \tag{4.31}$$

Expandindo $h^2(r)$ em torno de $r - r_0$, obtemos:

$$h^2(r) - h_0^2(r_0) \approx (r - r_0)\frac{dh^2}{dr} > 0 \Rightarrow \frac{dh^2}{dr} > 0, \text{ ou } h\frac{dh}{dr} > 0. \tag{4.32}$$

Lembremos que se trata de um critério de estabilidade de partículas individuais movendo-se no plano do disco. Uma análise de estabilidade mais completa deve levar em consideração o movimento coletivo das partículas do disco, o que envolve a perturbação de equações hidrodinâmicas e a solução de um problema não-trivial de autovalores (ver Apêndice B).

4.4 O método "deslocar, cortar, encher e refletir"

Na Sec. 4.1 discutimos o método inverso para construir discos com espessura infinitesimal. Uma generalização deste método foi proposta por González e Letelier [38] para gerar discos grossos e consiste no seguinte: após descartar a metade do espaço contendo as fontes ou singularidades, adiciona-se uma
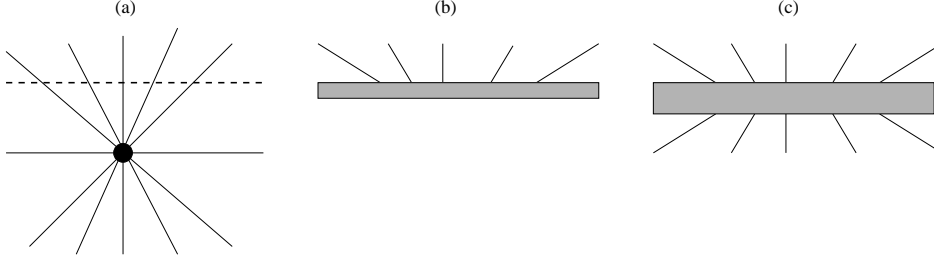
Figura 4.4: Ilustração do método "deslocar, cortar, encher e refletir" para a construção de discos grossos. (a) O espaço com a fonte ou singularidade é cortado pela superfície (linha tracejada). (b) Após descartar a metade do espaço contendo as fontes, uma camada grossa de matéria é adicionada. (c) A parte inferior da camada é usada para fazer a inversão.

camada grossa de matéria descrita por certas funções contínuas. Então, usa-se a parte inferior da camada para fazer a inversão da parte não-singular (Fig. 4.4). Este novo procedimento foi denominado método "deslocar, cortar, encher e refletir" pelos autores.

Matematicamente o método é equivalente a fazer a transformação $z \rightarrow h(z) + b$, onde $h(z)$ é uma função par e b uma constante positiva. Tomemos como exemplo o caso Newtoniano. Em coordenadas cilíndricas, o potencial Φ satisfaz a equação de Laplace:

$$\Phi_{,rr} + \frac{\Phi_{,r}}{r} + \Phi_{,zz} = 0. \tag{4.33}$$

Aplicando a transformação $z \rightarrow h(z) + b$, a Eq. (4.33) fornece:

$$\nabla^2 \Phi = h'' \Phi_{,h} + (h'^2 - 1)\Phi_{,hh}, \tag{4.34}$$

onde a linha denota derivada em relação a z. Pela equação de Poisson, a densidade de massa ρ_N associada é dada por:

$$\rho_N(r,z) = \frac{1}{4\pi G}\left[h'' \Phi_{,h} + (h'^2 - 1)\Phi_{,hh}\right]. \tag{4.35}$$

A função $h(z)$, além de par, deve ser escolhida de tal modo que $h(z)$ e $h'(z)$ sejam ambas contínuas na região $-a \leq z \leq a$, onde a espessura do disco vale $2a$. Além disso, $h'(z)$ e $h''(z)$ devem ser escolhidas de modo que a densidade de massa seja não-negativa e uma função monotonicamente decrescente em termos de r e z. Nota-se ainda pela Eq. (4.35) que, tomando $|h'| = 1$ para $|z| \geq a$, a densidade de massa se anula fora da região do disco. Partindo de

um polinômio de grau par para $h''(z)$, obtém-se a seguinte classe de funções $h(z)$ que satisfaz as restrições impostas:

$$h(z) = \begin{cases} -z + C, & z \leq a, \\ Az^2 + Bz^{2n+2}, & -a \leq z \leq a, \\ z + C, & z \geq a, \end{cases} \qquad (4.36)$$

onde:

$$A = \frac{2n+1-ac}{4na}, \quad B = \frac{ac-1}{4n(n+1)a^{2n+1}}, \quad C = -\frac{a(2n+1+ac)}{4(n+1)}, \quad (4.37)$$

$n = 1, 2, \ldots$ e c é o salto da derivada segunda em $|z| = a$. O caso particular $ac = 1$ foi o inicialmente adotado em [38].

4.5   Pares potencial-densidade como modelos de galáxias

O procedimento inverso tem sido amplamente usado para fornecer expressões analíticas simples para o campo gravitacional e distribuições de massa que se mostraram úteis na modelagem de diversas classes de galáxias e aglomerados globulares. Uma descrição ampla de tais modelos pode ser encontrada em [1] Alguns destes pares potencial-densidade são dados a seguir.

4.5.1   Modelo de Plummer

Um par potencial-densidade usado por Plummer [63] para descrever a distribuição de luminosidade em aglomerados globulares pode ser obtido fazendo-se a transformação $\mathsf{r} \to \sqrt{\mathsf{r}^2 + b^2}$ com $b > 0$ na expressão para o potencial Newtoniano de uma massa pontual em coordenadas esféricas. Disto resultam as seguintes expressões para o potencial gravitacional e a distribuição de massa:

$$\Phi(\mathsf{r}) = -\frac{Gm}{\sqrt{\mathsf{r}^2 + b^2}}, \qquad \rho_N(\mathsf{r}) = \frac{3b^2 m}{4\pi(\mathsf{r}^2 + b^2)^{5/2}}. \qquad (4.38)$$

4.5.2   Modelos de Miyamoto-Nagai

Miyamoto e Nagai [39] propuseram uma família de pares potencial-densidade adequados para descrever a distribuição de massa em galáxias espirais. O par mais simples é obtido aplicando a transformação $z \to a + \sqrt{z^2 + b^2}$ com

$a, b > 0$ ao potencial Newtoniano de uma massa m pontual em coordenadas cilíndricas. Obtém-se:

$$\Phi(r,z) = -\frac{Gm}{\left[r^2 + (a + \sqrt{z^2 + b^2})^2\right]^{1/2}}, \tag{4.39a}$$

$$\rho_N(r,z) = \frac{b^2 m}{4\pi} \frac{ar^2 + (a + 3\sqrt{z^2 + b^2})(a + \sqrt{z^2 + b^2})^2}{(z^2 + b^2)^{3/2} \left[r^2 + (a + \sqrt{z^2 + b^2})^2\right]^{5/2}}. \tag{4.39b}$$

Note-se que para $a = 0$ as expressões acima reduzem-se ao modelo de Plummer, por outro lado se $b = 0$ recuperamos o modelo de Kuzmin Eq. (4.1). Assim, o modelo de Miyamoto-Nagai permite gerar pares potencial-densidade intermediários entre os de uma esfera e um disco infinitesimalmente fino. Quanto menor for a razão b/a, maior será o grau de achatamento da distribuição de matéria. Miyamoto e Nagai ajustaram a soma de dois termos do par acima à curva de rotação da nossa galáxia e obtiveram uma razão $b/a \approx 0.1$.

Capítulo 5

Resumo dos Artigos e Conclusão

Neste capítulo descrevemos resumidamente os assuntos e resultados dos artigos publicados em periódicos durante o curso de doutorado (Sec. 5.1). Os artigos são reproduzidos nos Apêndices A a H. A conclusão do trabalho e comentários finais são apresentados na Sec. 5.2.

5.1   Resumo dos artigos

Apêndice A. Exact general relativistic perfect fluid disks with halos

O método "deslocar, cortar e refletir" (Sec. 4.1) é primeiramente aplicado à solução de Schwarzschild em coordenadas isotrópicas Eq. (3.20) para construir discos estáticos de fluido perfeito (isotropia entre pressões nas direções radial e azimutal). Impondo-se restrições sobre os parâmetros livres do disco, a condição forte de energia e velocidade de propagação do som sublumial são satisfeitos. A densidade superficial de energia e as pressões decaem rapidamente e monotonicamente com o raio de maneira a poder, em princípio, definir um raio de corte e considerar os discos finitos. O critério de estabilidade de Rayleigh mostra que as órbitas circulares de partículas-teste no plano do disco tendem a ser mais instáveis para discos altamente relativísticos. A velocidade circular das partículas apresenta um máximo e depois decai com $r^{-1/2}$.

Outras soluções que representam discos de fluido perfeito com halos são obtidas aplicando-se o método "deslocar, cortar e refletir" a soluções das equações de Einstein para esferas de fluido perfeito em coordenadas isotrópicas. São derivadas expressões para as densidades de energia, pressões,

31

velocidades de propagação do som, velocidade circular e momento angular de discos com halos obtidos a partir das soluções de Buchdahl Eq. (3.26) e soluções para esferas de fluido encontradas por Narlikar *et al* [48, 47]. As propriedades dos discos assim obtidos são semelhantes às dos discos no vácuo.

Apêndice B. Exact general relativistic static perfect fluid disks

A primeira parte do artigo contém os resultados do artigo anterior sobre discos de fluido perfeito obtidos a partir da solução de Schwarzschild. Na segunda parte, a estabilidade destes discos é estudada fazendo-se perturbações de primeira ordem nos componentes do tensor energia-momento do fluido no disco e analisando-se as equações perturbativas decorrentes das equações de conservação. O problema de autovalores resultante é resolvido numericamente. Obtém-se que as quantidades perturbadas do fluido apresentam soluções oscilatórias que favorecem a formação de anéis. A presença de pressão radial contribui para a estabilidade do disco.

Apêndice C. Exact relativistic static charged dust discs and non-axisymmetric structures

O procedimento "deslocar, cortar e refletir" é aplicado à classe de métricas conformastáticas (Sec. 3.4) para gerar distribuições de matéria feitas de poeira carregada. A sobreposição de dois buracos extremos de Reissner-Nordström alinhados ao longo do eixo z permite a construção de discos; quando os buracos negros são alinhados ao longo do eixo y obtém-se distribuições de poeira carregada no plano $z = 0$ sem simetria axial, mas simétricas em relação a um ou dois eixos coordenados, respectivamente, para massas diferentes ou iguais dos buracos-negros. Para estas distribuições de matéria estuda-se ainda o potencial efetivo de partículas-teste neutras em movimento geodésico.

Apêndice D. Exact relativistic static charged perfect fluid disks

Discos estáticos carregados de fluido perfeito são gerados aplicando-se o método "deslocar, cortar e refletir" à solução de Reissner-Nordström Eq. (3.22) em coordenadas isotrópias. De maneira semelhante ao caso não carregado, a densidade superficial de energia e pressões radial e azimutal decaem rápida- e monotonicamente com o raio, assim como a densidade superficial

de carga. A partir da equação de equilíbrio hidrostático de um fluido carregado sob a influência de um campo gravitacional, deriva-se uma condição de estabilidade semelhante à do critério de Rayleigh (Sec. 4.3). Encontra-se que a presença de carga tende a desestabilizar o disco.

Apêndice E. General relativistic model for the gravitational field of active galactic nuclei surrounded by a disk

Este artigo trata de um modelo extremamente simples, porém exato, de um núcleo ativo de galáxia: a sobreposição de um disco de Chazy-Curzon com um buraco negro de Schwarzschild central e duas barras, representando jatos de matéria ao longo do eixo de simetria em coordenadas de Weyl (Sec. 3.2). O principal objetivo é verificar qual a influência das barras sobre a matéria que compõe o disco e sua estabilidade. Em geral, a presença das barras aumenta as regiões de instabilidade do disco. O mesmo comportamento é observado pelo cálculo das freqüências epicíclica e vertical originárias da perturbação de órbitas geodésicas circulares no plano do disco. Por último, algumas órbitas fora do plano do disco são calculadas por meio da solução numérica das equações geodésicas.

Apêndice F. New models of general relativistic static thick disks

O método "deslocar, cortar, encher e refletir" (Sec. 4.4) é usado para construir novas soluções de discos grossos. Uma classe de funções usada no "enchimento" dos discos é deduzida impondo-se restrições às derivadas primeira e segunda das funções a fim de obter discos com propriedades fisicamente aceitáveis. Esta classe de funções é usada juntamente com a solução de Schwarzschild em coordenadas isotrópicas, coordenadas de Weyl e coordenadas canônicas para gerar discos grossos. Nestas últimas coordenadas uma função adicional deve ser utilizada para gerar soluções exatas de discos. Os modelos obtidos em coordenadas isotrópicas e de Weyl satisfazem as condições de energia. Os discos gerados em coordenadas canônicas possuem algumas propriedades semelhantes aos discos em coordenadas de Weyl, porém não satisfazem a condição dominante de energia.

Apêndice G. Relativistic models of galaxies

Usando uma forma particular para a métrica em coordenadas cilíndricas, obteve-se modelos que podem ser interpretados como versões relativísticas

de pares potencial-densidade Newtonianos (Sec. 4.5) usualmente usados como modelos de galáxias. Em particular, os componentes do tensor energia-momento são calculados para os dois primeiros potenciais de Miyamoto-Nagai e um potencial obtido por Satoh. Todos os potenciais geram distribuições de matéria com pressões e que satisfazem as condições de energia para certos intervalos dos parâmetros livres. Algumas órbitas geodésicas não-planares são calculadas numericamente para estes potenciais. Os efeitos de primeira ordem da rotação no perfil de velocidades são calculados por meio de uma forma aproximada da métrica de Kerr expressa em coordenadas isotrópicas.

Apêndice H. On multipolar analytical potentials for galaxies

Este artigo trata da teoria do potencial Newtoniano. Aplicando uma transformação do tipo Miyamoto-Nagai à expansão multipolar até o termo quadrupolar, obtemos pares potencial-densidade que generalizam os pares de Miyamoto-Nagai. Infelizmente para certos intervalos dos parâmetros livres as distribuições de densidade de matéria não são fisicamente aceitáveis. Para os pares apresentados calculam-se ainda o perfil de rotação e as freqüências epicíclica e vertical de oscilações em torno de órbitas circulares em equilíbrio no plano galáctico. Obtém-se que para valores menores dos parâmetros relacionados aos momentos multipolares, o ponto de máximo das curvas de rotação é deslocado para raios maiores, e ambas as freqüências epicíclica e vertical têm o valor reduzido para um raio fixo.

5.2 Conclusão

Nesta tese usamos o método inverso para construir diversas soluções exatas das equações de Einstein que representam espaços-tempo com distribuições discoidais de matéria. Um primeiro conjunto de soluções consiste em discos estáticos finos de fluido perfeito (pressões radial e azimutal iguais) com e sem halos em coordenadas isotrópicas. Neste mesmo sistema de coordenadas, obteve-se soluções de discos finos de fluido perfeito com carga elétrica. Utilizando-se das métricas conformastáticas, construiu-se modelos de discos constituídos por poeira carregada, além de estruturas sem simetria axial. Todos estes modelos foram construídos utilizando-se do procedimento "deslocar, cortar e refletir". Elaborou-se ainda um modelo relativístico muito simples de um núcleo ativo de galáxia composto pela sobreposição de um disco de Chazy-Curzon com um buraco negro de Schwarzschild central e duas barras representando jatos de matéria ao longo do eixo de simetria.

No que se refere a soluções estáticas de discos grossos, utilizou-se o método "deslocar, cortar, encher e refletir" juntamente com um novo conjunto de funções usadas no "enchimento" para estudar novos modelos de discos grossos em coordenadas isotrópicas, coordenadas de Weyl e coordenadas canônicas. Estes discos possuem espessura constante e finita. Por outro lado, ao utilizar-se uma forma particular para a métrica isotrópica em coordenadas cilíndricas, obteve-se modelos tridimensionais de distribuições de matéria que podem ser vistos como versões relativísticas de alguns pares potencial-densidade Newtonianos usados na modelagem de galáxias. Estas distribuições de matéria ocupam todo o espaço físico. Por fim, estudou-se modelos puramente Newtonianos de pares potencial-densidade obtidos pela aplicação de uma transformação à expansão multipolar. Estes pares generalizam os conhecidos pares de Miyamoto-Nagai usados como modelos para galáxias espirais.

Uma possível extensão dos trabalhos desenvolvidos consistiria na introdução de elementos físicos adicionais aos discos, como campos magnéticos e rotação. Em particular, seria interessante estudar como estes elementos alteram as propriedades dos discos grossos. O estudo da estabilidade destes sistemas por meio de perturbações do tensor energia-momento também é importante, embora se trate de um problema não-trivial. Outra área praticamente inexplorada é a elaboração de modelos de discos relativísticos com constante cosmológica. A sobreposição de discos e/ou outras estruturas (anéis, halos, jatos etc) com buracos negros consiste em outro tema com crescente interesse teórico e importância na astrofísica.

Neste ponto convém mencionar brevemente um dos problemas em aberto mais importantes da astronomia moderna: a origem, composição e influência da matéria escura no universo. As curvas de rotação para grandes raios obtidas para muitas galáxias mostram um comportamento muito diferente de uma curva com decaimento Kepleriano ($\propto r^{-1/2}$), permanecendo praticamente constantes ou decaindo muito pouco com o raio. A interpretação mais simples para isto é que essas galáxias encontram-se envolvidas por halos com raio indefinido feitos por um tipo de matéria não-visível mas cujos efeitos gravitacionais são mensuráveis. A exata natureza da matéria escura é incerta, possivelmente constituída por partículas elementares exóticas cuja existência ainda não foi detectada.

Em vista desta dificuldade, há propostas alternativas que procuram explicar a anomalia das curvas de rotação das galáxias sem a necessidade de matéria escura. Algumas delas incluem modificações na dinâmica Newtoniana para grandes distâncias [64] e modelos relativísticos de halos esféricos com pressões anisotrópicas comparáveis à densidade de energia ao redor de

galáxias [65]. Recentemente mostrou-se que o chamado cenário do mundo das branas permite a modelagem de halos galácticos por meio de uma equação de Einstein modificada [66]. Neste cenário, nosso espaço-tempo quadridimensional é interpretado como uma hipersuperfície (brana) imersa num espaço-tempo curvo com dimensão ≥ 5. A equação de Einstein efetiva contém um termo tensorial adicional originário desta imersão e que depende das propriedades geométricas do espaço-tempo com dimensão superior. Devemos lembrar que se trata apenas de uma possibilidade, uma vez que a teoria das branas encontra-se ainda num estágio bastante especulativo.

Por fim, durante os cerca de 90 anos desde sua elaboração, houve progressos extraordinários na compreensão e aplicações da Relatividade Geral. No entanto, a teoria é tão rica que ainda há muito por fazer e descobrir. Os detectores de ondas gravitacionais atualmente em construção e/ou fase de testes, certamente trarão um novo impulso à área, além de inevitáveis surpresas (boas ou ruins).

Bibliografia

[1] S. Binney and S. Tremaine, *Galactic Dynamics*, Princeton University Press, Princeton, N. J., 1987.

[2] J. H. Krolik, *Active Galactic Nuclei: from the Central Black Hole to the Galactic Environment*, Princeton University Press, Princeton, New Jersey, 1999.

[3] W. A. Bonnor and A. Sackfield, *Comm. Math. Phys.* **8**, 338 (1968).

[4] T. Morgan and L. Morgan, *Phys. Rev.* **183**, 1097 (1969).

[5] L. Morgan and T. Morgan, *Phys. Rev. D* **2**, 2756 (1970).

[6] D. Lynden-Bell and S. Pineault, *Mon. Not. R. Astron. Soc.* **185**, 679 (1978).

[7] P. S. Letelier and S. R. Oliveira, *J. Math. Phys.* **28**, 165 (1987).

[8] J. P. S. Lemos, *Class. Quantum Grav.* **6**, 1219 (1989).

[9] J. Bičák, D. Lynden-Bell and J. Katz, *Phys. Rev. D* **47**, 4334 (1993).

[10] J. Bičák, D. Lynden-Bell and C. Pichon, *Mon. Not. R. Astron. Soc.* **265**, 126 (1993).

[11] G. A. González and P. S. Letelier, *Class. Quantum Grav.* **16**, 479 (1999).

[12] P. S. Letelier, *Phys. Rev. D* **60**, 104042 (1999).

[13] J. Katz, J. Bičák and D. Lynden-Bell, *Class. Quantum Grav.* **16**, 4023 (1999).

[14] J. Bičák and T. Ledvinka, *Phys. Rev. Lett.* **71**, 1669 (1993).

[15] T. Ledvinka, M. Žofka and J. Bičák, em *Proceedings of the 8th Marcel Grossman Meeting in General Relativity*, editado por T. Piran, World Scientific, Singapore, 1999.

[16] G. A. González and P. S. Letelier, *Phys. Rev. D* **62**, 064025 (2000).

[17] G. A. González and O. A. Espitia, *Phys. Rev. D* **68**, 104028 (2003).

[18] G. García R. and G. A. González, *Phys. Rev. D* **69**, 124002 (2004).

[19] G. García R. and G. A. González, *Class. Quantum Grav.* **21**, 4845 (2004).

[20] G. García R. and G. A. González, *Phys. Rev. D* **70**, 104005 (2004).

[21] J. P. S. Lemos and P. S. Letelier, *Class. Quantum Grav.* **10**, L75 (1993).

[22] J. P. S. Lemos and P. S. Letelier, *Phys. Rev. D* **49**, 5135 (1994).

[23] J. P. S. Lemos and P. S. Letelier, *Int. J. Mod. Phys. D* **5**, 53 (1996).

[24] O. Semerák, T. Zellerin and M. Žáček, *Mon. Not. R. Astron. Soc.* **308**, 691 (1999).

[25] O. Semerák, M. Žáček and T. Zellerin, *Mon. Not. R. Astron. Soc.* **308**, 705 (1999).

[26] O. Semerák and M. Žáček, *Publ. Astron. Soc. Japan* **52**, 1067 (2000).

[27] O. Semerák, *Class. Quantum Grav.* **19**, 3829 (2002).

[28] O. Semerák, *Class. Quantum Grav.* **20**, 1613 (2003).

[29] T. Zellerin and O. Semerák, *Class. Quantum Grav.* **17**, 5103 (2000).

[30] G. Neugebauer and R. Meinel, *Phys. Rev. Lett.* **75**, 3046 (1995).

[31] C. Klein, *Class. Quantum Grav.* **14**, 2267 (1997).

[32] C. Klein and O. Richter, *Phys. Rev. Lett.* **83**, 2884 (1999).

[33] C. Klein, *Phys. Rev. D* **63**, 064033 (2001).

[34] J. Frauendiener and C. Klein, *Phys. Rev. D* **63**, 084025 (2001).

[35] C. Klein, *Phys. Rev. D* **65**, 084029 (2002).

[36] C. Klein, *Phys. Rev. D* **68**, 027501 (2003).

[37] C. Klein, *Ann. Phys.* **12**(10), 599 (2003).

[38] G. A. González and P. S. Letelier, *Phys. Rev. D* **69**, 044013 (2004).

[39] M. Miyamoto and R. Nagai, *Publ. Astron. Soc. Japan* **27**, 533 (1975).

[40] C. Satoh, *Publ. Astron. Soc. Japan* **32**, 41 (1980).

[41] S. Chandrasekhar, *The Mathematical Theory of Black Holes*, Oxford University Press, 1998.

[42] H. Stephani, D. Kramer, M. MacCallum, C. Hoenselaers and E. Herlt, *Exact Solutions to Einstein's Field Equations*, 2nd Ed., Cambridge University Press, Cambridge, 2003.

[43] H. Weyl, *Ann. Phys. Lpz.* **54**, 117 (1917).

[44] H. Weyl, *Ann. Phys. Lpz.* **59**, 185 (1919).

[45] M. Chazy, *Bull. Soc. Math. France* **52**, 17 (1924).

[46] H. Curzon, *Proc. London Math. Soc.* **23**, 477 (1924).

[47] V. V. Narlikar, G. K. Patwardhan and P. C. Vaidya, *Proc. Natl. Inst. Sci. India* **9**, 229 (1943).

[48] B. Kuchowicz, *Acta Phys. Polon.* **B3**, 209 (1972).

[49] H. A. Buchdahl, *Astrophys. J.* **140**, 1512 (1964).

[50] W. B. Bonnor and S. B. P. Wickramasuriya, *Mon. Not. R. Astron. Soc.* **170**, 643 (1975).

[51] W. B. Bonnor, *Gen. Rel. Grav.* **12**, 453 (1980).

[52] W. B. Bonnor, *Class. Quantum. Grav.* **15**, 351 (1998).

[53] M. Gürses, *Phys. Rev. D* **58**, 044001 (1998).

[54] V. Varela, *Gen. Rel. Grav.* **35**, 1815 (2003).

[55] S. D. Majumdar, *Phys. Rev.* **72**, 930 (1947).

[56] A. Papapetrou, *Proc. R. Ir. Acad. A* **51**, 191 (1947).

[57] G. G. Kuzmin, *Astron. Zh.* **33**, 27 (1956).

[58] A. Papapetrou and A. Hamoui, *Ann. Inst. Henri Poincaré* **9**, 179 (1968).

[59] A. Lichnerowicz, *C. R. Acad. Sci.* **273**, 528 (1971).

[60] A. H. Taub, *J. Math. Phys.* **21**, 1423 (1980).

[61] S. W. Hawking and G. F. R. Ellis, *The Large Scale Structure of Space-Time*, Cambridge University Press, Cambridge, 1973.

[62] Lord Rayleigh, *Proc. R. Soc. London A* **93**, 148 (1917); ver também L. D. Landau e E. M. Lifshitz, *Fluid Mechanics*, 2nd Ed., Pergamon Press, Oxford, 1987, §27.

[63] H. C. Plummer, *Mon. Not. R. Astron. Soc.* **71**, 460 (1911).

[64] M. Milgrom, *Astrophys. J.* **270**, 365 (1983).

[65] S. Bharadwaj and S. Kar, *Phys. Rev. D* **68**, 023516 (2003).

[66] S. Pal, S. Bharadwaj and S. Kar, *Phys. Lett. B* **609**, 194 (2005).

Apêndice A

Exact general relativistic perfect fluid disks with halos

Abstract

Using the well-known "displace, cut and reflect" method used to generate disks from given solutions of Einstein field equations, we construct static disks made of perfect fluid based on vacuum Schwarzschild's solution in isotropic coordinates. The same method is applied to different exact solutions to the Einstein's equations that represent static spheres of perfect fluids. We construct several models of disks with axially symmetric perfect fluid halos. All disks have some common features: surface energy density and pressures decrease monotonically and rapidly with radius. As the "cut" parameter a decreases, the disks become more relativistic, with surface energy density and pressure more concentrated near the center. Also, regions of unstable circular orbits are more likely to appear for high relativistic disks. Parameters can be chosen so that the sound velocity in the fluid and the tangential velocity of test particles in circular motion are less than the velocity of light. This tangential velocity first increases with radius and reaches a maximum.

A.1 Introduction

Axially symmetric solutions of Einstein's field equations corresponding to disklike configurations of matter are of great astrophysical interest, since they can be used as models of galaxies or accretion disks. These solutions can be static or stationary and with or without radial pressure. Solutions for static disks without radial pressure were first studied by Bonnor and Sackfield [1], and Morgan and Morgan [2], and with radial pressure by Morgan and Morgan [3]. Disks with radial tension have been considered in [4], and models of disks with electric fields [5], magnetic fields [6], and both magnetic and electric fields have been introduced recently [7]. Solutions for self-similar static disks were analyzed by Lynden-Bell and Pineault [8], and Lemos [9]. The superposition of static disks with black holes were considered by Lemos and Letelier [10–12], and Klein [13]. Also Bičák, Lynden-Bell and Katz [14] studied static disks as sources of known vacuum spacetimes and Bičák, Lynden-Bell and Pichon [15] found an infinite number of new static solutions. For a recent survey on relativistic gravitating disks, see [16].

The principal method to generate the above mentioned solution is the "displace, cut and reflect" method. One of the main problem of the solutions generated by using this simple method is that usually the matter content of the disk is anisotropic i. e., the radial pressure is different from the azimuthal pressure. In most of the solutions the radial pressure is null. This made these solutions rather unphysical. Even though, one can argue that when no radial pressure is present stability can be achieved if we have two circular streams of particles moving in opposite directions (counterrotating hypothesis, see for instance [14]).

In this article we apply the "displace, cut and reflect" method to spherically symmetric solutions of Einstein's field equations in isotropic coordinates to generate static disks made of a *perfect fluid*, i. e., with radial pressure equal to tangential pressure and also disks of perfect fluid surrounded by an halo made of perfect fluid matter.

The article is organized as follows. Section A.2 gives an overview of the "displace, cut and reflect" method. Also we present the basic equations used to calculate the main physical variables of the disks. In Sec. A.3 we apply the formalism to obtain the simplest model of disk, which is based on Schwarzschild's vacuum solution in isotropic coordinates. The generated class of disks is made of a perfect fluid with well behaved density and pressure. Section A.4 presents some models of disks with halos obtained from different known exact solutions of Einstein's field equations for static spheres of perfect fluid in isotropic coordinates. In Sec. A.5 we give some examples
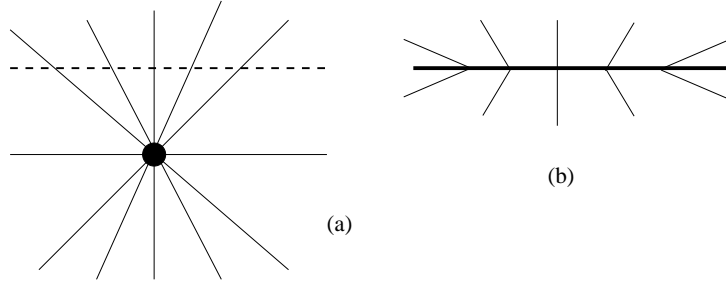
Figure A.1: An illustration of the "displace, cut and reflect" method for the generation of disks. In (a) the spacetime with a singularity is displaced and cut by a plane (dotted line), in (b) the part with singularities is disregarded and the upper part is reflected on the plane.

of disks with halo generated from spheres composed of fluid layers. Section A.6 is devoted to discussion of the results.

A.2   Einstein equations and disks

For a static, spherically symmetric spacetime the general line element in isotropic spherical coordinates can be cast as

$$\mathrm{d}s^2 = e^{\nu(r)}\mathrm{d}t^2 - e^{\lambda(r)}\left[\mathrm{d}r^2 + r^2(\mathrm{d}\theta^2 + \sin^2\theta\mathrm{d}\varphi^2)\right]. \qquad (\mathrm{A}.1)$$

In cylindrical coordinates (t,R,z,φ) the line element (A.1) takes the form

$$\mathrm{d}s^2 = e^{\nu(R,z)}\mathrm{d}t^2 - e^{\lambda(R,z)}\left(\mathrm{d}R^2 + \mathrm{d}z^2 + R^2\mathrm{d}\varphi^2\right). \qquad (\mathrm{A}.2)$$

The metric of the disk will be constructed using the well known "displace, cut and reflect" method that was used by Kuzmin [17] in Newtonian gravity and later in general relativity by many authors [4–16]. The material content of the disk will be described by functions that are distributions with support on the disk. The method can be divided in the following steps that are illustrated in Fig. A.1. First, in a space wherein we have a compact source of gravitational field, we choose a surface (in our case, the plane $z = 0$) that divides the space in two pieces: one with no singularities or sources and the other with the sources. Then we disregard the part of the space with singularities and use the surface to make an inversion of the nonsingular part of the space. This results in a space with a singularity that is a delta function with support on $z = 0$. This procedure is mathematically equivalent

43

to make the transformation $z \to |z| + a$, with a as constant. In the Einstein tensor we have first and second derivatives of z. Since $\partial_z |z| = 2\vartheta(z) - 1$ and $\partial_{zz} |z| = 2\delta(z)$, where $\vartheta(z)$ and $\delta(z)$ are, respectively, the Heaviside function and the Dirac distribution. Therefore the Einstein field equations will separate in two different pieces [18]: one valid for $z \neq 0$ (the usual Einstein's equations), and other involving distributions with an associated energy-momentum tensor, $T_{ab} = Q_{ab}\delta(z)$, with support on $z = 0$. For the metric (A.2), the non-zero components of Q_{ab} are

$$Q_t^t = \frac{1}{16\pi} \left[-b^{zz} + g^{zz}(b_R^R + b_z^z + b_\varphi^\varphi) \right], \qquad (A.3)$$

$$Q_R^R = Q_\varphi^\varphi = \frac{1}{16\pi} \left[-b^{zz} + g^{zz}(b_t^t + b_R^R + b_z^z) \right], \qquad (A.4)$$

where b_{ab} denotes the jump of the first derivatives of the metric tensor on the plane $z = 0$,

$$b_{ab} = g_{ab,z}|_{z=0^+} - g_{ab,z}|_{z=0^-}, \qquad (A.5)$$

and the other quantities are evaluated at $z = 0^+$. The "true" surface energy-momentum tensor of the disk can be written as $S_{ab} = \sqrt{-g_{zz}}Q_{ab}$, thus the surface energy density σ and the radial and azimuthal pressures or tensions (P) read:

$$\sigma = \sqrt{-g_{zz}}Q_t^t, \quad P = -\sqrt{-g_{zz}}Q_R^R = -\sqrt{-g_{zz}}Q_\varphi^\varphi. \qquad (A.6)$$

Note that when the same procedure is applied to an axially symmetric space-time in Weyl coordinates we have $Q_R^R = 0$, i. e., we have no radial pressure or tension.

This procedure in principle can be applied to any spacetime solution of the Einstein equations with or without source (stress tensor). The application to a static sphere of perfect fluid is schematized in Fig. A.2. The sphere is displaced and cut by a distance a less then its radius r_b. The part of the space that contains the center of the sphere is disregarded. After the inversion of the remaining space, we end up with a disk surrounded by a cap of perfect fluid. The properties of the inner part of the disk will depend on the internal fluid solution, but if the internal spherical fluid solution is joined to the standard external Schwarzschild solution, the physical properties of the outer part of the disk will be those originated from Schwarzschild's vacuum solution.

In isotropic coordinates the matching at the boundary of the fluid sphere leads to four continuity conditions: the two metric functions e^λ and e^ν
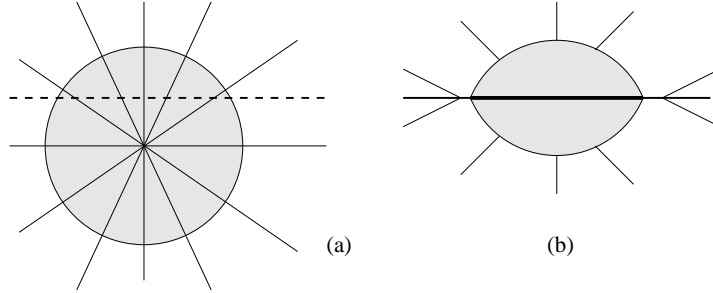
Figure A.2: An illustration of the "displace, cut and reflect" method for the generation of disks with halos. In (a) the sphere of perfect fluid is displaced and cut by a plane (dotted line); in (b) the lower part is disregarded and the upper part is reflected on the plane.

together with their first derivatives with respect to the radial coordinate should be continuous across the boundary. In addition, to have a compact body the pressure at the surface of the material sphere has to drop to zero. Also to have a meaningful solution the velocity of sound, $V^2 = dp/d\rho$, should be restricted to the interval $0 \leq V < 1$.

The Einstein equations for a static, spherically symmetric space time in isotropic coordinates for a perfect fluid source give us that density ρ and pressure p are related to the metric functions by

$$\rho = -\frac{e^{-\lambda}}{8\pi} \left[\lambda'' + \frac{1}{4}(\lambda')^2 + \frac{2\lambda'}{r} \right], \tag{A.7}$$

$$p = \frac{e^{-\lambda}}{8\pi} \left[\frac{1}{4}(\lambda')^2 + \frac{1}{2}\lambda'\nu' + \frac{1}{r}(\lambda' + \nu') \right], \tag{A.8}$$

where primes indicate differentiation with respect to r.

Also static spheres composed of various layers of fluid can be used to generate disks with halos of fluid layers (see Fig. A.3). The disk will then be composed of different axial symmetric "pieces" glued together. The matching conditions at the boundary of adjacent spherical fluid layers in isotropic coordinates involves four continuity conditions: the two metric functions e^λ and e^ν, the first derivative of λ with respect to the radial coordinate, and the pressure should be continuous across the boundary. At the most external boundary, the metric functions e^λ and e^ν, and their first derivatives with respect to the radial coordinate should be continuous across the boundary; also the pressure there should go to zero.
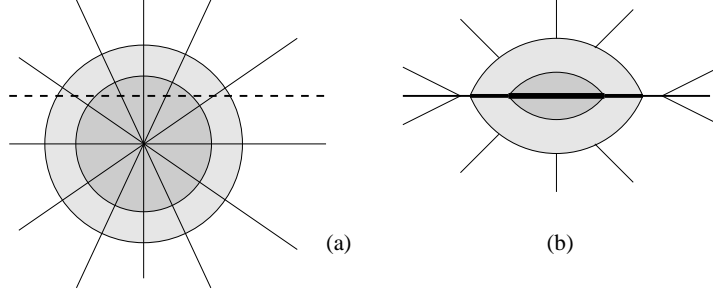
Figure A.3: An illustration of the "displace, cut and reflect" method for the generation of disks with various layers of halos. In (a) the sphere with different layers of fluid is displaced and cut with a plane (dotted line); in (b) the field is reflected on the plane.

A.3   The simplest disk

We first apply the "displace, cut and reflect" method to generate disks discussed in the previous section and depicted in Fig. A.1 to the Schwarzschild metric in isotropic coordinates (t, r, θ, φ),

$$\mathrm{d}s^2 = \frac{\left(1 - \frac{m}{2r}\right)^2}{\left(1 + \frac{m}{2r}\right)^2}\mathrm{d}t^2 - \left(1 + \frac{m}{2r}\right)^4 \left[\mathrm{d}r^2 + r^2(\mathrm{d}\theta^2 + \sin^2\theta\mathrm{d}\varphi^2)\right]. \tag{A.9}$$

Expressing solution (A.9) in cylindrical coordinates, and using Eqs. (A.3)–(A.6), we obtain a disk with surface energy density σ and radial and azimuthal pressures (or tensions) P given by

$$\sigma = \frac{4ma}{\pi(m + 2\sqrt{R^2 + a^2})^3}, \tag{A.10}$$

$$P = -\frac{2m^2a}{\pi(m + 2\sqrt{R^2 + a^2})^3(m - 2\sqrt{R^2 + a^2})}. \tag{A.11}$$

The total mass of the disk can be calculated with the help of Eq. (A.10):

$$\mathcal{M} = \int_0^\infty \int_0^{2\pi} \sigma\sqrt{g_{RR}g_{\varphi\varphi}}\,\mathrm{d}R\,\mathrm{d}\varphi = \frac{m}{4a}(m + 4a). \tag{A.12}$$

Eq. (A.10) shows that the disk's surface energy density is always positive (weak energy condition). Positive values (pressure) for the stresses in azimuthal and radial directions are obtained if $m < 2\sqrt{R^2 + a^2}$. The strong

energy condition, $\sigma + P_{\varphi\varphi} + P_{RR} = \sigma + 2P > 0$ is then satisfied. These properties characterize a fluid made of matter with the usual gravitational attractive property. This is not a trivial property of these disks since it is known that the "displace, cut and reflect" method sometimes gives disks made of exotic matter like cosmic strings, see for instance [19].

Another useful parameter is the velocity of sound propagation V, defined as $V^2 = dP/d\sigma$, which can be calculated using Eqs. (A.10) and (A.11):

$$V^2 = \frac{m(4\sqrt{R^2 + a^2} - m)}{3(m - 2\sqrt{R^2 + a^2})^2}.$$ (A.13)

The condition $V^2 < 1$ (no tachyonic matter) imposes the inequalities $m < \sqrt{R^2 + a^2}$ or $m > 3\sqrt{R^2 + a^2}$. If the pressure condition and the speed of sound less then the speed of light condition are to be simultaneously satisfied, then $m < \sqrt{R^2 + a^2}$. This inequality will be valid in all the disk if $m < a$.

With the presence of radial pressure one does not need the assumption of streams of rotating and counter rotating matter usually used to explain the stability of static disk models. However, a tangential velocity (rotation profile) can be calculated by assuming a test particle moves in a circular geodesic on the disk. We tacitly assume that this particle only interacts gravitationally with the fluid. This assumption is valid for the case of a particle moving in a very diluted gas like the gas made of stars that models a galaxy disk.

The geodesic equation for the R coordinate obtained from metric (A.2) is

$$e^\lambda \ddot{R} + \frac{1}{2}(e^\nu)_{,R}\dot{t}^2 - \frac{1}{2}(e^\lambda)_{,R}(\dot{R}^2 + \dot{z}^2) - \frac{1}{2}\left(e^\lambda R^2\right)_{,R}\dot{\varphi}^2 = 0.$$ (A.14)

For circular motion on the $z = 0$ plane, $\dot{R} = \ddot{R} = 0$ and $\dot{z} = 0$, then Eq. (A.14) reduces to

$$\frac{\dot{\varphi}^2}{\dot{t}^2} = \frac{(e^\nu)_{,R}}{(e^\lambda R^2)_{,R}}.$$ (A.15)

The tangential velocity measured by an observer at infinity is then

$$v_c^2 = -\frac{g_{\varphi\varphi}}{g_{tt}}\left(\frac{d\varphi}{dt}\right)^2 = R^2 \frac{e^\lambda(e^\nu)_{,R}}{e^\nu(R^2 e^\lambda)_{,R}}.$$ (A.16)

From the metric on the disk,

$$e^\nu = \frac{\left(1 - \frac{m}{2\sqrt{R^2+a^2}}\right)^2}{\left(1 + \frac{m}{2\sqrt{R^2+a^2}}\right)^2} \quad \text{and} \quad e^\lambda = \left(1 + \frac{m}{2\sqrt{R^2 + a^2}}\right)^4,$$ (A.17)

47

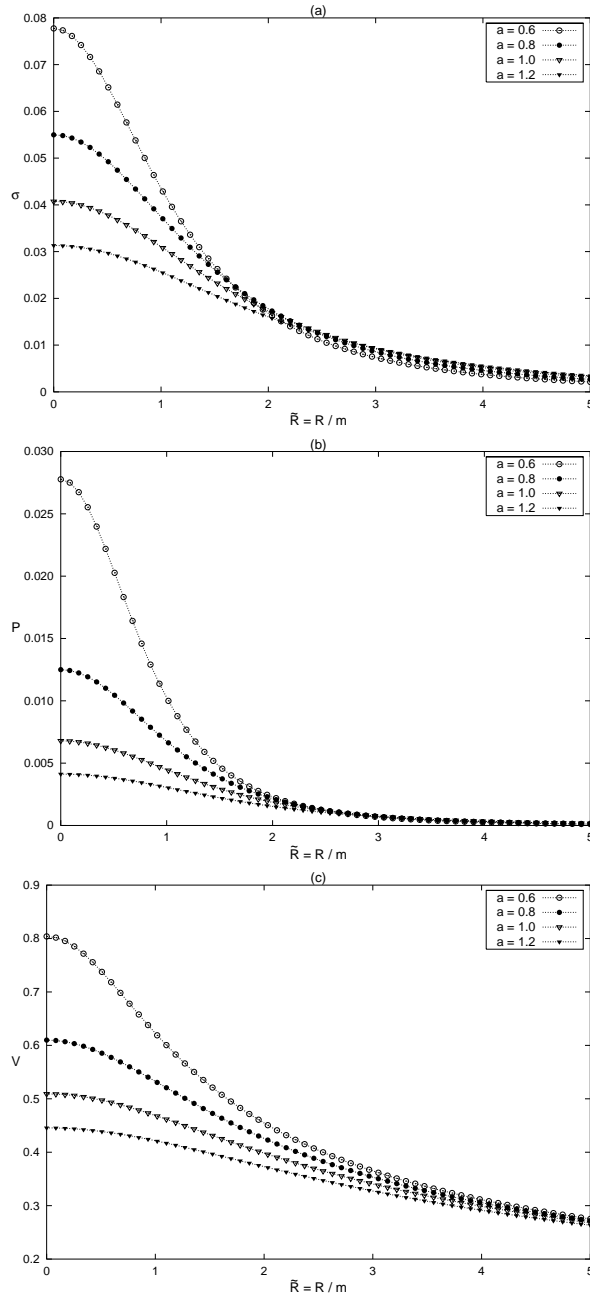Figure A.4: (a) The surface energy density σ, (b) pressures P, (c) sound velocity V with $m = 0.5$ and $a = 0.6$, 0.8,1.0, and 1.2 as function of $\tilde{R} = R/m$. We use geometric units $G = c = 1$.
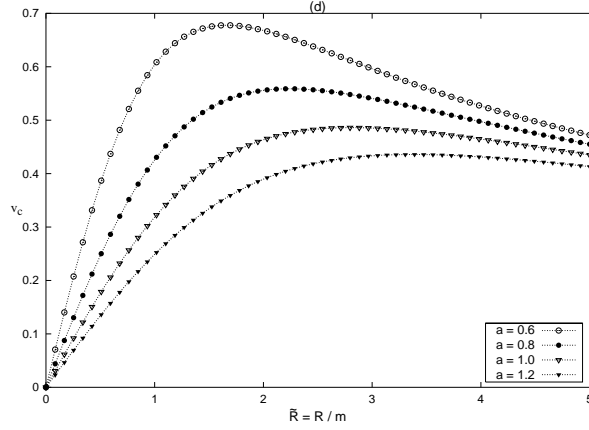
48

Figure A.4(d): The tangential velocity v_c (rotation curve or rotation profile) with $m = 0.5$ and $a = 0.6$, 0.8,1.0, and 1.2 as function of $\tilde{R} = R/m$. We use geometric units $G = c = 1$.

we find that Eq. (A.16) can be cast as,

$$v_c^2 = \frac{mR^2}{\left(1 - \frac{m}{2\sqrt{R^2+a^2}}\right)\left[(R^2+a^2)^{3/2} + \frac{m}{2}(a^2-R^2)\right]}. \tag{A.18}$$

For $R >> a$, Eq. (A.18) goes as $v_c = (m/R)^{1/2}$, the Newtonian circular velocity.

To determine the stability of circular orbits on the disk's plane, we use an extension of Rayleigh [20, 21] criteria of stability of a fluid at rest in a gravitational field

$$h\frac{dh}{dR} > 0, \tag{A.19}$$

where h is the specific angular momentum of a particle on the disk's plane:

$$h = -g_{\varphi\varphi}\frac{d\varphi}{ds} = -g_{\varphi\varphi}\frac{d\varphi}{dt}\frac{dt}{ds}. \tag{A.20}$$

Using Eq. (A.15) and the relation

$$1 = e^\nu\left(\frac{dt}{ds}\right)^2 - R^2 e^\lambda\left(\frac{d\varphi}{ds}\right)^2, \tag{A.21}$$

49
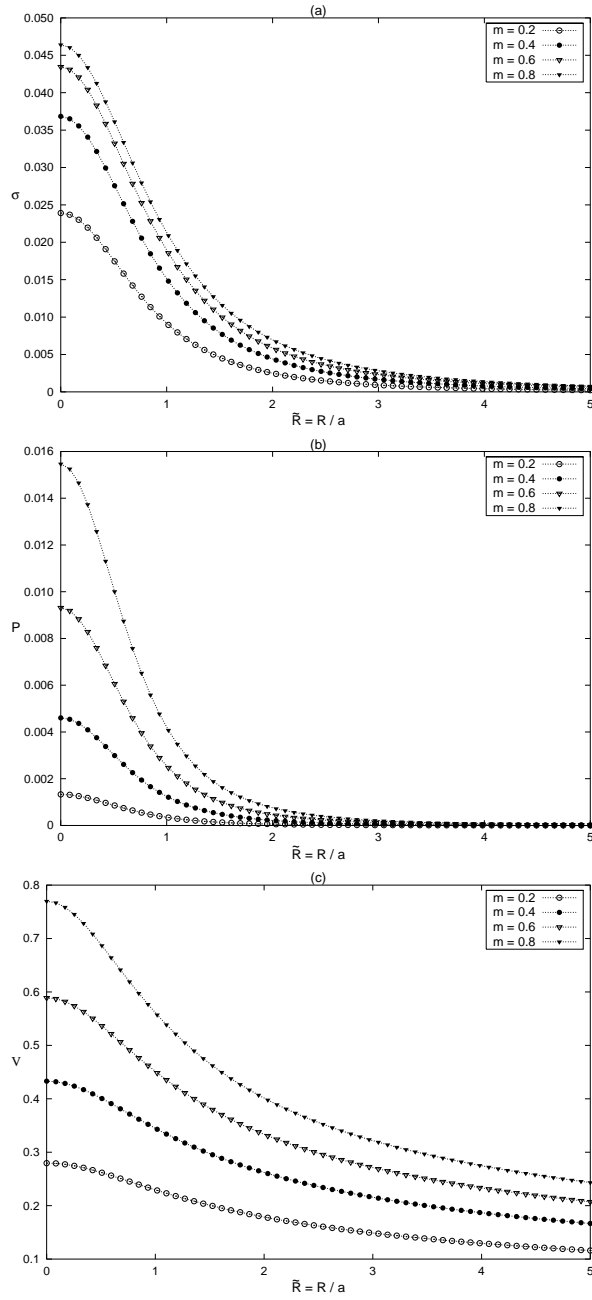
Figure A.5: (a) The surface energy density σ, (b) pressures P and (c) sound velocity V with $a = 1.0$ and $m = 0.2$, 0.4, 0.6, and 0.8 as function of $\tilde{R} = R/a$.

one obtains the following expression for h:

$$h = R^2 e^\lambda \sqrt{\frac{(e^\nu)_{,R}}{e^\nu (R^2 e^\lambda)_{,R} - R^2 e^\lambda (e^\nu)_{,R}}}. \tag{A.22}$$

For the functions (A.17), Eq. (A.22) reads

$$h = \frac{2\sqrt{m}R^2 \left(1 + \frac{m}{2\sqrt{R^2+a^2}}\right)^2 (R^2 + a^2)^{1/4}}{\sqrt{4(R^2 + a^2)^2 - 8mR^2\sqrt{R^2 + a^2} + m^2(R^2 - a^2)}}. \tag{A.23}$$

The stability criterion is always satisfied for $a/m \gtrsim 1.016$.

In Figs. A.4(a)–A.4(d) we show, respectively, the surface energy density, pressures, the sound velocity and curves of the tangential velocity (rotation curves) [Eq. (A.18)] with $m = 0.5$ and $a = 0.6$, 0.8, 1.0, and 1.2 as functions of $\tilde{R} = R/m$. Figures A.5(a)–A.5(c) display, respectively, the surface energy density, pressures and sound velocity with parameters $a = 1.0$ and $m = 0.2$, 0.4, 0.6, 0.8 as as functions of $\tilde{R} = R/m$. We see that the first three quantities decrease monotonically with the radius of the disk, as can be checked from Eqs. (A.10), (A.11) and (A.13). Energy density decreases rapidly enough in principle, to, define a cut off radius and consider the disk as finite.

A.4   Disks with halos

Now we study some disks with halos constructed from several exact solutions of the Einstein equations for static spheres of perfect fluid. A survey of these classes of solutions is presented in [22].

A.4.1   Buchdahl's Solution

The first situation that we shall study is similar to the one depicted in Fig. A.2 wherein we start with a sphere of perfect fluid. This case will not be exactly the same as the one presented in the mentioned figure because the sphere has no boundary. Hence the generated disk will be completely immersed in the fluid. An example of exact solution of the Einstein equations that represent a fluid sphere with no boundary is the Buchdahl solution that may be regarded as a reasonably close analog to the classical Lane-Emden index 5 polytrope [23]. The metric functions for this solution are:

$$e^\nu = \left(\frac{1 - \frac{A}{\sqrt{1+kr^2}}}{1 + \frac{A}{\sqrt{1+kr^2}}}\right)^2, \quad e^\lambda = \left(1 + \frac{A}{\sqrt{1+kr^2}}\right)^4, \tag{A.24}$$

51

where A and k are constants. Far from the origin the solution goes over into the external Schwarzschild metric, when $m = 2A/\sqrt{k}$. The density, pressure and sound velocity are given by:

$$\rho = \frac{3Ak}{2\pi(A + \sqrt{1 + kr^2})^5}, \quad p = \frac{kA^2}{2\pi(-A + \sqrt{1 + kr^2})(A + \sqrt{1 + kr^2})^5},$$
(A.25)

$$V^2 = \frac{2A(-2A + 3\sqrt{1 + kr^2})}{15(A - \sqrt{1 + kr^2})^2}.$$
(A.26)

The condition $V < 1$ is satisfied for $A < [(18 - \sqrt{39})/19]\sqrt{1 + kr^2}$.

Using Eq. (A.24) and Eqs. (A.3)–(A.6), we get the following expressions for the energy density, pressure and sound velocity of the disk:

$$\sigma = \frac{akA}{\pi \left[A + \sqrt{1 + k(R^2 + a^2)}\right]^3},$$
(A.27)

$$P = \frac{akA^2}{2\pi \left[-A + \sqrt{1 + k(R^2 + a^2)}\right]\left[A + \sqrt{1 + k(R^2 + a^2)}\right]^3},$$
(A.28)

$$V^2 = \frac{A\left[-A + 2\sqrt{1 + k(R^2 + a^2)}\right]}{3\left[A - \sqrt{1 + k(R^2 + a^2)}\right]^2}.$$
(A.29)

The conditions $V < 1$ and $P > 0$ are both satisfied if $A < \frac{1}{2}\sqrt{1 + ka^2}$. Figures A.6(a)–A.6(d) show, respectively, σ, P, V and rotation curves, Eq. (A.30), as functions of $\tilde{R} = R/m$ for the disk calculated from Buchdahl's solution.

In Figs. A.7(a) and A.7(b) we show, respectively, the density ρ together with pressure p, and sound velocity V of the halo along the axis z for $A = 0.6$; $k = 1$ and $a = 1$. Note that in this solution there is no boundary of the fluid sphere: the disk is completely immersed in the fluid.

The tangential velocity v_c calculated from metric coefficients (A.24) is

$$v_c^2 = \frac{2AkR^2}{\left(1 - A/\sqrt{1 + k(R^2 + a^2)}\right)\left\{[1 + k(R^2 + a^2)]^{3/2} + A[1 + k(a^2 - R^2)]\right\}}.$$
(A.30)

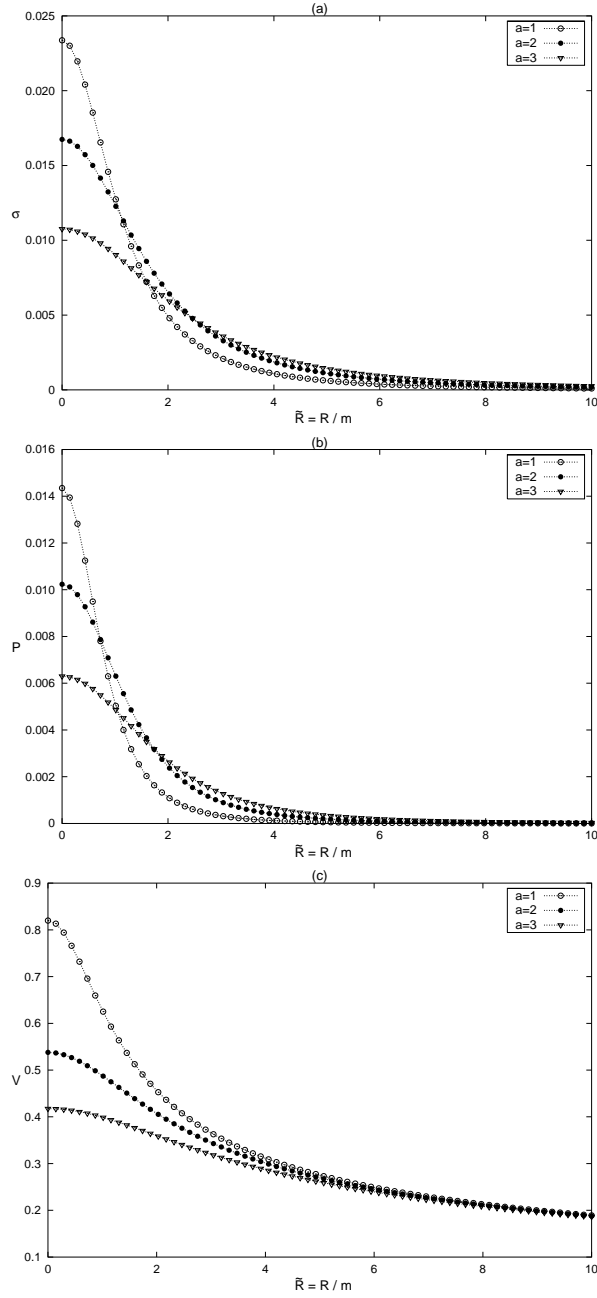For $R \gg a$, Eq. (A.30) goes as $v_c = (2A)^{1/2}/(R^{1/2}k^{1/4})$. The specific

Figure A.6: (a) The surface energy density σ, Eq. (A.27), (b) the pressure P Eq. (A.28), (c) the velocity of sound V Eq. (A.29) for the disk with $A = 0.6$; $k = 1$; for $a = 1$, 2 and 3 as function of $\tilde{R} = R/m$.

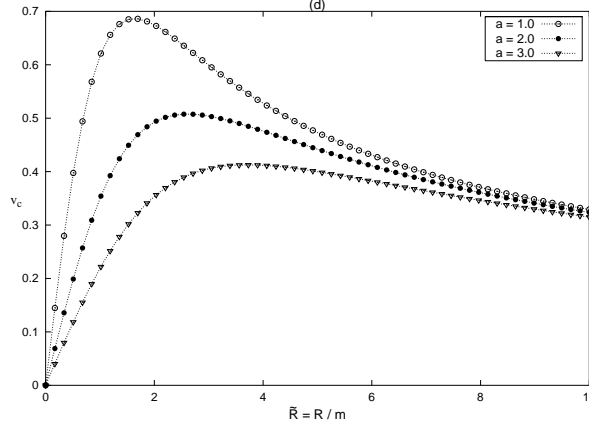Figure A.6(d): The tangential velocity v_c Eq. (A.30) for the disk with $A = 0.6$; $k = 1$; for $a = 1$, 2 and 3 as function of $\tilde{R} = R/m$.

angular momentum follows from Eqs. (A.22) and (A.24):

$$h = \frac{\sqrt{2Ak}R^2 \left(1 + \frac{A}{\sqrt{1+k(R^2+a^2)}}\right)^2 [1 + k(R^2 + a^2)]^{1/4}}{\sqrt{[1 + k(R^2 + a^2)]^2 - 4AkR^2\sqrt{1 + k(R^2 + a^2)} - A^2[1 + k(a^2 - R^2)]}}.$$

(A.31)

A.4.2 Narlikar-Patwardhan-Vaidya Solutions 1a and 1b

Now we shall study the generation of a disk solution with an halo exactly as the one depicted in Fig. A.2. We start with a solution of the Einstein equations in isotropic coordinates which represents a sphere with radius r_b of perfect fluid that on $r = r_b$ will be continuously matched to the vacuum Schwarzschild solution. Narlikar, Patwardhan and Vaidya (NPV) [24] gave the following two exact solutions of the Einstein equations for perfect fluid static spheres characterized by the metric functions (λ, ν_{1a}) and (λ, ν_{1b}),

$$e^\lambda = Cr^k,$$ (A.32)

$$e^{\nu_{1a}} = \left(A_{1a}r^{1-n+k/2} + B_{1a}r^{1+n+k/2}\right)^2 \quad \text{for} \ -2 + \sqrt{2} < k \leq 0, \text{(A.33)}$$

$$e^{\nu_{1b}} = r^{\sqrt{2}}\left[A_{1b} + B_{1b}\ln(r)\right]^2 \qquad \text{for} \ k = -2 + \sqrt{2}, \quad \text{(A.34)}$$

where A_{1a}, A_{1b}, B_{1a}, B_{1b}, C are constants and $n = \sqrt{1 + 2k + k^2/2}$. We shall refer to these solutions as NPV 1a and NPV 1b, respectively.
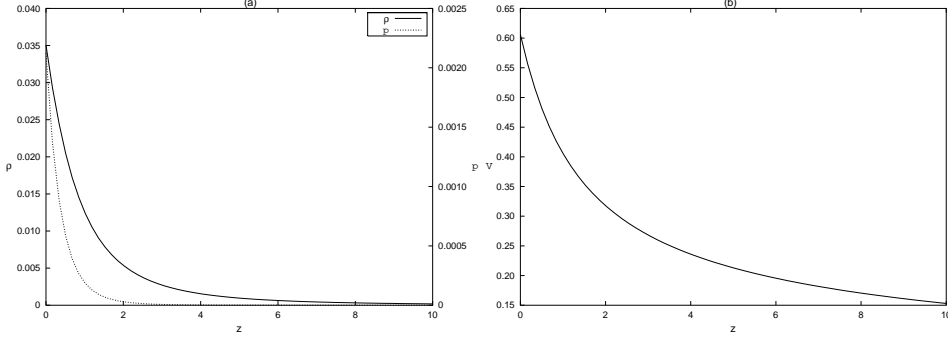
54

Figure A.7: (a) The density ρ and pressure p [Eq. (A.25)] and (b) the velocity of sound V [Eq. (A.26)] for the halo with $A = 0.6$; $k = 1$ and $a = 1$ along the z axis.

The density, pressure and sound velocity for the solutions (λ, ν_{1a}) and (λ, ν_{1b}), will be denoted by (ρ, p_{1a}, V_{1a}) and (ρ, p_{1b}, V_{1b}), respectively. We find,

$$\rho = \frac{-k(k+4)r^{-2-k}}{32\pi C}, \tag{A.35}$$

$$p_{1a} = \frac{1}{32\pi C r^{2+k}(A_{1a} + B_{1a}r^{2n})} \left\{ A_{1a} \left[3k^2 + 8(1-n) - 4k(n-3) \right] \right.$$
$$\left. + B_{1a} \left[3k^2 + 8(1+n) + 4k(n+3) \right] r^{2n} \right\}, \tag{A.36}$$

$$p_{1b} = \frac{A_{1b} + B_{1b}\ln(r) + 2\sqrt{2}B_{1b}}{16\pi C[A_{1b} + B_{1b}\ln(r)]}, \tag{A.37}$$

$$V_{1a}^2 = \frac{1}{k(k+4)(A_{1a} + B_{1a}r^{2n})^2} \left\{ A_{1a}^2 \left[-3k^2 + 8(n-1) + 4k(n-3) \right] \right.$$
$$\left. - B_{1a}^2 r^{4n} \left[3k^2 + 8(1+n) + 4k(n+3) \right] - 2A_{1a}B_{1a}r^{2n} \times \right.$$
$$\left. \left[3k(k+4) + 8(1-n^2) \right] \right\}, \tag{A.38}$$

$$V_{1b}^2 = \frac{2B_{1b}^2 r^{\sqrt{2}}}{[A_{1b} + B_{1b}\ln(r)]^2}. \tag{A.39}$$

The condition of continuity of the metric functions (λ, ν) given by Eqs. (A.32)–(A.34) and the corresponding functions in Eq. (A.9) at the boundary $r = r_b$ leads to following expressions:

$$\frac{m}{2r_b} = -\frac{k}{k+4}, \quad C = r_b^{-k}\left(\frac{4}{k+4}\right)^4, \tag{A.40}$$

55

$$A_{1a} = -\frac{3k^2 + 8(1+n) + 4k(n+3)}{16nr_b^{1-n+k/2}}, \quad B_{1a} = \frac{3k^2 + 8(1-n) - 4k(n-3)}{16nr_b^{1+n+k/2}},$$

$$\text{(A.41)}$$

$$A_{1b} = -\frac{2\sqrt{2} + \ln(r_b)}{4r_b^{1/\sqrt{2}}}, \quad B_{1b} = \frac{1}{4r_b^{1/\sqrt{2}}}. \tag{A.42}$$

V_{1a} has its maximum at $r = 0$, and V_{1b} at $r = r_b$. Condition $V_{1b}(r_b) < 1$ is satisfied if $r_b < 4^{1/\sqrt{2}}$.

Using Eqs. (A.32)–(A.34) in Eqs. (A.3)–(A.6), we get the following expressions for the energy density, pressure and sound velocity of the disk:

$$\sigma = -\frac{ka}{4\pi\sqrt{C}\mathcal{R}^{1+k/4}}, \tag{A.43}$$

$$P_{1a} = \frac{a}{4\pi\sqrt{C}\mathcal{R}^{1+k/4}} \frac{[A_{1a}(k-n+1) + B_{1a}(k+n+1)\mathcal{R}^n]}{[A_{1a} + B_{1a}\mathcal{R}^n]}, \tag{A.44}$$

$$P_{1b} = \frac{a}{4\pi\sqrt{C}\mathcal{R}^{1/2+\sqrt{2}/4}[2A_{1b} + B_{1b}\ln(\mathcal{R})]} \left[2A_{1b}(\sqrt{2}-1) + 2B_{1b}\right.$$
$$\left. + B_{1b}(\sqrt{2}-1)\ln(\mathcal{R})\right], \tag{A.45}$$

$$V_{1a}^2 = \frac{1}{k(k+4)\left[A_{1a}\mathcal{R}^{-n/2} + B_{1a}\mathcal{R}^{n/2}\right]^2} \left[-B_{1a}^2\mathcal{R}^n(k^2 + 5k + nk + 4n + 4)\right.$$
$$\left. + A_{1a}^2\mathcal{R}^{-n}(-k^2 - 5k + nk + 4n - 4) + 2A_{1a}B_{1a}(-k^2 - 5k + 4n^2 - 4)\right],$$

$$\text{(A.46)}$$

$$V_{1b}^2 = \frac{1}{2(2A_{1b} + B_{1b}\ln(\mathcal{R}))^2} \left[B_{1b}^2\sqrt{2}\ln^2(\mathcal{R}) + 2B_{1b}(2B_{1b} + B_{1b}\sqrt{2} + 2A_{1b}\sqrt{2})\right.$$
$$\left. \times \ln(\mathcal{R}) + 4A_{1b}B_{1b}(2+\sqrt{2}) + 4\sqrt{2}A_{1b}^2 + 8B_{1b}^2\right], \tag{A.47}$$

where $\mathcal{R} = R^2 + a^2$. V_{1a} and V_{1b} have their maximum values at $R = 0$. Because the expressions are rather involved, the restrictions on the constants, to ensure that the velocities are positive and less then one, are best made graphically. The curves of σ, P and V as function of $\tilde{R} = R/m$ with parameters $k = -1/2$; $r_b = 2$ and $a = 0.5, 1.0, 1.5$ are displayed in Figs. A.8(a)–A.8(c), respectively. Figures A.9(a)–A.9(b) show the density ρ, pressure p and velocity of sound V for the halo with parameters $k = -1/2$; $r_b = 2$, for $a = 0.5$ along the axis z. The same physical quantities are shown in Figs. A.10(a)–A.10(c) and A.11(a)–A.11(b) with $k = -2 + \sqrt{2}$. We note that σ and P are continuous at the boundary between the internal

and external parts of the disk, but the velocity of sound has a discontinuity.

The tangential velocity v_c is given by

$$v_{c1a}^2 = 2R^2 \frac{A_{1a}(1 - n + k/2) + B_{1a}(1 + n + k/2)(R^2 + a^2)^n}{[A_{1a} + B_{1a}(R^2 + a^2)^n][R^2(k + 2) + 2a^2]}, \qquad (A.48)$$

$$v_{c1b}^2 = R^2 \frac{2\sqrt{2}A_{1b} + B_{1b}[4 + \sqrt{2}\ln(R^2 + a^2)]}{[2A_{1b} + B_{1b}\ln(R^2 + a^2)][2a^2 + \sqrt{2}R^2]}, \qquad (A.49)$$

and the specific angular momentum h,

$$h_{1a} = \sqrt{C}R^2(R^2 + a^2)^{k/4}\sqrt{\frac{A_{1a}(1 - n + k/2) + B_{1a}(1 + n + k/2)(R^2 + a^2)^n}{A_{1a}(a^2 + nR^2) + B_{1a}(a^2 - nR^2)(R^2 + a^2)^n}}, \qquad (A.50)$$

$$h_{1b} = \sqrt{C}R^2(R^2 + a^2)^{-1/2 + \sqrt{2}/4}\sqrt{\frac{2B_{1b} + \sqrt{2}[A_{1b} + B_{1b}\ln(\sqrt{R^2 + a^2})]}{2a^2[A_{1b} + B_{1b}\ln(\sqrt{R^2 + a^2})] - 2B_{1b}R^2}}. \qquad (A.51)$$

In Figs. A.12(a) and A.12(b), the curves of tangential velocity [Eq. (A.48)] and $h(dh/d\tilde{R})$ [Eq. (A.50)], respectively, are displayed as functions of $\tilde{R} = R/m$ with $k = -1/2$; $r_b = 2$; $a = 0.5$, 1.0,1.5. The same quantities are shown in Figs. A.13(a) and A.13(b) with $k = -2 + \sqrt{2}$. For $a = 0.5$ the disks have a small region of unstable orbits immediately after the "boundary radius".

A.4.3   Narlikar-Patwardhan-Vaidya Solutions 2a and 2b

As in the previous sections we study the generation of a disk solution with an halo exactly as the one depicted in Fig. A.2. We also start with a solution of the Einstein equations in isotropic coordinates, which represents a sphere of radius r_b of perfect fluid that on $r = r_b$ will the continuously matched to the vacuum Schwarzschild solution. We will use two other solutions found by Narlikar, Patwardhan and Vaidya [24] that we shall refer as NPV 2a and NPV 2b, respectively, which are characterized by the metric functions (λ, ν_{2a}) and (λ, ν_{2b}),

$$e^\lambda = \frac{1}{\left(A_1 r^{1 + n/2} + A_2 r^{1 - n/2}\right)^2} \qquad (A.52)$$

$$e^{\nu_{2a}} = \frac{\left(B_{1a} r^{1 + x/2} + B_{2a} r^{1 - x/2}\right)^2}{\left(A_1 r^{1 + n/2} + A_2 r^{1 - n/2}\right)^2} \qquad \text{for } \sqrt{2} < n \leq 2, \qquad (A.53)$$

$$e^{\nu_{2b}} = \frac{[B_{1b} + B_{2b}\ln(r)]^2}{\left(A_1 r^{1/\sqrt{2}} + A_2 r^{-1/\sqrt{2}}\right)^2} \qquad \text{for } n = \sqrt{2}. \qquad (A.54)$$
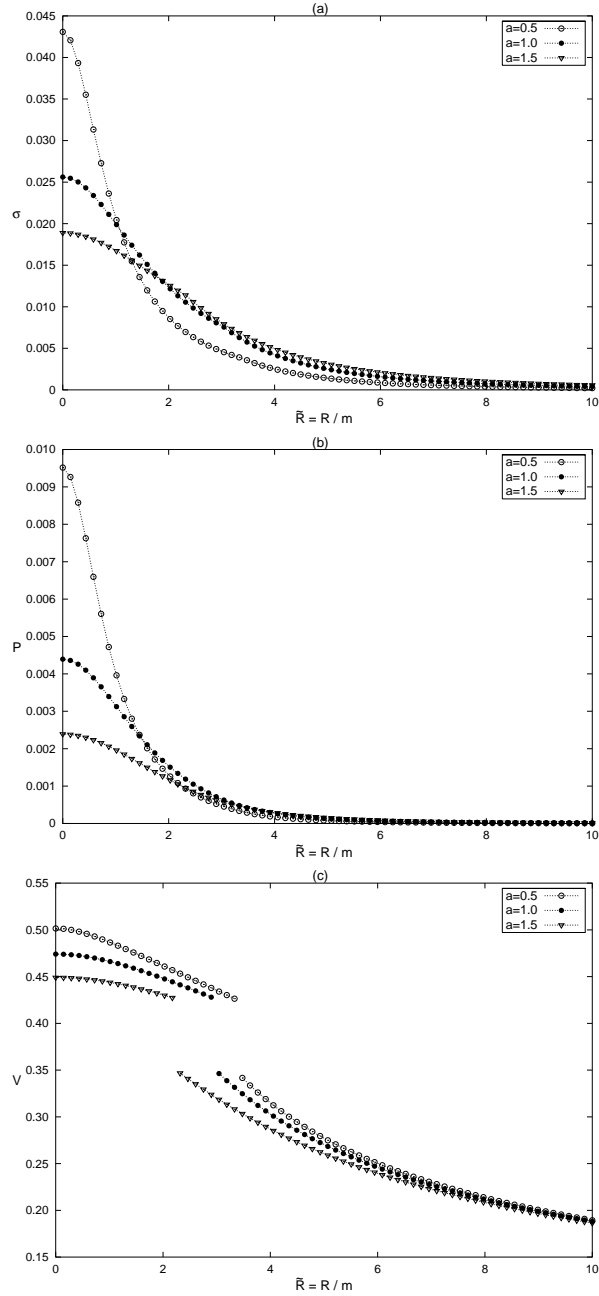
Figure A.8: (a) The surface energy density σ [Eq. (A.43)], (b) the pressure P [Eq. (A.44) and (c) the velocity of sound V [Eq. (A.46)] for the disk with $k = -1/2$; $r_b = 2$; for $a = 0.5$, 1.0 and 1.5 as function of $\tilde{R} = R/m$.
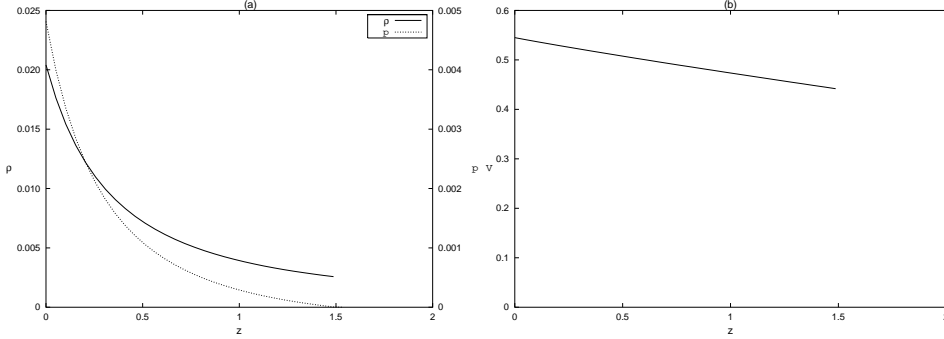
Figure A.9: (a) The density ρ [Eq. (A.35)] and pressure p [Eq. (A.36)], and (b) the velocity of sound V [Eq. (A.38)] for the halo with $k = -1/2$; $r_b = 2$; for $a = 0.5$ along the z axis.

where the A's and B's are constants and $x = \sqrt{2n^2 - 4}$. The solution (λ, ν_{2a}) with $n = 2$ corresponds to Schwarzschild's internal solution in isotropic coordinates (see for instance Ref. [22]). This solution has constant density and is conformally flat when $B_{1a} = 0$.

The density, pressure and sound velocity for the solutions (λ, ν_{2a}) and (λ, ν_{2b}), will be denoted by (ρ, p_{2a}, V_{2a}) and (ρ, p_{2b}, V_{2b}), respectively. We find,

$$\rho = \frac{1}{32\pi} \left[(4 - n^2) \left(A_1 r^{n/2} + A_2 r^{-n/2} \right)^2 + 12n^2 A_1 A_2 \right], \tag{A.55}$$

$$p_{2a} = \frac{1}{32\pi} \left[-12n^2 A_1 A_2 + (3n^2 - 4) \left(A_1 r^{n/2} + A_2 r^{-n/2} \right)^2 \right.$$
$$\left. + \frac{2nx(B_{2a} - B_{1a}r^x)}{B_{2a} + B_{1a}r^x} \left(A_1^2 r^n - A_2^2 r^{-n} \right) \right], \tag{A.56}$$

$$p_{2b} = \frac{1}{16\pi(B_{1b} + B_{2b}\ln(r))} \left[(B_{1b} + B_{2b}\ln(r)) \left(A_1^2 r^{\sqrt{2}} + A_2^2 r^{-\sqrt{2}} - 10A_1 A_2 \right) \right.$$
$$\left. + 2\sqrt{2}B_{2b} \left(A_2^2 r^{-\sqrt{2}} - A_1^2 r^{\sqrt{2}} \right) \right], \tag{A.57}$$

$$V_{2a}^2 = \frac{1}{(4 - n^2) \left(A_1^2 r^n - A_2^2 r^{-n} \right) (B_{2a} + B_{1a}r^x)^2} \left\{ B_{2a}^2 \left[A_1^2 r^n (3n^2 + 2nx - 4) \right. \right.$$
$$\left. + A_2^2 r^{-n}(-3n^2 + 2nx + 4) \right] + B_{1a}^2 r^{2x} \left[A_1^2 r^n (3n^2 - 2nx - 4) \right.$$
$$\left. + A_2^2 r^{-n}(-3n^2 - 2nx + 4) \right] + 2B_{1a}B_{2a}r^x \left[A_1^2 r^n (3n^2 - 2x^2 - 4) \right.$$
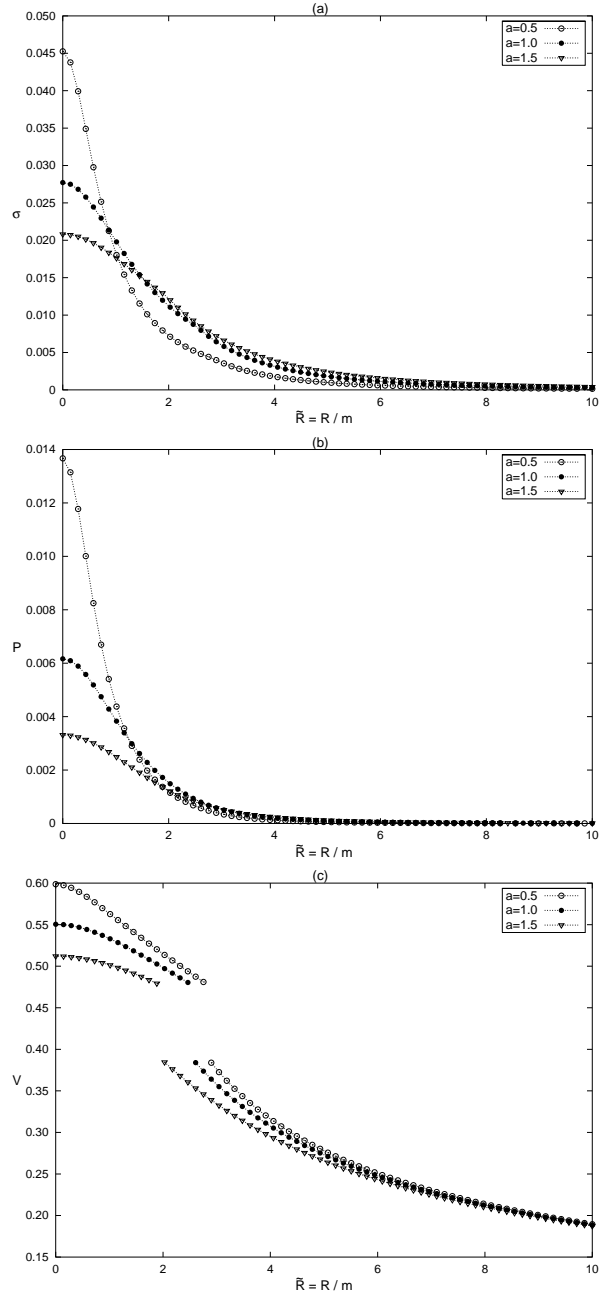$$\left. \left. + A_2^2 r^{-n}(-3n^2 + 2x^2 + 4) \right] \right\}, \tag{A.58}$$

Figure A.10: (a) The surface energy density σ [Eq. (A.43)], (b) the pressure P [Eq. (A.45)], (c) the velocity of sound V [Eq. (A.47)] for the disk with $k = -2 + \sqrt{2}$ and $r_b = 2$; for $a = 0.5$, 1.0 and 1.5 as function of $\tilde{R} = R/m$.
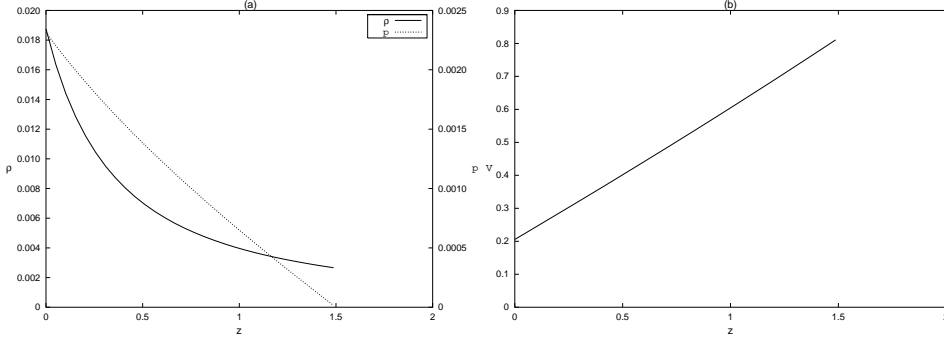
Figure A.11: (a) The density ρ [Eq. (A.35)] and pressure p [Eq. (A.37)] and (b) the velocity of sound V [Eq. (A.39)] for the halo with $k = -2 + \sqrt{2}$ and $r_b = 2$; for $a = 0.5$ along the axis z.

$$
\begin{aligned}
V_{2b}^2 = {} & \frac{1}{[B_{1b} + B_{2b}\ln(r)]^2 \left(A_1^2 r^{\sqrt{2}} - A_2^2 r^{-\sqrt{2}}\right)} \Big\{ A_1^2 r^{\sqrt{2}} [(B_{1b} + B_{2b}\ln(r)) \\
& \times (B_{1b} + B_{2b}\ln(r) - 2\sqrt{2}B_{2b}) + 2B_{2b}^2] - A_2^2 r^{-\sqrt{2}} \\
& \times \Big[(B_{1b} + B_{2b}\ln(r))(B_{1b} + B_{2b}\ln(r) + 2\sqrt{2}B_{2b}) + 2B_{2b}^2 \Big] \Big\}.
\end{aligned}
\tag{A.59}
$$

The condition of continuity of the metric functions (λ, ν) given by Eqs. (A.52)–(A.54) and the corresponding functions in Eq. (A.9) at the boundary $r = r_b$ leads to the following expressions:

$$
A_1 = \frac{1}{n r_b^{2+n/2}\left(1 + \frac{m}{2r_b}\right)^3} \left[\frac{m}{2} - r_b\left(1 - \frac{n}{2} - \frac{mn}{4r_b}\right)\right],
\tag{A.60}
$$

$$
A_2 = \frac{1}{r_b^{2-n/2}\left(1 + \frac{m}{2r_b}\right)^3} \left[-\frac{m}{2n} + r_b\left(\frac{1}{2} + \frac{1}{n} + \frac{m}{4r_b}\right)\right],
\tag{A.61}
$$

$$
B_{1a} = \frac{-4r_b^2\left(1 - \frac{2m}{r_b}\right) - m^2 + 2xr_b^2\left(1 - \frac{m^2}{4r_b^2}\right)}{4xr_b^{3+x/2}\left(1 + \frac{m}{2r_b}\right)^4},
\tag{A.62}
$$

$$
B_{2a} = \frac{4r_b^2\left(1 - \frac{2m}{r_b}\right) + m^2 + 2xr_b^2\left(1 - \frac{m^2}{4r_b^2}\right)}{4xr_b^{3-x/2}\left(1 + \frac{m}{2r_b}\right)^4},
\tag{A.63}
$$

$$
B_{1b} = \frac{1}{4r_b^3\left(1 + \frac{m}{2r_b}\right)^4} \left[4r_b^2 - m^2 + (m^2 - 8mr_b + 4r_b^2)\ln(r_b)\right],
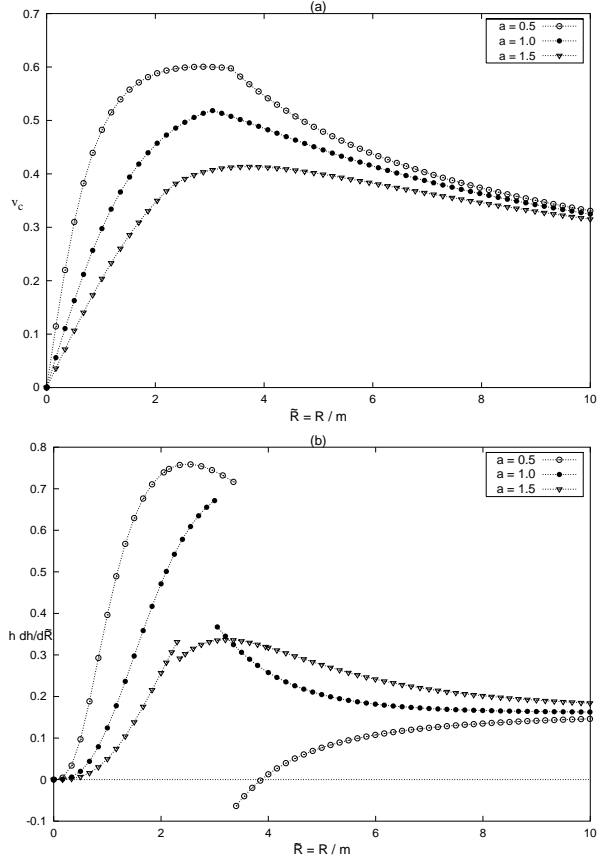\tag{A.64}
$$

61

Figure A.12: (a) The tangential velocity v_{c1a} [Eq. (A.48)] and (b) the curves of $h(dh/d\tilde{R})$ [Eq. (A.50)] with $k = -1/2$ and $r_b = 2$; for $a = 0.5$, 1.0, and 1.5 as function of $\tilde{R} = R/m$. A region of instability appears on the disk generated with parameter $a = 0.5$.
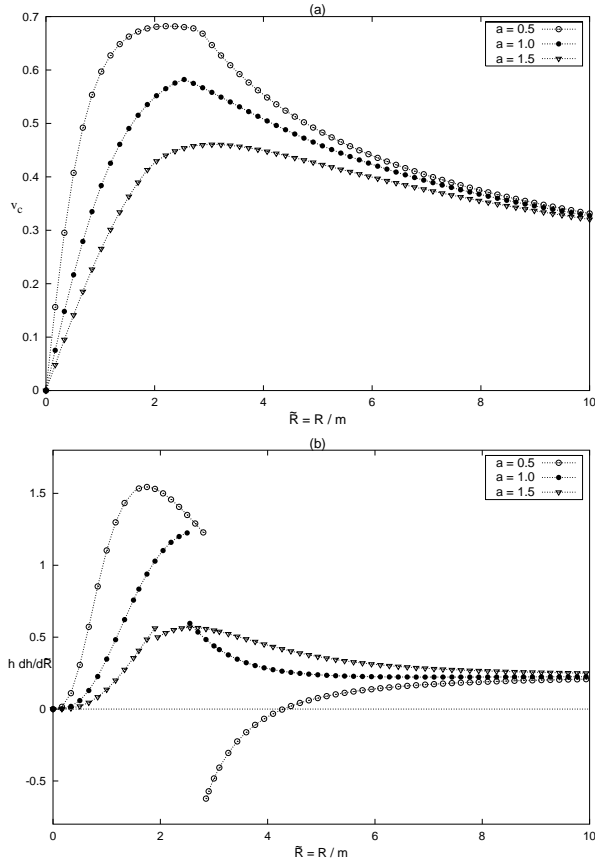
Figure A.13: (a) The tangential velocity v_{c1b} [Eq. (A.49)] and (b) the curves of $h(dh/d\tilde{R})$ [Eq. (A.51)] with $k = -2 + \sqrt{2}$ and $r_b = 2$; for $a = 0.5$, 1.0, and 1.5 as function of $\tilde{R} = R/m$. As in the previous case, the same region of instability occurs.

$$B_{2b} = -\frac{m^2 - 8mr_b + 4r_b^2}{4r_b^3 \left(1 + \frac{m}{2r_b}\right)^4}. \tag{A.65}$$

V_{2a} has its maximum at $r = r_b$, and V_{2b} at $r = 0$.

Using Eqs. (A.52)–(A.54) in Eqs. (A.3)–(A.6), we get the expressions for the energy density, pressure and sound velocity of the disk:

$$\sigma = \frac{a}{4\pi}\left[A_1(2+n)\mathcal{R}^{-1/2+n/4} + A_2(2-n)\mathcal{R}^{-1/2-n/4}\right], \tag{A.66}$$

$$P_{2a} = -\frac{a}{8\pi\left(B_{1a}\mathcal{R}^{1/2+x/4} + B_{2a}\mathcal{R}^{1/2-x/4}\right)}\left[B_{1a}A_1(2+2n-x)\mathcal{R}^{(x+n)/4}\right.$$
$$+B_{1a}A_2(2-2n-x)\mathcal{R}^{(x-n)/4} + B_{2a}A_1(2+2n+x)\mathcal{R}^{(-x+n)/4}$$
$$\left.+B_{2a}A_2(2-2n+x)\mathcal{R}^{-(x+n)/4}\right], \tag{A.67}$$

$$P_{2b} = -\frac{a}{4\pi[2B_{1b} + B_{2b}\ln(\mathcal{R})]}\left\{2(1+\sqrt{2})B_{1b}A_1\mathcal{R}^{-1/2+\sqrt{2}/4}\right.$$
$$+2(1-\sqrt{2})B_{1b}A_2\mathcal{R}^{-1/2-\sqrt{2}/4} + \left[(1+\sqrt{2})\ln(\mathcal{R}) - 2\right]B_{2b}A_1\mathcal{R}^{-1/2+\sqrt{2}/4}$$
$$\left.+ \left[(1-\sqrt{2})\ln(\mathcal{R}) - 2\right]B_{2b}A_2\mathcal{R}^{-1/2-\sqrt{2}/4}\right\}, \tag{A.68}$$

$$V_{2a}^2 = \frac{1}{2(4-n^2)\left[A_2 + A_1\mathcal{R}^{n/2}\right]\left[B_{2a} + B_{1a}\mathcal{R}^{x/2}\right]^2}\left\{A_1\mathcal{R}^{n/2}\right.$$
$$\left[B_{1a}^2(n-2)(2n-x+2)\mathcal{R}^x + B_{2a}^2(n-2)(2n+x+2)\right.$$
$$\left.-4B_{1a}B_{2a}(-n^2+n+x^2+2)\mathcal{R}^{x/2}\right] + A_2\left[B_{1a}^2(n+2)(2n+x-2)\mathcal{R}^x\right.$$
$$\left.\left.+B_{2a}^2(n+2)(2n-x-2) - 4B_{1a}B_{2a}(-n^2-n+x^2+2)\mathcal{R}^{x/2}\right]\right\}, \tag{A.69}$$

$$V_{2b}^2 = -\frac{2B_{1b} + 2B_{2b} + B_{2b}\ln(\mathcal{R})}{2[2B_{1b} + B_{2b}\ln(\mathcal{R})]^2[A_2 + A_1\mathcal{R}^{1/\sqrt{2}}]}\left\{\left[\sqrt{2}\ln(\mathcal{R}) - 4\right]\right.$$
$$\left.\times B_{2b}A_1\mathcal{R}^{1/\sqrt{2}} - \left[\sqrt{2}\ln(\mathcal{R}) + 4\right]B_{2b}A_2 + 2\sqrt{2}B_{1b}\left[A_1\mathcal{R}^{1/\sqrt{2}} - A_2\right]\right\}, \tag{A.70}$$

where $\mathcal{R} = R^2 + a^2$. The curves of σ, P and V as functions of $\tilde{R} = R/m$ with parameters $n = 1.8$; $m = 0.5$, and $r_b = 2$ for $a = 0.5$, 1.0,1.5 are displayed in Figs. A.14(a) – A.14(c), respectively. Figures A.15(a) – A.15(b) show the density ρ, pressure p and velocity of sound V for the halo with parameters $n = 1.8$; $m = 0.5$; $r_b = 2$, for $a = 0.5$ along the axis z. The same physical quantities are shown in Figs. A.16 and A.17 with $n = \sqrt{2}$.
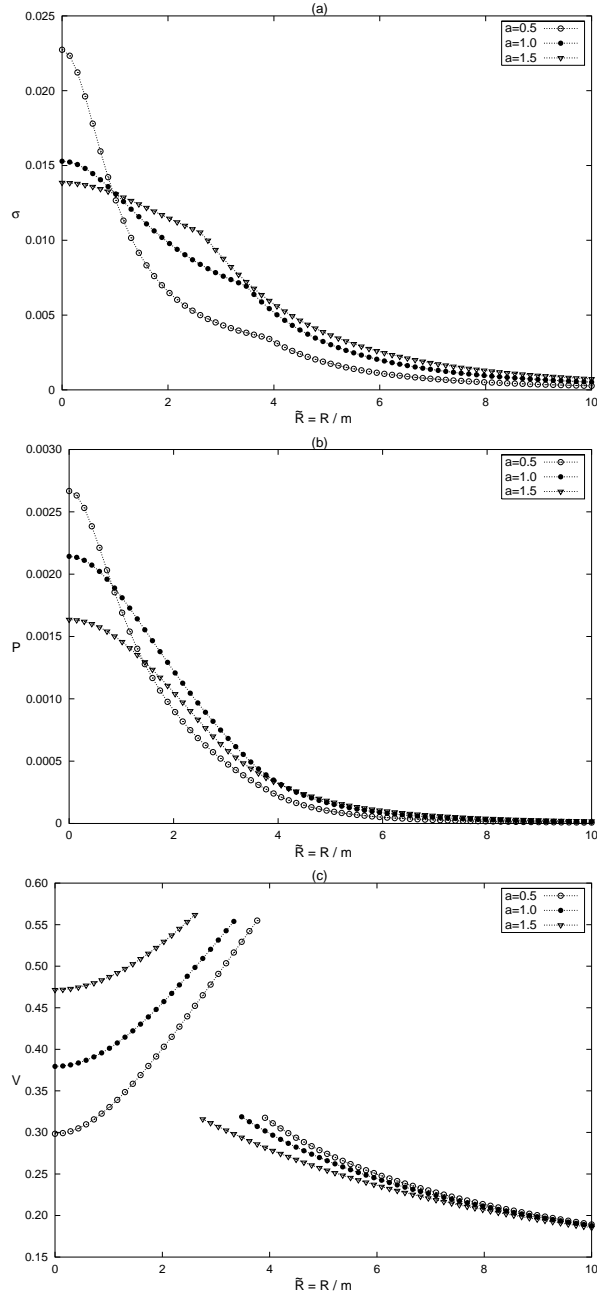
Figure A.14: (a) The surface energy density σ [Eq. (A.66)], (b) the pressure P [Eq. (A.67)], (c) the velocity of sound V [Eq. (A.69)] for the disk with $n = 1.8$; $m = 0.5$; $r_b = 2$; for $a = 0.5$, 1.0 and 1.5 as function of $\tilde{R} = R/m$.
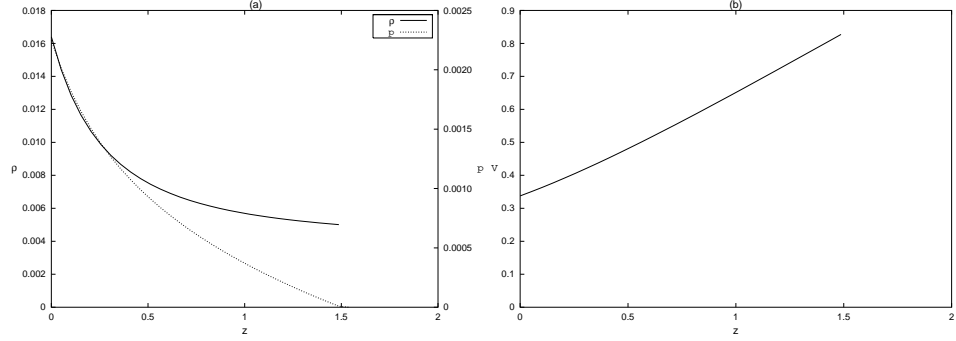
Figure A.15: (a) The density ρ [Eq. (A.55)] and pressure p [Eq. (A.56)], (b) the velocity of sound V [Eq. (A.58)] for the halo with $n = 1.8$; $m = 0.5$; $r_b = 2$; for $a = 0.5$ along the z axis.

The tangential velocity v_c is given by

$$
v_{c2a}^2 = \frac{R^2}{[B_{1a}\mathcal{R}^{x/2} + B_{2a}][A_1\mathcal{R}^{n/2}(2a^2 - nR^2) + A_2(2a^2 + nR^2)]} \times
$$
$$
\left\{ A_2[B_{1a}(n+x)\mathcal{R}^{x/2} + B_{2a}(n-x)] - A_1\mathcal{R}^{n/2}[B_{1a}(n-x)\mathcal{R}^{x/2} \right.
$$
$$
\left. + B_{2a}(n+x)] \right\}, \tag{A.71}
$$

$$
v_{c2b}^2 = \frac{R^2}{[2B_{1b} + B_{2b}\ln(\mathcal{R})][A_1\mathcal{R}^{\sqrt{2}/2}(2a^2 - \sqrt{2}R^2) + A_2(2a^2 + \sqrt{2}R^2)]} \times
$$
$$
\left\{ A_2[2\sqrt{2}B_{1b} + B_{2b}(4 + \sqrt{2}\ln(\mathcal{R}))] - A_1\mathcal{R}^{\sqrt{2}/2}[2\sqrt{2}B_{1b} \right.
$$
$$
\left. + B_{2b}(-4 + \sqrt{2}\ln(\mathcal{R}))] \right\}, \tag{A.72}
$$

and the specific angular momentum h

$$
h_{2a} = \frac{R^2\mathcal{R}^{-1/2+n/4}}{(A_1\mathcal{R}^{n/2} + A_2)^{3/2}\sqrt{B_{1a}(2a^2 - xR^2)\mathcal{R}^{x/2} + B_{2a}(2a^2 + xR^2)}} \times
$$
$$
\left\{ A_2[B_{1a}(n+x)\mathcal{R}^{x/2} + B_{2a}(n-x)] - A_1\mathcal{R}^{n/2}[B_{1a}(n-x)\mathcal{R}^{x/2} \right.
$$
$$
\left. + B_{2a}(n+x)] \right\}^{1/2}, \tag{A.73}
$$

$$
h_{2b} = \frac{R^2\mathcal{R}^{-1/2+\sqrt{2}/4}}{[A_1\mathcal{R}^{\sqrt{2}/2} + A_2]^{3/2}\sqrt{4a^2 B_{1b} + 2B_{2b}[-2R^2 + a^2\ln(\mathcal{R})]}} \times
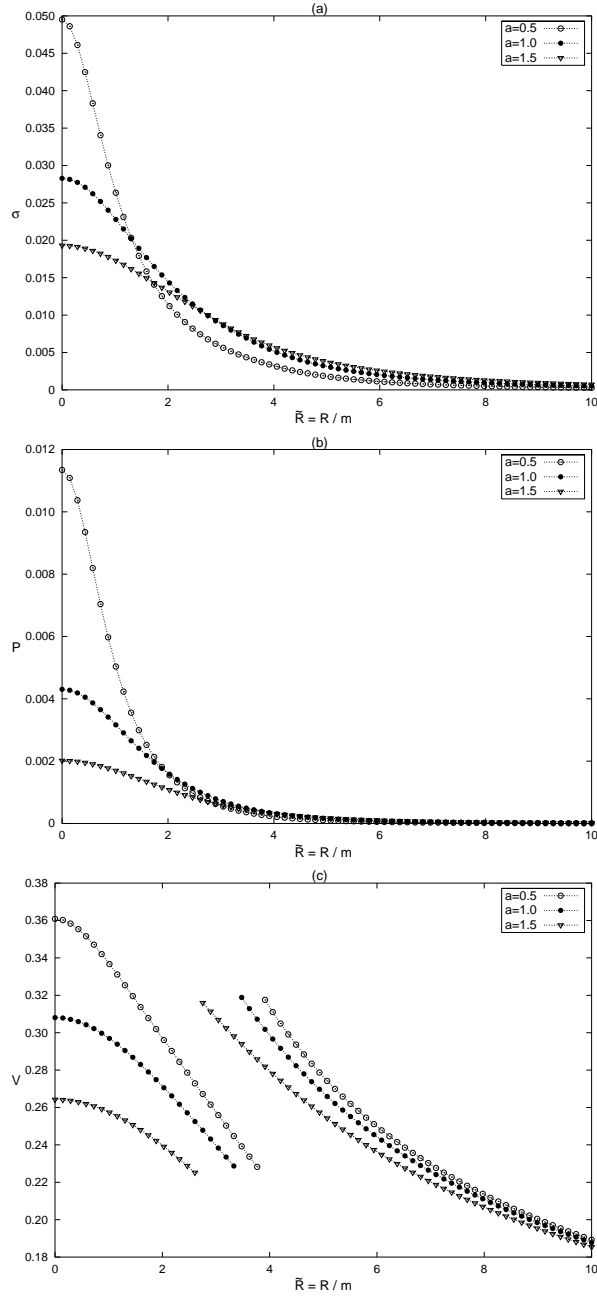$$

Figure A.16: (a) The surface energy density σ [Eq. (A.66)], (b) the pressure P [Eq. (A.68)], (c) the velocity of sound V [Eq. (A.70)] for the disk with $n = \sqrt{2}$; $r_b = 2$; $m = 0.5$; for $a = 0.5$, 1.0 and 1.5 as function of $\tilde{R} = R/m$.
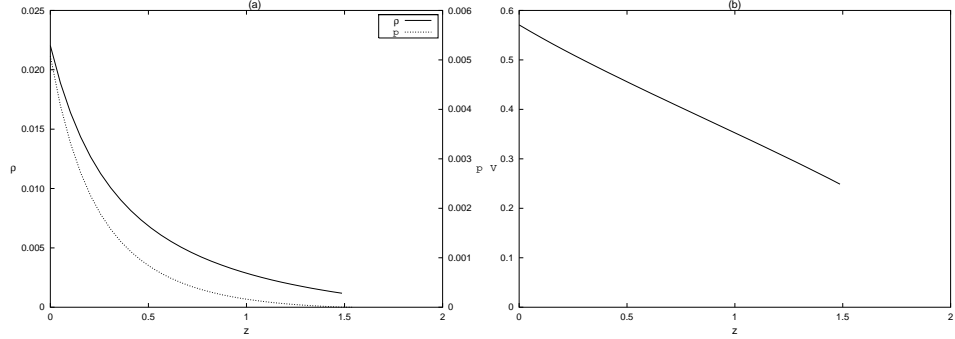
67

Figure A.17: (a) The density ρ [Eq. (A.55)] and pressure p [Eq. (A.57)], (b) the velocity of sound V [Eq. (A.59)] for the halo with $n = \sqrt{2}$; $r_b = 2$; for $a = 0.5$ along the z axis.

$$\left\{ A_2[2\sqrt{2}B_{1b} + B_{2b}(4 + \sqrt{2}\ln(\mathcal{R}))] - A_1\mathcal{R}^{\sqrt{2}/2}[2\sqrt{2}B_{1b} \right.$$
$$\left. + B_{2b}(-4 + \sqrt{2}\ln(\mathcal{R}))] \right\}^{1/2}. \tag{A.74}$$

In Figs. A.18(a) and A.18(b), the curves of tangential velocities Eq. (A.71) and $h(dh/d\tilde{R})$ Eq. (A.73), respectively, are displayed as functions of $\tilde{R} = R/m$ with $n = 1.8$; $m = 0.5$; $r_b = 2$; $a = 0.5$, 1.0,1.5. Figure A.19 shows the same quantities with $n = \sqrt{2}$. Unlike solution 2, no unstable circular orbits are present for the disks constructed with these parameters.

A.5 Disks with composite halos from spherical solutions

We study two examples of disks with halos constructed from spheres of fluids with two layers as the ones depicted in Fig. A.3.

A.5.1 Internal Schwarzschild solution and Buchdahl solution

Let us consider that a fluid sphere is formed by two layers: The internal layer, $0 \le r < r_1$, will be taken as the internal Schwarzschild solution (solution $2a$ with $n = 2$),

$$e^\nu = \frac{\left(B_1 r^2 + B_2\right)^2}{\left(A_1 r^2 + A_2\right)^2}, \quad e^\lambda = \frac{1}{\left(A_1 r^2 + A_2\right)^2}. \tag{A.75}$$
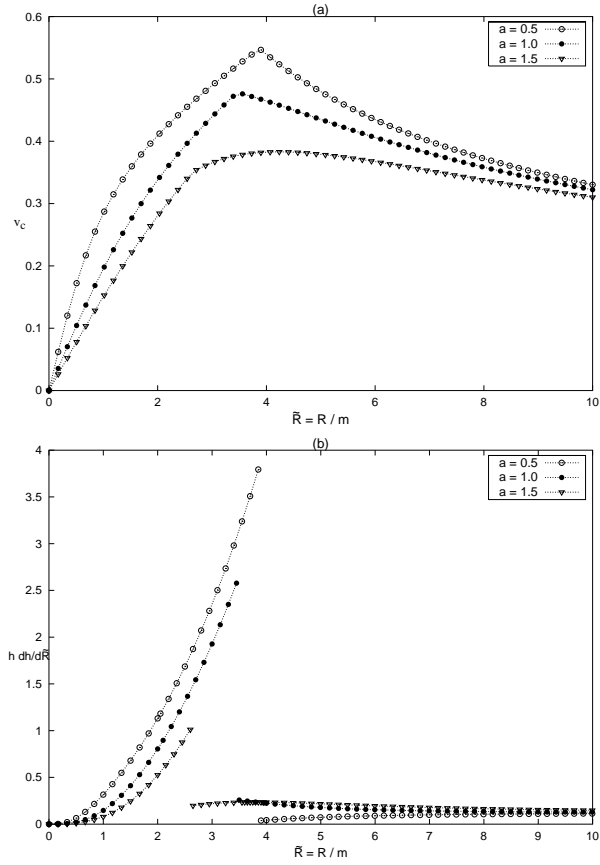
Figure A.18: (a) The tangential velocity v_{c2a} [Eq. (A.71)], and (b) the curves of $h(dh/d\tilde{R})$ [Eq. (A.73)] with $n = 1.8$; $m = 0.5$; $r_b = 2$; for $a = 0.5$, 1.0, and 1.5 as function of $\tilde{R} = R/m$. The disks have no unstable orbits for these parameters.
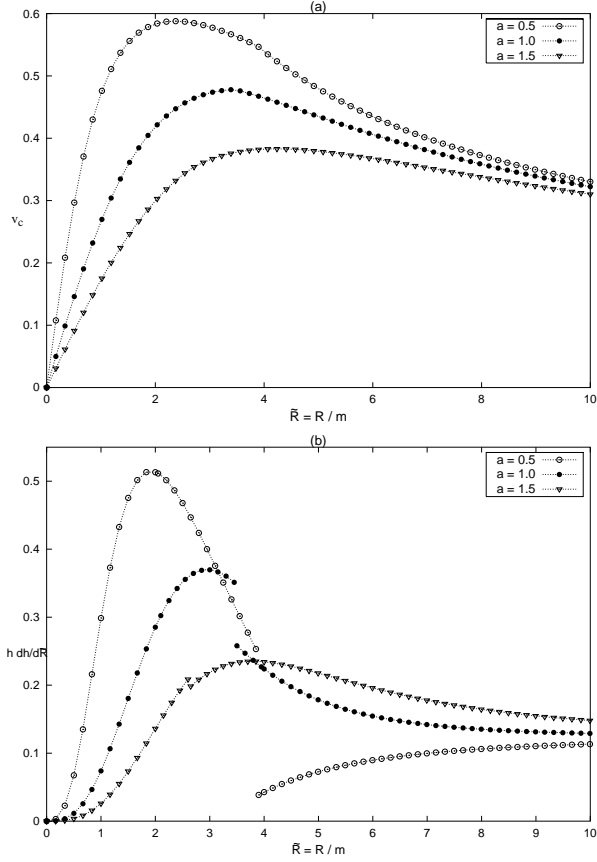
Figure A.19: (a) The tangential velocity v_{c2b} [Eq. (A.72)], and (b) the curves of $h(dh/d\tilde{R})$ [Eq. (A.74)] with $n = \sqrt{2}$; $m = 0.5$; $r_b = 2$; for $a = 0.5$, 1.0, and 1.5 as function of $\tilde{R} = R/m$. The disks have no unstable orbits for these parameters.

The external layer, $r > r_1$ is taken as the Buchdahl solution,

$$e^\nu = \left(\frac{1 - \frac{C}{\sqrt{1+kr^2}}}{1 + \frac{C}{\sqrt{1+kr^2}}} \right)^2, \quad e^\lambda = \left(1 + \frac{C}{\sqrt{1+kr^2}} \right)^4. \tag{A.76}$$

Note that the external layer has no boundary, i. e., this layer has infinite radius.

According to the continuity conditions at $r = r_1$, the constants are related through

$$A_1 = \frac{Ck}{\left(C + \sqrt{1 + kr_1^2} \right)^3}, \quad A_2 = \frac{1 + \frac{C}{(1+kr_1^2)^{3/2}}}{\left(1 + \frac{C}{\sqrt{1+kr_1^2}} \right)^3}, \tag{A.77}$$

$$B_1 = \frac{Ck}{(1 + kr_1^2)\left(1 + \frac{C}{\sqrt{1+kr_1^2}} \right)^3} D, \tag{A.78}$$

$$D = \frac{\left[C(1 - 3kr_1^2) - \frac{C^2}{\sqrt{1+kr_1^2}}(1 - kr_1^2) + 2(1 + kr_1^2)^{3/2} \right]}{\left[(1 + kr_1^2)^2 + 2C\sqrt{1 + kr_1^2} + C^2(1 - kr_1^2) \right]}, \tag{A.79}$$

$$B_2 = \frac{1 - \frac{C}{\sqrt{1+kr_1^2}}}{\left(1 + \frac{C}{\sqrt{1+kr_1^2}} \right)^3} - B_1 r_1^2. \tag{A.80}$$

With these relations, one verifies that, using Eqs. (A.27) and (A.66), Eqs. (A.28) and (A.67), both the energy density and the pressure are continuous at the radius $R = \sqrt{r_1^2 - a^2}$ of the disk.

Figures A.20(a)–A.20(c) show, respectively, σ, P and V for the disk obtained from fluid layers Eq. (A.75) and (A.76) with parameters $m = 1$; $k = 1$; $r_1 = 2$; for $a = 0.5$, 1.0 and 1.5 as function of $\tilde{R} = R/m$. The density ρ, pressure p, and velocity of sound V, for the halo along the z axis with the same parameters for $a = 0.5$ is shown in Fig. A.21.

In Figs. A.22(a) and A.22(b), the curves of tangential velocities and of $h(dh/d\tilde{R})$, respectively, are displayed as functions of $\tilde{R} = R/m$.
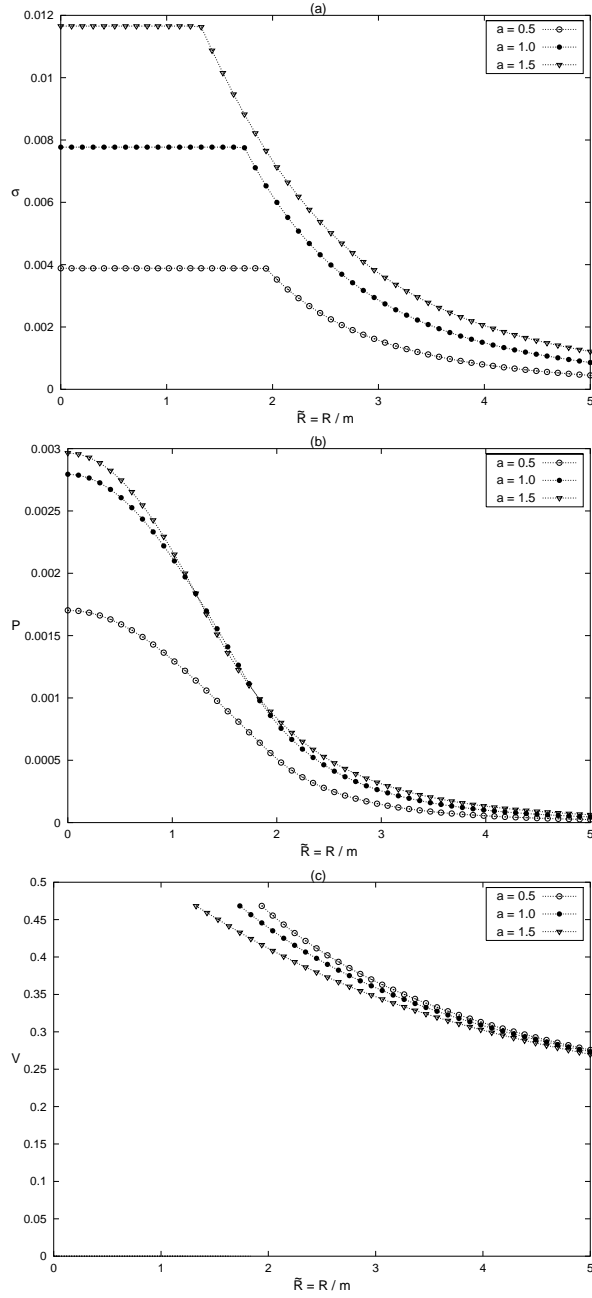
71

Figure A.20: (a) The surface energy density σ, (b) the pressure P, and (c) the velocity of sound V for the disk generated from spherical fluid layers Eqs. (A.75) and (A.76) with $m = 1$; $k = 1$; $r_1 = 2$; for $a = 0.5$, 1.0 and 1.5 as function of $\tilde{R} = R/m$.
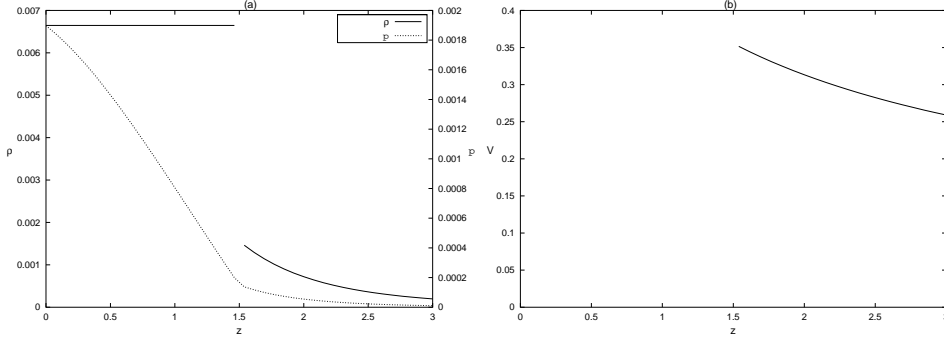
Figure A.21: (a) The density ρ and pressure p, (b) the velocity of sound V for the halo formed by fluid layers Eqs. (A.75) and (A.76) with $m = 1$; $k = 1$; $r_1 = 2$ and $a = 0.5$ along the z axis.

A.5.2 NPV Solution 2b with $n = \sqrt{2}$ and NPV solution 1b with $k = -2 + \sqrt{2}$

Now we consider a sphere composed with two finite layers: The internal layer, $0 \leq r < r_1$, is taken as the NPV solution 2b with $n = \sqrt{2}$,

$$e^\nu = \frac{(B_1 + B_2 \ln(r))^2}{\left(A_1 r^{\sqrt{2}/2} + A_2 r^{-\sqrt{2}/2}\right)^2}, \quad e^\lambda = \frac{1}{\left(A_1 r^{1+\sqrt{2}/2} + A_2 r^{1-\sqrt{2}/2}\right)^2}. \quad \text{(A.81)}$$

The external layer, $r_1 < r < r_2$, is taken as the NPV solution 1b with $k = -2 + \sqrt{2}$,

$$e^\nu = r^{\sqrt{2}} (A_3 + B_3 \ln(r))^2, \quad e^\lambda = C r^{-2+\sqrt{2}}. \quad \text{(A.82)}$$

The spacetime outside the sphere, $r > r_2$, will be taken as the Schwarzschild's vacuum solution in isotropic coordinates:

$$e^\nu = \frac{\left(1 - \frac{m}{2r}\right)^2}{\left(1 + \frac{m}{2r}\right)^2}, \quad e^\lambda = \left(1 + \frac{m}{2r}\right)^4. \quad \text{(A.83)}$$

In this case the pressure should be zero at $r = r_2$. The continuity conditions at $r = r_1$ and $r = r_2$ give the relations

$$\frac{m}{r_2} = \frac{\sqrt{2}(2 - \sqrt{2})}{1 + \sqrt{2}}, \quad C = \frac{64 r_2^{2-\sqrt{2}}}{(1 + \sqrt{2})^4}, \quad B_3 = \frac{1}{4 r_2^{1/\sqrt{2}}}, \quad A_3 = -\frac{2\sqrt{2} + \ln(r_2)}{r_2^{1/\sqrt{2}}}, \quad \text{(A.84)}$$
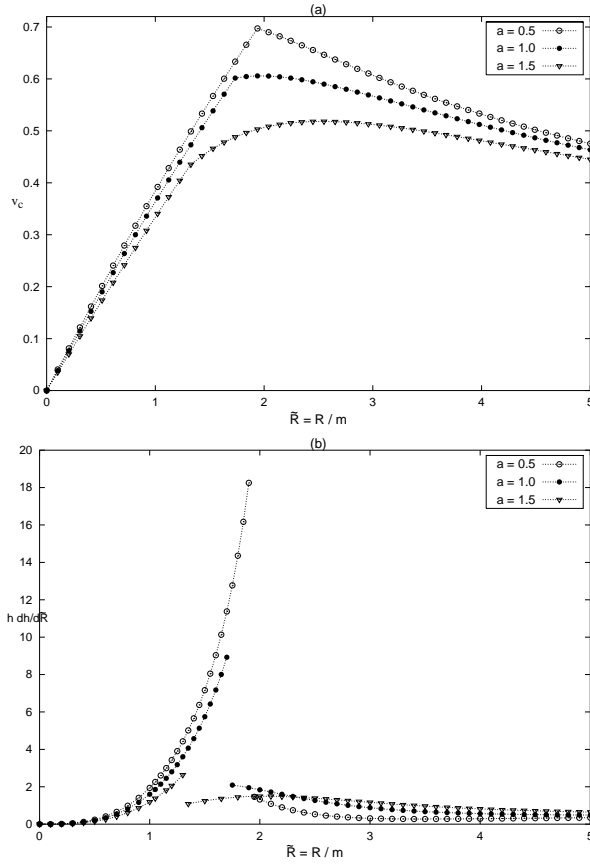
73

Figure A.22: (a) The tangential velocity v_c, (b) the curves of $h(dh/d\tilde{R})$ for the disk generated from fluid layers Eqs. (A.75) and (A.76) with $m = 1$; $k = 1$; $r_1 = 2$; for $a = 0.5$, 1.0 and 1.5 as function of $\tilde{R} = R/m$. The disks obtained with these parameters have no unstable orbits.

$$A_1 = 0, \; A_2 = \frac{1}{\sqrt{C}}, \; B_2 = \frac{r_1^{\sqrt{2}}}{2\sqrt{2C}} \left[(A_3 + B_3 \ln(r_1)) \left(1 - r_1^{-\sqrt{2}}\right) + 2\sqrt{2}B_3 \right],$$

$$\text{(A.85)}$$

$$B_1 = \frac{r_1^{\sqrt{2}}}{2\sqrt{2C}} \left[(A_3 + B_3 \ln(r_1)) \left(2\sqrt{2}r_1^{-\sqrt{2}} - \ln(r_1) + \ln(r_1)r_1^{-\sqrt{2}} \right) \right.$$
$$\left. - 2\sqrt{2}B_3 \ln(r_1) \right]. \tag{A.86}$$

Using Eqs. (A.43) and (A.66), the energy density of the disk at $R = \sqrt{r_1^2 - a^2}$ is continuous, but not the pressure. The difference between Eqs. (A.68) and (A.45) is

$$\Delta P = \frac{a(r_1^{\sqrt{2}/2} - r_1^{-\sqrt{2}/2})}{16\pi\sqrt{C}r_1(A_3 + B_3 \ln(r_1))} \left[\sqrt{2}(A_3 + B_3 \ln(r_1)) + 4B_3 \right]. \tag{A.87}$$

The pressure is continuous if $r_1^{\sqrt{2}/2} - r_1^{-\sqrt{2}/2} = 0 \rightarrow r_1 = 1$.

Figures A.23(a)–A.23(c) show, respectively, σ, P and V for the disk obtained from fluid layers (A.81) and (A.82) with parameters $r_1 = 1$; $r_2 = 2$; for $a = 0.3$, 0.6 and 0.9 as function of $\tilde{R} = R/m$. The density ρ, pressure p, and velocity of sound V, for the halo along the z axis with the same parameters for $a = 0.3$ is shown in Figs. A.24. In Figs. A.25(a) and A.25(b), the curves of tangential velocities and of $h(dh/d\tilde{R})$, respectively, are displayed as functions of $\tilde{R} = R/m$. In this case, regions of unstable orbits exist for parameters $a = 0.3$ and $a = 0.6$.

A.6 Discussion

The "displace, cut and reflect" method applied to solutions of Einstein field equations in isotropic coordinates can generate disks with positive energy density and equal radial and azimuthal pressures (perfect fluid). With solutions of static spheres of perfect fluid it is possible to construct disks of perfect fluid surrounded also by a perfect fluid matter. As far we know these are the first disk models of this kind in the literature.

All disks constructed as examples have some common features: surface energy density and pressures decrease monotonically and rapidly with radius. As the "cut" parameter a decreases, the disks become more relativistic, with surface energy density and pressure more concentrated near the center. Also regions of unstable circular orbits are more likely to appear for highly relativistic disks. Parameters can be chosen so that the sound velocity in the
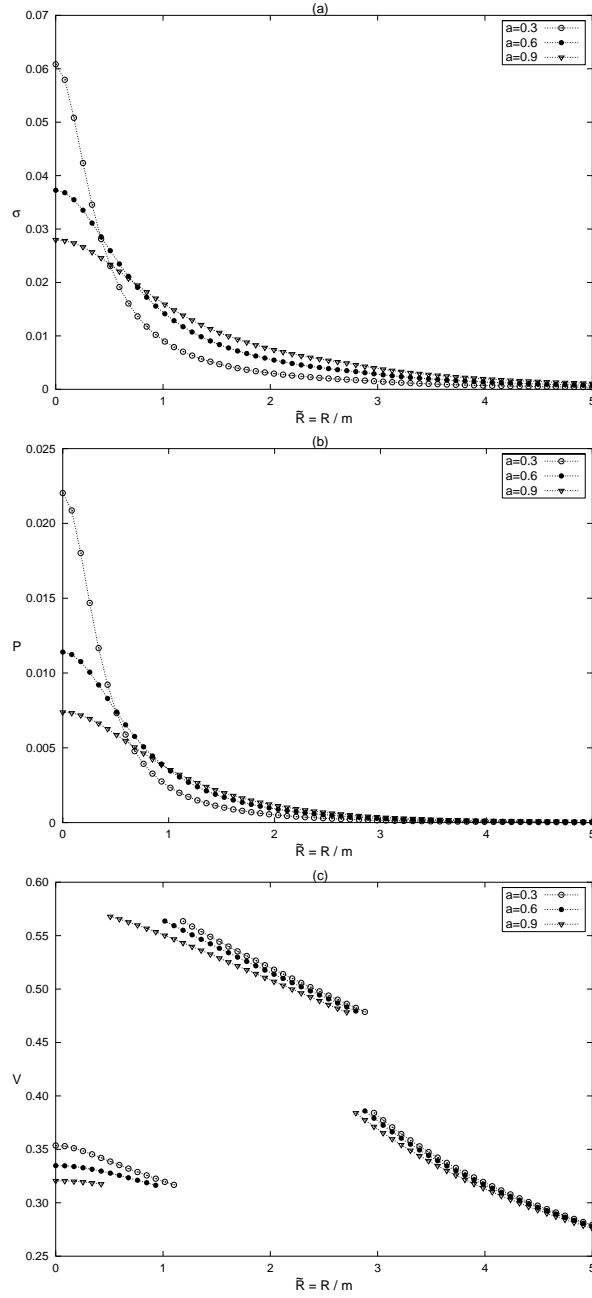
Figure A.23: (a) The surface energy density σ, (b) the pressure P, (c) the velocity of sound V for the disk generated from spherical fluid layers Eqs. (A.81) and (A.82) with $r_1 = 1$; $r_2 = 2$; for $a = 0.3$, 0.6 and 0.9 as function of $\tilde{R} = R/m$.
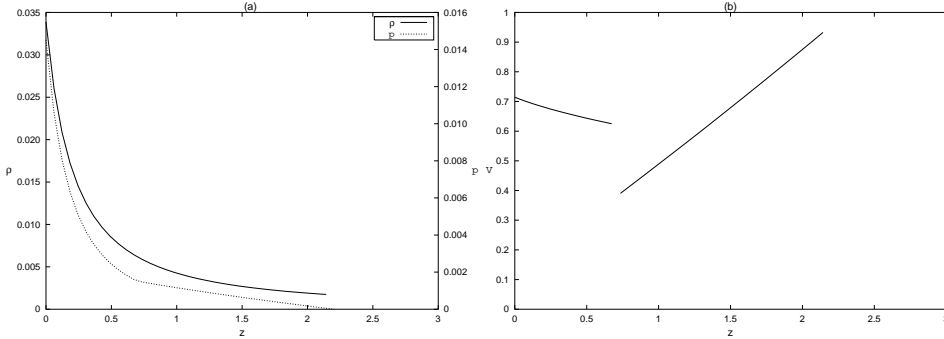
Figure A.24: (a) The density ρ and pressure p, (b) the velocity of sound V for the halo formed by fluid layers Eqs. (A.81) and (A.82) with $r_1 = 1$; $r_2 = 2$ and $a = 0.3$ along the axis z.

fluid and the tangential velocity of test particles in circular motion are less than the velocity of light. This tangential velocity first increases with radius and reaches a maximum. Then, for large radii, it decreases as $1/\sqrt{R}$, in case of disks generated from Schwarzschild and Buchdahl's solutions. The sound velocity is also a decreasing function of radius, except in solution NPV 2a with $\sqrt{2} < n \leq 2$, where it reaches its maximum value at the boundary. In principle, other solutions of static spheres of perfect fluid could be used to generate other disk + halo configurations, but it is not guaranteed that the disks will have the characteristics of normal fluid matter.

We believe that the presented disks can be used to describe a more realistic model of galaxies than most of the already studied disks since the counterrotation hypothesis is not needed to have a stable configuration.

We want to finish our discussion by presenting a table that summarizes our results about disks in a unified manner.

In Table A. 1 we list the seed metric coefficients, matching conditions at the boundaries, and relevant physical quantities of all disks studied in this work. The numbers refer to the equations presented along the paper and NPV stands for Narlikar, Patwardhan, and Vaidya as before.
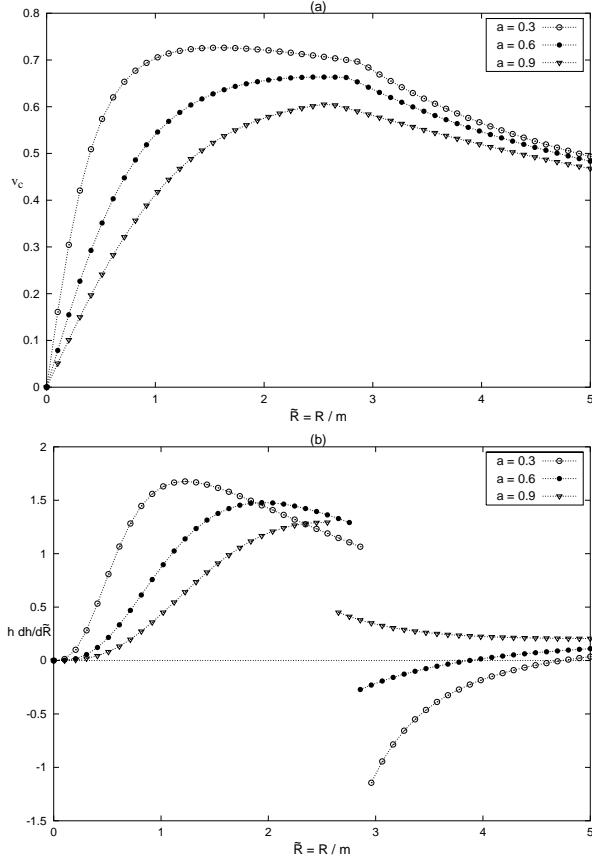
Acknowledgments

Figure A.25: (a) The tangential velocity v_c, and (b) the curves of $h(dh/d\tilde{R})$ for the disk generated from spherical fluid layers Eqs. (A.81) and (A.82) with $r_1 = 1$; $r_2 = 2$; for $a = 0.3$, 0.6 and 0.9 as function of $\tilde{R} = R/m$. Regions of unstable circular orbits appear for the disks obtained with parameters $a = 0.3$ and 0.6.

Table A.1: Disks properties

Solution	Metric coefficients	Matching conditions	Energy density	Pressure	Sound velocity	Angular momentum
External Schwarzschild	(A.9)	–	(A.10)	(A.11)	(A.13)	(A.23)
Buchdahl	(A.24)	–	(A.27)	(A.28)	(A.29)	(A.31)
NPV 1a	(A.32), (A.33)	(A.40), (A.41)	(A.43)	(A.44)	(A.46)	(A.50)
NPV 1b	(A.32), (A.34)	(A.40), (A.42)	(A.43)	(A.45)	(A.47)	(A.51)
NPV 2a	(A.52), (A.53)	(A.60)–(A.63)	(A.66)	(A.67)	(A.69)	(A.73)
NPV 2b	(A.52), (A.54)	(A.60), (A.61), (A.64), (A.65)	(A.66)	(A.68)	(A.70)	(A.74)
Internal Schwarzschild +Buchdahl	(A.75), (A.76)	(A.77)–(A.80)	(A.66), (A.27)	(A.67), (A.28)	(A.69), (A.29)	(A.73), (A.31)
NPV 2b+NPV 1b +external Schwarzschild	(A.81), (A.82), (A.83)	(A.84)–(A.86)	(A.66), (A.43), (A.10)	(A.68), (A.45), (A.11)	(A.70), (A.47), (A.13)	(A.74), (A.51), (A.23)

Bibliography

[1] W. A. Bonnor and A. Sackfield, Commun. Math. Phys. **8**, 338 (1968).

[2] T. Morgan and L. Morgan, Phys. Rev. **183**, 1097 (1969).

[3] L. Morgan and T. Morgan, Phys. Rev. D **2**, 2756 (1970).

[4] G. González and P. S. Letelier, Class. Quantum Grav. **16**, 479 (1999).

[5] T. Ledvinka, M. Zofka, and J. Bičák, in *Proceedings of the 8th Marcel Grossman Meeting in General Relativity*, edited by T. Piran (World Scientific, Singapore, 1999), pp. 339-341.

[6] P. S. Letelier, Phys. Rev. D **60**, 104042 (1999).

[7] J. Katz, J. Bičák, and D. Lynden-Bell, Class. Quantum Grav. **16**, 4023 (1999).

[8] D. Lynden-Bell and S. Pineault, Mon. Not. R. Astron. Soc. **185**, 679 (1978).

[9] J. P. S. Lemos, Class. Quantum Grav. **6**, 1219 (1989).

[10] J. P. S. Lemos and P. S. Letelier, Class. Quantum Grav. **10**, L75 (1993).

[11] J. P. S. Lemos and P. S. Letelier, Phys. Rev D **49**, 5135 (1994).

[12] J. P. S. Lemos and P. S. Letelier, Int. J. Mod. Phys. D **5**, 53 (1996).

[13] C. Klein, Class. Quantum Grav. **14**, 2267 (1997).

[14] J. Bičák, D. Lynden-Bell and J. Katz, Phys. Rev. D **47**, 4334 (1993).

[15] J. Bičák, D. Lynden-Bell and C. Pichon, Mon. Not. R. Astron. Soc. **265**, 126 (1993).

[16] O. Semerák, in *Gravitation: Following the Prague Inspiration*, to Celebrate the 60th Birthday of Jiri Bičák, edited by O. Semerák, J. Podolsky and M. Zofka (World Scientific, Singapore, 2002), p. 111, available at http://xxx.lanl.gov/abs/gr-qc/0204025.

[17] G. G. Kuzmin, Astron. Zh. **33**, 27 (1956).

[18] A. H. Taub, J. Math. Phys. **21**, 1423 (1980).

[19] J.P.S. Lemos and P.S. Letelier, Phys Lett. A **153**, 288 (1991).

[20] Lord Rayleigh, Proc. R. Soc. Lond. A **93**, 148 (1916).

[21] L. D. Landau and E. M. Lifshitz, *Fluid Mechanics*, 2nd ed. (Pergamon, Oxford, 1987), Sec. 27.

[22] B. Kuchowicz, Acta Phys. Pol. B **3**, 209 (1972).

[23] H. A. Buchdahl, Astrophys. J., **140**, 1512 (1964).

[24] V. V. Narlikar, G. K. Patwardhan, P. C. Vaidya, Proc. Natl. Inst. Sci. India, **9**, 229 (1943).

Apêndice B

Exact general relativistic static perfect fluid disks

Abstract

Using the well-known "displace, cut and reflect" method used to generate disks from given solutions of Einstein field equations, we construct static disks made of perfect fluid based on vacuum Schwarzschild's solution in isotropic coordinates. The surface energy density and pressures of the disks decrease monotonically and rapidly with radius. As the "cut" parameter a decreases, the disks become more relativistic, with surface energy density and pressure more concentrated near the center. The stability of the perfect fluid disks is investigated under a general first order perturbation of the energy momentum tensor. In particular we consider temporal, radial and azimuthal "test matter" perturbations of the quantities involved on the plane $z = 0$. We find that the presence of radial pressure which supports gravitational attraction stabilizes the disk and the perturbation favors the formation of rings.

B.1 Introduction

Axially symmetric solutions of Einstein's field equations corresponding to disklike configurations of matter are of great astrophysical interest, since

they can be used as models of galaxies or accretion disks. These solutions can be static or stationary and with or without radial pressure. Solutions for static disks without radial pressure were first studied by Bonnor and Sackfield [1], and Morgan and Morgan [2], and with radial pressure by Morgan and Morgan [3]. Disks with radial tension have been considered in [4], and models of disks with electric fields [5], magnetic fields [6], and both magnetic and electric fields have been studied [7]. Solutions for self-similar static disks were analyzed by Lynden-Bell and Pineault [8], and Lemos [9]. The superposition of static disks with black holes were first considered by Lemos and Letelier [10–12]. Also Bičák, Lynden-Bell and Katz [13] studied static disks as sources of known vacuum spacetimes and Bičák, Lynden-Bell and Pichon [14] found an infinity number of new static solutions. Thick static relativistic disks in various coordinate systems were presented in [15]. For a recent survey on relativistic gravitating disks, see for instance [16].

In the works cited above an inverse style method was used to solve the Einstein equations, i. e., the energy-momentum tensor is computed from the metric representing the disk. Another approach to generate disks is by solving the Einstein equations given a source (energy-momentum tensor). This has been used by the Jena group to generate several exact solutions of disks [17–24].

The study of stability is vital to the acceptance and applicability of the different disks models mentioned. When applied to stellar structures, different types of perturbations usually give an insight on the formation of bars, rings or other stellar patterns. In General Relativity, the stability analysis is usually done by studying the particle motion along geodesics and not perturbing the energy-momentum tensor of the fluid and its conservation equations. The stability of particle motion along geodesics has been studied by transforming the Rayleigh criteria of stability [25, 26] into a General Relativistic formulation, see [27] and references therein.

In this article we apply the "displace, cut and reflect" method to spherically symmetric solutions of Einstein's field equations in isotropic coordinates to generate static disks made of a *perfect fluid*, i. e., with radial pressure equal to tangential pressure [28]. We first study the disk stability through the Rayleigh criteria of stability. Then we study numerically the stability of the disks by performing a general first order perturbation on the temporal, radial and azimuthal components of the quantities involved in the energy momentum tensor of the fluid and analyzing the corresponding perturbed conservation equations of motion [29]. The perturbations considered do not modified the background metric obtained from the solution of Einstein equations, i. e. are treated as "test matter".
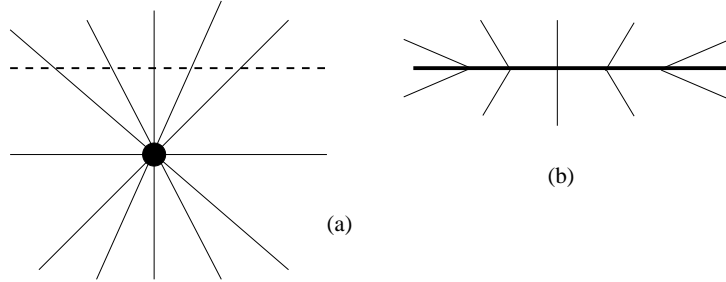
Figure B.1: An illustration of the "displace, cut and reflect" method for the generation of disks. In (a) the spacetime with a singularity is displaced and cut by a plane (dotted line), in (b) the part with singularities is disregarded and the upper part is reflected on the plane.

B.2 Einstein equations and disks

For a static spherically symmetric spacetime the general line element in isotropic cylindrical coordinates (t,R,z,φ) can be cast as,

$$\mathrm{d}s^2 = e^{\nu(R,z)}\mathrm{d}t^2 - e^{\lambda(R,z)}\left(\mathrm{d}R^2 + \mathrm{d}z^2 + R^2\mathrm{d}\varphi^2\right). \qquad \text{(B.1)}$$

The metric of the disk will be constructed using the well known "displace, cut and reflect" method that was used by Kuzmin [30] in Newtonian gravity and later in general relativity by many authors [4–14]. The material content of the disk will be described by functions that are distributions with support on the disk. The method can be divided in the following steps that are illustrated in Fig. B.1: First, in a space wherein we have a compact source of gravitational field, we choose a surface (in our case, the plane $z = 0$) that divides the space in two pieces: one with no singularities or sources and the other with the sources. Then we disregard the part of the space with singularities and use the surface to make an inversion of the nonsingular part of the space. This results in a space with a singularity that is a delta function with support on $z = 0$. This procedure is mathematically equivalent to make the transformation $z \rightarrow |z| + a$, with a constant. In the Einstein tensor we have first and second derivatives of z. Since $\partial_z|z| = 2\vartheta(z) - 1$ and $\partial_{zz}|z| = 2\delta(z)$, where $\vartheta(z)$ and $\delta(z)$ are, respectively, the Heaviside function and the Dirac distribution. Therefore the Einstein field equations will separate in two different pieces [31]: one valid for $z \neq 0$ (the usual Einstein's equations), and other involving distributions with an associated energy-momentum tensor, $T_{ab} = Q_{ab}\delta(z)$, with support on $z = 0$. For the

85

metric (B.1), the non-zero components of Q_{ab} are

$$Q_t^t = \frac{1}{16\pi} \left[-b^{zz} + g^{zz}(b_R^R + b_z^z + b_\varphi^\varphi) \right], \tag{B.2}$$

$$Q_R^R = Q_\varphi^\varphi = \frac{1}{16\pi} \left[-b^{zz} + g^{zz}(b_t^t + b_R^R + b_z^z) \right], \tag{B.3}$$

where b_{ab} denote the jump of the first derivatives of the metric tensor on the plane $z = 0$,

$$b_{ab} = g_{ab,z}|_{z=0^+} - g_{ab,z}|_{z=0^-}, \tag{B.4}$$

and the other quantities are evaluated at $z = 0^+$. The "true" surface energy-momentum tensor of the disk can be written as $S_{ab} = \sqrt{-g_{zz}}Q_{ab}$, thus the surface energy density σ and the radial and azimuthal pressures or tensions (P) read:

$$\sigma = \sqrt{-g_{zz}}Q_t^t, \quad P = -\sqrt{-g_{zz}}Q_R^R = -\sqrt{-g_{zz}}Q_\varphi^\varphi. \tag{B.5}$$

Note that when the same procedure is applied to an axially symmetric space-time in Weyl coordinates we have $Q_R^R = 0$, i.e., we have no radial pressure or tension.

B.3   Perfect Fluid Disk in Isotropic Coordinates

Now we apply the "displace, cut and reflect" method to generate disks discussed in the previous section and depicted in Fig. B.1 to the Schwarzschild metric in isotropic coordinates (t, r, θ, φ),

$$ds^2 = \frac{\left(1 - \frac{m}{2r}\right)^2}{\left(1 + \frac{m}{2r}\right)^2}dt^2 - \left(1 + \frac{m}{2r}\right)^4 \left[dr^2 + r^2(d\theta^2 + \sin^2\theta d\varphi^2)\right]. \tag{B.6}$$

Expressing solution (B.6) in cylindrical coordinates, and using Eq. (B.2)–(B.5), we obtain a disk with surface energy density σ and radial and azimuthal pressures (or tensions) P given by

$$\sigma = \frac{4ma}{\pi(m + 2\sqrt{R^2 + a^2})^3}, \tag{B.7}$$

$$P = -\frac{2m^2a}{\pi(m + 2\sqrt{R^2 + a^2})^3(m - 2\sqrt{R^2 + a^2})}. \tag{B.8}$$

86

The total mass of the disk can be calculated with the help of Eq. (B.7):

$$\mathcal{M} = \int_0^\infty \int_0^{2\pi} \sigma \sqrt{g_{RR} g_{\varphi\varphi}} \, dR \, d\varphi = \frac{m}{4a}(m + 4a). \qquad \text{(B.9)}$$

Thus, for $a > 0$, the disk always has a finite mass.

Eq. (B.7) shows that the disk's surface energy density is always positive (weak energy condition). Positive values (pressure) for the stresses in azimuthal and radial directions are obtained if $m < 2\sqrt{R^2 + a^2}$. The strong energy condition, $\sigma + P_{\varphi\varphi} + P_{RR} = \sigma + 2P > 0$ is then satisfied. These properties characterize a fluid made of matter with the usual gravitational attractive property. This is not a trivial property of these disks since it is known that the "displace, cut and reflect" method sometimes gives disks made of exotic matter like cosmic strings, see for instance [32].

Another useful parameter is the velocity of sound propagation V, defined as $V^2 = \frac{dP}{d\sigma}$, which can be calculated using Eq. (B.7) and Eq. (B.8):

$$V^2 = \frac{m(4\sqrt{R^2 + a^2} - m)}{3(m - 2\sqrt{R^2 + a^2})^2}. \qquad \text{(B.10)}$$

The condition $V^2 < 1$ (no tachyonic matter) imposes the inequalities $m < \sqrt{R^2 + a^2}$ or $m > 3\sqrt{R^2 + a^2}$. If the pressure condition and the speed of sound less then the speed of light condition are to be simultaneously satisfied, then $m < \sqrt{R^2 + a^2}$. This inequality will be valid in all the disk if $m < a$.

To determine the stability of circular orbits on the disk's plane, we use the General Relativistic extension of Rayleigh [25, 26] criteria of stability of a fluid at rest in a gravitational field

$$h \frac{dh}{dR} > 0, \qquad \text{(B.11)}$$

where h is the specific angular momentum of a particle on the disk's plane:

$$h = -g_{\varphi\varphi} \frac{d\varphi}{ds} = -g_{\varphi\varphi} \frac{d\varphi}{dt} \frac{dt}{ds}. \qquad \text{(B.12)}$$

Using the geodesic equation for circular motion on the $z = 0$ plane one obtains the following expression for h:

$$h = R^2 e^\lambda \sqrt{\frac{(e^\nu)_{,R}}{e^\nu (R^2 e^\lambda)_{,R} - R^2 e^\lambda (e^\nu)_{,R}}}. \qquad \text{(B.13)}$$
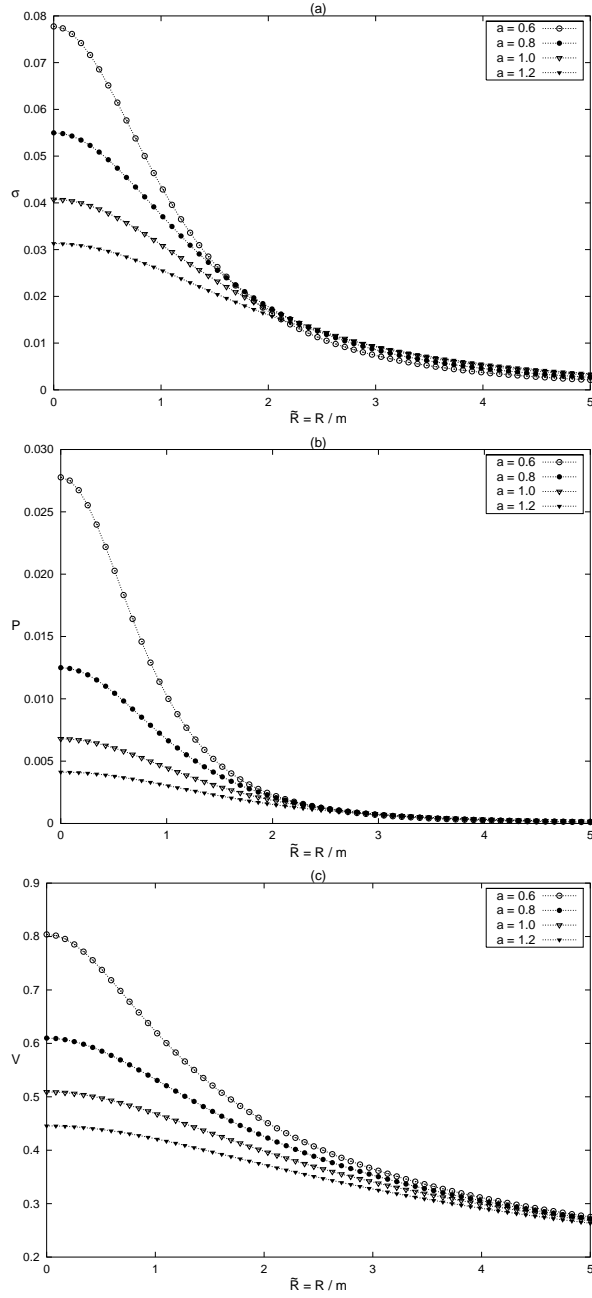
Figure B.2: (a) The surface energy density σ, (b) pressures P and (c) sound velocity V with $m = 0.5$ and $a = 0.6$, 0.8, 1.0, and 1.2 as function of $\tilde{R} = R/m$. We use geometric units $G = c = 1$.

For the metric (B.6), Eq. (B.13) reads

$$h = \frac{2\sqrt{m}R^2 \left(1 + \frac{m}{2\sqrt{R^2+a^2}}\right)^2 (R^2 + a^2)^{1/4}}{\sqrt{4(R^2 + a^2)^2 - 8mR^2\sqrt{R^2 + a^2} + m^2(R^2 - a^2)}}. \tag{B.14}$$

The stability criterion is always satisfied for $\frac{a}{m} \gtrsim 1.016$.

In Figures B.2(a)–(c) we show, respectively, the surface energy density, pressures and the sound velocity with parameters $m = 0.5$ and $a = 0.6$, 0.8, 1.0, and 1.2 as functions of $\tilde{R} = R/m$. We see that these quantities decrease monotonically with the radius of the disk, as can be checked from Eq. (B.7), (B.8) and (B.10). Energy density decreases rapidly enough to, in principle, define a cut off radius and consider the disk as finite.

B.4   Stability of Perfect Fluid Disks

Now we study the stability of the perfect fluid disks by performing a general first order perturbation of the energy-momentum tensor. We express the unperturbed energy-momentum tensor as

$$T^{\mu\nu} = (\sigma U^\mu U^\nu + p_r X^\mu X^\nu + p_\varphi Y^\mu Y^\nu)\delta(z), \tag{B.15}$$

where σ is the surface energy density, p_r and p_φ are, respectively, the radial and azimuthal pressures, and (U^μ, X^μ, Y^μ) are the components of the orthonormal tetrad

$$U^\mu = e^{-\nu/2}(1, 0, 0, 0),$$
$$X^\mu = e^{-\lambda/2}(0, 1, 0, 0),$$
$$Y^\mu = \frac{e^{-\lambda/2}}{R}(0, 0, 0, 1) \tag{B.16}$$

Due to the form of the energy-momentum tensor Eq. (B.15), all quantities are only functions of the radial coordinate. Thus we construct the perturbation A_P^μ of a quantity A^μ in the form

$$A_P^\mu(t, r, \varphi) = A^\mu(r) + \delta A^\mu(t, r, \varphi), \tag{B.17}$$

where $A^\mu(r)$ is the unperturbed quantity and $\delta A^\mu(t, r, \varphi)$ is the perturbation. Applying Eq. (B.17) in Eq. (B.15) and assuming that the perturbed energy-momentum tensor does not modify the background metric, i. e., the

perturbation $\delta T^{\mu\nu}$ acts as a test fluid, the perturbed conservation equations for thin disks can be written as

$$(\delta T^{\mu\nu})_{;\nu}|_{z=0} = 0, \tag{B.18}$$

where $;\nu$ denotes covariant derivative with respect to the coordinate ν. Assuming a perturbation of the form

$$\delta A^{\mu}(t, r, \varphi) = \delta A^{\mu}(r) e^{i(k_\varphi \varphi - wt)}, \tag{B.19}$$

the perturbed conservation equations Eq. (B.18) can be written as

$$\mu = t \quad \delta U^r_{,r}(\sigma U^t + \xi_1 p_r X^r) + \delta U^r [\mathrm{F}(t, r, \sigma U^t) + \xi_{1,r} p_r X^r$$
$$+ \xi_1 \mathrm{F}(t, r, p_r X^r)] + \delta U^\varphi [ik_\varphi(\sigma U^t + \xi_2 p_\varphi Y^\varphi)] + \delta\sigma(-iwU^t U^t) = 0, \tag{B.20}$$

$$\mu = r \quad \delta p_{r,r}(X^r X^r) + \delta U^r [-iw(\sigma U^t + \xi_1 p_r X^r)] + \delta\sigma(U^t U^t \Gamma^r_{tt})$$
$$+ \delta p_r \mathrm{G}(r, r, X^r X^r) + \delta p_\varphi(Y^\varphi Y^\varphi \Gamma^r_{\varphi\varphi}) = 0, \tag{B.21}$$

$$\mu = \varphi \quad \delta U^\varphi [-w(\sigma U^t + \xi_2 p_\varphi Y^\varphi)] + \delta p_\varphi(k_\varphi Y^\varphi Y^\varphi) = 0, \tag{B.22}$$

where δU^r and δU^φ are perturbed components of the tetrad, $\xi_1 = -X_r/U_t$, $\xi_2 = -Y_\varphi/U_t$ and

$$\mathrm{F}(I, J, K) = K_{,J} + K(2\Gamma^I_{IJ} + \Gamma^\alpha_{\alpha J}), \tag{B.23}$$

$$\mathrm{G}(I, J, K) = K_{,J} + K(\Gamma^I_{IJ} + \Gamma^\alpha_{\alpha J}), \tag{B.24}$$

where $\Gamma^\alpha_{\beta\gamma}$ are the Christoffel symbols.

We want our perturbations to be in accordance with the equation of state of the fluid, i.e. $p = p(r)$ and $\sigma = \sigma(r)$. Thus, δp_r and $\delta\sigma$ satisfy

$$\delta p = \delta p_r = \delta p_\varphi = p_{,r} \mathrm{d}r, \tag{B.25}$$

$$\delta\sigma = \sigma_{,r} \mathrm{d}r, \tag{B.26}$$

from which we find the useful relation

$$\delta p = \left(\frac{p_{,r}}{\sigma_{,r}}\right) \delta\sigma. \tag{B.27}$$

Substituting δU^r and δU^φ in Eq. (B.20) from Eq. (B.21) and Eq. (B.22), and using relation Eq. (B.27), we find a second order differential equation for the energy density perturbation $\delta\sigma$ of the form

$$A_S \delta\sigma_{,rr} + B_S \delta\sigma_{,r} + C_S \delta\sigma = 0, \tag{B.28}$$

where (A_S, B_S, C_S) are functions of (r, a, m, w, k_φ). To study stability of the disks we need a criterion to make a cut-off in the radial coordinate to create a finite disk. The cut-off radius R_{cut} of the disk is set by the following criterion: the matter within the thin disk formed by the cut-off radius is more than 90% of the total energy density of the infinite disk. The second order equation Eq. (B.28) is solved with two boundary conditions, one in $r \approx 0$ and the other in the cut-off radius set by the criterion established above. At $r \approx 0$ we set the perturbation to be $\approx 10\%$ of the unperturbed energy density value and at the edge of the disk $\delta\sigma|_{r=R_{\mathrm{cut}}} = 0$. The last condition is imposed because we want the perturbation to vanish when r tends to the outer radius.

Now, we consider the isotropic Schwarzschild thin disk with parameters $(a = 0.5, m = 0.4)$. With these parameters, the outer radius of the disk is set to $r = 4$ (approximately 90% of the energy density is inside the disk). In Fig. B.3 we show the amplitude profiles of the true energy density perturbation $\tilde{\delta\sigma}$ for different modes of the perturbation Eq. (B.19). We see from Fig. B.3 that the energy density perturbation profiles are stable and have an oscillatory character. When we increase the parameter w the number of oscillations within the disk increases and when we increase the wave number k the amplitude of the oscillations decreases. Note that the amplitudes of the modes decay quickly when we increase the value of the wave number. From Fig. B.3 we see that there is a factor of approximately 10^{-3} between the modes $(w = 1, k = 0)$ and $(w = 1, k = 2)$. In Fig. B.4, we present the amplitude profiles of the true pressure perturbation and the physical radial velocity perturbation $(\delta\tilde{U}^r = \delta U^r \sqrt{g_{rr}})$ for the first three w modes with $k = 0$, and the amplitude profile of the physical azimuthal velocity perturbation $(\delta\tilde{U}^\varphi = \delta U^\varphi \sqrt{g_{\varphi\varphi}})$ for the first three w modes with $k = 1$. The modes of the azimuthal velocity perturbation with $k = 0$ are equal to zero. We see from Fig. B.4 that the pressure perturbation has the same qualitative aspects of the density perturbation. The azimuthal velocity perturbation amplitude shows an oscillatory behavior but the difference between it and the radial velocity perturbation is that after the first oscillations the maximum value of the amplitude remains almost constant for the rest of the disk.

B.5   Conclusion

The "displace, cut and reflect" method applied to the Schwarzschild solution in isotropic coordinates can generate disks with positive energy density and equal radial and azimuthal pressures (perfect fluid). Surface energy density
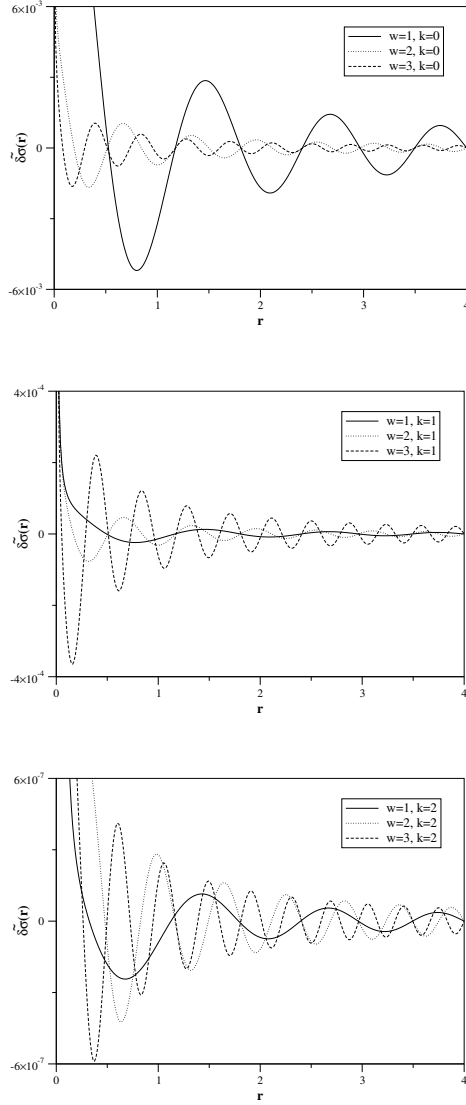
Figure B.3: Profiles of the energy density perturbation amplitudes of the isotropic Schwarzschild thin disk with parameters (a=0.5,m=0.4). The first three different w modes for the first three wave number k are plotted, we see that increasing the w mode the number of oscillations within the disk increases while increasing the wave number k the amplitude decreases.
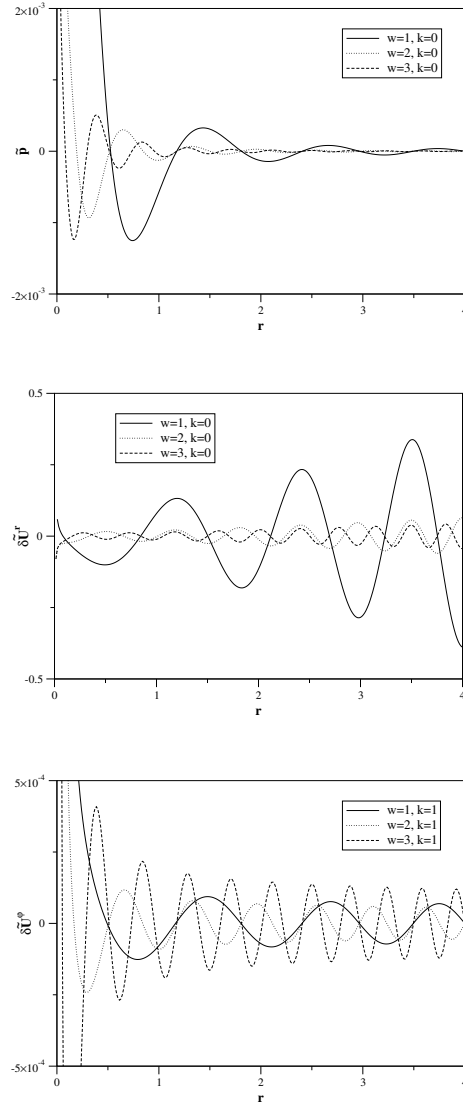
Figure B.4: Profiles of the true pressure perturbation, physical velocity and physical azimuthal velocity amplitudes of the isotropic Schwarzschild thin disk with parameters (a=0.5,m=0.4). We see that the qualitative aspects of the pressure perturbation are the same of the energy density perturbation. The amplitude of the radial velocity increases when we get near the edge of the disk, in that circumstances we must compare these velocity values to the particle escape velocity to make the perturbation consistent with the model. The azimuthal velocity amplitude is almost constant far from the center of the disk.

and pressures decrease monotonically and rapidly with radius. As the "cut" parameter a decreases, the disks become more relativistic, with surface energy density and pressure more concentrated near the center. Also regions of unstable circular orbits are more likely to appear for high relativistic disks. The stability analysis using a general first order perturbation of the disk's energy-momentum tensor shows that the fluid variables, in the isotropic Schwarzschild thin disk, present an oscillatory character with the amplitudes vanishing when r approaches the outmost radius. In the case of the azimuthal perturbation, the amplitude is almost constant within the disk. In general, when we increase the parameter w the number of oscillations increases inside the disk and the amplitudes decrease. When we increase the wave number k the values of the amplitudes decrease abruptly. We note that the perturbation Eq. (B.19) made in the isotropic Schwarzschild thin disk favors the formation of rings. As expected, the presence of a radial pressure is fundamental to the stability of thin disks.

Bibliography

[1] W. A. Bonnor and A. Sackfield, *Commun. Math. Phys.* **8**, 338 (1968).

[2] T. Morgan and L. Morgan, *Phys. Rev.* **183**, 1097 (1969).

[3] L. Morgan and T. Morgan, *Phys. Rev. D* **2**, 2756 (1970).

[4] G. González and P. S. Letelier, *Class. Quantum Grav.* **16**, 479 (1999).

[5] T. Ledvinka, M. Zofka, and J. Bičák, in *Proceedings of the 8th Marcel Grossman Meeting in General Relativity*, edited by T. Piran (World Scientific, Singapore, 1999), pp. 339-341.

[6] P. S. Letelier, *Phys. Rev. D* **60**, 104042 (1999).

[7] J. Katz, J. Bičák, and D. Lynden-Bell, *Class. Quantum Grav.* **16**, 4023 (1999).

[8] D. Lynden-Bell and S. Pineault, *Mon. Not. R. Astron. Soc.* **185**, 679 (1978)

[9] J. P. S. Lemos, *Class. Quan. Grav.* **6**, 1219 (1989)

[10] J. P. S. Lemos and P. S. Letelier, *Class. Quan. Grav.* **10**, L75 (1993)

[11] J. P. S. Lemos and P. S. Letelier, *Phys. Rev D* **49**, 5135 (1994)

[12] J. P. S. Lemos and P. S. Letelier, *Int. J. Mod. Phys. D* **5**, 53 (1996).

[13] J. Bičák, D. Lynden-Bell and J. Katz, *Phys. Rev.D* **47**, 4334 (1993).

[14] J. Bičák, D. Lynden-Bell and C. Pichon, *Mon. Not. R. Astron. Soc.* **265**, 126 (1993).

[15] G. González and P. S. Letelier, *Phys. Rev. D***69**, 044013 (2004).

[16] V. Karas, J. M. Huré and O. Semerák, *Class. Quantum Grav.* **21**, R1 (2004).

[17] C. Klein, *Class. Quantum Grav.* **14**, 2267 (1997).

[18] G. Neugebauer and R. Meinel, *Phys. Rev. Lett.* **75**, 3046 (1995).

[19] C. Klein and O. Richter, *Phys. Rev. Lett.* **83**, 2884 (1999).

[20] C. Klein, *Phys. Rev. D***63**, 064033 (2001).

[21] J. Frauendiener and C. Klein, *Phys. Rev. D***63**, 084025 (2001).

[22] C. Klein, *Phys. Rev. D***65**, 084029 (2002).

[23] C. Klein, *Phys. Rev. D***68**, 027501 (2003).

[24] C. Klein, *Ann. Phys.* **12** (10), 599 (2003).

[25] Lord Rayleigh, *Proc. R. Soc. Lond. Ser. A* **93**, 148 (1916).

[26] L. D. Landau, E. M. Lifshitz, *Fluid Mechanics*, 2nd Ed. (Pergamon Press, Oxford, 1987), §27.

[27] P.S. Letelier, *Phys. Rev. D* **68**, 104002 (2003).

[28] D. Vogt and P. S. Letelier, *Phys. Rev. D* **68**, 084010 (2003).

[29] M. Ujevic and P. S. Letelier, *On the Stability of General Relativistic Geometric Thin Disks*, Phys. Rev. D (in press).

[30] G. G. Kuzmin, *Astron. Zh.*, **33**, 27 (1956).

[31] A. H. Taub, *J. Math. Phys.* **21**, 1423 (1980).

[32] J.P.S. Lemos and P.S. Letelier, *Phys Lett. A* **153**, 288 (1991).

Apêndice C

Exact relativistic static charged dust discs and non-axisymmetric structures

Abstract

The well-known 'displace, cut and reflect' method used to generate discs from given solutions of Einstein field equations is applied to the superposition of two extreme Reissner-Nordström black holes to construct discs made of charged dust and also non-axisymmetric planar distributions of charged dust on the $z = 0$ plane. They are symmetric with respect to two or one coordinate axes, depending on whether the black holes have equal or unequal masses, respectively. For these non-axisymmetric distributions of matter we also study the effective potential for geodesic motion of neutral test particles.

PACS numbers: 04.20.Jb, 04.40.–b, 04.40.Nr

C.1   Introduction

Solutions of Einstein's field equations representing disc-like configurations of matter are of great astrophysical interest, since they can be used as models of galaxies or accretion discs. Disc solutions can be static or stationary

and with or without radial pressure. Solutions for static thin discs without radial pressure were first studied by Bonnor and Sackfield [1] and Morgan and Morgan [2], and with radial pressure by Morgan and Morgan [3]. Other classes of static thin disc solutions have been obtained [4–7], while stationary thin discs were studied in [8–10]. An exact solution to the problem of a rigidly rotating disc of dust in terms of ultraelliptic functions was reported in [11]. Also thin discs with radial tension [12], magnetic fields [13] and both electric and magnetic fields [14] have been studied. The nonlinear superposition of a disc and a black hole was first considered by Lemos and Letelier [15]. Models of thin discs and thin discs with halos made of perfect fluids were considered in [16]. The generalization of the 'displace, cut and reflect' method (section C.2) of constructing thick static discs was considered by González and Letelier [17].

An interesting class of solutions of the Einstein-Maxwell field equations is the conformastatic spacetimes with charged dust, in which the charge density is equal to the mass density. Therefore, the matter is in equilibrium because the mutual gravitational attractions are balanced by the electrical repulsions. This kind of matter has been called by some authors 'electrically counterpoised dust' (ECD). Distributions of ECD in equilibrium in both classical and relativistic theories were studied by Bonnor [18]. Models of oblate and prolate spheroids made of ECD were considered, respectively, in [19, 20]. Gürses [21] and Varela [22] studied static spheres of ECD. Disc sources for conformastationary metrics (the stationary version of conformastatic metrics) were considered in [14]. Although one may intuitively expect that astrophysical objects do not have a net charge, there exists the possibility that electrons escape from a compact star, leaving behind a positively charged one (see, for example, [23, 24]).

In this paper we apply the well known 'displace, cut and reflect' method to the superposition of two extreme Reissner-Nordström black holes aligned on the z-axis to generate static discs of ECD on the $z = 0$ plane. Next we repeat the same procedure for Reissner-Nordström black holes aligned on the y-axis and generate non-axisymmetric distributions of ECD on the plane $z = 0$. We briefly study the effective potential of geodesic motion of neutral test particles on these structures.

The paper is divided as follows. Section C.2 discusses the Einstein-Maxwell equations, the 'displace, cut and reflect' method and the particular class of conformastat metrics. In section C.3 discs of charged dust are constructed using the superposition of two aligned Reissner-Nordström black holes and in section C.4 we obtain non-axisymmetric distributions of charged dust. We also present some analysis of the geodesic motion on these matter

distributions. Finally, in section C.5, we summarize our results.

C.2   Einstein-Maxwell equations, discs and conformastatic spacetimes

We consider a static spacetime with coordinates (t, x, y, z) and a line element of the form

$$\mathrm{d}s^2 = e^{\nu(x,y,z)}\mathrm{d}t^2 - e^{\lambda(x,y,z)}\left(\mathrm{d}x^2 + \mathrm{d}y^2 + \mathrm{d}z^2\right). \qquad \text{(C.1)}$$

The Einstein-Maxwell system of equations is given by

$$G_{\mu\nu} = 8\pi T_{\mu\nu}, \qquad \text{(C.2)}$$

$$T_{\mu\nu} = \frac{1}{4\pi}\left(F^{\sigma}{}_{\mu}F_{\nu\sigma} + \frac{1}{4}g_{\mu\nu}F_{\rho\sigma}F^{\rho\sigma}\right), \qquad \text{(C.3)}$$

$$F^{\mu\nu}{}_{;\mu} = 0, \qquad \text{(C.4)}$$

$$F_{\mu\nu} = A_{\nu,\mu} - A_{\mu,\nu}, \qquad \text{(C.5)}$$

where all symbols have their usual meaning. We use geometric units $G = c = 1$.

The method used to generate the metric of the disc and its material content is the well known 'displace, cut and reflect' method that was first used by Kuzmin [25] and Toomre [26] to construct Newtonian models of discs, and later extended to general relativity (see, for example [6, 10]).

The material and electric content of the disc will be described by functions that are distributions with support on the disc. The method can be divided into the following steps: first, in a space wherein we have a compact source of gravitational field, we choose a surface (in our case, the plane $z = 0$) that divides the space into two pieces: one with no singularities or sources and the other with the sources. Then we disregard the part of the space with singularities and use the surface to make an inversion of the nonsingular part of the space. This results in a space with a singularity that is a delta function with support on $z = 0$. This procedure is mathematically equivalent to making the transformation $z \to |z| + a$, with a constant. In the Einstein tensor we have first and second derivatives of z. Remembering that $\partial_z|z| = 2\vartheta(z) - 1$ and $\partial_{zz}|z| = 2\delta(z)$, where $\vartheta(z)$ and $\delta(z)$ are, respectively, the Heaviside function and the Dirac distribution, the Einstein-Maxwell equations give us

$$G_{\mu\nu} = 8\pi(T_{\mu\nu}^{\text{elm.}} + Q_{\mu\nu}\delta(z)), \qquad \text{(C.6)}$$

$$F^{\mu\nu}{}_{;\mu} = 4\pi J^{\nu}\delta(z), \tag{C.7}$$

where $T_{\mu\nu}^{\text{elm.}}$ is the electromagnetic tensor equation (C.3), $Q_{\mu\nu}$ is the energy-momentum tensor on the plane $z = 0$ and J^{ν} is the current density on the plane $z = 0$.

For the metric equation (C.1), the non-zero components of $Q_{\mu\nu}$ are

$$Q_t^t = \frac{1}{8\pi}g^{zz}b_x^x, \tag{C.8}$$

$$Q_x^x = Q_y^y = \frac{1}{16\pi}g^{zz}(b_t^t + b_x^x), \tag{C.9}$$

where $b_{\mu\nu}$ denotes the jump of the first derivatives of the metric tensor on the plane $z = 0$,

$$b_{\mu\nu} = g_{\mu\nu,z}|_{z=0^+} - g_{\mu\nu,z}|_{z=0^-}, \tag{C.10}$$

and the other quantities are evaluated at $z = 0^+$. The electromagnetic potential for an electric field is

$$A_\mu = (\phi, 0, 0, 0). \tag{C.11}$$

Using equations (C.11) and (C.7), the only non-zero component of the current density on the plane $z = 0$ is

$$J^t = \frac{1}{4\pi}g^{zz}g^{tt}a_t, \tag{C.12}$$

where a_μ denotes the jump of the first derivatives of the electromagnetic potential on the plane $z = 0$,

$$a_\mu = A_{\mu,z}|_{z=0^+} - A_{\mu,z}|_{z=0^-}, \tag{C.13}$$

and the other quantities are evaluated at $z = 0^+$. The 'physical measure' of length in the direction ∂_z for metric (C.1) is $\sqrt{-g_{zz}}$, then the invariant distribution is $\delta(z)/\sqrt{-g_{zz}}$. Thus the 'true' surface energy density σ and pressures or tensions P are:

$$\sigma = \sqrt{-g_{zz}}Q_t^t, \quad P = -\sqrt{-g_{zz}}Q_x^x = -\sqrt{-g_{zz}}Q_y^y. \tag{C.14}$$

Since $J^\mu = \varrho U^\mu$, where $U^\mu = \delta_t^\mu/\sqrt{g_{tt}}$, the 'true' surface charge density ρ is

$$\rho = \sqrt{-g_{zz}g_{tt}}J^t. \tag{C.15}$$

Let us now specialize metric equation (C.1) to a conformastat form by considering

$$e^{\nu(x,y,z)} = V^{-2}(x,y,z) \quad \text{and} \quad e^{\lambda(x,y,z)} = V^2(x,y,z). \qquad (C.16)$$

With this choice, in the absence of matter, the Einstein-Maxwell equations are satisfied provided (a) V satisfies Laplace equation and (b) the relation between V and the electric potential $\phi(x,y,z)$ is of the form (see, for example, [27] and the appendix of [28] for a detailed deduction)

$$\phi = \pm \frac{1}{V} + \text{const.} \qquad (C.17)$$

When static charged dust matter is included, the above conditions imply that charge density must be equal to the mass density. An interesting feature of conformastat metrics is that they permit the construction of complete asymmetrical relativistic configurations of matter in equibrium. With metric coefficients given by (C.16), we find the following expressions for the energy density and pressure, equation (C.14):

$$\sigma = -\frac{V_{,z}}{2\pi V^2}, \qquad (C.18)$$

$$P = 0. \qquad (C.19)$$

With condition (C.17), equation (C.15) gives

$$\rho = -\frac{V_{,z}}{2\pi V^2}, \qquad (C.20)$$

where we have chosen the negative sign in equation (C.17) that corresponds to positive charges. Thus we have a distribution of charged dust matter where the charge density is equal to the mass density on the plane $z = 0$. We use now a particular form of the function V to construct discs and non-axisymmetric distributions of ECD.

C.3 Aligned extreme Reissner-Nordström black holes on the z-axis

Electrovacuum solutions representing extreme Reissner-Nordström black holes in arbitrary positions in static equilibrium have been found by Majumdar [29] and Papapetrou [30]. Such solutions can be constructed because,
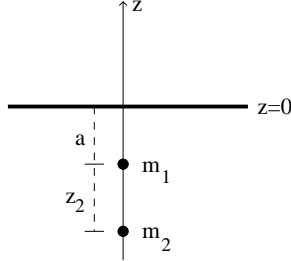
Figure C.1: Schematic drawing of the configuration used to construct charged dust discs.

as previously stated, the functions $V(x, y, z)$ must satisfy the Laplace equation and thus can be superposed. Suppose we have two extreme Reissner-Nordström black holes on the z-axis, the first with mass m_1 at $z = 0$ and the second with mass m_2 at $z = -z_2$ (figure C.1). For convenience we use cylindrical coordinates (t, R, z, φ). The function V representing the superposition is given by

$$V = 1 + \frac{m_1}{\sqrt{R^2 + z^2}} + \frac{m_2}{\sqrt{R^2 + (z + z_2)^2}}. \tag{C.21}$$

If we apply the 'displace, cut and reflect' method to the system represented by equation (C.21), we have for the energy density equation (C.18):

$$\sigma = \frac{m_1 a \mathcal{R}_2^{3/2} + m_2(a + z_2)\mathcal{R}_1^{3/2}}{2\pi\sqrt{\mathcal{R}_1 \mathcal{R}_2} \left(\sqrt{\mathcal{R}_1 \mathcal{R}_2} + m_1\sqrt{\mathcal{R}_2} + m_2\sqrt{\mathcal{R}_1}\right)^2}, \tag{C.22}$$

where $\mathcal{R}_1 = R^2 + a^2$ and $\mathcal{R}_2 = R^2 + (z_2 + a)^2$. Note that σ is always non-negative. In figure C.2 we graph the energy density of the disc equation (C.22) as a function of R in two situations: in (a) we fix $m_1 = 2$, $a = 1$, $z_2 = 1$ and change m_2, in (b) we fix $m_1 = 1$, $m_2 = 1$, $a = 1$ and change z_2. In situation (a) we note that as m_2 is increased, the energy density is more uniformly distributed along the radius. In (b) $z_2 = 0$ corresponds to one black hole with mass $m_1 = 2$ (curve $m_2 = 0$ in (a)). The energy density on $R = 0$ assumes a minimum value when $z_2 = 1$, and then increases as z_2 is increased. The curve with $z_2 = 1 \times 10^6$ (mass m_2 is very far away) corresponds to a disc generated solely by m_1.
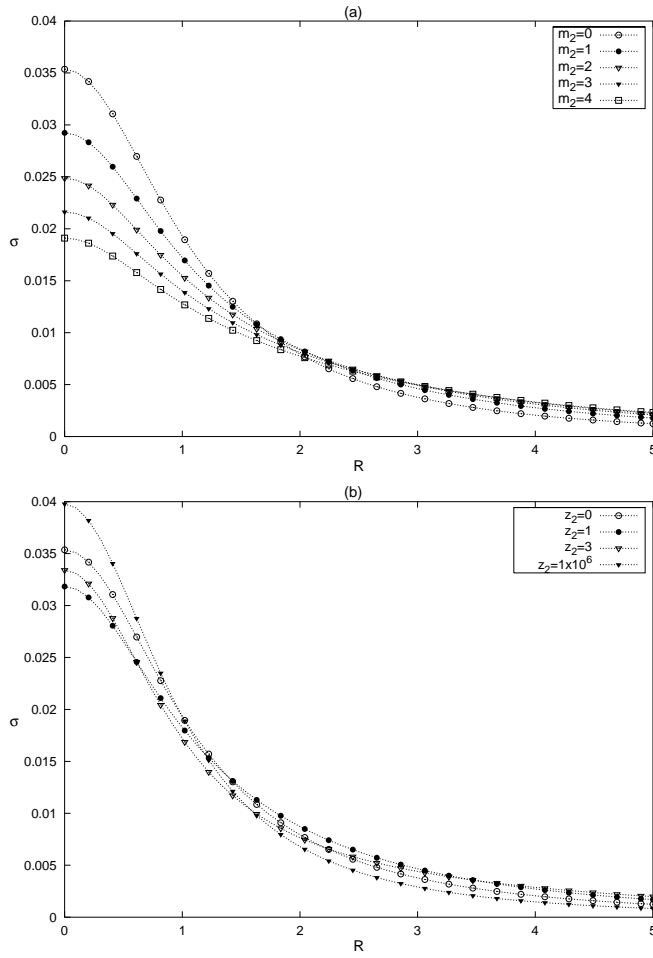
102

Figure C.2: Energy density σ equation (C.22) as a function of R. (a) $m_1 = 2$, $a = 1$, $z_2 = 1$ are fixed and m_2 is changed from $m_2 = 0$ to $m_2 = 4$. (b) $m_1 = 1$, $m_2 = 1$, $a = 1$ are fixed and z_2 is changed: $z_2 = 0$, 1, 3 and 1×10^6.
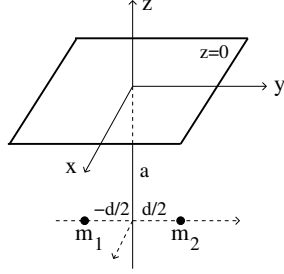
Figure C.3: Schematic drawing of the configuration used to construct asymmetric charged dust distributions.

C.4 Aligned extreme Reissner-Nordström black holes on the y-axis

Now we take two extreme Reissner-Nordström black holes, with masses m_1 and m_2, located at (x, y, z) coordinates $(0, d/2, 0)$ and $(0, -d/2, 0)$, respectively (figure C.3). The function V is written as

$$V = 1 + \frac{m_1}{\sqrt{x^2 + (y - \frac{d}{2})^2 + z^2}} + \frac{m_2}{\sqrt{x^2 + (y + \frac{d}{2})^2 + z^2}}. \tag{C.23}$$

Using again the 'displace, cut and reflect' method, we obtain an expression for the energy density equation (C.18):

$$\sigma = \frac{a}{2\pi} \frac{m_1 \mathsf{R}_2^{3/2} + m_2 \mathsf{R}_1^{3/2}}{\sqrt{\mathsf{R}_1 \mathsf{R}_2} \left(\sqrt{\mathsf{R}_1 \mathsf{R}_2} + m_1 \sqrt{\mathsf{R}_2} + m_2 \sqrt{\mathsf{R}_1}\right)^2}, \tag{C.24}$$

where $\mathsf{R}_1 = x^2 + (y - d/2)^2 + a^2$ and $\mathsf{R}_2 = x^2 + (y + d/2)^2 + a^2$. Equation (C.24) represents a non-axisymmetric distribution of matter on the $z = 0$ plane. In general it is symmetric only with respect to the y-axis, but when $m_1 = m_2$ it is also symmetric with respect to the x-axis. The extreme points (x_c, y_c) of the energy density, given by $\vec{\nabla}\sigma = 0$, are $x_c = 0$ and the roots of:

$$2 \left(\frac{m_1}{\mathsf{R}_{1c}^{3/2}} + \frac{m_2}{\mathsf{R}_{2c}^{3/2}}\right) \left[\frac{m_1(y_c - \frac{d}{2})}{\mathsf{R}_{1c}^{3/2}} + \frac{m_2(y_c + \frac{d}{2})}{\mathsf{R}_{2c}^{3/2}}\right] - 3 \left[\frac{m_1(y_c - \frac{d}{2})}{\mathsf{R}_{1c}^{5/2}}\right.$$
$$\left. + \frac{m_2(y_c + \frac{d}{2})}{\mathsf{R}_{2c}^{5/2}}\right] \left(1 + \frac{m_1}{\sqrt{\mathsf{R}_{1c}}} + \frac{m_2}{\sqrt{\mathsf{R}_{2c}}}\right) = 0, \tag{C.25}$$

where $\mathsf{R}_{1c} = (y_c - d/2)^2 + a^2$ and $\mathsf{R}_{2c} = (y_c + d/2)^2 + a^2$. For $m_1 = m_2$ we note that $y_c = 0$ is always a root of equation (C.25). Figures C.4(a)–(c) are
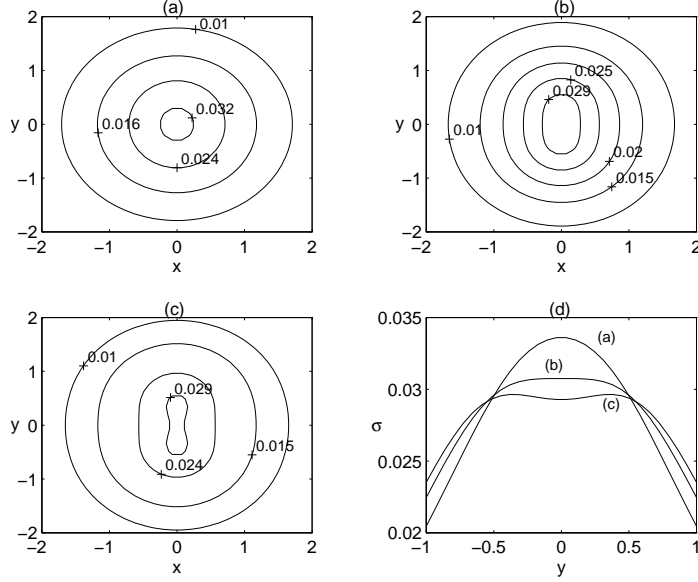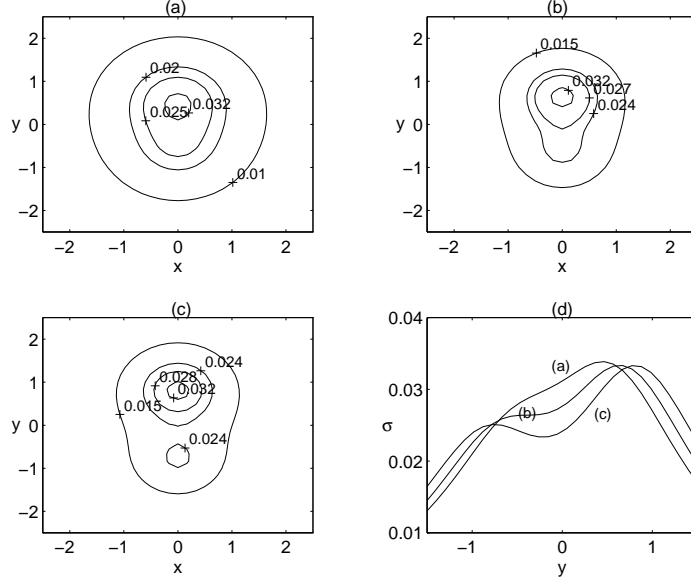
104

Figure C.4: Level curves of the energy density equation (C.24), with $m_1 = 1$, $m_2 = 1$, $a = 1$ and (a) $d = 0.5$, (b) $d = 0.85$, (c) $d = 1$. (d) The energy density is plotted along $x = 0$, showing the extreme points y_c for cases (a)–(c).

a contour plot of equation (C.24) for $m_1 = 1$, $m_2 = 1$, $a = 1$ and (a) $d = 0.5$, (b) $d = 0.85$, (c) $d = 1$. We note that as d is increased, $y_c = 0$ changes from a maximum to a local minimum point, and two other symmetrical extreme points appear. This is seen in figure C.4(d), where σ is plotted along $x = 0$ for cases (a), (b) and (c). The transition of the extreme point $y_c = 0$ from a local maximum to a local minimum is determined by $\sigma_{,yy} = 0$ evaluated at $(x_c, y_c) = (0, 0)$. In the particular case when $m_1 = m_2 = a = k$, this becomes

$$12k^4 - 9d^2 k^2 - 3d^4 + 4k(k^2 - 2d^2)\sqrt{4k^2 + d^2} = 0. \tag{C.26}$$

Equation (C.26) has a real root

$$d = k\frac{\sqrt{2 + 2\sqrt{145}}}{6} \approx 0.8511k. \tag{C.27}$$

Figures C.5(a)–(c) are other contour plots of the energy density with $m_1 = 1$, $m_2 = 0.5$, $a = 1$ and (a) $d = 1$, (b) $d = 1.3$ and (c) $d = 1.6$. For

105

Figure C.5: Level curves of the energy density equation (C.24), with $m_1 = 1$, $m_2 = 0.5$, $a = 1$ and (a) $d = 1$, (b) $d = 1.3$, (c) $d = 1.6$. (d) The energy density is plotted along $x = 0$, showing the extreme points y_c for cases (a)–(c).

$d \lesssim 1.3$ there is one maximum extreme point y_c. When $d \gtrsim 1.3$, there appear two maximum and one minimum extreme points y_c, all in asymmetrical positions. This is pictured in figure C.5(d).

It is also interesting to study the effective potential of geodesic motion of neutral test particles for this kind of matter distribution. The Lagrangean associated with the metric (C.1) is

$$2\mathcal{L} = V^{-2}\dot{t}^2 - V^2(\dot{x}^2 + \dot{y}^2 + \dot{z}^2), \tag{C.28}$$

where the dots indicate derivatives with respect to the parameter s. One of Lagrange's equations gives

$$\frac{d}{ds}\left(\frac{\partial \mathcal{L}}{\partial \dot{t}}\right) - \frac{\partial \mathcal{L}}{\partial t} = 0 \Rightarrow V^{-2}\dot{t} = E = \text{const.} \tag{C.29}$$

For time-like geodesic motion on the xy plane, we may write

$$1 = V^{-2}\dot{t}^2 - V^2(\dot{x}^2 + \dot{y}^2) \rightarrow \dot{x}^2 + \dot{y}^2 + \frac{1}{V^2} = E^2. \tag{C.30}$$

106

Thus we can define an effective potential $V_{\text{eff.}}$ as

$$V_{\text{eff.}} = \frac{1}{V^2}. \tag{C.31}$$

For our matter distribution, equation (C.31) reads

$$V_{\text{eff.}} = \frac{1}{\left[1 + \frac{m_1}{\sqrt{x^2+(y-\frac{d}{2})^2+a^2}} + \frac{m_2}{\sqrt{x^2+(y+\frac{d}{2})^2+a^2}}\right]^2}. \tag{C.32}$$

Calculating $\vec{\nabla}V_{\text{eff.}} = 0$, one obtains the extreme points $x_c = 0$ and the roots of

$$\frac{m_1(y_c - \frac{d}{2})}{\left[\left(y_c - \frac{d}{2}\right)^2 + a^2\right]^{3/2}} + \frac{m_2(y_c + \frac{d}{2})}{\left[\left(y_c + \frac{d}{2}\right)^2 + a^2\right]^{3/2}} = 0. \tag{C.33}$$

For $m_1 = m_2$, $y_c = 0$ is always a root of equation (C.33). Figures C.6(a)–(c) are a contour plot of equation (C.32) for $m_1 = 1$, $m_2 = 1$, $a = 1$ and (a) $d = 1$, (b) $d = 1.4$, (c) $d = 2$. As d is increased, $y_c = 0$ changes from a maximum to a local minimum point, and two other symmetrical extreme points appear. This is seen in figure C.6(d), where $V_{\text{eff.}}$ is plotted along $x = 0$ for cases (a), (b) and (c). The transition of the extreme point $y_c = 0$ from a local maximum to a local minimum is determined by $(V_{\text{eff.}})_{,yy} = 0$ evaluated at $(x_c, y_c) = (0,0)$. Setting $m_1 = m_2 = m$, we obtain

$$(2a^2 - d^2)(4m + \sqrt{d^2 + 4a^2}) = 0, \tag{C.34}$$

which has a real root $d = a\sqrt{2}$.

Figures C.7(a)–(c) are another contour plot of $V_{\text{eff.}}$ with $m_1 = 1$, $m_2 = 0.5$, $a = 1$ and (a) $d = 2$, (b) $d = 2.5$ and (c) $d = 3$. For $d \lesssim 2.5$ there is one minimum extreme point y_c. When $d \gtrsim 2.5$, there appear two minimum and one maximum extreme points y_c, all in asymmetrical positions. This is pictured in figure C.7(d).

C.5 Discussion

We applied the 'displace, cut and reflect' method to a conformastat form of the metric to generate discs made of electrically counterpoised dust in equilibrium. The seed metric used was two extreme Reissner-Nordström
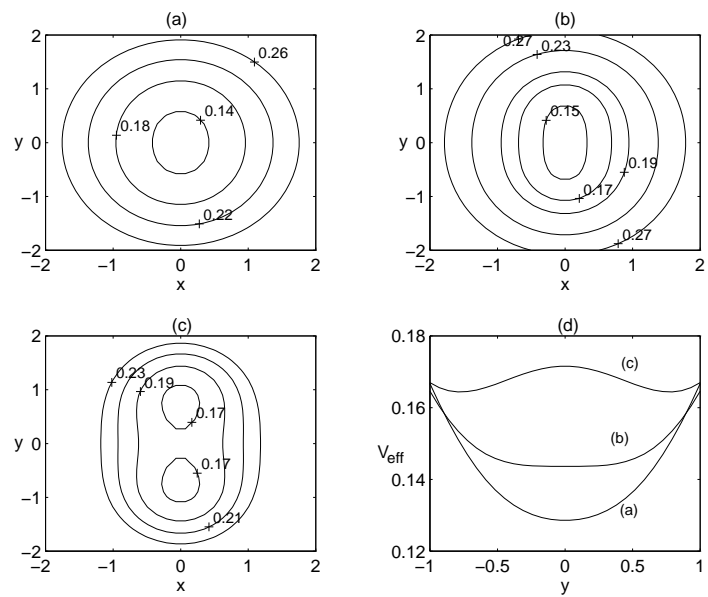
Figure C.6: Level curves of the effective potential equation (C.32), with $m_1 = 1$, $m_2 = 1$, $a = 1$ and (a) $d = 1$, (b) $d = 1.4$, (c) $d = 2$. (d) The effective potential is plotted along $x = 0$, showing the extreme points y_c for cases (a)–(c).
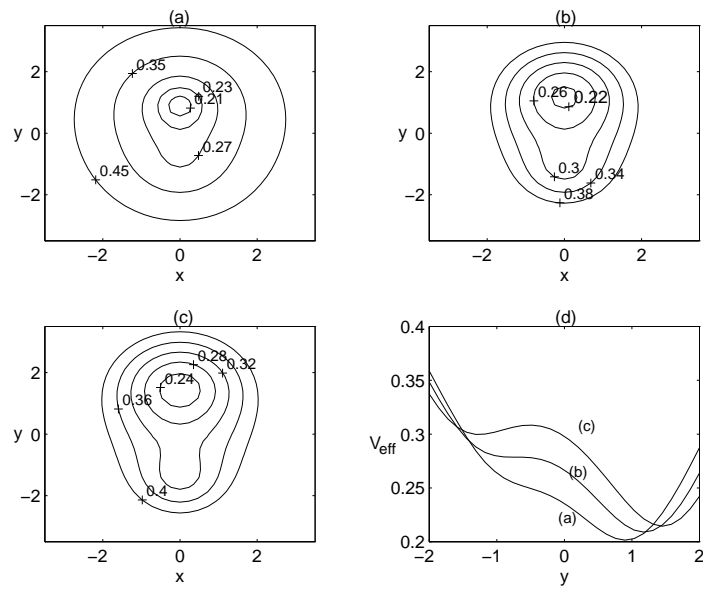
Figure C.7: Level curves of the effective potential equation (C.32), with $m_1 = 1$, $m_2 = 0.5$, $a = 1$ and (a) $d = 2$, (b) $d = 2.5$, (c) $d = 3$. (d) The effective potential is plotted along $x = 0$, showing the extreme points y_c for cases (a)–(c).

black holes placed along the symmetry axis. The non-axisymmetric matter distribution of ECD on the $z = 0$ plane was obtained from the metric of two extreme Reissner-Nordström black holes located along the y-axis. To our knowledge no such configurations of matter satisfying Einstein's field equations exist in the literature. We studied the variation of the energy density distribution by varying the coordinate distance between the black holes as well as their masses. For equal black hole masses the energy density distribution is symmetric with respect to both the x- and y-axes, while for unequal masses it possesses symmetry only with respect to the y-axis. The effective potential for geodesic motion of neutral test particles on the plane of such a matter distribution was also analysed.

Of course one could extend the procedure used in this paper to generate complete asymmetric planar configurations of ECD by putting $N > 2$ extreme Reissner-Nordström black holes in arbitrary positions on the xy plane and then applying the 'displace, cut and reflect' method.

Acknowledgments

Bibliography

[1] Bonnor W A and Sackfield A 1968 *Commun. Math. Phys.* **8** 338

[2] Morgan T and Morgan L 1969 *Phys. Rev.* **183** 1097

[3] Morgan L and Morgan T 1970 *Phys. Rev.* D **2** 2756

[4] Lynden-Bell D and Pineault S 1978 *Mon. Not. R. Astron. Soc.* **185** 679

[5] Lemos J P S 1989 *Class. Quantum Grav.* **6** 1219

[6] Bičák J, Lynden-Bell D and Katz J 1993 *Phys. Rev.* D **47** 4334

[7] Bičák J, Lynden-Bell D and Pichon C 1993 *Mon. Not. R. Astron. Soc.* **265** 126

[8] Bičák J and Ledvinka T 1993 *Phys. Rev. Lett.* **71** 1669

[9] Ledvinka T, Zofka M and Bičák J 1999 *Proceedings of the 8th Marcel Grossman Meeting in General Relativity* ed T Piran (Singapore: World Scientific) p 339-41

[10] González G and Letelier P S 2000 *Phys. Rev.* D **62** 064025

[11] Neugebauer G and Meinel R 1995 *Phys. Rev. Lett.* **75** 3046

[12] González G and Letelier P S 1999 *Class. Quantum Grav.* **16** 479

[13] Letelier P S 1999 *Phys. Rev.* D **60** 104042

[14] Katz J, Bičák J and Lynden-Bell D 1999 *Class. Quantum Grav.* **16** 4023

[15] Lemos J P S and Letelier P S 1993 *Class. Quantum Grav.* **10** L75

[16] Vogt D and Letelier P S 2003 *Phys. Rev.* D **68** 084010

[17] González G and Letelier P S 2004 *Phys. Rev.* D **69** 044013

[18] Bonnor W B 1980 *Gen. Rel. Grav.* **12** 453

[19] Bonnor W B and Wickramasuriya S B P 1975 *Mon. Not. R. Astron. Soc.* **170** 643

[20] Bonnor W B 1998 *Class. Quantum Grav.* **15** 351

[21] Gürses M 1998 *Phys. Rev.* D **58** 044001

[22] Varela V 2003 *Gen. Rel. Grav.* **35** 1815

[23] Rosseland S 1924 *Mon. Not. R. Astron. Soc.* **84** 720

[24] Bally J and Harrison E R 1978 *Astrophys. J.* **220** 743

[25] Kuzmin G G 1956 *Astron. Zh.* **33** 27

[26] Toomre A 1962 *Astrophys. J.* **138** 385

[27] Synge J L 1971 *Relativity the General Theory* (Amsterdam: North-Holland) chapter X, section 4, p. 367

[28] Lynden-Bell D, Bičák J and Katz J 1999 *Ann. Phys.* **271** 1

[29] Majumdar S D 1947 *Phys. Rev.* **72** 930

[30] Papapetrou A 1947 *Proc. R. Irish Acad.* A **51** 191

Apêndice D

Exact relativistic static charged perfect fluid disks

Abstract

Using the well-known "displace, cut and reflect" method used to generate disks from given solutions of Einstein field equations, we construct static charged disks made of perfect fluid based on the Reissner-Nordström solution in isotropic coordinates. We also derive a simple stability condition for charged and non charged perfect fluid disks. As expected, we find that the presence of charge increases the regions of instability of the disks.

PACS numbers: 04.40.–b, 04.20.Jb, 04.40.Nr, 98.62.Mw

D.1 Introduction

Axisymmetric solutions of Einstein field equations corresponding to disklike configurations of matter have been extensively studied. These solutions can be static or stationary and with or without radial pressure. Solutions for static thin disks without radial pressure were first studied by Bonnor and Sackfield [1], and Morgan and Morgan [2], and with radial pressure by Morgan and Morgan [3]. Other classes of static thin disk solutions have been obtained [4–7], while stationary thin disks were studied in [8–10]. Also thin

disks with radial tension [11], magnetic fields [12] and both electric and magnetic fields [13] have been studied. An exact solution to the problem of a rigidly rotating disk of dust in terms of ultra-elliptic functions was reported in [14], while models of static relativistic counterrotating dust disks were recently presented in [15]. Structures of nonaxisymmetric matter distributions of static charged dust were also recently studied [16]. The non-linear superposition of a disk and a black hole was first considered by Lemos and Letelier [17]. Models of thin disks and thin disks with halos made of perfect fluids were considered in [18]. The generalization of the "displace, cut and reflect" method (Sec. D.2) to construct thick static disks was considered by González and Letelier [19]. For a recent review on relativistic accretion disks see [20].

Gravitationally bound stellar objects are likely to be positively charged due to the fact that the electrons are lighter than the protons so the formers can more easily scape from the stellar object. One should expect to have an equilibrium situation when the electrostatic energy of the electron (eV) is of the order of its thermal energy (kT) [21], then the scape would stop. Similar considerations can be found in Ref. [22].

The aim of this paper is to present a charged version of perfect fluid disks that were studied in [18]. They are constructed with the well known "displace, cut and reflect" method applied to the Reissner-Nordström metric in isotropic coordinates. The stability of this new model of charged disks will also be considered. We present an extension of the Rayleigh criteria of stability [23] for the case of relativistic disks made of a charged perfect fluid. We find a simple condition to have gravitationally bounded disks.

The paper is divided as follows. Sec. D.2 discusses the formalism which can be used to construct disks given a solution of Einstein-Maxwell equations, and the main physical variables of the disk. In Sec. D.3, Rayleigh inspired criteria of stability criteria for the stability of charged and non-charged perfect fluid disks is established. The properties and stability of the charged disks are discussed in Sec. D.4. Finally, in Sec. D.5, we discuss our results and make some considerations about the construction of charged perfect fluid disks with halos. The "displace, cut and reflect" method is reviewed in the Appendix.

D.2   Einstein-Maxwell Equations and Disks

The isotropic metric representing a static spherically symmetric space-time can be expressed as

$$ds^2 = e^{\nu(r)}dt^2 - e^{\lambda(r)}(dr^2 + r^2 d\Omega^2), \tag{D.1}$$

where $d\Omega^2 = d\theta^2 + \sin^2\theta d\varphi^2$. The same metric in cylindrical coordinates (t, R, z, φ) reads:

$$ds^2 = e^{\nu(R,z)}dt^2 - e^{\lambda(R,z)}\left(dR^2 + dz^2 + R^2 d\varphi^2\right). \tag{D.2}$$

The Einstein-Maxwell system of equations is given by

$$G_{\mu\nu} = 8\pi T_{\mu\nu}, \tag{D.3}$$

$$T_{\mu\nu} = \frac{1}{4\pi}\left(F_\mu{}^\sigma F_{\nu\sigma} + \frac{1}{4}g_{\mu\nu}F_{\rho\sigma}F^{\rho\sigma}\right), \tag{D.4}$$

$$F^{\mu\nu}{}_{;\mu} = 0, \tag{D.5}$$

$$F_{\mu\nu} = A_{\nu,\mu} - A_{\mu,\nu}, \tag{D.6}$$

where all symbols have their usual meaning. We use geometric units with $G = c = 1$.

The method used to generate the metric of the disk and its material content is the well known "displace, cut and reflect" method (see the Appendix) that was first used by Kuzmin [24] and Toomre [25] to construct Newtonian models of disks, and later extended to general relativity (see, for example [6, 10]). Given a solution of the Einstein-Maxwell equation, this procedure is mathematically equivalent to apply the transformation $z \to |z| + a$, with a constant, on that solution. In the Einstein tensor we have first and second derivatives of z. Remembering that $\partial_z|z| = 2\vartheta(z) - 1$ and $\partial_{zz}|z| = 2\delta(z)$, where $\vartheta(z)$ and $\delta(z)$ are, respectively, the Heaviside function and the Dirac distribution, Einstein-Maxwell equations give us

$$G_{\mu\nu} = 8\pi(T_{\mu\nu}^{\text{elm.}} + Q_{\mu\nu}\delta(z)), \tag{D.7}$$

$$F^{\mu\nu}{}_{;\mu} = 4\pi J^\nu\delta(z), \tag{D.8}$$

where $T_{\mu\nu}^{\text{elm.}}$ is the electromagnetic tensor Eq. (D.4), $Q_{\mu\nu}$ is the energy-momentum tensor on the plane $z = 0$ and J^ν is the current density on the plane $z = 0$. For the metric (D.2), the nonzero components of $Q_{\mu\nu}$ are

$$Q_t^t = \frac{1}{16\pi}\left[-b^{zz} + g^{zz}(b_R^R + b_z^z + b_\varphi^\varphi)\right], \tag{D.9}$$

115

$$Q_R^R = Q_\varphi^\varphi = \frac{1}{16\pi} \left[-b^{zz} + g^{zz}(b_t^t + b_R^R + b_z^z) \right], \tag{D.10}$$

where $b_{\mu\nu}$ denotes the jump of the first derivatives of the metric tensor on the plane $z = 0$,

$$b_{\mu\nu} = g_{\mu\nu,z}|_{z=0^+} - g_{\mu\nu,z}|_{z=0^-}, \tag{D.11}$$

and the other quantities are evaluated at $z = 0^+$. The electromagnetic potential for an electric field is

$$A_\mu = (\phi, 0, 0, 0). \tag{D.12}$$

Using Eq. (D.12) and Eq. (D.8), the only nonzero component of the current density on the plane $z = 0$ is

$$J^t = \frac{1}{4\pi} g^{zz} g^{tt} a_t, \tag{D.13}$$

where a_μ denotes the jump of the first derivatives of the electromagnetic potential on the plane $z = 0$,

$$a_\mu = A_{\mu,z}|_{z=0^+} - A_{\mu,z}|_{z=0^-}, \tag{D.14}$$

and the other quantities are evaluated at $z = 0^+$. The "physical measure" of length in the direction ∂_z for metric (D.2) is $\sqrt{-g_{zz}}$, then the invariant distribution is $\delta(z)/\sqrt{-g_{zz}}$. Thus the "true" surface energy density σ and the azimuthal and radial pressures or tensions (P) are

$$\sigma = \sqrt{-g_{zz}} Q_t^t, \quad P = -\sqrt{-g_{zz}} Q_R^R = -\sqrt{-g_{zz}} Q_\varphi^\varphi. \tag{D.15}$$

Since $J^\mu = \rho U^\mu$, where $U^\mu = \delta_t^\mu/\sqrt{g_{tt}}$, the "true" surface charge density ρ is

$$\rho = \sqrt{-g_{zz} g_{tt}} J^t. \tag{D.16}$$

D.3   Stability Conditions for Perfect Fluid Disks

One way to explain stability of static disks without radial pressure is to assume that the particles on the disk plane move under the action of their own gravitational field in such a way that as many particles move clockwise as counterclockwise (counterrotating model). With this assumption, stability of the matter on the disk can be associated with stability of circular orbits

along geodesics (see [26] for a detailed explanation). The usual stability criteria for circular orbits is adapted from the Rayleigh criteria of stability for a rotating fluid [23]. One finds that stability against small radial perturbations is achieved when

$$h\frac{dh}{dr} > 0, \tag{D.17}$$

where h is the specific angular momentum of the circular orbit.

In the case of perfect fluid disks the situation is somewhat different, since radial pressure can equilibrate the inward gravitational force and no counterrotating hypothesis is needed. Using $T^{\mu\nu}{}_{;\nu} = 0$ where $T^{\mu\nu}$ is the sum of the energy-momentum tensor for a perfect fluid and Eq. (D.4), the equilibrium condition in the radial direction on the plane $z = 0$ is given by

$$\frac{1}{2}(P + \sigma)(e^\nu)_{,R} = -\rho e^{\nu/2}\phi_{,R} - e^\nu P_{,R}. \tag{D.18}$$

The left side of Eq. (D.18) can be interpreted as the gravitational force which equilibrates the pressure and electric forces that appear on the right side. Now suppose an element of fluid at radius R is displaced to $R + \Delta R$ keeeping P, σ and ρ constant. The right side of Eq. (D.18) becomes

$$-e^{\nu(R+\Delta R)/2}\phi_{,R}(R + \Delta R)\rho(R) - e^{\nu(R+\Delta R)}P_{,R}(R). \tag{D.19}$$

These "forces" should be compared with the right side of Eq. (D.18) at radius $R + \Delta R$:

$$-e^{\nu(R+\Delta R)/2}\phi_{,R}(R + \Delta R)\rho(R + \Delta R) - e^{\nu(R+\Delta R)}P_{,R}(R + \Delta R). \tag{D.20}$$

To have stability expression (D.19) must be less then expression (D.20). Expanding $\rho(R + \Delta R)$ and $P_{,R}(R + \Delta R)$ around R, we get

$$e^{\nu/2}\phi_{,R}\rho_{,R} + e^\nu P_{,RR} < 0. \tag{D.21}$$

For an uncharged fluid, condition (D.21) reduces to $P_{,RR} < 0$.

Note that this criterium of stability refers only to radial perturbations of the pressure and charge. It really gives us a condition to have gravitationally bounded systems. In other words the disks do not explode, but they can collapse. In the general case, the study of the stability of gravitating systems reduces to the much harder problem of the study of the eigenvalue problem for a nontrivial elliptic operator [27].

117

D.4 Charged Perfect Fluid Disks

We apply now the results of the previous sections to construct charged disks. The Reissner-Nordström solution in Schwarzschild coordinates is given by

$$\mathrm{d}s^2 = \left(1 - \frac{2m}{r} + \frac{Q^2}{r^2}\right)\mathrm{d}t^2 - \frac{\mathrm{d}r^2}{\left(1 - \frac{2m}{r} + \frac{Q^2}{r^2}\right)} - r^2 d\Omega^2, \tag{D.22}$$

where m and Q are, respectively, the mass and charge of the black hole, and $m > Q$. The electromagnetic potential associated to solution (D.22) is

$$A_\mu = \left(\frac{Q}{r}, 0, 0, 0\right). \tag{D.23}$$

With the radial coordinate transformation

$$r = r'\left(1 + \frac{m+Q}{2r'}\right)\left(1 + \frac{m-Q}{2r'}\right), \tag{D.24}$$

metric (D.22) and Eq. (D.23) can be expressed in isotropic coordinates (t, r', θ, φ) as

$$\mathrm{d}s^2 = \frac{\left[1 - \frac{(m^2-Q^2)}{4r'^2}\right]^2}{\left[1 + \frac{(m+Q)}{2r'}\right]^2 \left[1 + \frac{(m-Q)}{2r'}\right]^2}\mathrm{d}t^2 - \left[1 + \frac{(m+Q)}{2r'}\right]^2$$

$$\times \left[1 + \frac{(m-Q)}{2r'}\right]^2 (\mathrm{d}r'^2 + r'^2\mathrm{d}\theta^2 + r'^2\sin^2\theta\mathrm{d}\varphi^2), \tag{D.25}$$

$$A_\mu = \left(\frac{Q}{r'\left(1 + \frac{m+Q}{2r'}\right)\left(1 + \frac{m-Q}{2r'}\right)}, 0, 0, 0\right). \tag{D.26}$$

Transforming Eq. (D.25) and (D.26) to cylindrical coordinates, and using Eq. (D.15) and (D.16), we obtain a disk with surface energy density $\sigma = \bar{\sigma}/m$, equal radial and azimuthal pressures (or tensions) $P = \bar{P}/m$ and surface charge density $\rho = \bar{\rho}/m$ where

$$\bar{\sigma} = \frac{4\tilde{a}}{\pi} \frac{2\sqrt{\tilde{R}^2 + \tilde{a}^2} + 1 - \tilde{Q}^2}{[(1 + 2\sqrt{\tilde{R}^2 + \tilde{a}^2})^2 - \tilde{Q}^2]^2}, \tag{D.27}$$

$$\bar{P} = -\frac{2\tilde{a}}{\pi} \frac{1 - \tilde{Q}^2}{[(1 + 2\sqrt{\tilde{R}^2 + \tilde{a}^2})^2 - \tilde{Q}^2][1 - \tilde{Q}^2 - 4(\tilde{R}^2 + \tilde{a}^2)]}, \tag{D.28}$$

118

$$\bar{\rho} = \frac{8\tilde{Q}\tilde{a}\sqrt{\tilde{R}^2 + \tilde{a}^2}}{\pi\left[4\sqrt{\tilde{R}^2 + \tilde{a}^2}(1 + \sqrt{\tilde{R}^2 + \tilde{a}^2}) + 1 - \tilde{Q}^2\right]^2}, \tag{D.29}$$

with $\tilde{R} = R/m$, $\tilde{a} = a/m$ and $\tilde{Q} = Q/m$.

Eq. (D.27) shows that the disk's surface density is always positive (weak energy condition) for $\tilde{Q} < 1$. Positive values (pression) for the stresses in azimuthal and radial directions are obtained if $\tilde{a} > \sqrt{1 - \tilde{Q}^2}/2$. The velocity of sound propagation V, defined as $V^2 = \frac{dP}{d\sigma}$, is calculated using Eq. (D.27) and Eq. (D.28):

$$V^2 =$$

$$\frac{(1 - \tilde{Q}^2)[(1 + 2\sqrt{\tilde{R}^2 + \tilde{a}^2})^2 - \tilde{Q}^2][(1 + 2\sqrt{\tilde{R}^2 + \tilde{a}^2})^2(1 - 4\sqrt{\tilde{R}^2 + \tilde{a}^2}) - \tilde{Q}^2]}{[1 - \tilde{Q}^2 - 4(\tilde{R}^2 + \tilde{a}^2)]^2[-3(1 + 2\sqrt{\tilde{R}^2 + \tilde{a}^2})^2 + \tilde{Q}^2(3 + 8\sqrt{\tilde{R}^2 + \tilde{a}^2})]}. \tag{D.30}$$

Figure D.1 shows the curves of $V^2 = 1$ (solid curve) and of $\tilde{a} = \sqrt{1 - \tilde{Q}^2}/2$ (dotted curve) where $\bar{P}$ changes sign as functions of the parameters $\tilde{a} = a/m$ and $\tilde{Q} = Q/m$. Above the dotted curve, stresses are positive (pressure) for all $\tilde{R}$ and above the solid curve, condition $V^2 < 1$ is also satisfied for all $\tilde{R}$. Thus, choosing values for $\tilde{a}$ and $\tilde{Q}$ that lie above the solid curve ensures that the entire disk will have pressures and sublumial sound velocities. We also note that when we increase the charge, the range of the cut parameter a (that generates disks for which the conditions stated above are satisfied) is enlarged. Figure D.2(a)–D.2(d) shows, respectively, the surface energy density $\bar{\sigma}$, pressures $\bar{P}$, sound velocity V and charge density $\bar{\rho}$ with $\tilde{a} = 1$, $\tilde{Q} = 0$, 0.3, 0.6 and 0.9 as functions of $\tilde{R}$. As charge increases, the disks become less relativistic for the same cut parameter; energy density and pressures are lowered and charge density becomes more concentrated near the disk center.

Figure D.3(a) is a graph of curves where Eq. (D.21) changes sign. The curves have been plotted only for ranges of parameter $\tilde{a}$ where $V^2 < 1$ (Fig. D.1). At the left of each curve, the stability condition (D.21) is satisfied. Thus, the disks are stable only in a small region near their centers. We also note that the charge decreases the radii of stability. The left side of Eq. D.21 is plotted in Fig. D.3(b) for the same parameters as in Fig. D.2.
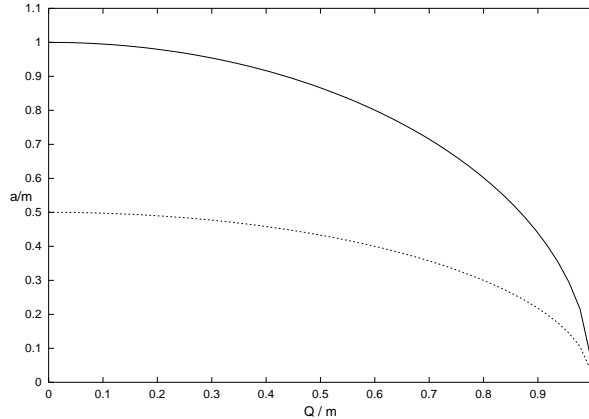
Figure D.1: Curve $V^2 = 1$ (solid curve) as a function of the parameters $\tilde{a} = a/m$ and $\tilde{Q} = Q/m$ for the charged disk of perfect fluid. Also $\tilde{a} = \sqrt{1 - \tilde{Q}^2}/2$ (dotted curve).

D.5 Discussion

We applied the "displace, cut and reflect" method on the Reissner-Nordström solution in isotropic coordinates and generated static charged disks made of perfect fluid. We also derived a simple criteria for the stability for charged and uncharged perfect fluid disks that is an extension of the Rayleigh criteria of stability for rotating fluids. The addition of charge decreases the energy density and pressures near the disk's centers, while charge density in enhanced there. Furthermore, presence of charge decreases the stable regions of the disks that are reduced to small regions near the center even in the absence of charge. This is a rather different result from that of our previous stability analysis of the uncharged perfect fluid disk [18] based on the stability study of circular orbits of test particles, where we found that the disks were completely stable for $\tilde{a} \gtrsim 1.016$. It is worthwhile to note that the criteria used to study stability of disks made of counterrotating matter is based on a particle consideration, whereas the stability criteria derived for perfect fluid disks is based on collective phenomena. Therefore, the stability criteria derived in this paper seems to us to be more appropriate for the study of perfect fluid disks.

In principle it is possible to add charged halos to the disks presented in this work by applying the "displace, cut and reflect" method to a static charged sphere of perfect fluid in isotropic coordinates (see the Appendix).
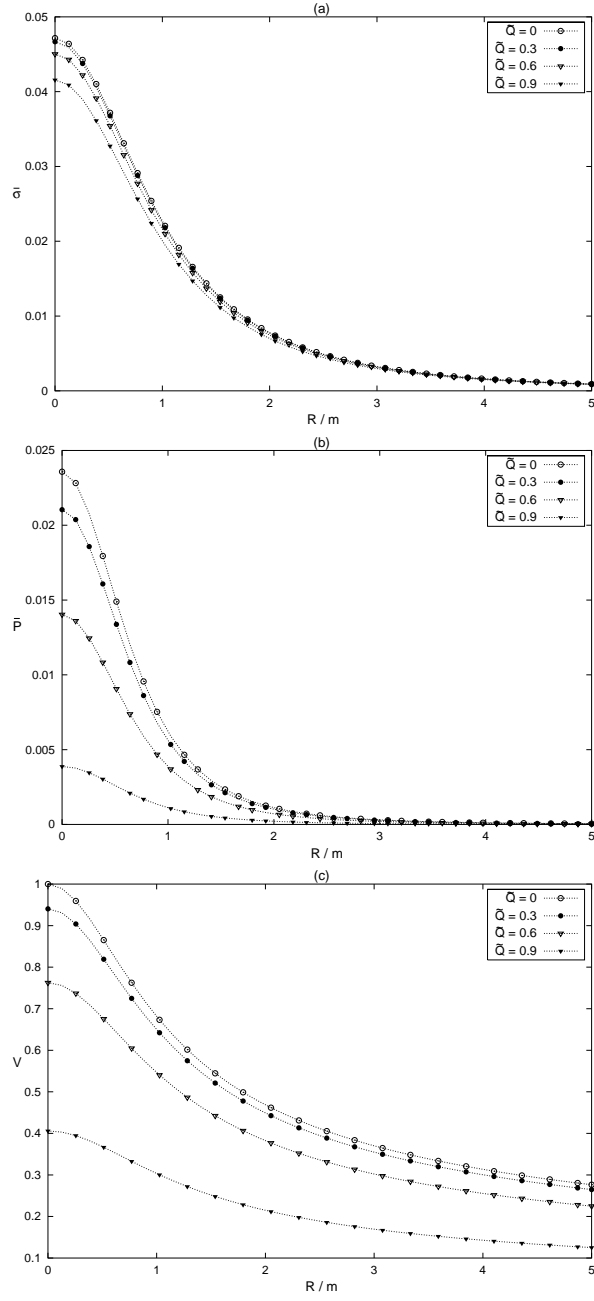
Figure D.2: (a) The surface energy density $\bar{\sigma}$, Eq. (D.27), (b) the pressure $\bar{P}$, Eq. (D.28), (c) the sound velocity V Eq. (D.30) for the disk with $\tilde{a} = 1$, $\tilde{Q} = 0$, 0.3, 0.6 and 0.9 as functions of $\tilde{R}$.
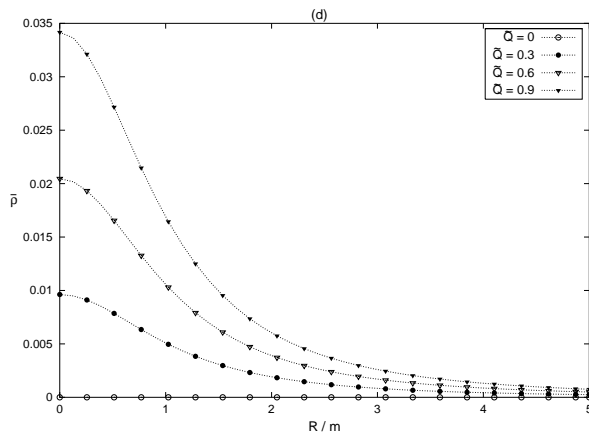
Figure D.2(d): The charge density $\bar{\rho}$, Eq. (D.29) for the disk with $\tilde{a} = 1$, $\tilde{Q} = 0$, 0.3, 0.6 and 0.9 as functions of $\tilde{R}$.

The halos could have a charge of the same sign or opposite sign of the disk's charge such that the entire object could be neutral or have an arbitrary charge. Although there exist many exact solutions for charged fluid spheres in Schwarzschild coordinates (see, for example, [28]), we have not found in the literature similar solutions in isotropic coordinates. This may be due to the fact that in these coordinates the Einstein-Maxwell equations for a charged perfect fluid are reduced to a system of highly nonlinear coupled second order differential equations for both metric functions $\nu(r)$ and $\lambda(r)$ and for the electrostatic potential $\phi(r)$, so the task of finding exact solutions is more involved than in canonical spherical coordinates. We believe that this search for exact solutions in isotropic coordinates is worthwhile.

Acknowledgments

Appendix

In this appendix we give an overview of the "displace, cut and reflect" method used to generate the metric and its material and electric content from a known solution of the Einstein-Maxwell field equations. The method can be divided into the following steps that are illustrated in Fig. D.4: First, in a space wherein we have a compact source of gravitational field, we choose
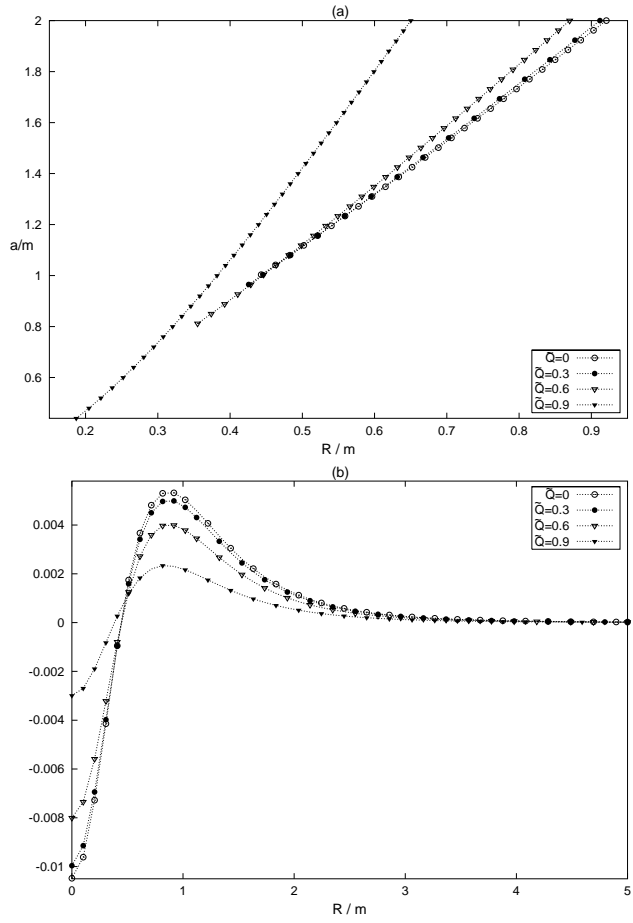
Figure D.3: (a) Curves where Eq. (D.21) defining stability changes sign as functions of radius $\tilde{R}$, cut parameter $\tilde{a}$ and charge $\tilde{Q}$. Disks are stable at the left of each curve. (b) Curves of the left side of Eq. (D.21) for the same parameters as in Fig. D.2.
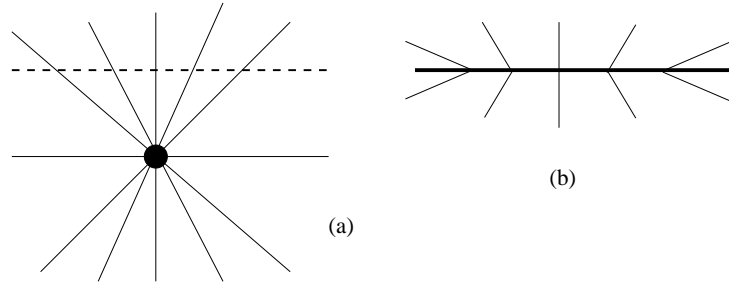
Figure D.4: An illustration of the "displace, cut and reflect" method for the generation of disks. In (a) the spacetime with a singularity is displaced and cut by a plane (dotted line), in (b) the part with singularities is disregarded and the upper part is reflected on the plane.

a surface (in our case, the plane $z = 0$) that divides the space in two pieces: one with no singularities or sources and the other with the sources. Then we disregard the part of the space with singularities and use the surface to make an inversion of the nonsingular part of the space. This results in a space with a singularity that is a delta function with support on $z = 0$. The same procedure can be used with a static sphere of charged perfect fluid to generate charged disks with halos, as depicted in Fig. D.5: the sphere is displaced and cut by a distance a less then its radius. The part of the space that contains the center of the sphere is disregarded. After the inversion of the remaining space, one ends up with a charged disk surrounded by a cap of charged perfect fluid. If the internal fluid solution is matched to the Reissner-Nordström metric Eq. (D.25), the outer part of the disk will have the physical properties deduced in Sec. D.4, while the properties of the inner part will depend on the particular fluid solution.

Bibliography

[1] W. A. Bonnor and A. Sackfield, Commun. Math. Phys. **8**, 338 (1968).

[2] T. Morgan and L. Morgan, Phys. Rev. **183**, 1097 (1969).

[3] L. Morgan and T. Morgan, Phys. Rev. D **2**, 2756 (1970).

[4] D. Lynden-Bell and S. Pineault, Mon. Not. R. Astron. Soc. **185**, 679 (1978).

[5] J. P. S. Lemos, Classical Quantum Gravity **6**, 1219 (1989).
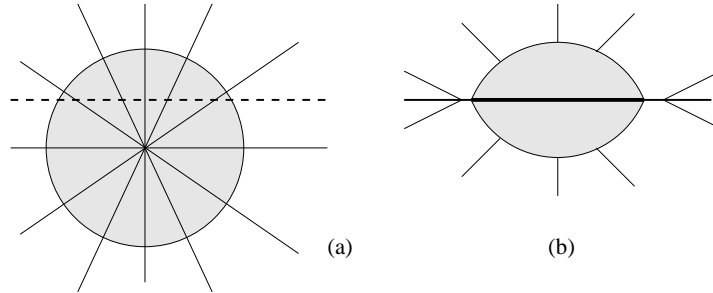
Figure D.5: An illustration of the "displace, cut and reflect" method for the generation of charged disks with halos. In (a) the sphere of perfect fluid is displaced and cut by a plane (dotted line), in (b) the part that contains the center of the sphere is disregarded and the upper part is reflected on the plane.

[6] J. Bičák, D. Lynden-Bell and J. Katz, Phys. Rev. D **47**, 4334 (1993).

[7] J. Bičák, D. Lynden-Bell and C. Pichon, Mon. Not. R. Astron. Soc. **265**, 126 (1993).

[8] J. Bičák and T. Ledvinka, Phys. Rev. Lett. **71**, 1669 (1993).

[9] T. Ledvinka, M. Zofka and J. Bičák, in *Proceedings of the 8th Marcel Grossman Meeting in General Relativity*, edited by T. Piran (World Scientific, Singapore, 1999), p. 339-341.

[10] G. González and P. S. Letelier, Phys. Rev. D **62**, 064025 (2000).

[11] G. González and P. S. Letelier, Classical Quantum Gravity **16**, 479 (1999).

[12] P. S. Letelier, Phys. Rev. D **60**, 104042 (1999).

[13] J. Katz, J. Bičák and D. Lynden-Bell, Classical Quantum Gravity **16**, 4023 (1999).

[14] G. Neugebauer and R. Meinel, Phys. Rev. Lett. **75**, 3046 (1995).

[15] G. García R. and G. González, Phys. Rev. D **69**, 124002 (2004).

[16] D. Vogt and P. S. Letelier, Classical Quantum Gravity (to be published).

[17] J. P. S. Lemos and P. S. Letelier, Classical Quantum Gravity **10**, L75 (1993).

[18] D. Vogt and P. S. Letelier, Phys. Rev. D **68**, 084010 (2003).

[19] G. González and P. S. Letelier, Phys. Rev. D **69**, 044013 (2004).

[20] V. Karas, J.-M. Huré and O. Semerák, Classical Quantum Gravity **21**, R1 (2004).

[21] J. Bally and E.R. Harrison, Astrophys. J. **220**, 743 (1978).

[22] V.F. Shvartsman, Zh. Eksp. Teor. Fiz. **60**, 881 (1971) [Sov. Phys. JETP **33**, 475 (1971)].

[23] Lord Rayleigh, Proc. R. Soc. London A **93**, 148 (1917); see also L. D. Landau and E. M. Lifshitz, in *Fluid Mechanics* (Pergamon Press, Oxford, 1987), 2nd Ed. Sec. 27.

[24] G. G. Kuzmin, Astron. Zh. **33**, 27 (1956).

[25] A. Toomre, Astrophys. J. **138**, 385 (1962).

[26] P. S. Letelier, Phys. Rev. D **68**, 104002 (2003).

[27] See for instance, A.N. Friedman and V.L.K. Polyachenko, *Physics of Gravitating Systems* (Springer-Verlag, New York, 1983).

[28] B. V. Ivanov, Phys. Rev. D **65**, 104001 (2002).

Apêndice E

General relativistic model for the gravitational field of active galactic nuclei surrounded by a disk

Abstract

An exact but simple general relativistic model for the gravitational field of active galactic nuclei is constructed, based on the superposition in Weyl coordinates of a black hole, a Chazy-Curzon disk and two rods, which represent matter jets. The influence of the rods on the matter properties of the disk and on its stability is examined. We find that in general they contribute to destabilize the disk. Also the oscillation frequencies for perturbed circular geodesics on the disk are computed, and some geodesic orbits for the superposed metric are numerically calculated.

PACS numbers: 04.40.–b, 04.20.Jb, 98.58 Fd, 98.62 Mw

E.1   Introduction

There is strong observational evidence that active galactic nuclei (AGN), X-ray transients and gamma-ray bursts (GRBs) are associated with accretion onto black holes, and that these sources are able to form collimated,

ultrarelativistic flows (relativistic jets).

The exact mechanisms to explain the production of jets are still uncertain, but they probably involve the interaction between a spinning black hole, the accretion disk, and electromagnetic fields in strong gravitational fields (see, for example, [1–3] and references therein).

Thus, a reasonably accurate general relativistic model of an AGN would require an exact solution of Einstein-Maxwell field equations that describes a superposition of a Kerr black hole with a stationary disk and electromagnetic fields. Not even an exact solution of a stationary black hole-disk system has been found yet. Solutions for static thin disks without radial pressure were first studied by Bonnor and Sackfield [4], and Morgan and Morgan [5], and with radial pressure by Morgan and Morgan [6]. Several classes of exact solutions of the Einstein field equations corresponding to static thin disks with or without radial pressure have been obtained by different authors [7–16]. Thin rotating disks were considered in [17, 18]. Perfect fluid disks with halos [19] and charged perfect fluid disks [20] were also studied, whereas thick relativistic disks were reported in [21]. Several solutions of the Einstein equations coupled to matter that represent disks have also been studied by the Jena group [22–29].

The static superposition of a disk and a black hole was first considered by Lemos and Letelier [10]. Zellerin and Semerák [30] found a stationary metric that reduces to the superposition of a disk and a black hole in the static limit and thus may represent a stationary disk-black hole system. The analysis of their solution is complicated by the fact that the metric functions cannot be analytically computed. For a survey on self gravitating relativistic thin disks, see for instance [31].

The aim of this paper is to consider the gravitational field of an AGN through a simple model: the *static* superposition of a black hole with a Chazy-Curzon disk and two rods placed on the symmetry axis, which will represent jets. Our principal interest here is to see how the presence of the rods affect the matter properties and stability of the disk.

The article is divided as follows. In Sec. E.2 we review the "displace, cut and reflect" method used to construct thin disks from a known solution of Einstein field equations in Weyl coordinates. Section E.3 summarizes the formalism to superpose thin disks and other Weyl solutions. Section E.4 discusses Schwarzschild solution and the metric of a finite rod in Weyl coordinates. In Sec. E.5 the results of Secs. E.3 and E.4 are then applied to construct the superposition of disk, black hole and rods and the resulting energy-momentum tensor. In Sec. E.6 the disk stability is studied through small horizontal and vertical oscillations about equatorial circular geodesics.

In Sec. E.7 some geodesic orbits for the superposed metric are numerically calculated. Finally, Sec. E.8 is devoted to discussion of the results. We take units such that $c = G = 1$.

E.2 Thin disk solutions in Weyl coordinates

In absence of matter, the general metric for a static axially symmetric space-time in Weyl's canonical coordinates (t, r, z, φ) is given by

$$\mathrm{d}s^2 = -e^\phi \mathrm{d}t^2 + e^{\nu-\phi}(\mathrm{d}r^2 + \mathrm{d}z^2) + r^2 e^{-\phi}\mathrm{d}\varphi^2, \tag{E.1}$$

where ϕ and ν are functions of r and z only. Einstein vacuum field equations for the metric Eq. (E.1) yield [32, 33]

$$\phi_{,rr} + \frac{\phi_{,r}}{r} + \phi_{,zz} = 0, \tag{E.2a}$$

$$\nu[\phi] = \frac{1}{2}\int r\left[(\phi_{,r}^2 - \phi_{,z}^2)\mathrm{d}r + 2\phi_{,r}\phi_{,z}\mathrm{d}z\right]. \tag{E.2b}$$

Given a solution of Eqs. (E.2a) and (E.2b), one can construct a thin disk by using the well known "displace, cut and reflect" method, due to Kuzmin [34]. First, a surface $(z = 0)$ is chosen so that it divides the usual space in two parts: one with no singularities or sources, and the other with them. Then the part of the space with singularities or sources is disregarded. At last, the surface is used to make an inversion of the nonsingular part of the space. The result will be a space with a singularity that is a delta function with support on $z = 0$. The method is mathematically equivalent to making a transformation $z \to |z| + a$, where a is a constant.

The application of the formalism of distributions in curved spacetimes to the Weyl metric Eq. (E.1) is exposed in [13]. One finds that the components of the distributional energy-momentum tensor $[T^a{}_b]$ on the disk are

$$-T^t{}_t = e^{\phi-\nu}(2 - r\phi_{,r})\phi_{,z}\delta(z), \tag{E.3}$$

$$T^\varphi{}_\varphi = e^{\phi-\nu}r\phi_{,r}\phi_{,z}\delta(z), \tag{E.4}$$

$$T^r{}_r = T^z{}_z = 0, \tag{E.5}$$

where $\delta(z)$ is the Dirac distribution with support on the disk and is understood that $\phi_{,z} = \lim_{z\to 0^+} \phi_{,z}$. The "true" energy density and azimuthal pressure are, respectively,

$$\sigma = e^{(\nu-\phi)/2}(-T^t{}_t), \tag{E.6}$$

129

$$p = e^{(\nu-\phi)/2} T^{\varphi}{}_{\varphi}. \tag{E.7}$$

To explain the disk stability in absence of radial pressure, one may assume the counter-rotating hypothesis, where the particles on the disk move in such a way that there are as many particles moving in clockwise as in counterclockwise direction. The velocity V of counter-rotation of the particles in the disk is given by [9, 35]

$$V^2 = \frac{p}{\sigma} \tag{E.8}$$

If $V^2 < 1$, the particles travel at sublumial velocities. The specific angular momentum h of particles on the disk moving in circular orbits along geodesics reads

$$h = r^{3/2} e^{-\phi/2} \sqrt{\frac{\phi_{,r}}{2(1 - r\phi_{,r})}}. \tag{E.9}$$

The stability of circular orbits on the disk plane can be determined with an extension of Rayleigh criteria of stability of a fluid at rest in a gravitational field: $h\frac{dh}{dr} > 0$ [36]. Using Eq. (E.9) this is equivalent to

$$\phi_{,r}(-3r\phi_{,r} + 3 + r^2\phi_{,r}^2) + r\phi_{,rr} > 0. \tag{E.10}$$

E.3   Superposition of thin disks and other Weyl solutions

An important property of the Weyl metric Eq. (E.1) is that the field Eq. (E.2a) for the potential ϕ is the Laplace equation in cylindrical coordinates. Since Laplace's equation is linear, if ϕ_1 and ϕ_2 are solutions, then the superposition $\phi = \phi_1 + \phi_2$ is also a solution. The other metric function Eq. (E.2b) is nonlinear, and so cannot be superposed. But one can show that the relation

$$\nu[\phi_1 + \phi_2] = \nu[\phi_1] + \nu[\phi_2] + 2\nu[\phi_1, \phi_2], \tag{E.11}$$

where

$$\nu[\phi_1, \phi_2] = \frac{1}{2}\int r[(\phi_{1,r}\phi_{2,r} - \phi_{1,z}\phi_{2,z})dr + (\phi_{1,r}\phi_{2,z} + \phi_{1,z}\phi_{2,r})dz], \tag{E.12}$$

holds. Other useful relations are given in [8].

The energy-momentum tensor of the combined system disk and black hole has been computed by Lemos and Letelier [13]. Let ϕ_D and ϕ_{BH} be the metric potentials of the disk and of the black hole, respectively. Then the components $[T^a{}_b]$ of the superposition are

$$-T^t{}_t = e^{\phi_D+\phi_{BH}-\nu}\left[2 - r(\phi_D + \phi_{BH})_{,r}\right]\phi_{D,z}\delta(z), \qquad \text{(E.13)}$$

$$T^\varphi{}_\varphi = e^{\phi_D+\phi_{BH}-\nu}r(\phi_D + \phi_{BH})_{,r}\phi_{D,z}\delta(z), \qquad \text{(E.14)}$$

$$T^r{}_r = T^z{}_z = 0, \qquad \text{(E.15)}$$

where $\nu = \nu[\phi_D + \phi_{BH}]$, and again $\phi_{D,z} = \lim_{z\to 0^+}\phi_{D,z}$. The "true" energy density and azimuthal pressure read

$$\sigma = e^{(\nu-\phi_D-\phi_{BH})/2}(-T^t{}_t), \qquad \text{(E.16)}$$

$$p = e^{(\nu-\phi_D-\phi_{BH})/2}T^\varphi{}_\varphi. \qquad \text{(E.17)}$$

Equation (E.13) and (E.14) show that the potential of the black hole interacts with the disk and changes its matter properties. Although Eqs. (E.13)–(E.17) have been derived for superposition of disk and black hole, they are also valid when the potential function ϕ_{BH} is a sum of other Weyl solutions, like the superposition of a black hole and rods.

E.4 Black holes and rods in Weyl coordinates

The Schwarzschild black hole metric function ϕ_{BH} in Weyl coordinates is given by

$$\phi_{BH} = \ln\left(\frac{r_1 + r_2 - 2M}{r_1 + r_2 + 2M}\right), \qquad \text{(E.18)}$$

where $r_1^2 = (M - z)^2 + r^2$ and $r_2^2 = (M + z)^2 + r^2$. The function $\phi(r, z)$ can be related to the Newtonian potential U by

$$\phi = 2U. \qquad \text{(E.19)}$$

Thus, the metric potential ϕ_R of a finite rod of linear mass density λ lying on the z axis and located along $[c_1, c_2]$ is

$$\phi_R = -2\lambda\ln\left[\frac{c_2 - z + \sqrt{r^2 + (c_2 - z)^2}}{c_1 - z + \sqrt{r^2 + (c_1 - z)^2}}\right]. \qquad \text{(E.20)}$$

The calculation of the other metric function ν for Eqs. (E.18) and (E.20) and later for the superposed metric, is considerably simplified when one defines the following μ function

$$\mu_k = \alpha_k - z + \sqrt{r^2 + (\alpha_k - z)^2}, \tag{E.21}$$

where α_k is an arbitrary constant. This function is a natural consequence of the formalism of the inverse scattering method [37, 38]. Equations (E.18) and (E.20) can be rewritten as

$$\phi_{BH} = \ln\left(\frac{\mu_1}{\mu_2}\right), \tag{E.22}$$

$$\phi_R = -2\lambda\ln\left(\frac{\mu_3}{\mu_4}\right), \tag{E.23}$$

where we defined

$$\mu_1 = -M - z + \sqrt{r^2 + (M+z)^2}, \quad \mu_2 = M - z + \sqrt{r^2 + (M-z)^2},$$
$$\mu_3 = c_2 - z + \sqrt{r^2 + (c_2-z)^2}, \quad\quad \mu_4 = c_1 - z + \sqrt{r^2 + (c_1-z)^2}.$$

On using Eq. (E.11)

$$\nu[\ln\mu_i - \ln\mu_j] = \nu[\ln\mu_i] + \nu[\ln\mu_j] - 2\nu[\ln\mu_i, \ln\mu_j]; \tag{E.24}$$

the result

$$\nu[\ln\mu_i, \ln\mu_j] = \ln(\mu_i - \mu_j), \tag{E.25}$$

which also follows from the inverse scattering method; and the identity

$$(r^2 + \mu_i\mu_j)(\mu_i - \mu_j) = 2(\alpha_i - \alpha_j)\mu_i\mu_j, \tag{E.26}$$

one obtains following expressions for the metric function ν

$$\nu_{BH} = \ln\left[\frac{(r^2 + \mu_1\mu_2)^2}{(r^2 + \mu_1^2)(r^2 + \mu_2^2)}\right], \tag{E.27}$$

$$\nu_R = 4\lambda^2\ln\left[\frac{(r^2 + \mu_3\mu_4)^2}{(r^2 + \mu_3^2)(r^2 + \mu_4^2)}\right]. \tag{E.28}$$
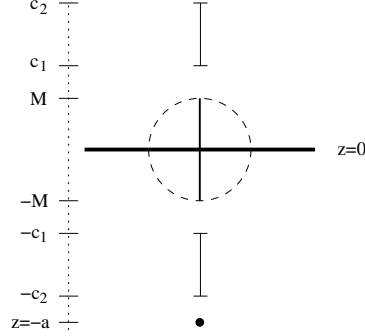
Figure E.1: Superposition of a black hole with mass M, two rods and a Chazy-Curzon disk on the plane $z = 0$.

E.5   Superposition of disk, black hole and rods

We now consider the superposition illustrated in Fig. E.1: a black hole with mass M whose center is on $z = 0$, two rods with equal mass density λ, each one with mass $\mathcal{M}$ located along $[-c_2, -c_1]$ and $[c_1, c_2]$ on the z axis, and a disk on the plane $z = 0$ constructed with the "displace, cut and reflect method" from the Chazy-Curzon solution with mass m, whose singularity lies on $z = -a$:

$$\phi_D = -\frac{2m}{\sqrt{r^2 + (|z| + a)^2}}. \tag{E.29}$$

It should be remembered that in Weyl coordinates a black hole with mass M is represented by a rod with length $2M$, thus in Fig. E.1 we put a dotted circle around the rod in the middle. Such a configuration is not gravitationally stable: a consequence of the nonlinearity of Eq. (E.2b) is the appearence of gravitationally inert singular structures like struts between the rods and the black hole that keep them appart. Also in the superposition of the disk with the black hole, superlumial regions $(V^2 > 1)$ exist because there is matter up to the event horizon.

The metric function ϕ of the superposition can be expressed as

$$\phi = -2\lambda \ln \left(\frac{\mu_3}{\mu_4} \right) + \ln \left(\frac{\mu_1}{\mu_2} \right) - 2\lambda \ln \left(\frac{\mu_5}{\mu_6} \right) + \phi_D, \tag{E.30}$$

with $\mu_5 = -c_1 - z + \sqrt{r^2 + (c_1 + z)^2}$ and $\mu_6 = -c_2 - z + \sqrt{r^2 + (c_2 + z)^2}$.

Now we consider the case when both rods just touch the horizon of the black hole, that is, when $c_1 = M$. Then $\mu_4 = \mu_2$ and $\mu_5 = \mu_1$. From Eqs.

133

(E.13), (E.14) and (E.8), we get following conditions:

$$\sigma > 0 \rightarrow \sqrt{\tilde{r}^2 + \tilde{c}_2^2} \left[(\tilde{r}^2 + \tilde{a}^2)^{3/2} (\sqrt{1 + \tilde{r}^2} - 1) - \alpha \tilde{r}^2 \sqrt{1 + \tilde{r}^2} \right]$$

$$+ 2\lambda (\tilde{r}^2 + \tilde{a}^2)^{3/2} \left(\sqrt{\tilde{r}^2 + \tilde{c}_2^2} - \tilde{c}_2 \sqrt{1 + \tilde{r}^2} \right) > 0, \tag{E.31}$$

$$p > 0 \rightarrow \sqrt{\tilde{r}^2 + \tilde{c}_2^2} \left[\alpha \tilde{r}^2 \sqrt{1 + \tilde{r}^2} + (\tilde{r}^2 + \tilde{a}^2)^{3/2} \right]$$

$$- 2\lambda (\tilde{r}^2 + \tilde{a}^2)^{3/2} \left(\sqrt{\tilde{r}^2 + \tilde{c}_2^2} - \tilde{c}_2 \sqrt{1 + \tilde{r}^2} \right) > 0, \tag{E.32}$$

$$V^2 < 1 \rightarrow \sqrt{\tilde{r}^2 + \tilde{c}_2^2} \left[2\alpha \tilde{r}^2 \sqrt{1 + \tilde{r}^2} + (\tilde{r}^2 + \tilde{a}^2)^{3/2} (2 - \sqrt{1 + \tilde{r}^2}) \right]$$

$$- 4\lambda (\tilde{r}^2 + \tilde{a}^2)^{3/2} \left(\sqrt{\tilde{r}^2 + \tilde{c}_2^2} - \tilde{c}_2 \sqrt{1 + \tilde{r}^2} \right) < 0, \tag{E.33}$$

where $\tilde{r} = r/M$, $\tilde{a} = a/M$, $\tilde{c}_2 = c_2/M$, $\alpha = m/M$, $\beta = \mathcal{M}/M$ and $\lambda = \mathcal{M}/(c_2 - M) = \beta/(\tilde{c}_2 - 1)$. The conditions imposed are that of weak energy ($\sigma > 0$), azimuthal pressure ($p > 0$) and sublumial velocity ($V^2 < 1$) of counter-rotation of particles on the disk. For $\tilde{r} \rightarrow \infty$, all three conditions are satisfied. In the regions where $V^2 < 1$, the weak energy condition is always satisfied, as can be seen by inequalities (E.31) and (E.33).

Figure E.2(a)–E.2(c) shows curves of $V^2 = 1$ (dotted curves) and of $hdh/dr = 0$ (solid curves) as function of λ and $\tilde{r}$ for three different values of α. The mass of each rod is kept constant $\beta = 0.5$ and the cut parameter takes values $\tilde{a} = 1$ and $\tilde{a} = 3$ in E.2(a) and E.2(b), respectively. At the right of each dotted curve we have $V^2 < 1$ and the unstable regions of the disk appear between the curves of $hdh/dr = 0$. We note that in general with increasing mass of the disk and smaller length of the rods, the disk becomes more unstable and the regions of superlumial velocity also increase. There is, however, an interval of values for the rod's mass density where the zone of stability is increased, as can be seen in the lower part of the curve $hdh/dr = 0$ for $\alpha = 0.001$ in Fig. E.2(a). This is probably due to the prolate quadrupole moment of the rods, which scale as $\mathcal{M}l^2$, where l is their length. Thus, for larger rods, the effect of prolate deformations may overwhelm the effect of the oblate quadrupole moment of the disk, and increase stability (see [39] for a detailed discussion of the effect of quadrupolar fields on the stability of circular orbits).

Figure E.3(a) and E.3(b) shows again curves of $V^2 = 1$ (dotted curves) and of $hdh/dr = 0$ (solid curves) as function of λ and $\tilde{r}$ for three different values of α, but now the length of each rod is kept constant ($\tilde{c}_2 = 11$) and
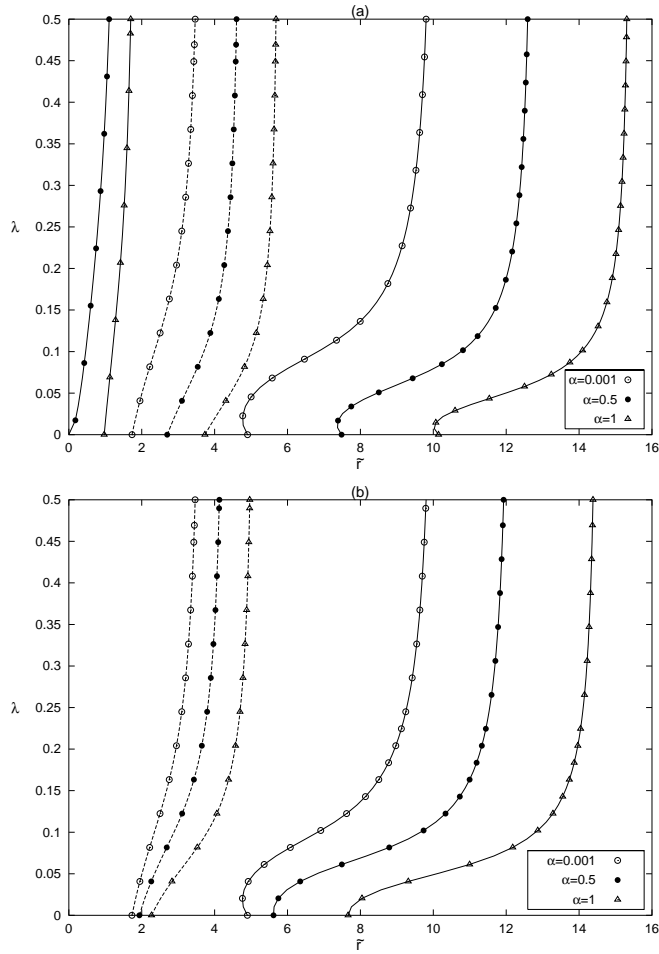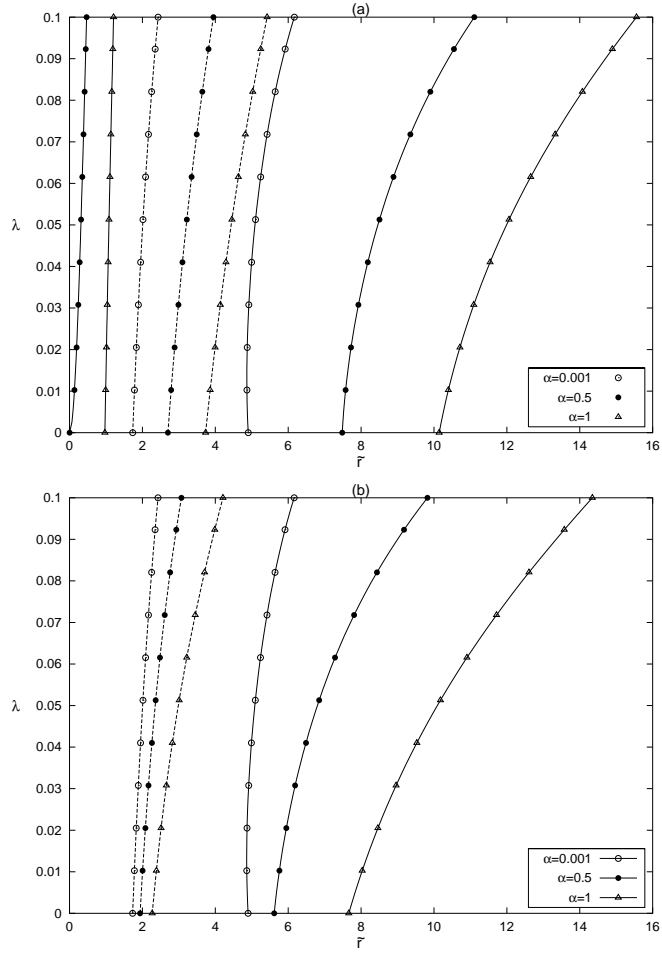
Figure E.2: Curves of $V^2 = 1$ (dotted curves) and of $hdh/dr = 0$ (solid curves) for the Chazy-Curzon disk in presence of a black hole and two rods. We keep the mass of each rod constant $\beta = 0.5$ and vary its mass density λ. In (a)-(b) we take, respectively, $\tilde{a} = 1$ and $\tilde{a} = 3$.

Figure E.3: Curves of $V^2 = 1$ (dotted curves) and of $hdh/dr = 0$ (solid curves) for the Chazy-Curzon disk in presence of a black hole and two rods. We keep the length of each rod constant $\tilde{c}_2 = 11$ and vary its mass density λ (or equivalent, its mass). In (a)-(b) we take, respectively, $\tilde{a} = 1$ and $\tilde{a} = 3$.

the cut parameter takes values $\tilde{a} = 1$ and $\tilde{a} = 3$ in E.3(a) and E.3(b), respectively. With increasing masses of the disk and of the rods, the zones of instability and superlumial velocity of the disk are enhanced. In Fig. E.4(a)–E.4(d) we plot the energy density $\bar{\sigma} = M\sigma$, azimuthal pressure $\bar{p} = Mp$, square of the counterrotating velocity V and specific angular momentum $\bar{h} = Mh$ as functions of $\tilde{r}$ for $\tilde{a} = 3$, $\alpha = 1$, $\tilde{c}_2 = 11$ (constant length) and different values of the rod's linear mass density λ. The curves were computed using Eqs. (E.13)–(E.17), (E.8), (E.9) and (E.30). The expression for the corresponding metric function ν is given in the Appendix. Energy density is lowered for a fixed radius as the rods become more massive, while pressure is slightly increased. Velocity of counter-rotation and specific angular momentum are enhanced by increasing mass of the rods, as can also be deduced from Fig. E.3(b).

E.6   Horizontal and vertical oscillations of the disk

It is interesting to study the disk stability through the computation of horizontal (epicyclic) and vertical oscillation frequencies from perturbations of equatorial circular geodesics. Semerák and Žáček [40] have done such calculations for the superposition of a Schwarzschild black hole with the Lemos-Letelier disk. They found that heavier disks are more stable with respect to horizontal perturbations near their inner rims, whereas they are less stable with respect to vertical perturbations. For astrophysical relevance, it is important to determine not only the stability of circular motion on the disk plane, but also stability in the vertical direction.

Using the perturbed equations for equatorial circular geodesics, the epicyclic frequency with respect to infinity ω_h and the vertical oscillation frequency with respect to infinity ω_v for the metric (E.1) are given by (see [40] for a detailed deduction)

$$\omega_h^2 = \frac{e^{2\phi-\nu}}{2 - r\phi_{,r}} \left(\phi_{,rr} + r\phi_{,r}^3 - 3\phi_{,r}^2 + \frac{3}{r}\phi_{,r} \right), \tag{E.34}$$

$$\omega_v^2 = \frac{e^{2\phi-\nu}}{2 - r\phi_{,r}} \left[\phi_{,zz} - 2\phi_z^2(1 - r\phi_{,r}) \right]. \tag{E.35}$$

In Eq. (E.35) the function ϕ_z is obtained from the limit $\lim_{z\to 0^{\pm}} \phi_z$ and $\phi_{,zz}$ follows from Eq. (E.2a). Stable horizontal and vertical orbits are only possible where $\omega_h^2 > 0$ and $\omega_v^2 > 0$, respectively. Note that condition $\omega_h^2 > 0$ is equivalent to condition (E.10) which follows from Rayleigh stability criteria.
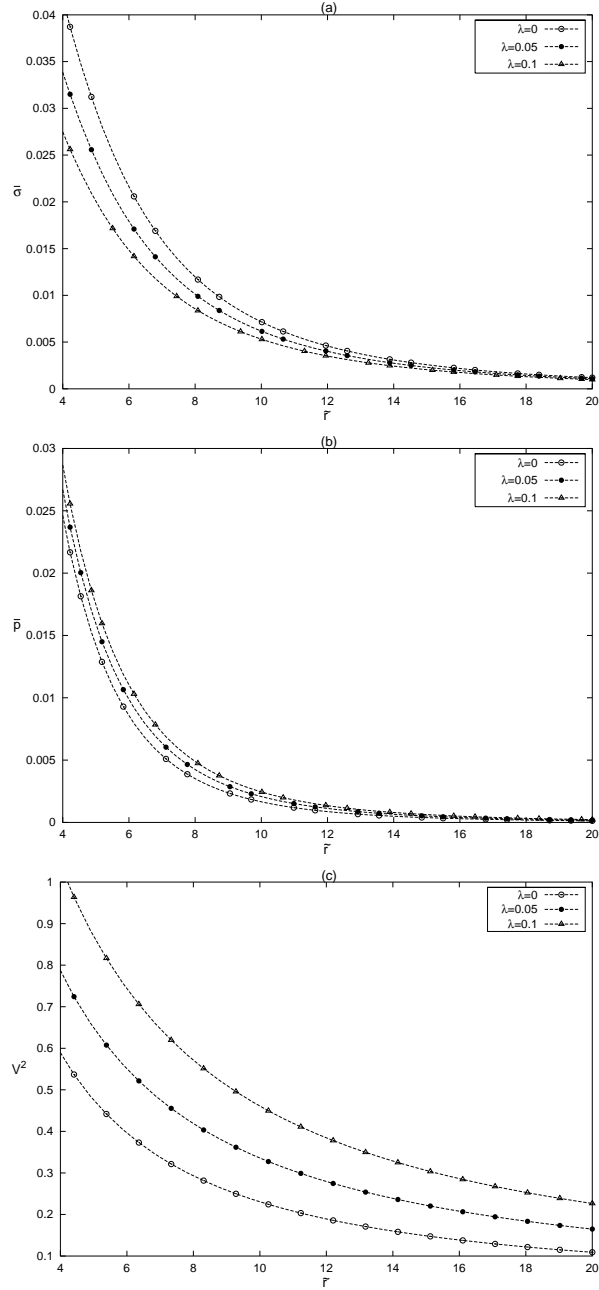
137

Figure E.4: (a) Energy density $\bar{\sigma}$, (b) azimuthal pressure $\bar{p}$, (c) counter-rotating velocity V^2 as functions of $\tilde{r}$ for $\alpha = 1$, $\tilde{a} = 3$, $\tilde{c}_2 = 11$ and three different values for the rod's mass density λ.
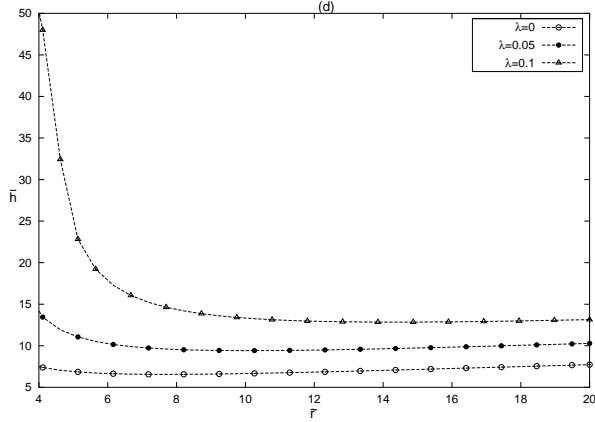
138

Figure E.4(d): Specific angular momentum $\bar{h}$ as function of $\tilde{r}$ for $\alpha = 1$, $\tilde{a} = 3$, $\tilde{c}_2 = 11$ and three different values for the rod's mass density λ.

We compute first the frequencies for an isolated Chazy-Curzon disk, since is seems that such a calculation has not been done before for this class of disks. In Fig. E.5(a) we plot the epicyclic frequency as functions of radius r/m and cut parameter a/m. For $a/m > 1.015$ the disks always are stable and the epicyclic frequency is lowered for less relativistic disks. Highly relativistic disks (curve with $a/m = 0.8$ for example) develop annular regions of instability. The curves of vertical oscillation frequencies are depicted in Fig. E.5(b). We note that in this case highly relativistic disks are more stable in the vertical direction. In Eq. (E.35) the term with ϕ_z is small compared to $\phi_{,zz}$, thus if we consider only

$$\phi_{,zz} = \frac{2m}{(r^2 + a^2)^{5/2}}(r^2 - 2a^2), \tag{E.36}$$

we note that vertical oscillations are zero at $r = a\sqrt{2}$, so the regions of vertical stability are enlarged as the cut parameter a is decreased.

Now we consider the superposition of a Curzon disk and a black hole *without* rods. Figure E.6 shows curves of (a) horizontal $\bar{\omega}_h = M\omega_h$ and (b) vertical $\bar{\omega}_v = M\omega_v$ oscillation frequencies of the disk with $\alpha = 1$ and four different values of the "cut" parameter $\tilde{a}$. Now we always have regions of horizontal instability that begin at the innermost stable circular orbit and decrease for less relativistic disks. With respect to vertical oscillations, it is seen from Fig. E.6(b) that there are no regions of vertical instabilities. Thus one can conclude that the black hole desestabilizes the Curzon disk in the horizontal direction, whereas the opposite is true for the vertical direction.
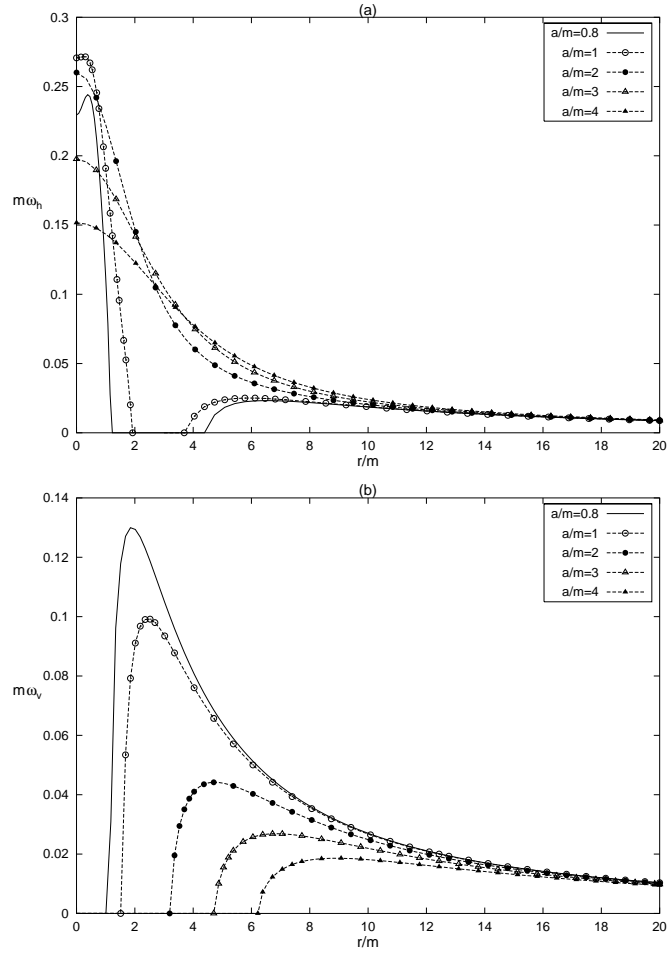
Figure E.5: Radial profiles of (a) the epicyclic frequency $m\omega_h$ and (b) the vertical oscillation frequency $m\omega_v$ for an isolated Chazy-Curzon disk.
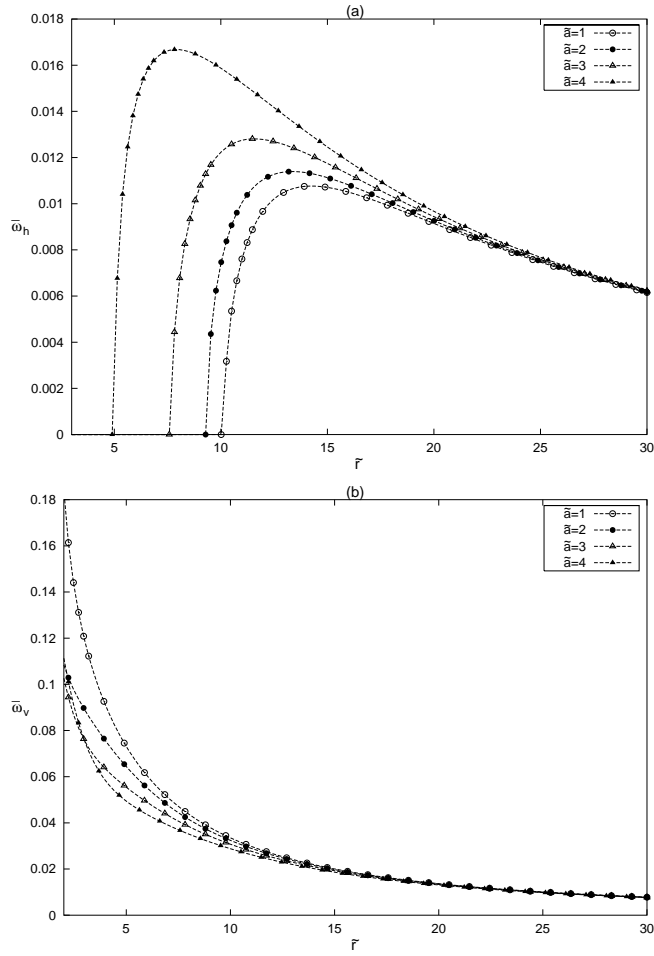
Figure E.6: Radial profiles of (a) horizontal and (b) vertical oscillation frequencies of Chazy-Curzon disk with a black hole without rods. Parameters: $\alpha = 1$, $\tilde{a} = 1$, 2, 3 and 4.
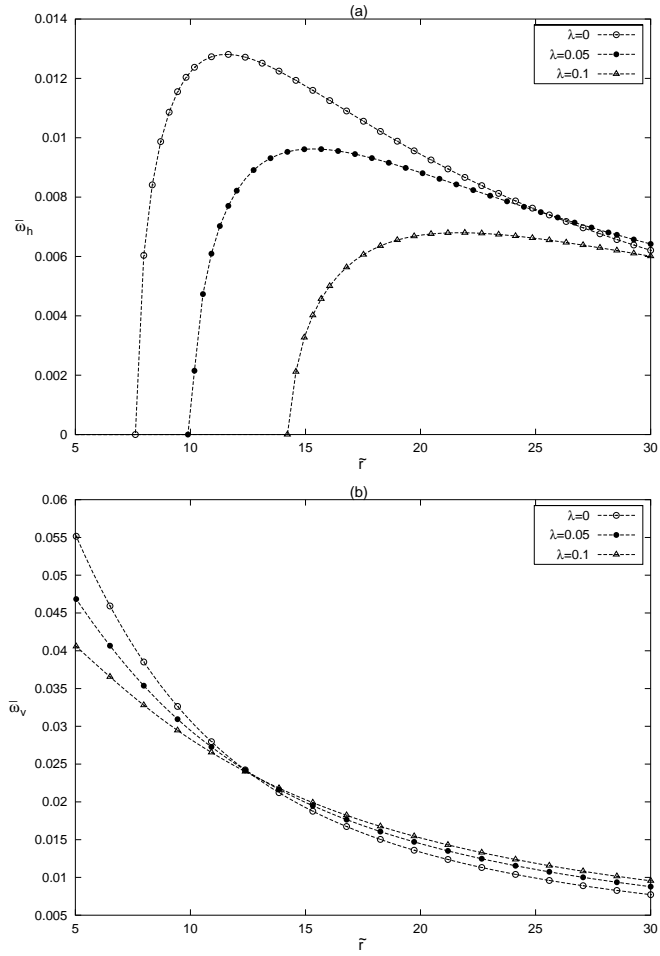
Figure E.7: Radial profiles of (a) horizontal and (b) vertical oscillation frequencies of Chazy-Curzon disk with black hole and rods. Parameters are $\tilde{c}_2 = 11$, $\alpha = 1$, $\tilde{a} = 3$, $\lambda = 0$, 0.05 and 0.1.

In Fig. E.7(a) and E.7(b) we graph again $\bar{\omega}_h = M\omega_h$ and $\bar{\omega}_v = M\omega_v$, respectively, for the Chazy-Curzon disk with black hole and rods, with their length fixed and vary the linear mass density λ. As expected from the curves of Fig. E.3(b), the more massive the rods, the larger are the disk's unstable regions in the horizontal direction. The rods also tend to lower the vertical oscillation frequencies near the disk's center, but unstable regions do not appear.

E.7 Geodesic orbits

In the previous section perturbations of equatorial circular geodesics were used to discuss disk stability for the system disk + black hole + rods. Now we solve numerically the geodesic equations of motion

$$\ddot{x}^\mu + \Gamma^\mu_{\alpha\beta}\dot{x}^\alpha\dot{x}^\beta = 0, \tag{E.37}$$

for metric Eq. (E.1), where $\Gamma^\mu_{\alpha\beta}$ are the Christoffel symbols and the dot denote differentiation with respect to the proper time. Defining the orthonormal tetrad $\{V^a, W^a, Y^a, Z^a\}$ where

$$V^a = e^{-\phi/2}(1,0,0,0), \tag{E.38a}$$

$$W^a = e^{(\phi-\nu)/2}(0,1,0,0), \tag{E.38b}$$

$$Y^a = e^{(\phi-\nu)/2}(0,0,1,0), \tag{E.38c}$$

$$Z^a = \frac{e^{\phi/2}}{r}(0,0,0,1), \tag{E.38d}$$

the tetrad components of the four-velocity v^a read

$$v^a = \gamma(1, v\sin\psi\cos\chi, v\sin\psi\sin\chi, v\cos\psi), \tag{E.39}$$

with $\gamma = 1/\sqrt{1-v^2}$. The specific energy and angular momentum of the test particle are

$$\mathcal{E} = e^\phi\dot{t} = e^{\phi/2}\gamma, \tag{E.40}$$

$$h = r^2 e^{-\phi}\dot{\varphi} = re^{-\phi/2}\gamma v\cos\psi. \tag{E.41}$$

As initial conditions we take a position at radius r_0 on the disk's plane and components of the four-velocity $v_0^a = \gamma(1, 0, v_0\sin\psi, v_0\cos\psi)$, where v_0 is equal to the tangential velocity of circular orbits at radius r_0. We choose initial radii such that the energy is slightly higher than the escape energy.

143

Figure E.8(a) and E.8(b) shows the orbits of particles in the presence of the black hole and Curzon disk without rods. The parameters are $\alpha = 1$, $\tilde{a} = 3$, $\tilde{r}_0 = 3.9$, $\mathcal{E} \approx 1.01$ and different initial angles ψ. Figure E.8(a) is a projection of the orbits on the $x - z$ plane. The coordinates have been transformed from Weyl to Schwarzschild coordinates $(t, \mathsf{r}, \theta, \varphi)$ via the relations

$$r = \sqrt{\mathsf{r}(\mathsf{r} - 2M)} \sin \theta, \qquad z = (\mathsf{r} - M) \cos \theta, \qquad \text{(E.42)}$$

and then to $x = \mathsf{r} \sin \theta \cos \varphi$, $y = \mathsf{r} \sin \theta \sin \varphi$ and $z = \mathsf{r} \cos \theta$.

In Fig. E.9(a)–E.9(d) we have computed some orbits now with the rods. The parameters are $\alpha = 1$, $\tilde{a} = 3$, $\tilde{r}_0 = 7.43$, $\lambda = 0.1$, $\tilde{c}_2 = 11$, $\mathcal{E} \approx 1.01$ and different initial angles ψ. The orbit with $\psi = 89^o$ has been placed in a separate graph for better visualization. For low initial angles, the rods have little effect on the trajectories, but this is not true as the particles approach the z axis. The orbit in Fig. E.9(c) and E.9(d) even suggests that we can expect chaotic behaviour for orbits that pass very near the rods. In fact, it has been shown [41] that prolate quadrupole deformations can introduce chaotic motion of geodesic test particles. In the oblate case, only regular motion was found.

E.8   Discussion

We presented a very simplified, although exact, general relativistic model of an active galactic nuclei based on a superposition of a Schwarzschild black hole, a Chazy-Curzon disk and two rods placed on the symmetry axis, representing jets. We found that the presence of the rods enhances the disk regions with superlumial velocities. Using an extension of Rayleigh criteria of stability, it was found that in general the rods also increase the regions of instability, but when the rods are large and the disk's mass is low they can contribute to stabilize the disk. Also disk stability in the vertical direction was studied through perturbation of circular geodesics. The rods contribute to lower the vertical oscillation frequencies near the disk's center. Some geodesic orbits calculated numerically for the system black hole + disk + rods show the possibility of chaotic trajectories near the rods.

The model here presented should be viewed as a first approach. As was stated in the introduction, more realistic models of active galactic nuclei should incorporate rotation and electromagnetic fields. However, the analysis of such a model would not be trivial, because of the large number of free parameters involved.
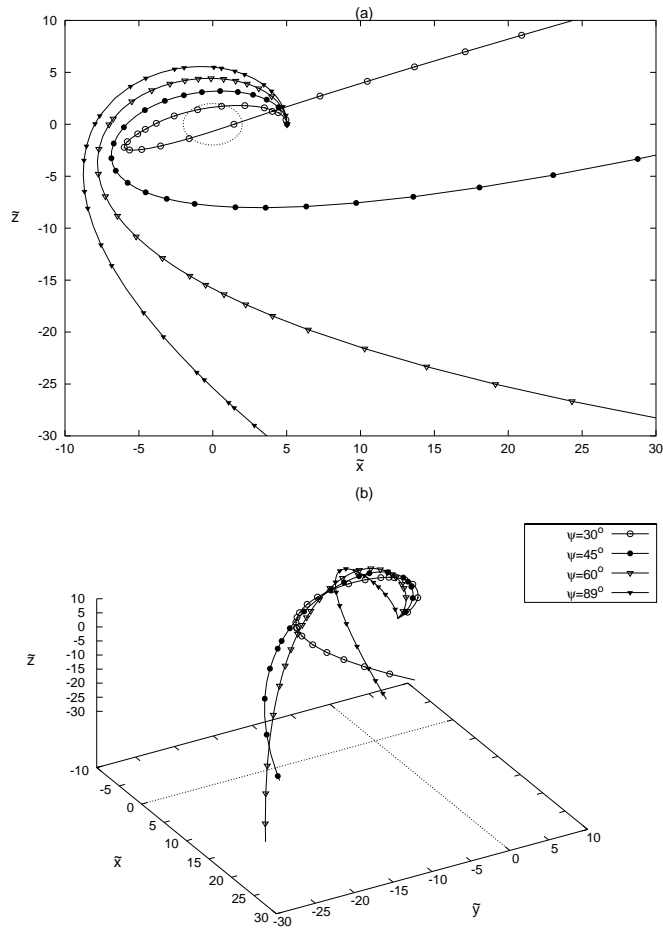
Figure E.8: Geodesic orbits for the superposition Curzon disk + black hole without rods. Parameters: $\alpha = 1$, $\tilde{a} = 3$, $\mathcal{E} \approx 1.01$, $\tilde{r}_0 = 3.9$. (a) Projection on the $x - z$ plane of the curves in (b).

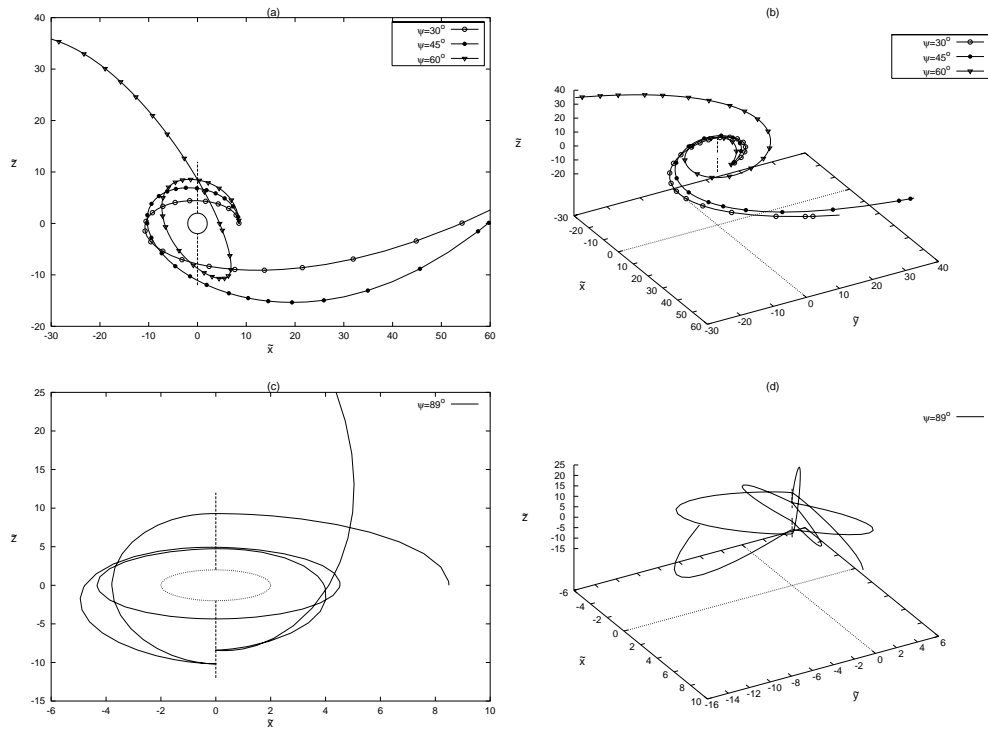Figure E.9: Geodesic orbits for the superposition Curzon disk + black hole with rods. Parameters: $\alpha = 1$, $\tilde{a} = 3$, $\lambda = 0.1$, $\tilde{c}_2 = 11$, $\mathcal{E} \approx 1.01$ $\tilde{r}_0 = 7.43$. The curve for $\psi = 89^o$ is displayed in (c) and (d) for better visualization.

Appendix

The metric function Eq. (E.2b) for the superposition of a black hole, two rods and a disk generated from Chazy-Curzon solution can be calculated as follows. We rewrite potential Eq. (E.30) as

$$\phi = \phi_{R1} + \phi_{BH} + \phi_{R2} + \phi_D^+, \qquad (E.43)$$

where

$$\phi_{R1} = -2\lambda \ln\left(\frac{\mu_3}{\mu_4}\right), \qquad \phi_{BH} = -2\lambda \ln\left(\frac{\mu_1}{\mu_2}\right)$$

$$\phi_{R2} = -2\lambda \ln\left(\frac{\mu_5}{\mu_6}\right), \qquad \phi_D^+ = \frac{m}{\epsilon} \ln\left(\frac{\mu_7}{\mu_8}\right), \qquad (E.44)$$

with $\mu_7 = -a - \epsilon - z + \sqrt{r^2 + (-a - \epsilon - z)^2}$ and $\mu_8 = -a + \epsilon - z + \sqrt{r^2 + (-a + \epsilon - z)^2}$. In the limit $\epsilon \to 0$ expression for ϕ_D^+ reduces to the Chazy-Curzon disk Eq. (E.29) on $z > 0$. Thus all terms can be expressed as μ potentials. Using repeatedly properties (E.24)–(E.26) we get

$$\begin{aligned}
\nu[\phi_{R1} + \phi_{BH} + \phi_{R2} + \phi_D^+] &= \nu[\phi_{R1}] + \nu[\phi_{BH}] + \nu[\phi_{R2}] + \nu[\phi_D^+] \\
&+ 2\nu[\phi_{R1}, \phi_{BH}] + 2\nu[\phi_{R1}, \phi_{R2}] + 2\nu[\phi_{R1}, \phi_D^+] + 2\nu[\phi_{BH}, \phi_{R2}] \\
&+ 2\nu[\phi_{BH}, \phi_D^+] + 2\nu[\phi_{R2}, \phi_D^+], \qquad (E.45)
\end{aligned}$$

with

$$\nu[\phi_{R1}] = 4\lambda^2 \ln\left[\frac{(r^2 + \mu_3\mu_4)^2}{(r^2 + \mu_3^2)(r^2 + \mu_4^2)}\right], \quad \nu[\phi_{BH}] = \ln\left[\frac{(r^2 + \mu_1\mu_2)^2}{(r^2 + \mu_1^2)(r^2 + \mu_2^2)}\right],$$

$$\nu[\phi_{R2}] = 4\lambda^2 \ln\left[\frac{(r^2 + \mu_5\mu_6)^2}{(r^2 + \mu_5^2)(r^2 + \mu_6^2)}\right], \quad \nu[\phi_D^+] = -\frac{m^2 r^2}{[r^2 + (z+a)^2]^2},$$

$$\nu[\phi_{R1}, \phi_{BH}] = 2\lambda \ln\left[\frac{(r^2 + \mu_1\mu_3)(r^2 + \mu_2\mu_4)}{(r^2 + \mu_1\mu_4)(r^2 + \mu_2\mu_3)}\right],$$

$$\nu[\phi_{R1}, \phi_{R2}] = 4\lambda^2 \ln\left[\frac{(r^2 + \mu_3\mu_6)(r^2 + \mu_4\mu_5)}{(r^2 + \mu_3\mu_5)(r^2 + \mu_4\mu_6)}\right],$$

$$\nu[\phi_{R1}, \phi_D^+] = \frac{2\lambda m}{(a + c_1)(a + c_2)\sqrt{r^2 + (a+z)^2}}\left[(a + c_2)\sqrt{r^2 + (c_1 - z)^2}\right.$$

$$\left. -(a + c_1)\sqrt{r^2 + (c_2 - z)^2} + (c_1 - c_2)\sqrt{r^2 + (a+z)^2}\right],$$

$$\nu[\phi_{BH}, \phi_{R2}] = 2\lambda \ln\left[\frac{(r^2 + \mu_1\mu_5)(r^2 + \mu_2\mu_6)}{(r^2 + \mu_1\mu_6)(r^2 + \mu_2\mu_5)}\right],$$

$$\nu[\phi_{BH}, \phi_D^+] = \frac{m}{(a^2 - M^2)\sqrt{r^2 + (a+z)^2}} \left[(a+M)\sqrt{r^2 + (M+z)^2} \right.$$
$$\left. -(a-M)\sqrt{r^2 + (M-z)^2} - 2M\sqrt{r^2 + (a+z)^2} \right],$$
$$\nu[\phi_{R2}, \phi_D^+] = \frac{2\lambda m}{(a-c_1)(a-c_2)\sqrt{r^2 + (a+z)^2}} \left[(c_2 - a)\sqrt{r^2 + (c_1 + z)^2} \right.$$
$$\left. -(c_1 - a)\sqrt{r^2 + (c_2 + z)^2} + (c_1 - c_2)\sqrt{r^2 + (a+z)^2} \right].$$

In the particular case $c_1 = M$ ($\mu_4 = \mu_2$ and $\mu_5 = \mu_1$), and on $z = 0$, Eq. (E.45) simplifies to

$$\nu[\phi_{R1} + \phi_{BH} + \phi_{R2} + \phi_D^+] =$$
$$\ln \left[\frac{r^{16\lambda^2 - 8\lambda + 2}(r^2 + \mu_1\mu_6)^{8\lambda^2 - 4\lambda}(r^2 + \mu_2\mu_3)^{8\lambda^2 - 4\lambda}}{(r^2 + c_2^2)^{4\lambda^2}(r^2 + M^2)^{4\lambda^2 - 4\lambda + 1}(r^2 + \mu_1\mu_3)^{8\lambda^2 - 4\lambda}(r^2 + \mu_2\mu_6)^{8\lambda^2 - 4\lambda}} \right]$$
$$- \frac{m^2 r^2}{(r^2 + a^2)^2} + \frac{8\lambda m}{(a^2 - c_2^2)(a^2 - M^2)\sqrt{r^2 + a^2}} \left[c_2(a^2 - M^2)\sqrt{r^2 + c_2^2} \right.$$
$$\left. -M(a^2 - c_2^2)\sqrt{r^2 + M^2} + (M - c_2)(a^2 + Mc_2)\sqrt{r^2 + a^2} \right]$$
$$+ 4mM \frac{(\sqrt{r^2 + M^2} - \sqrt{r^2 + a^2})}{(a^2 - M^2)\sqrt{r^2 + a^2}}. \tag{E.46}$$

Acknowledgments

Bibliography

[1] *Jets from Stars and Galactic Nuclei*, edited by W. Kundt (Springer, New York, 1996).

[2] J. H. Krolik, *Active Galactic Nuclei: from the Central Black Hole to the Galactic Environment* (Princeton University Press, Princeton, New Jersey, 1999).

[3] R. D. Blandford, Prog. Theor. Phys. Suppl. **143**, 182 (2001).

[4] W. A. Bonnor and A. Sackfield, Comm. Math. Phys. **8**, 338 (1968).

[5] T. Morgan and L. Morgan, Phys. Rev. **183**, 1097 (1969).

[6] L. Morgan and T. Morgan, Phys. Rev. D **2**, 2756 (1970).

[7] D. Lynden-Bell and S. Pineault, Mon. Not. R. Astron. Soc. **185**, 679 (1978).

[8] P. S. Letelier and S. R. Oliveira, J. Math. Phys. **28**, 165 (1987).

[9] J. P. S. Lemos, Classical Quantum Gravity **6**, 1219 (1989).

[10] J. P. S. Lemos and P. S. Letelier, Classical Quantum Gravity **10**, L75 (1993).

[11] J. Bičák, D. Lynden-Bell and J. Katz, Phys. Rev. D **47**, 4334 (1993).

[12] J. Bičák, D. Lynden-Bell and C. Pichon, Mon. Not. R. Astron. Soc. **265**, 126 (1993).

[13] J. P. S. Lemos and P. S. Letelier, Phys. Rev. D **49**, 5135 (1994).

[14] J. P. S. Lemos and P. S. Letelier, Int. J. Mod. Phys. D **5**, 53 (1996).

[15] G. González and O. A. Espitia, Phys. Rev. D **68**, 104028 (2003).

[16] G. García and G. González, Phys. Rev. D **69**, 124002 (2004).

[17] J. Bičák and T. Ledvinka, Phys. Rev. Lett. **71**, 1669 (1993).

[18] G. González and P. S. Letelier, Phys. Rev. D **62**, 064025 (2000).

[19] D. Vogt and P. S. Letelier, Phys. Rev. D **68**, 084010 (2003).

[20] D. Vogt and P. S. Letelier, "Exact Relativistic Static Charged Perfect Fluid Disks" (to be published).

[21] G. González and P. S. Letelier, Phys. Rev. D **69**, 044013 (2004).

[22] C. Klein, Classical Quantum Gravity **14**, 2267 (1997).

[23] G. Neugebauer and R. Meinel, Phys. Rev. Lett. **75**, 3046 (1995).

[24] C. Klein and O. Richter, Phys. Rev. Lett. **83**, 2884 (1999).

[25] C. Klein, Phys. Rev. D **63**, 064033 (2001).

[26] J. Frauendiener and C. Klein, Phys. Rev. D **63**, 084025 (2001).

[27] C. Klein, Phys. Rev. D **65**, 084029 (2002).

[28] C. Klein, Phys. Rev. D **68**, 027501 (2003).

[29] C. Klein, Ann. Phys. **12**, 599 (2003).

[30] T. Zellerin and O. Semerák, Classical Quantum Gravity **17**, 5103 (2000).

[31] V. Karas, J. M. Huré and O. Semerák, Classical Quantum Gravity **21**, R1 (2004).

[32] H. Weyl, Ann. Phys. **54**, 117 (1917).

[33] H. Weyl, Ann. Phys. **59**, 185 (1919).

[34] G. G. Kuzmin, Astron. Zh. **33**, 27 (1956).

[35] J. P. S. Lemos, Mon. Not. R. Astron. Soc. **230**, 451 (1988).

[36] Lord Rayleigh, Proc. R. Soc. London A **93**, 148 (1917); see also L. D. Landau and E. M. Lifshitz, *Fluid Mechanics* (Pergamon Press, Oxford, 1987), 2nd ed., §27.

[37] V. A. Belinsky and V. E. Zakharov, Zh. Eksp. Teor. Fiz. **75**, 1955 (1978) [Sov. Phys. JETP **48**, 985 (1978)].

[38] V. A. Belinsky and V. E. Zakharov, Zh. Eksp. Teor. Fiz. **77**, 3 (1979) [Sov. Phys. JETP **50**, 1 (1979)].

[39] P. S. Letelier, Phys. Rev. D **68**, 104002 (2003).

[40] O. Semerák and M. Žáček, Publ. Astron. Soc. Jpn. **52**, 1067 (2000).

[41] E. Gueron and P. S. Letelier, Phys. Rev. E **63**, 035201(R) (2001); **66**, 046611 (2002).

Apêndice F

New models of general relativistic static thick disks

Abstract

New families of exact general relativistic thick disks are constructed using the "displace, cut, fill and reflect" method. A class of functions used to fill the disks is derived imposing conditions on the first and second derivatives to generate physically acceptable disks. The analysis of the function's curvature further restrict the ranges of the free parameters that allow physically acceptable disks. Then this class of functions together with the Schwarzschild metric is employed to construct thick disks in isotropic, Weyl and Schwarzschild canonical coordinates. In these last coordinates an additional function must be added to one of the metric coefficients to generate exact disks. Disks in isotropic and Weyl coordinates satisfy all energy conditions, but those in Schwarzschild canonical coordinates do not satisfy the dominant energy condition.

151

F.1 Introduction

Exact solutions of Einstein's field equations with axial symmetry play an important role in the astrophysical applications of general relativity, since the natural shape of an isolated self-gravitating fluid is axially symmetric. In particular, disklike configurations of matter are of great interest, since they can be used as models of galaxies and accretion disks.

Solutions for static thin disks without radial pressure were first studied by Bonnor and Sackfield [1], and Morgan and Morgan [2], and with radial pressure by Morgan and Morgan [3]. Several classes of exact solutions of the Einstein field equations corresponding to static thin disks with or without radial pressure have been obtained by different authors [4–13]. Thin rotating disks that can be considered as a source of the Kerr metric were presented in [14], while rotating disks with heat flow were studied in [15]. Also thin disks with radial tension [16], magnetic fields [17] and magnetic and electric fields [18] were considered. The nonlinear superposition of a disk and a black hole was first obtained by Lemos and Letelier [7]. Perfect fluid disks with halos [19] and charged perfect fluid disks [20] were also studied. For a survey on self-gravitating relativistic thin disks, see for instance [21].

In the works cited above, an inverse style method was used to solve the Einstein equations, i. e., the energy-momentum tensor is computed from the metric representing the disk. Another approach to generate disks is by solving the Einstein equations given a source (energy-momentum tensor). This has been used to generate several exact solutions of thin disks [22, 24–29].

Even though in a first approximation thin disks can be used as useful models of galaxies, in a more realistic model the thickness of the disk should be considered. The addition of a new dimension may change the dynamical properties of the disk source, e. g., its stability. Thick static relativistic disks in various coordinate systems were presented in [30]. The method used to construct the thick disks is a generalization of the well known "displace, cut and reflect" method used to generate thin disks from vacuum solutions of Einstein equations. This generalization adds a new step and thus can be named "displace, cut, *fill* and reflect" method. In [30] a particular function with properties that will be discussed later was used to "fill" the disks.

In this article we present a class of the functions mentioned above and use them together with the Schwarzschild metric to construct more models of exact relativistic thick disks. In Sec. F.2 we discuss briefly the main idea of the displace, cut, fill and reflect method and use the Newtonian Kuzmin-Toomre disk to put constraints on the parameter in the class of

fill functions so that the disks are physically acceptable. Then in Sec. F.3 we take the Schwarzschild solution in isotropic cylindrical coordinates to generate thick disks. These disks have equal radial and azimuthal pressures but are different from vertical pressures. In Sec. F.4 the same procedure is repeated in Weyl coordinates. The resulting disks have radial tensions that have the same modulus as the vertical pressures, azimuthal tensions near the center and azimuthal pressures for larger disk radii. In Sec. F.5 thick disks are constructed in canonical Schwarzschild coordinates, which were not previously studied. Here an additional function must be added in order to generate exact disks. The disks show similar characteristics of those constructed in Weyl coordinates, but radial tensions are different from vertical pressures. Finally, in Sec. F.6 we summarize the main results.

F.2   Newtonian Thick Disks

The method used to construct a thick disk is described in detail in [30] and consists in a modification of the displace, cut and reflect method, due to Kuzmin [31]. The "thickening" is obtained by the introduction of a thick shell after the cut and before the inversion of the space, thus the modified method can be named displace, cut, fill and reflect.

Mathematically the procedure is equivalent to making the transformation $z \rightarrow h(z) + b$, where b is a constant and $h(z)$ an even function of z. In order to generate thick disks with well-defined properties, the function $h(z)$ and its first derivative should be continuous in the region $-a \leq z \leq a$, where $2a$ is the disk thickness. Furthermore, the first and second derivatives of $h(z)$ with respect to z should be chosen such that the mass density of the disk (i) be non-negative everywhere and (ii) be a monotonously decreasing function of r and z. These conditions strongly restrict the possible functional forms for $h(z)$. In the case of Newtonian gravity, the potential $\Phi(r, z)$ satisfies the Laplace equation

$$\Phi_{,rr} + \frac{\Phi_r}{r} + \Phi_{,zz} = 0. \tag{F.1}$$

After we make the transformation $z \rightarrow h(z) + b$, Eq. (F.1) leads to

$$\nabla^2 \Phi = h'' \Phi_{,h} + (h'^2 - 1)\Phi_{,hh}, \tag{F.2}$$

where primes indicate differentiation with respect to z. From Eq. (F.2) we have that, if $|h'| = 1$ and thus $h'' = 0$ when $|z| \geq a$, the mass density

vanishes outside the disk. For $|z| \leq a$, we get from the Poisson equation

$$\rho = \frac{1}{4\pi G}\left[h''\Phi_{,h} + (h'^2 - 1)\Phi_{,hh}\right].$$ (F.3)

If we start from an even and positive polynomial for $h''(z)$, we arrive at a class of functions $h(z)$ that satisfy all the requirements stated above given by

$$h(z) = \begin{cases} -z + C, & z \leq -a, \\ Az^2 + Bz^{2n+2}, & -a \leq z \leq a, \\ z + C, & z \geq a, \end{cases}$$ (F.4)

with

$$A = \frac{2n+1-ac}{4na}, \quad B = \frac{ac-1}{4n(n+1)a^{2n+1}}, \quad C = -\frac{a(2n+1+ac)}{4(n+1)}.$$

Here $n = 1, 2, \ldots$, and c is the jump of the second derivative on $z = \pm a$. The special case when $ac = 1$ was considered in [30]. As an example we consider the gravitational potential of a mass point in cylindrical coordinates

$$\Phi = -\frac{Gm}{\sqrt{r^2 + z^2}}.$$ (F.5)

By doing the transformation $z \to h(z) + b$ in the previous potential and using Eq. (F.3), we obtain the mass density

$$\tilde{\rho} = \frac{\tilde{m}}{4\pi}\left[\frac{\tilde{h}''(\tilde{h} + \tilde{b}) + \tilde{h}'^2 - 1}{R^3} + \frac{3(1 - \tilde{h}'^2)(\tilde{h} + \tilde{b})^2}{R^5}\right],$$ (F.6)

with $R^2 = \tilde{r}^2 + (\tilde{h} + \tilde{b})^2$ and the variables and parameters were rescaled in terms of the disk half-thickness: $\tilde{r} = r/a$, $\tilde{h} = h/a$, $\tilde{b} = b/a$, $\tilde{m} = m/a$, $\tilde{\rho} = a^2\rho$ and with $\tilde{c} = c/a$ and $\tilde{z} = z/a$ in Eq. (F.4). The mass density will be positive if

$$\tilde{h}''(\tilde{h} + \tilde{b}) + \tilde{h}'^2 - 1 \geq 0.$$ (F.7)

When $\tilde{z} = 0$, condition (F.7) reduces to

$$\tilde{b}\frac{2n+1-\tilde{c}}{2n} - 1 \geq 0 \to \tilde{b} \geq \frac{2n}{2n+1-\tilde{c}},$$ (F.8)

154

and $\tilde{c} < 2n + 1$ to make $\tilde{b}$ positive. When $\tilde{z} = \pm 1$, (F.7) gives $\tilde{c}(\tilde{h} + \tilde{b}) \geq 0$, or $\tilde{c} \geq 0$. Thus the parameter $\tilde{c}$ is restricted to $0 \leq \tilde{c} < 2n + 1$.

The total mass $\tilde{\mathcal{M}}$ of the disk is easily calculated

$$\tilde{\mathcal{M}} = \int_0^{2\pi} \int_{\tilde{z}=-1}^1 \int_{\tilde{r}=0}^\infty \tilde{\rho}\, \tilde{r}\, \mathrm{d}\tilde{r}\, \mathrm{d}\tilde{z}\, \mathrm{d}\varphi = \tilde{m}, \tag{F.9}$$

thus the disks have finite mass.

In Fig. F.1 we plot the curves of $\tilde{h}(\tilde{z})$ and its first and second derivatives with $n = 1$ for $\tilde{c} = 0$, 0.5, 1 and 2. We also plot the curvature $\tilde{\kappa}$ of $\tilde{h}$, calculated from the expression

$$\tilde{\kappa} = \frac{|\tilde{h}''|}{(1 + \tilde{h}'^2)^{3/2}}. \tag{F.10}$$

Figures F.2 and F.3 show the mass density for a Newtonian thick disk calculated with the function $\tilde{h}(\tilde{z})$ depicted in Fig. F.1(a) and with parameters $\tilde{m} = 1$ and $\tilde{b} = 2$. In Fig. F.4 we plot again $\tilde{h}(\tilde{z})$ with $n = 2$ and the same values for $\tilde{c}$ as in Fig. F.1; and the mass density for a Newtonian disk using this function with parameters $\tilde{m} = 1$ and $\tilde{b} = 2$ is shown in Figs. F.5 and F.6. We note that the mass distribution along $\tilde{r} = 0$ has a similar shape to the curves for the curvature $\tilde{\kappa}$. Above some value of the jump $\tilde{c}$, the maximum of the mass density at $(\tilde{r}, \tilde{z}) = (0,0)$ becomes a local minimum point and two other maximum points appear. This may be interpreted as a split from one into two disklike distributions of matter, a configuration that does not seem to be physically reasonable. Thus, we restrict the interval of values for $\tilde{c}$ such that the mass density has only a central maximum. The critical points of the curvature function are given by

$$\tilde{h}'''(1 + \tilde{h}'^2) - 3h'\tilde{h}''^2 = 0. \tag{F.11}$$

For $n = 1$, this condition leads to $\tilde{z} = 0$ and the roots of

$$7(\tilde{c} - 1)^3 \tilde{z}^6 + 11(3 - \tilde{c})(\tilde{c} - 1)^2 \tilde{z}^4 + 5(3 - \tilde{c})^2(\tilde{c} - 1)\tilde{z}^2$$
$$- 8(\tilde{c} - 1) + (3 - \tilde{c})^3 = 0. \tag{F.12}$$

To have $\tilde{z} = 0$ as only critical point, Eq. (F.12) should not have real roots. A graphical analysis shows that this happens if $\tilde{c} \lesssim 1.46$. For $n = 2$, the polynomial equation in question is

$$55(\tilde{c} - 1)^3 \tilde{z}^{12} + 65(5 - \tilde{c})(\tilde{c} - 1)^2 \tilde{z}^8 + 13(5 - \tilde{c})^2(\tilde{c} - 1)\tilde{z}^4$$
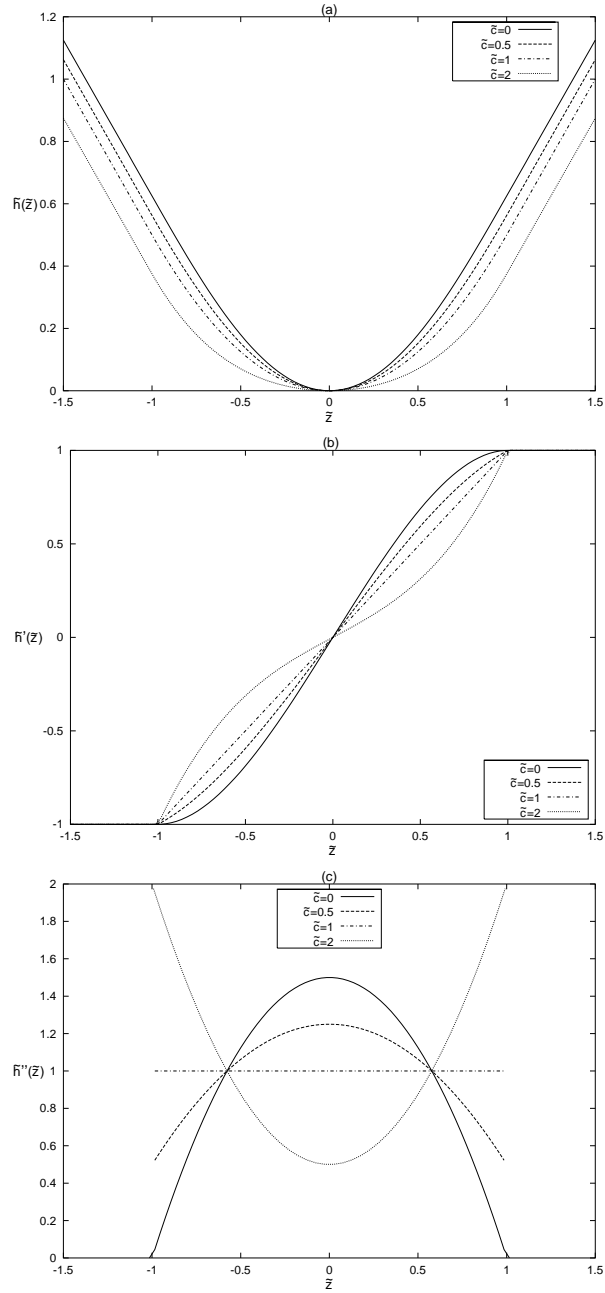$$- 320(\tilde{c} - 1)\tilde{z}^2 + 3(5 - \tilde{c})^3 = 0, \tag{F.13}$$

Figure F.1: (a) The function $\tilde{h}(\tilde{z})$ and (b) its first and (c) second derivatives with $n = 1$ for $\tilde{c} = 0$, 0.5, 1 and 2.
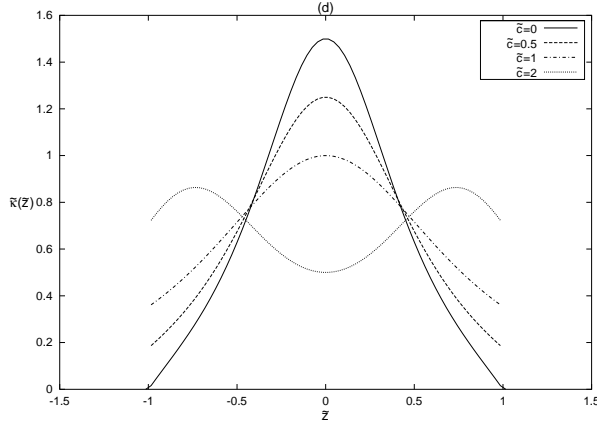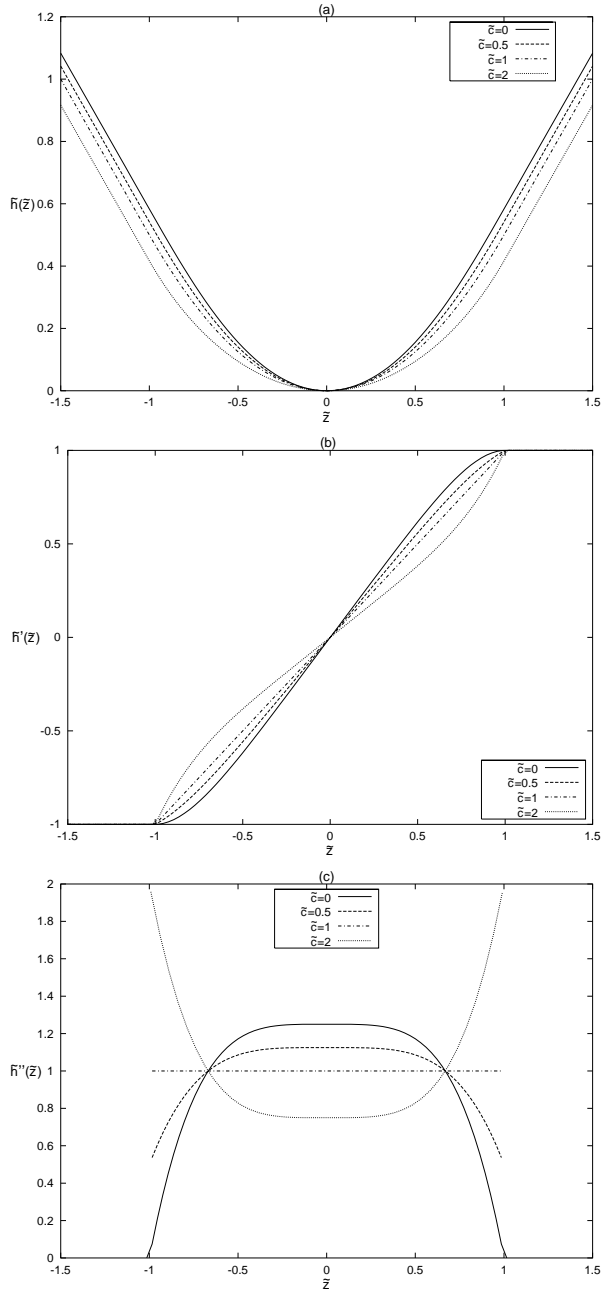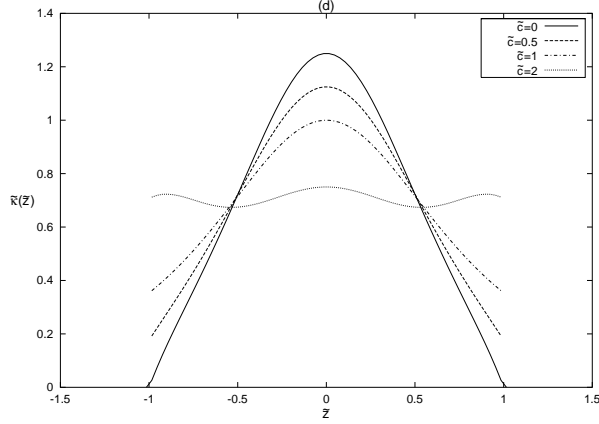
Figure F.1(d): The curvature $\tilde{\kappa}(\tilde{z})$ with $n = 1$ for $\tilde{c} = 0$, 0.5, 1 and 2.

which does not have real roots if $\tilde{c} \lesssim 1.81$.

The level curves in Fig. F.3 and in Figs. F.5 and F.6 also indicate some undesirable features of the disks: some isodensity curves show that the density decreases towards the disk's center. This happens even for $n = 1$, $\tilde{c} = 1$ in Fig. F.3(a) and $n = 2$, $\tilde{c} = 0$ in Fig. F.5(a). Thus, in practice, the ranges for the parameter $\tilde{c}$ that allow physically acceptable disks is even more restricted than those stated above. Using graphical analysis, we find that large values for the "cut" parameter $\tilde{b}$ allow a larger "good" range for the parameter $\tilde{c}$, but in the next sections when the procedure will be applied in general relativity, large values for $\tilde{b}$ will also mean less relativistic disks.

F.3 Thick Disks from the Schwarzschild Metric in Isotropic Coordinates

In cylindrical coordinates (t, r, z, φ) the isotropic metric takes the form

$$\mathrm{d}s^2 = -e^{2\nu}\mathrm{d}t^2 + e^{2\mu}(\mathrm{d}r^2 + \mathrm{d}z^2 + r^2\mathrm{d}\varphi^2), \tag{F.14}$$

where the functions ν and μ depend on r and z. The Schwarzschild solution for metric Eq. (F.14) can be expressed as

$$\nu = \ln\left[\frac{2R - m}{2R + m}\right], \tag{F.15a}$$

$$\mu = 2\ln\left[1 + \frac{m}{2R}\right], \tag{F.15b}$$

157
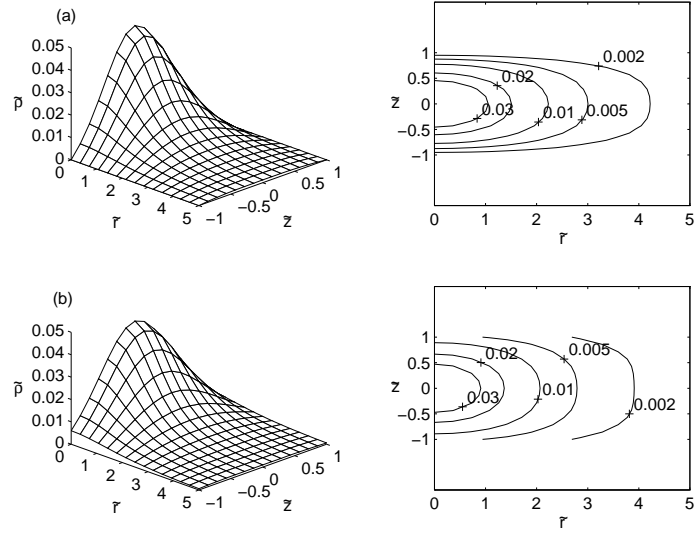
Figure F.2: The mass density Eq. (F.6) for a Newtonian thick disk with parameters $\tilde{m} = 1$, $\tilde{b} = 2$, $n = 1$ and (a) $\tilde{c} = 0$, (b) $\tilde{c} = 0.5$. Some levels curves of the density are displayed on the right graphs.
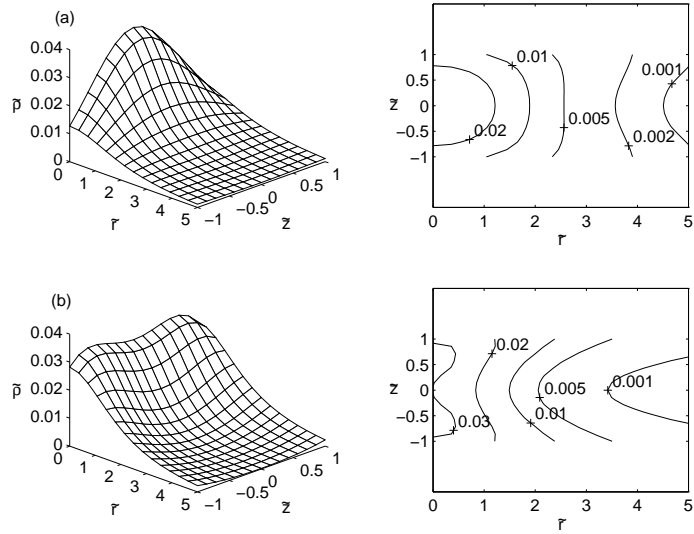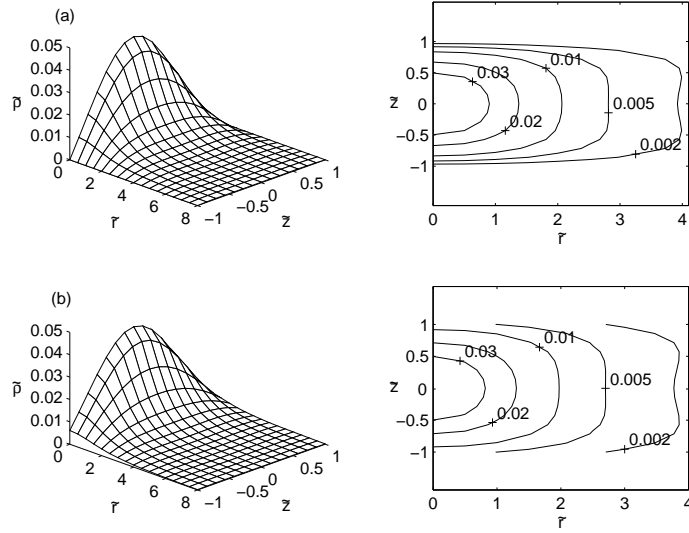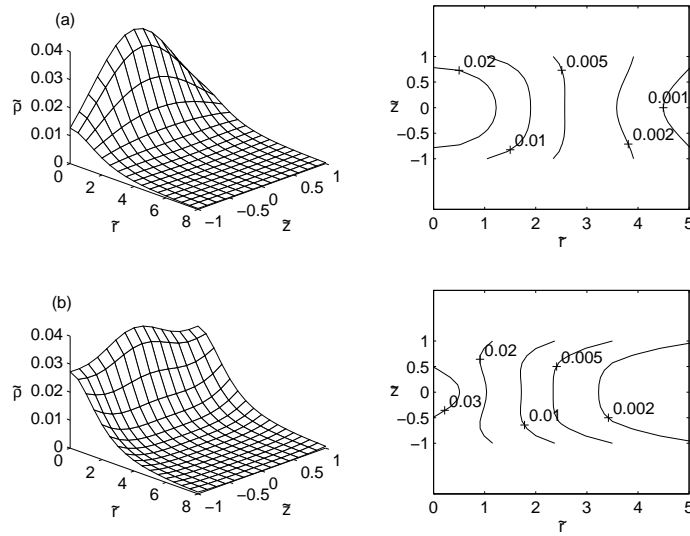

Figure F.3: The mass density Eq. (F.6) for a Newtonian thick disk with parameters $\tilde{m} = 1$, $\tilde{b} = 2$, $n = 1$ and (a) $\tilde{c} = 1$, (b) $\tilde{c} = 2$. Some levels curves of the density are displayed on the right graphs.

Figure F.4: (a) The function $\tilde{h}(\tilde{z})$ and its (b) first and (c) second derivatives with $n = 2$ for $\tilde{c} = 0$, 0.5, 1 and 2.

Figure F.4(d): The curvature $\tilde{\kappa}(\tilde{z})$ with $n = 2$ for $\tilde{c} = 0$, 0.5, 1 and 2.

where $m > 0$ and $R^2 = r^2 + z^2$. The displace, cut, fill and reflect method applied to the above solution is equivalent to put $R^2 = r^2 + (h + b)^2$ where $b > 0$ and $h(z)$ given by Eq. (F.4). The metric function and its derivatives are continuous in the interval $r = [0, +\infty[$ and $|z| < a$, and on $z = \pm a$ their continuity is guaranteed by the continuity of $h(z)$ and $h'(z)$ on $z = \pm a$. For $|z| > a$, Eq. (F.14) satisfies the vacuum Einstein equations. For $|z| < a$, the components of the energy-momentum tensor of the disk are computed from the Einstein equations

$$T_{ab} = R_{ab} - \frac{1}{2}g_{ab}R, \qquad (F.16)$$

where we use units such that $c = 8\pi G = 1$. Defining the orthonormal tetrad $\{V^a, W^a, Y^a, Z^a\}$ with $V^a = (e^{-\nu}, 0, 0, 0)$, $W^a = (0, e^{-\mu}, 0, 0)$, $Y^a = (0, 0, e^{-\mu}, 0)$, $Z^a = (0, 0, 0, e^{-\mu}/r)$ and using Eq. (F.16), the energy-momentum tensor can be written as

$$T_{ab} = \sigma V_a V_b + p_r W_a W_b + p_z Y_a Y_b + p_\varphi Z_a Z_b, \qquad (F.17)$$

where $\sigma = -T_t^t$ is the energy density, $p_r = T_r^r$ is the radial stress, which is equal to the azimuthal stress $p_\varphi = T_\varphi^\varphi$, and $p_z = T_z^z$ is the vertical stress. The effective Newtonian density is given by $\rho = \sigma + p_r + p_z + p_\varphi$. To satisfy the strong energy condition we must have $\rho \geq 0$, the weak energy condition requires $\sigma \geq 0$ and the dominant energy condition requires $|p_r/\sigma| \leq 1$, $|p_z/\sigma| \leq 1$ and $|p_\varphi/\sigma| \leq 1$. Using Eqs. (F.15a) and (F.15b), we obtain [32]

$$\tilde{\sigma} = \frac{64\tilde{m}}{(\tilde{m} + 2\tilde{R})^5}\left[3(\tilde{h} + \tilde{b})^2(1 - \tilde{h}'^2) + \tilde{R}^2[\tilde{h}'^2 - 1 + \tilde{h}''(\tilde{h} + \tilde{b})]\right], \qquad (F.18a)$$

160

Figure F.5: The mass density Eq. (F.6) for a Newtonian thick disk with parameters $\tilde{m} = 1$, $\tilde{b} = 2$, $n = 2$ and (a) $\tilde{c} = 0$, (b) $\tilde{c} = 0.5$. Some levels curves of the density are displayed on the right graphs.
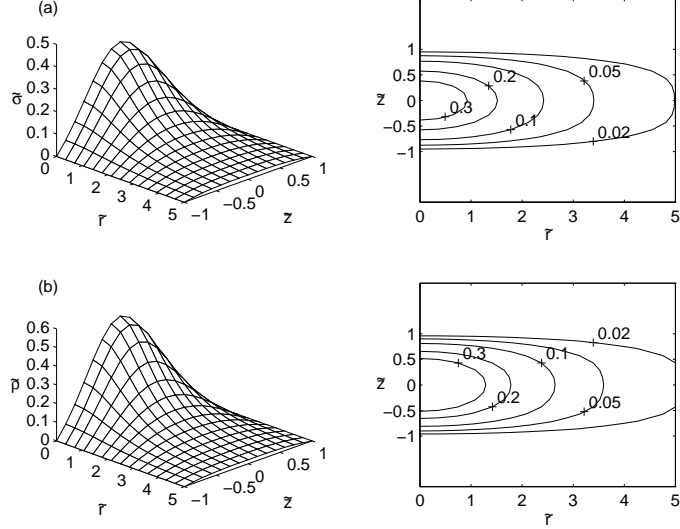

Figure F.6: The mass density Eq. (F.6) for a Newtonian thick disk with parameters $\tilde{m} = 1$, $\tilde{b} = 2$, $n = 2$ and (a) $\tilde{c} = 1$, (b) $\tilde{c} = 2$. Some levels curves of the density are displayed on the right graphs.

Figure F.7: (a) Energy density, (b) effective Newtonian density for a thick disk in isotropic coordinates. Parameters: $\tilde{m} = 1$, $\tilde{b} = 2$, $n = 1$ and $\tilde{c} = 0$.

$$\tilde{\rho} = \frac{128\tilde{m}\tilde{R}}{(\tilde{m} + 2\tilde{R})^5(-\tilde{m} + 2\tilde{R})}\left[3(\tilde{h} + \tilde{b})^2(1 - \tilde{h}'^2) + \tilde{R}^2[\tilde{h}'^2 - 1 + \tilde{h}''(\tilde{h} + \tilde{b})]\right],$$

(F.18b)

$$\tilde{p}_r = \tilde{p}_\varphi = \frac{32\tilde{m}^2}{(\tilde{m} + 2\tilde{R})^5(-\tilde{m} + 2\tilde{R})}\left[2(\tilde{h} + \tilde{b})^2(1 - \tilde{h}'^2)\right.$$
$$\left. + \tilde{R}^2[\tilde{h}'^2 - 1 + \tilde{h}''(\tilde{h} + \tilde{b})]\right],$$

(F.18c)

$$\tilde{p}_z = \frac{64\tilde{m}^2(1 - \tilde{h}'^2)(\tilde{h} + \tilde{b})^2}{(\tilde{m} + 2\tilde{R})^5(-\tilde{m} + 2\tilde{R})},$$

(F.18d)

where $\tilde{\sigma} = a^2\sigma$, $\tilde{\rho} = a^2\rho$, $\tilde{p}_r = a^2 p_r$, $\tilde{p}_z = a^2 p_z$, and the other dimensionless variables were defined in Sec. F.2.

From Eqs. (F.18a), (F.18b) and (F.18c) we can see that, if condition (F.7) is satisfied, we have $\tilde{\sigma} \geq 0$, $\tilde{\rho} \geq 0$ and $\tilde{p}_r = \tilde{p}_\varphi \geq 0$ (pressures). Thus $\tilde{b} \geq 2n/(2n + 1 - \tilde{c})$ and $0 \leq \tilde{c} \leq 2n + 1$. We also have vertical pressure. To ensure nonsingular behaviour of the expressions, we impose that $0 < \tilde{m} < 2\tilde{b}$.

In Figs. F.7 and F.8 we plot the surfaces and level curves for the energy density, effective Newtonian density, radial and azimuthal pressures and vertical pressure for a thick disk with parameters $\tilde{m} = 1$, $\tilde{b} = 2$, $n = 1$ and
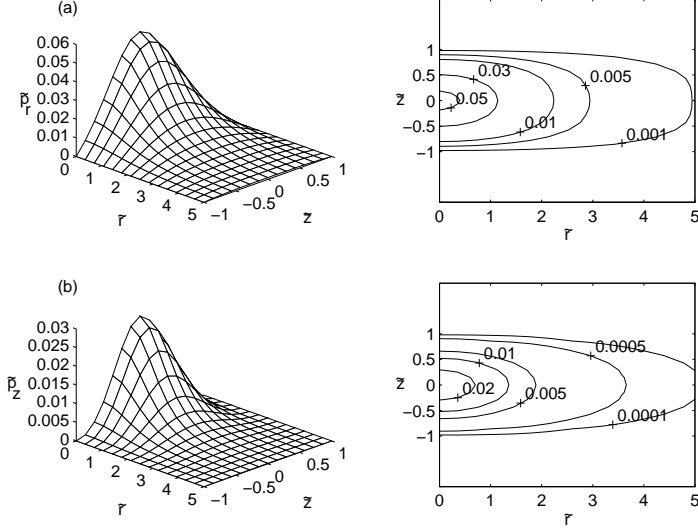
162

Figure F.8: (a) Radial and azimuthal pressures, (b) vertical pressure for a thick disk in isotropic coordinates. Parameters: $\tilde{m} = 1$, $\tilde{b} = 2$, $n = 1$ and $\tilde{c} = 0$.

$\tilde{c} = 0$. The ratio between any pressure and energy density is less than 0.15. Thus all energy conditions are satisfied. The shape of the level curves also show that for these parameters the disk is physically acceptable.

F.4 Thick Disks from the Schwarzschild Metric in Weyl Coordinates

The general metric for a static axially symmetric spacetime in Weyl's canonical coordinates (t, r, z, φ) is given by

$$\mathrm{d}s^2 = -e^{2\Phi}\mathrm{d}t^2 + e^{-2\Phi}\left[e^{2\Lambda}(\mathrm{d}r^2 + \mathrm{d}z^2) + r^2\mathrm{d}\varphi^2\right], \qquad (\text{F.19})$$

where Φ and Λ are functions of r and z. The Einstein vacuum equations for this metric reduce to the Weyl equations [33, 34]

$$\Phi_{,rr} + \frac{\Phi_r}{r} + \Phi_{,zz} = 0, \qquad (\text{F.20a})$$

$$\Lambda_r = r(\Phi_r^2 - \Phi_z^2), \qquad (\text{F.20b})$$

$$\Lambda_z = 2r\Phi_r\Phi_z. \qquad (\text{F.20c})$$

163

In these coordinates, Schwarzschild solution assumes the form [33]

$$\Phi = \frac{1}{2} \ln \left[\frac{R_1 + R_2 - 2m}{R_1 + R_2 + 2m} \right], \tag{F.21a}$$

$$\Lambda = \frac{1}{2} \ln \left[\frac{(R_1 + R_2)^2 - 4m^2}{4R_1 R_2} \right], \tag{F.21b}$$

where $R_1^2 = r^2 + (m+z)^2$, $R_2^2 = r^2 + (-m+z)^2$ and $m > 0$. By applying the transformation $z \rightarrow h(z) + b$ on Eqs. (F.21a) and (F.21b), using Eqs. (F.20a)–(F.20c) and Einstein equations (F.16), the energy-momentum tensor can be written as

$$T_{ab} = \epsilon V_a V_b + p_r W_a W_b + p_z Y_a Y_b + p_\varphi Z_a Z_b, \tag{F.22}$$

with the orthonormal tetrad $\{V^a, W^a, Y^a, Z^a\}$ where $V^a = (e^{-\Phi}, 0, 0, 0)$, $W^a = (0, e^{\Phi - \Lambda}, 0, 0)$, $Y^a = (0, 0, e^{\Phi - \Lambda}, 0)$ and $Z^a = (0, 0, 0, e^{\Phi}/r)$. In Eq. (F.22) $\epsilon = -T_t^t$ is the energy density and $p_r = T_r^r$, $p_z = T_z^z = -T_r^r$, $p_\varphi = T_\varphi^\varphi$ are respectively, the radial, vertical and azimuthal stresses. The effective Newtonian density is given by $\rho = \epsilon + p_\varphi$. The explicit expressions are

$$\tilde{\rho} = \frac{e^{2(\Phi - \Lambda)}}{\tilde{R}_1^3 \tilde{R}_2^3} \left\{ \tilde{h}''(\tilde{R}_1 - \tilde{R}_2) \tilde{R}_1^2 \tilde{R}_2^2 + (1 - \tilde{h}'^2) \left[(\tilde{h} + \tilde{b})(\tilde{R}_1^3 - \tilde{R}_2^3) \right. \right.$$
$$\left. \left. - \tilde{m}(\tilde{R}_1^3 + \tilde{R}_2^3) \right] \right\}, \tag{F.23a}$$

$$\tilde{\epsilon} = \tilde{\rho} \left[1 - \frac{2\tilde{m}\tilde{r}^2(\tilde{R}_1 + \tilde{R}_2)}{\tilde{R}_1 \tilde{R}_2 [(\tilde{R}_1 + \tilde{R}_2)^2 - 4\tilde{m}^2]} \right] + \frac{e^{2(\Phi - \Lambda)}(1 - \tilde{h}'^2)(\tilde{R}_1 - \tilde{R}_2)}{4\tilde{R}_1^4 \tilde{R}_2^4}$$
$$\times \left[(\tilde{R}_1 - \tilde{R}_2) \tilde{R}_1^2 \tilde{R}_2^2 - 2\tilde{r}^2(\tilde{R}_1^3 - \tilde{R}_2^3) \right], \tag{F.23b}$$

$$\tilde{p}_\varphi = \frac{2\tilde{m}\tilde{\rho}\tilde{r}^2(\tilde{R}_1 + \tilde{R}_2)}{\tilde{R}_1 \tilde{R}_2 [(\tilde{R}_1 + \tilde{R}_2)^2 - 4\tilde{m}^2]} + \frac{e^{2(\Phi - \Lambda)}(\tilde{h}'^2 - 1)(\tilde{R}_1 - \tilde{R}_2)}{4\tilde{R}_1^4 \tilde{R}_2^4}$$
$$\times \left[(\tilde{R}_1 - \tilde{R}_2) \tilde{R}_1^2 \tilde{R}_2^2 - 2\tilde{r}^2(\tilde{R}_1^3 - \tilde{R}_2^3) \right], \tag{F.23c}$$

$$\tilde{p}_r = \frac{4\tilde{m}^2 e^{2(\Phi - \Lambda)}(\tilde{h}'^2 - 1)(\tilde{h} + \tilde{b})^2}{\tilde{R}_1^2 \tilde{R}_2^2 (\tilde{R}_1 + \tilde{R}_2)^2}, \tag{F.23d}$$

$$\tilde{p}_z = \frac{4\tilde{m}^2 e^{2(\Phi - \Lambda)}(1 - \tilde{h}'^2)(\tilde{h} + \tilde{b})^2}{\tilde{R}_1^2 \tilde{R}_2^2 (\tilde{R}_1 + \tilde{R}_2)^2}, \tag{F.23e}$$

From Eqs. (F.23d) and (F.23e) we have vertical pressures and radial tensions. From Eq. (F.23b) the condition $\tilde{\epsilon} \geq 0$ on $|\tilde{z}| = 1$ gives

$$\frac{2\tilde{m}\tilde{r}^2(\tilde{R}_1 + \tilde{R}_2)}{\tilde{R}_1 \tilde{R}_2 [(\tilde{R}_1 + \tilde{R}_2)^2 - 4\tilde{m}^2]} \leq 1. \tag{F.24}$$

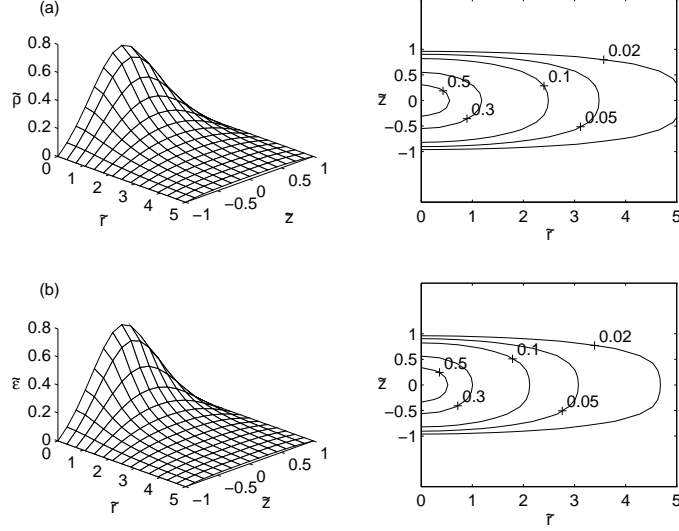Figure F.9: (a) Effective Newtonian density, (b) energy density for a thick disk in Weyl coordinates. Parameters: $\tilde{m} = 1$, $\tilde{b} = 2$, $n = 1$ and $\tilde{c} = 0$.

Since $\tilde{R}_1 > \tilde{r}$, $\tilde{R}_2 > \tilde{r}$, and $\tilde{R}_1 + \tilde{R}_2 \geq 2\tilde{b}$, we have

$$\frac{\tilde{m}\tilde{b}}{\tilde{b}^2 - \tilde{m}^2} \leq 1, \tag{F.25}$$

which is equivalent to $\tilde{m} \leq (\sqrt{5} - 1)\tilde{b}/2$ [35]. It is not easy to obtain other constraints over the parameters $\tilde{m}$ and $\tilde{b}$ in order to satisfy all energy conditions. The analysis is better done graphically.

In Figs. F.9 and F.10 we plot the surfaces and level curves for the effective Newtonian density, energy density, vertical pressure and the azimuthal stresses for a thick disk with parameters $\tilde{m} = 1$, $\tilde{b} = 2$, $n = 1$, and $\tilde{c} = 0$. For these values we have $\tilde{\rho} \geq 0$ and $\tilde{\epsilon} \geq 0$ everywhere. The ratio between any pressure or tension and energy density is less than 0.35, thus the dominant energy condition is also satisfied.

165
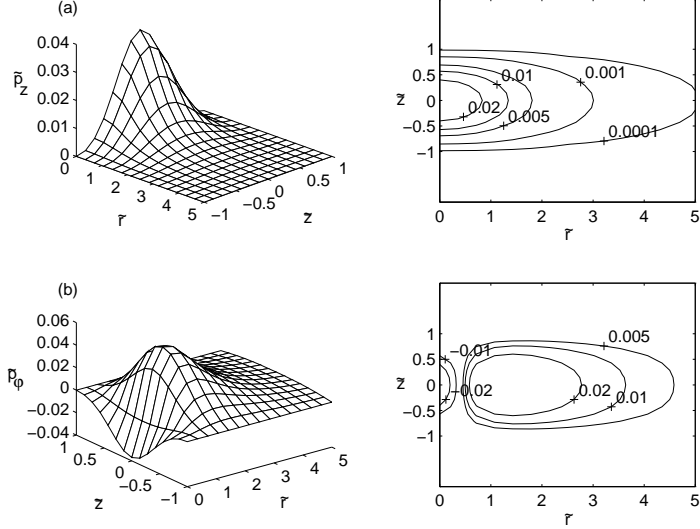
Figure F.10: (a) Vertical pressures, (b) azimuthal stresses for a thick disk in Weyl coordinates. Parameters: $\tilde{m} = 1$, $\tilde{b} = 2$, $n = 1$ and $\tilde{c} = 0$.

F.5   Thick Disks from the Schwarzschild Metric in Schwarzschild Coordinates

The Schwarzschild metric in Schwarzschild canonical coordinates (t, r, θ, φ) is written as

$$ds^2 = - \left(1 - \frac{2m}{r} \right) dt^2 + \frac{1}{\left(1 - \frac{2m}{r} \right)} dr^2 + r^2(d\theta^2 + \sin^2\theta d\varphi^2), \quad (\text{F.26})$$

where m is a positive constant. In cylindrical coordinates (t, R, z, φ), Eq. (F.26) can be cast as

$$ds^2 = - \left(1 - \frac{2m}{\mathcal{R}} \right) dt^2 + \frac{\mathcal{R}^3 - 2mz^2}{\mathcal{R}^2(\mathcal{R} - 2m)} dR^2 + \frac{4mRz}{\mathcal{R}^2(\mathcal{R} - 2m)} dRdz$$
$$+ \frac{\mathcal{R}^3 - 2mR^2}{\mathcal{R}^2(\mathcal{R} - 2m)} dz^2 + R^2 d\varphi^2, \quad (\text{F.27})$$

where $\mathcal{R}^2 = R^2 + z^2$. The displace, cut, fill and reflect method cannot be directly applied to metric Eq. (F.27), since the component g_{Rz} is not an even function of z. But we can multiply it by an odd function of z, which we choose to be the first derivative of $h(z)$. So we make the transformations $z \rightarrow$

166

$h(z)+b$ *and* $g_{Rz} \to g_{Rz}h'(z)$ in Eq. (F.27), and use the Einstein equations Eq. (F.16) to compute the components of the disk's energy-momentum tensor. With $h(z)$ defined by Eq. (F.4), the metric equation (F.27) satisfies the vacuum Einstein equations for $|z| > a$ and the metric functions together with their derivatives with respect to z are continuous on $z = \pm a$. Note that the function multiplying g_{Rz} may be other kind of function not necessarily related to $h(z)$, but its possible form is also limited by the requirements that the generated disks are physically acceptable, as was discussed in Sec. F.2. The physical variables of the disk are obtained by solving the eigenvalue problem for T_b^a: $T_b^a\xi^b = \lambda\xi^a$. We find that T^{ab} can be put in the form

$$T^{ab} = \epsilon U^a U^b + p_+ V^a V^b + p_- X^a X^b + p_\varphi W^a W^b, \qquad \text{(F.28)}$$

where

$$\epsilon = -T_t^t, \qquad U^a = \frac{1}{\sqrt{-g_{tt}}}(1,0,0,0),$$

$$p_\pm = \frac{T_r^r + T_z^z}{2} \pm \frac{1}{2}\sqrt{(T_r^r - T_z^z)^2 + 4T_z^r T_r^z},$$

$$V^a = (0, V^r, V^z, 0), \qquad X^a = (0, X^r, X^z, 0),$$

$$p_\varphi = T_\varphi^\varphi, \qquad W^a = \frac{1}{R}(0,0,0,1), \qquad \text{(F.29)}$$

and

$$V^r = \frac{1}{\sqrt{g_{RR} - 2g_{Rz}\Delta + g_{zz}\Delta^2}}, \quad V^z = -\Delta V^r, \quad \Delta = \frac{T_r^r - p_+}{T_z^r},$$

$$X^r = \frac{1}{\sqrt{g_{RR} - 2g_{Rz}\Gamma + g_{zz}\Gamma^2}}, \quad X^z = -\Gamma X^r, \quad \Gamma = \frac{T_r^r - p_-}{T_z^r}. \qquad \text{(F.30)}$$

The effective Newtonian density reads $\rho = \epsilon + p_+ + p_- + p_\varphi = \epsilon + T_r^r + T_z^z + p_\varphi$.

Although the expressions are exact, we do not state them explicitly, since they have dozens of terms. The analysis must also be done graphically. We find that p_+ is a pressure along a direction mostly vertical and p_- is a tension along a direction mostly radial. In Figs. F.11–F.13 we graph the surfaces and level curves of the energy density, the effective Newtonian density, the pressure mostly vertical, the tension mostly radial and the azimuthal stresses with parameters $\tilde{m} = 1$, $\tilde{b} = 5$, $n = 1$ and $\tilde{c} = 0$. The variables and parameters were rescaled as in the previous sections. While densities and the radial tension decrease monotonously with $\tilde{r}$ and $\tilde{z} \to \pm 1$, the upward pressure first increases with radius and then decreases monotonously. The
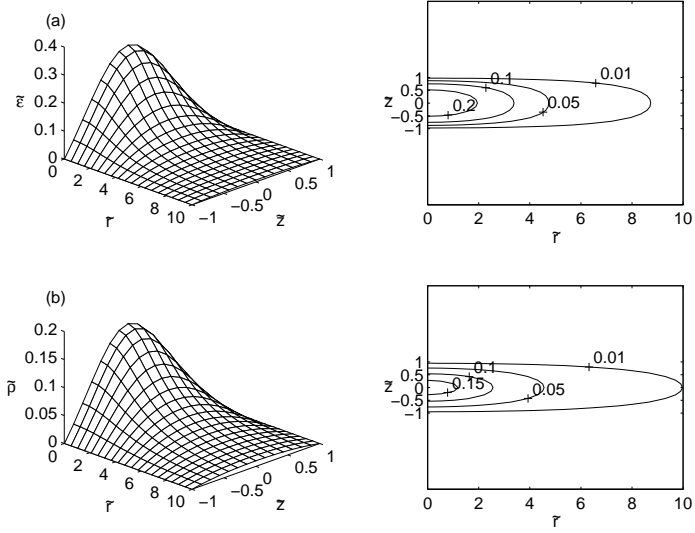
Figure F.11: (a) Energy density, (b) effective Newtonian density for a thick disk in Schwarzschild coordinates. Parameters: $\tilde{m} = 1$, $\tilde{b} = 5$, $n = 1$ and $\tilde{c} = 0$.
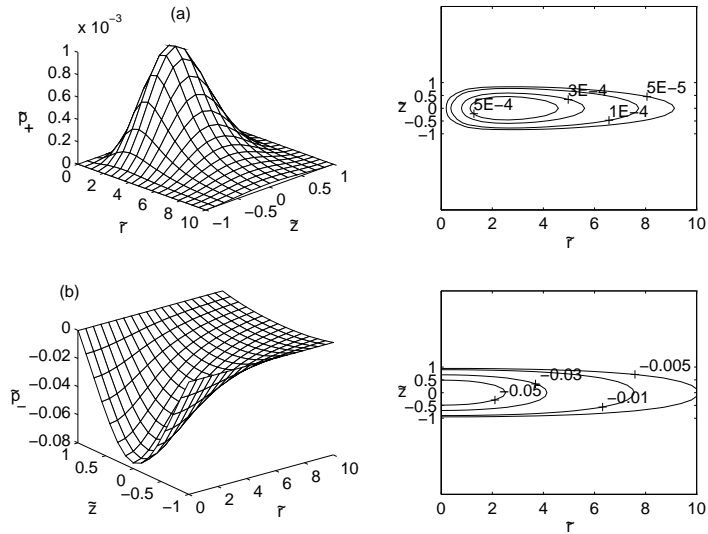

Figure F.12: (a) The pressure mostly vertical, (b) tension mostly radial for a thick disk in Schwarzschild coordinates. Parameters: $\tilde{m} = 1$, $\tilde{b} = 5$, $n = 1$ and $\tilde{c} = 0$.
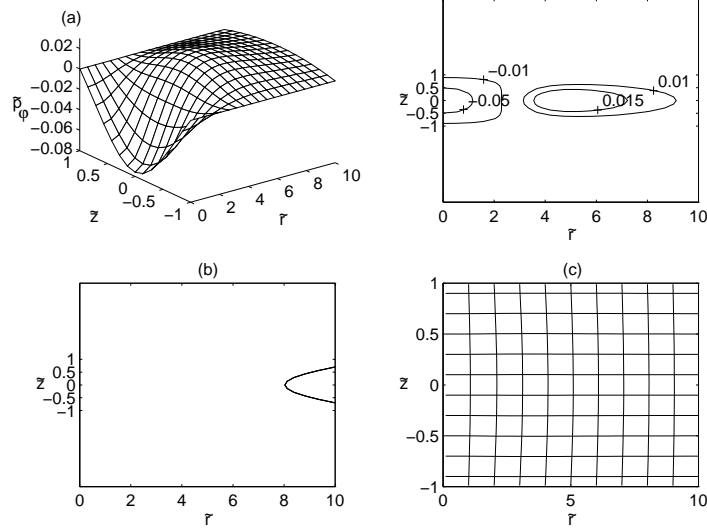
Figure F.13: (a) The azimuthal stresses, (b) the level curve of $|p_\varphi/\epsilon| = 1$ and (c) the lines of flow calculated from Eqs. (F.31a) and (F.31b). Parameters: $\tilde{m} = 1$, $\tilde{b} = 5$, $n = 1$ and $\tilde{c} = 0$.

azimuthal stresses are negative near the disk's center, then increase to a positive maximum at the $\tilde{z} = 0$ plane and then decrease monotonously. In some sense this new class of disks has similar characteristics of those obtained in Weyl coordinates, but here the almost radial tensions are different from the almost vertical pressures. Unfortunately the dominant energy condition does not hold with respect to the azimuthal stresses. Figure F.13(b) shows the level curve of $|p_\varphi/\epsilon| = 1$. For $\tilde{r} \gtrsim 8$ the dominant energy condition is not satisfied. This also seems to happen for larger values of $\tilde{b}$. In Fig. F.13(c) we plot the lines of flow calculated by numerically solving the differential equations

$$\frac{dV^z}{dV^r} = \frac{V^z}{V^r},$$ \hfill (F.31a)

$$\frac{dX^z}{dX^r} = \frac{X^z}{X^r}.$$ \hfill (F.31b)

The vertical and horizontal lines in Fig. F.13(c) are, respectively, the lines of flow associated with Eqs. (F.31a) and (F.31b). We note that the lines are very parallel to the coordinate axes. This happens because the component T^z_r is about two orders of magnitude smaller than the other components of the energy-momentum tensor, thus the eigenvalues $p_\pm$ are almost equal

to the corresponding diagonal elements. We call then the eigenvalue p_+ with eigenvector V^a the pressure mostly vertical and the eigenvalue p_- with eigenvector X^a the tension mostly radial.

F.6   Discussion

The displace, cut, fill and reflect method and a class of functions used to fill was used to construct new classes of thick general relativistic disks that generalize the models studied in a previous work [30]. The Newtonian Kuzmin-Toomre disks were used to put constraints on the parameter in the class of fill functions so that the disks were physically acceptable. Then the Schwarzschild solution was used to construct disks in isotropic cylindrical coordinates, Weyl coordinates and canonical Schwarzschild coordinates. In isotropic coordinates the disks have equal radial and azimuthal pressures (isotropic fluid) but different vertical pressures. Disks in Weyl coordinates present radial tensions that are equal in modulus as vertical pressures, azimuthal tensions near the disk's center and azimuthal pressures for larger radii. All disks are in agreement with the strong, weak and dominant energy conditions.

In canonical Schwarzschild coordinates the displace, cut, fill and reflect method cannot be applied directly and an additional odd function must be added to generate exact disks. We find that the disks have tensions along a direction mostly radial that are different from the pressures along a direction mostly vertical, and the azimuthal stresses have similar behavior as in disks in Weyl coordinates. These disks are in agreement with the strong and weak energy conditions, but the azimuthal stresses do not satisfy the dominant energy condition.

Bibliography

[1] W. A. Bonnor and A. Sackfield, Comm. Math. Phys. **8**, 338 (1968).

[2] T. Morgan and L. Morgan, Phys. Rev. **183**, 1097 (1969).

[3] L. Morgan and T. Morgan, Phys. Rev. D **2**, 2756 (1970).

[4] D. Lynden-Bell and S. Pineault, Mon. Not. R. Astron. Soc. **185**, 679 (1978).

[5] P. S. Letelier and S. R. Oliveira, J. Math. Phys. (N.Y.) **28**, 165 (1987).

[6] J. P. S. Lemos, Classical Quantum Gravity **6**, 1219 (1989).

[7] J. P. S. Lemos and P. S. Letelier, Classical Quantum Gravity **10**, L75 (1993).

[8] J. Bičák, D. Lynden-Bell and J. Katz, Phys. Rev. D **47**, 4334 (1993).

[9] J. Bičák, D. Lynden-Bell and C. Pichon, Mon. Not. R. Astron. Soc. **265**, 126 (1993).

[10] J. P. S. Lemos and P. S. Letelier, Phys. Rev. D **49**, 5135 (1994).

[11] J. P. S. Lemos and P. S. Letelier, Int. J. Mod. Phys. D **5**, 53 (1996).

[12] G. González and O. A. Espitia, Phys. Rev. D **68**, 104028 (2003).

[13] G. García and G. González, Phys. Rev. D **69**, 124002 (2004).

[14] J. Bičák and T. Ledvinka, Phys. Rev. Lett. **71**, 1669 (1993).

[15] G. González and P. S. Letelier, Phys. Rev. D **62**, 064025 (2000).

[16] G. González and P. S. Letelier, Classical Quantum Gravity **16**, 479 (1999).

[17] P. S. Letelier, Phys. Rev. D **60**, 104042 (1999).

[18] J. Katz, J. Bičák and D. Lynden-Bell, Classical Quantum Gravity **16**, 4023 (1999).

[19] D. Vogt and P. S. Letelier, Phys. Rev. D **68**, 08410 (2003).

[20] D. Vogt and P. S. Letelier, Phys. Rev. D **70**, 064003 (2004).

[21] V. Karas, J. M. Huré and O. Semerák, Classical Quantum Gravity **21**, R1 (2004).

[22] C. Klein, Classical Quantum Gravity **14**, 2267 (1997).

[23] G. Neugebauer and R. Meinel, Phys. Rev. Lett. **75**, 3046 (1995).

[24] C. Klein and O. Richter, Phys. Rev. Lett. **83**, 2884 (1999).

[25] C. Klein, Phys. Rev. D **63**, 064033 (2001).

[26] J. Frauendiener and C. Klein, Phys. Rev. D **63**, 084025 (2001).

[27] C. Klein, Phys. Rev. D **65**, 084029 (2002).

[28] C. Klein, Phys. Rev. D **68**, 027501 (2003).

[29] C. Klein, Ann. Phys. (N.Y.) **12** (10), 599 (2003).

[30] G. González and P. S. Letelier, Phys. Rev. D **69**, 044013 (2004).

[31] G. G. Kuzmin, Astron. Zh. **33**, 27 (1956).

[32] These expressions are the generalizations of Eqs. (30a)–(30e) of Ref. [30]. There is a misprint in Eqs. (30a) and (30b), where the numerical factor multiplying the equations should be 32.

[33] H. Weyl, Ann. Phys. (Leipzig) **54**, 117 (1917).

[34] H. Weyl, Ann. Phys. (Leipzig) **59**, 185 (1919).

[35] Note that this inequality is different from condition (24) deduced in Ref. [30], because Eq. (22b) in that paper has an error in the term that multiplies $\tilde{\rho}$: the product $\tilde{R}_1 \tilde{R}_2$ in the denominator should not be squared [see Eq. (F.23b)]. The corrected inequality is $0 < \tilde{m} < (\tilde{b}^2 - \tilde{k}^2)/\tilde{b}$.

Apêndice G

Relativistic Models of Galaxies

Abstract

A special form of the isotropic metric in cylindrical coordinates is used to construct what may be interpreted as the general relativistic versions of some well-known potential-density pairs used in Newtonian gravity to model three-dimensional distributions of matter in galaxies. The components of the energy-momentum tensor are calculated for the first two Miyamoto-Nagai potentials and a particular potential due to Satoh. The three potentials yield distributions of matter in which all tensions are pressures and all energy conditions are satisfied for certain ranges of the free parameters. A few non-planar geodesic orbits are computed for one of the potentials and compared with the Newtonian case. Rotation is also incorporated to the models and the effects of the source rotation on the rotation profile are calculated as first-order corrections by using an approximate form of the Kerr metric in isotropic coordinates.

Key words: relativity – stellar dynamics – celestial mechanics – galaxies: kinematics and dynamics.

G.1   Introduction

Analytical axially symmetric solutions of gravitating matter provide very accurate models for the mass distribution of galaxies. In Newtonian the-

173

ory, models for globular clusters and spherical galaxies were presented by Plummer (1911) and King (1966). On the other hand, to describe the mass distribution within highly flattened axisymmetric galaxies, Toomre (1963) found a family of density potential pairs, the first of which was first derived by Kuzmin (1956). Later, Miyamoto & Nagai (1975) and Nagai & Miyamoto (1976) 'thickened-up' Toomre's series of disc models to yield pairs of three-dimensional potential and density functions. In a similar way, Satoh (1980) obtained a family of three-dimensional axisymmetric mass distributions from the higher order Plummer models. For a detailed account and the description of other potential-density pairs used in galactic models, see for example Binney & Tremaine (1987).

In general relativity, several exact disc-like solutions have been found, among them the static discs without radial pressure studied by Bonnor & Sackfield (1968) and Morgan & Morgan (1969), and discs with radial pressure by Morgan & Morgan (1970). Several classes of exact solutions of the Einstein field equations corresponding to static thin discs with or without radial pressure have been obtained by different authors (Lynden-Bell & Pineault 1978; Letelier & Oliveira 1987; Lemos 1989; Bičák, Lynden-Bell & Katz 1993a; Bičák, Lynden-Bell & Pichon 1993b; Lemos & Letelier 1993, 1994, 1996; González & Espitia 2003; García & González 2004). Thin rotating discs that can be considered as a source of the Kerr metric were presented by Bičák & Ledvinka (1993), while rotating discs with heat flow were studied by González & Letelier (2000). Also thin discs with radial tension (González & Letelier 1999), magnetic fields (Letelier 1999) and magnetic and electric fields (Katz, Bičák & Lynden-Bell 1999) were considered. The non-linear superposition of a disc and a black hole was first obtained by Lemos & Letelier (1993). Perfect fluid discs with haloes were studied by Vogt & Letelier (2003) and charged perfect fluid discs by Vogt & Letelier (2004). The stability of some general relativistic thin disc models using a first-order perturbation of the energy-momentum tensor was investigated by Ujevic & Letelier (2004). For a survey on self-gravitating relativistic discs, see for instance Karas, Huré & Semerák (2004).

In the works cited above, an inverse style method was used to solve the Einstein equations, i. e., the energy-momentum tensor is computed from the metric representing the disc. Another approach to generate discs is by solving the Einstein equations given a source (energy-momentum tensor). Essentially, they are obtained by solving a Riemann-Hilbert problem and are highly non-trivial. This has been used by the Jena group to generate several exact solutions of discs (Neugebauer & Meinel 1995; Klein 1997, 2001, 2002, 2003a,b; Klein & Richter 1999; Frauendiener & Klein 2001).

Recently, González & Letelier (2004) constructed models of static relativistic thick discs in various coordinate systems. Although the discs have constant thickness, the matter density decreases rapidly with radius and the z coordinate, and in principle they may also be used to represent both the disc part and the central bulges of galaxies.

The aim of this work is to consider more realistic three-dimensional models for the gravitational field of galaxies in a general relativistic context. The distribution of matter fills all the space, but the total mass is finite. Essentially we formulate general relativistic versions in isotropic coordinates of the potential-density pairs deduced by Miyamoyo and Nagai (1975), Nagai & Miyamoto (1976) and Satoh (1980). Also, the influence of galactic rotation on the rotation profile of test particles on the galactic plane is estimated using an approximate form of the Kerr metric in isotropic coordinates.

The paper is organized as follows. In Section G.2 we present a special form of the isotropic metric and the components of the energy-momentum tensor as functions of the metric coefficients, from which the physical properties of the galactic matter distributions can be calculated. We also derive expressions for the tangential circular velocity and specific angular momentum of test particles in circular motion on the galactic plane. These results are then applied in Sections G.3 and G.4 to construct general relativistic analogues of two Miyamoto-Nagai models and one galactic model proposed by Satoh. As an example of application of these models, in Section G.5 we calculate a few geodesic orbits and compare them with the Newtonian case. In Section G.6 we deduce the first-order effects of galactic rotation on the tangential circular velocity of geodesic motion of particles on the galactic plane using an approximate form of the Kerr metric in isotropic coordinates, and apply the result to the above-mentioned models. Finally, we summarize our results in Section G.7.

G.2 Einstein Equations in Isotropic Coordinates

Let us consider the particular case of axial symmetric space-times whose metric can be written in an isotropic form in cylindrical coordinates (t, R, z, φ),

$$\mathrm{d}s^2 = e^{\nu(R,z)}c^2\mathrm{d}t^2 - e^{\lambda(R,z)}\left(\mathrm{d}R^2 + \mathrm{d}z^2 + R^2\mathrm{d}\varphi^2\right). \qquad (G.1)$$

In order to construct a general relativistic formulation of the known Newtonian models for the mass distribution of galaxies, it is convenient to use a particular form of metric equation (G.1), suggested by generalizing the form

of the Schwarzschild metric in isotropic coordinates

$$ds^2 = \left(\frac{1-f}{1+f}\right)^2 c^2 dt^2 - (1+f)^4 \left(dR^2 + dz^2 + R^2 d\varphi^2\right), \qquad \text{(G.2)}$$

where $f = f(R, z)$. Metric equation (G.2) gives the Schwarzschild solution when f is taken as

$$f = \frac{GM}{2c^2\sqrt{R^2 + z^2}}. \qquad \text{(G.3)}$$

For metric equation (G.2), the Einstein equations $G_{\mu\nu} = -(8\pi G/c^4)T_{\mu\nu}$ yield the following expressions for the components of the energy-momentum tensor[1]

$$T_t^t = -\frac{c^4}{2\pi G(1+f)^5}\left(f_{,RR} + f_{,zz} + \frac{f_{,R}}{R}\right), \qquad \text{(G.4a)}$$

$$T_R^R = \frac{c^4}{4\pi G(1+f)^5(1-f)}\left(ff_{,zz} + \frac{ff_{,R}}{R} + 2f_{,R}^2 - f_{,z}^2\right), \qquad \text{(G.4b)}$$

$$T_z^z = \frac{c^4}{4\pi G(1+f)^5(1-f)}\left(ff_{,RR} + \frac{ff_{,R}}{R} + 2f_{,z}^2 - f_{,R}^2\right), \qquad \text{(G.4c)}$$

$$T_z^R = T_R^z = -\frac{c^4}{4\pi G(1+f)^5(1-f)}\left(ff_{,Rz} - 3f_{,R}f_{,z}\right), \qquad \text{(G.4d)}$$

$$T_\varphi^\varphi = \frac{c^4}{4\pi G(1+f)^5(1-f)}\left[f\left(f_{,RR} + f_{,zz}\right) - f_{,R}^2 - f_{,z}^2\right]. \qquad \text{(G.4e)}$$

The energy density is given by $\sigma = T_t^t/c^2$, and the stresses (pressures or tensions) along a particular direction read $P_i = -T_i^i$ when the energy-momentum tensor is diagonal. It is a surprising fact that the component T_t^t is proportional to the usual Laplacian of the function f in flat cylindrical coordinates. Note that in the Newtonian limit when $f \ll 1$, equation (G.4a) reduces to the Poisson equation

$$\nabla^2 \Phi = 4\pi G \rho_N, \qquad \text{(G.5)}$$

if the function f is related to the gravitational potential Φ by

$$f = -\frac{\Phi}{2c^2}. \qquad \text{(G.6)}$$

---

[1] The Einstein tensor was computed using MAPLE and the result was checked using REDUCE.

The energy-momentum tensor will be diagonal ($T_z^R = T_R^z = 0$) provided f has the form

$$f = \frac{C}{\sqrt{w(R) + g(z)}},$$ (G.7)

where C is a constant and $w(R)$ and $g(z)$ are arbitrary functions. Furthermore, the components T_R^R and T_φ^φ will be equal (isotropic radial and azimuthal stresses) only if $w(R) = R^2$.

Two physical quantities of interest related to the circular motion of test particles along geodesics on the galactic plane are the tangential velocity v_c (rotation profile) and the specific angular momentum h. The assumption of geodesic motion is valid for the case of a particle moving in a very diluted gas like the gas made of stars that models a galaxy disc. For metric equation (G.1) the expressions are (Vogt & Letelier 2003)

$$v_c^2 = c^2 R^2 \frac{e^\lambda (e^\nu)_{,R}}{e^\nu (R^2 e^\lambda)_{,R}},$$ (G.8)

$$h = cR^2 e^\lambda \sqrt{\frac{(e^\nu)_{,R}}{e^\nu (R^2 e^\lambda)_{,R} - R^2 e^\lambda (e^\nu)_{,R}}},$$ (G.9)

where all functions are evaluated on $z = 0$. The angular momentum can be used to determine the stability of circular orbits on the galactic plane by using an extension of the Rayleigh criteria of stability of a fluid at rest in a gravitational field (Rayleigh 1917; see also Landau & Lifshitz 1987)

$$h\frac{dh}{dR}\bigg|_{z=0} > 0.$$ (G.10)

For the specific metric form equation (G.2), equations (G.8) and (G.9) simplify to

$$v_c^2 = -\frac{2c^2 R f_{,R}}{(1-f)(1+f+2Rf_{,R})},$$ (G.11)

$$h = cR^2 (1+f)^2 \sqrt{\frac{-2f_{,R}}{R[1-f^2 + 2Rf_{,R}(2-f)]}},$$ (G.12)

G.3   General Relativistic Miyamoto-Nagai Models

G.3.1   First Model

The simplest gravitational potential proposed by Miyamoto & Nagai (1975) and Nagai & Miyamoto (1976) to represent stratifications of mass in the

central bulges and in the disc parts of galaxies is given by

$$\Phi(R,z) = -\frac{GM}{\sqrt{R^2 + (a + \sqrt{z^2 + b^2})^2}}, \qquad (\text{G.13})$$

where a and b are positive constants. The corresponding three-dimensional density distribution $\rho_N(R,z)$ is easily derived from Poisson equation (G.5)

$$\rho_N(R,z) = \frac{b^2 M}{4\pi} \frac{aR^2 + (a + 3\sqrt{z^2 + b^2})(a + \sqrt{z^2 + b^2})^2}{\left[R^2 + (a + \sqrt{z^2 + b^2})^2\right]^{5/2} (z^2 + b^2)^{3/2}}. \qquad (\text{G.14})$$

Now we consider the function $f(R,z)$ defined in the previous section as

$$f(R,z) = \frac{GM}{2c^2\sqrt{R^2 + (a + \sqrt{z^2 + b^2})^2}}. \qquad (\text{G.15})$$

Substituting equation (G.15) in equations (G.4a)–(G.4e) we find the following expressions for the non-zero components of the energy-momentum tensor

$$\bar{\sigma} = \frac{\tilde{b}^2\left[\tilde{a}\tilde{R}^2 + (\tilde{a} + \xi)^2(\tilde{a} + 3\xi)\right]}{4\pi\xi^3\left[1 + \sqrt{\tilde{R}^2 + (\tilde{a} + \xi)^2}\right]^5}, \qquad (\text{G.16a})$$

$$\bar{p}_R = \bar{p}_\varphi = \frac{\tilde{b}^2}{8\pi\xi^3} \frac{\left[\tilde{a}\tilde{R}^2 + (\tilde{a} + \xi)^2(\tilde{a} + 2\xi)\right]}{\left[1 + \sqrt{\tilde{R}^2 + (\tilde{a} + \xi)^2}\right]^5\left[-1 + \sqrt{\tilde{R}^2 + (\tilde{a} + \xi)^2}\right]}, \qquad (\text{G.16b})$$

$$\bar{p}_z = \frac{\tilde{b}^2(\tilde{a} + \xi)^2}{4\pi\xi^2\left[1 + \sqrt{\tilde{R}^2 + (\tilde{a} + \xi)^2}\right]^5\left[-1 + \sqrt{\tilde{R}^2 + (\tilde{a} + \xi)^2}\right]}, \qquad (\text{G.16c})$$

where the variables and parameters were rescaled in terms of the Schwarzschild radius in isotropic spherical coordinates $r_s = GM/(2c^2)$:[2] $\tilde{R} = R/r_s$, $\tilde{z} = z/r_s$, $\tilde{a} = a/r_s$, $\tilde{b} = b/r_s$, $\sigma = \frac{M}{r_s^3}\bar{\sigma}$, $p_i = \frac{Mc^2}{r_s^3}\bar{p}_i$ and $\xi = \sqrt{\tilde{z}^2 + \tilde{b}^2}$. The 'effective Newtonian density' $\rho = \sigma + p_R/c^2 + p_\varphi/c^2 + p_z/c^2$ reads

$$\bar{\rho} = \frac{\tilde{b}^2\sqrt{\tilde{R}^2 + (\tilde{a} + \xi)^2}\left[\tilde{a}\tilde{R}^2 + (\tilde{a} + \xi)^2(\tilde{a} + 3\xi)\right]}{4\pi\xi^3\left[1 + \sqrt{\tilde{R}^2 + (\tilde{a} + \xi)^2}\right]^5\left[-1 + \sqrt{\tilde{R}^2 + (\tilde{a} + \xi)^2}\right]}, \qquad (\text{G.17})$$

[2]Note that the Schwarzschild radius r_s in isotropic spherical coordinates is related to Schwarzschild radius r'_s in canonical spherical coordinates by $r_s = r'_s/4$.
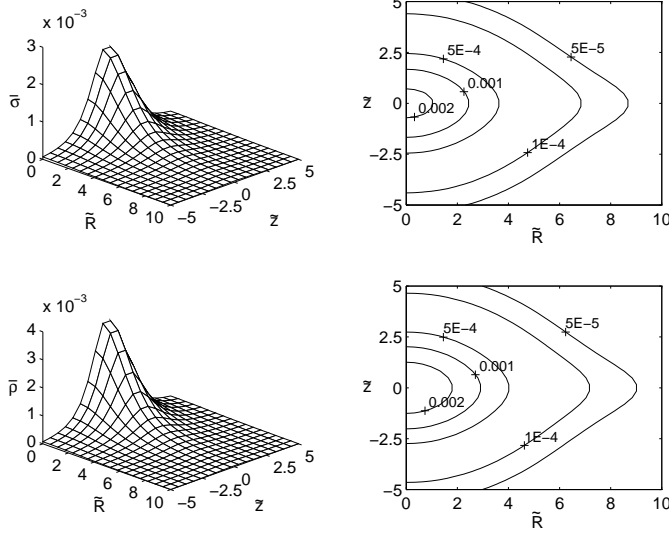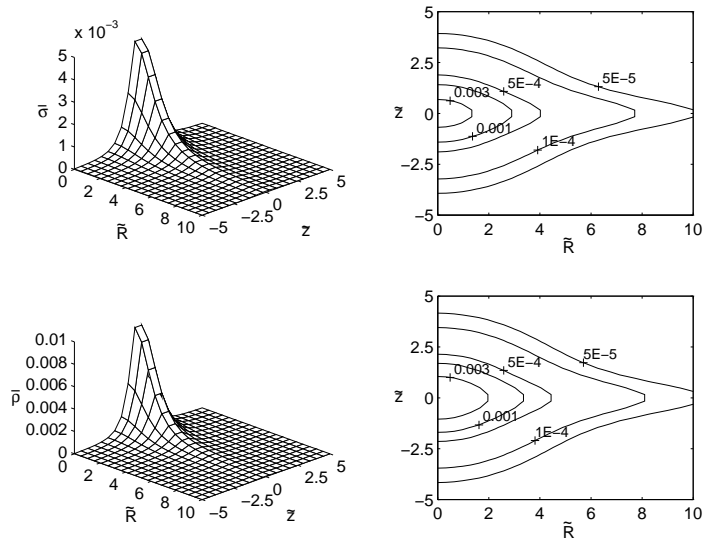
Figure G.1: Surface plot and level curves of the energy density $\bar{\sigma}$ equation (G.16a) and 'effective Newtonian density' $\bar{\rho}$ equation (G.17) with parameters $\tilde{a} = 1$ and $\tilde{b} = 2$.

with $\rho = \frac{M}{r_s^3}\bar{\rho}$.

The strong energy condition requires that $\rho \geq 0$, whereas the weak energy condition imposes the condition $\sigma \geq 0$. The dominant energy condition requires $|p_R/\sigma| \leq c^2$, $|p_z/\sigma| \leq c^2$ and $|p_\varphi/\sigma| \leq c^2$. Equations (G.16a)–(G.17) show that the densities are positive everywhere and so are the stresses (pressures) if we impose the condition $\tilde{a}+\tilde{b} > 1$. Moreover, we have isotropic pressures along the radial and azimuthal directions. When $\tilde{R}$, $\tilde{z}$, $\tilde{a}$, $\tilde{b} \gg 1$, the first-order expansion of equation (G.17) is

$$\bar{\rho} \approx \frac{\tilde{b}^2 \left[\tilde{a}\tilde{R}^2 + (\tilde{a} + \xi)^2(\tilde{a} + 3\xi)\right]}{4\pi\xi^3 \left[\tilde{R}^2 + (\tilde{a} + \xi)^2\right]^{5/2}} \left[1 - \frac{4}{\sqrt{\tilde{R}^2 + (\tilde{a} + \xi)^2}}\right]. \qquad \text{(G.18)}$$

Thus, the first-order general relativistic correction lowers the mass density.

In Figs G.1 and G.2 we show the surfaces and level curves of the densities and pressures equations (G.16a)–(G.17) for parameters $\tilde{a} = 1$, $\tilde{b} = 2$ and the same physical quantities for parameters $\tilde{a} = 1$, $\tilde{b} = 1$ are displayed in Figs G.3 and G.4. As in the Newtonian case, the lower the ratio b/a, the flatter the mass distributions, and the pressure distributions show similar
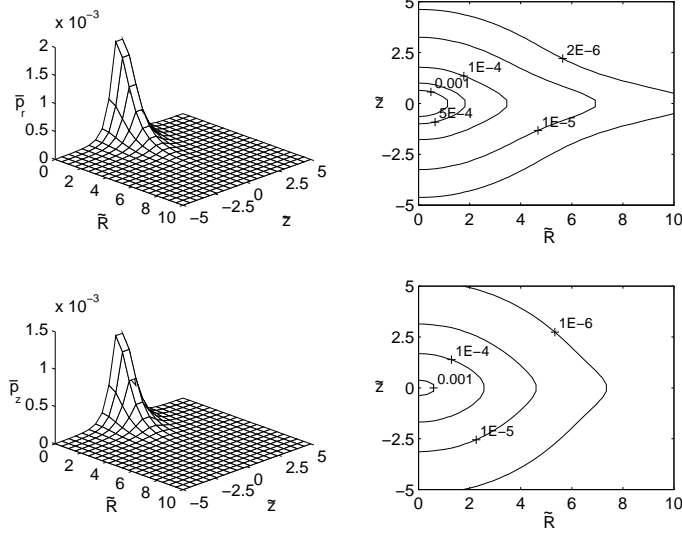
179
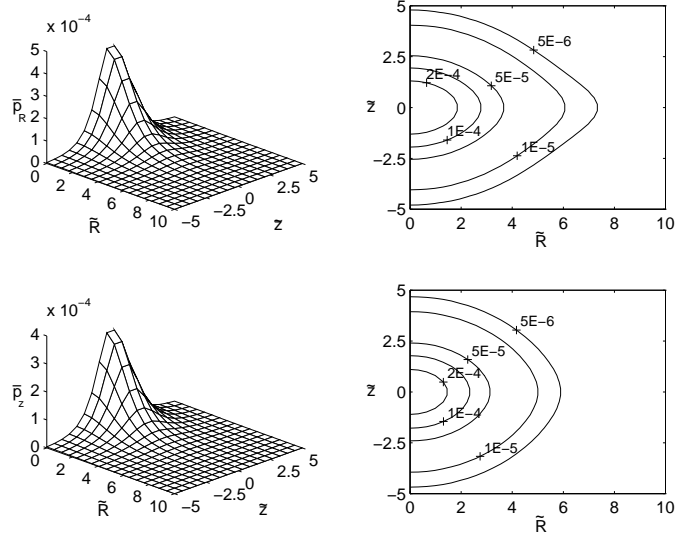
Figure G.2: Surface plot and level curves of the radial pressure $\bar{p}_R$ equation (G.16b) and vertical pressure $\bar{p}_z$ equation (G.16c) with parameters $\tilde{a} = 1$ and $\tilde{b} = 2$.

Figure G.3: Surface plot and level curves of the energy density $\bar{\sigma}$ equation (G.16a) and 'effective Newtonian density' $\bar{\rho}$ equation (G.17) with parameters $\tilde{a} = 1$ and $\tilde{b} = 1$.

Figure G.4: Surface plot and level curves of the radial pressure $\bar{p}_R$ equation (G.16b) and vertical pressure $\bar{p}_z$ equation (G.16c) with parameters $\tilde{a} = 1$ and $\tilde{b} = 1$.

behaviour. For $\tilde{a} = 1$, $\tilde{b} = 2$ we have $\tilde{p}_R/\tilde{\sigma} < 0.2$ and $\tilde{p}_z/\tilde{\sigma} < 0.15$ and for $\tilde{a} = 1$, $\tilde{b} = 1$ the ratios are $\tilde{p}_R/\tilde{\sigma} < 0.4$ and $\tilde{p}_z/\tilde{\sigma} < 0.3$. Thus, for these parameters all energy conditions are satisfied.

The tangential circular velocity equation (G.11) and specific angular momentum equation (G.12) for f given by equation (G.15) evaluated on $z = 0$ read

$$\left(\frac{v_c}{c}\right)^2 = \frac{2\tilde{R}^2\sqrt{\tilde{R}^2 + \eta^2}}{\left(-1 + \sqrt{\tilde{R}^2 + \eta^2}\right)\left[-\tilde{R}^2 + \eta^2 + (\tilde{R}^2 + \eta^2)^{3/2}\right]}, \qquad (G.19)$$

$$\bar{h} = \frac{\sqrt{2}\tilde{R}^2\left(1 + \sqrt{\tilde{R}^2 + \eta^2}\right)^2}{(\tilde{R}^2 + \eta^2)^{3/4}\sqrt{(\tilde{R}^2 + \eta^2)^2 + \tilde{R}^2 - \eta^2 - 4\tilde{R}^2\sqrt{\tilde{R}^2 + \eta^2}}}, \qquad (G.20)$$

where we defined $h = cr_s\bar{h}$ and $\eta = \tilde{a} + \tilde{b}$. The first-order expansion of

181

equation (G.19) reads

$$\frac{v_c}{c} = \frac{\tilde{R}\sqrt{2}}{\left[\tilde{R}^2 + (\tilde{a} + \tilde{b})^2\right]^{3/4}} \left\{ 1 + \frac{\tilde{R}^2}{\left[\tilde{R}^2 + (\tilde{a} + \tilde{b})^2\right]^{3/2}} \right\}. \qquad \text{(G.21)}$$

Figs G.5(a) and (b) show, respectively, the rotation profile equation (G.19) and the curves of specific angular momentum equation (G.20) for parameters $\tilde{a} = 1$ and $\tilde{b} = 2$, $\tilde{b} = 1$ and $\tilde{b} = 0.5$. In Fig. G.5(a) the dashed curves represent the Newtonian tangential velocities. Relativistic tangential velocities are always higher than the Newtonian ones, as suggested by the first-order correction in equation (G.21). The curves of specific angular momentum show that the circular orbits on the plane $\tilde{z} = 0$ turn out to be unstable for higher flattened matter distributions (the curve for $\tilde{b} = 0.5$). The orbits for the parameters $\tilde{a} = 1$, $\tilde{b} = 2$ are all stable, whereas in the case of $\tilde{b} = 1$ a small region of instability appears between $\tilde{R} \approx 5$ and $\tilde{R} \approx 6$. The Newtonian limit of equation (G.20) gives

$$\bar{h} = \frac{\sqrt{2}\tilde{R}^2}{[\tilde{R}^2 + (\tilde{a} + \tilde{b})^2]^{3/4}}, \qquad \text{(G.22)}$$

from which it is easily checked that $(d\bar{h}/d\tilde{R}) \geq 0$ for all $\tilde{a}$, $\tilde{b}$ and $\tilde{R}$. Thus, the instability is a pure relativistic effect (the same is verified for circular orbits around the superposition of black holes and axially symmetric structures in Weyl coordinates; see Letelier (2003)).

G.3.2 Second Model

Another pair of potential and density functions presented by Miyamoto and Nagai as a generalization of the Toomre model 2 is described by

$$\Phi(R, z) = -\frac{GM}{\sqrt{R^2 + (a + \zeta)^2}} \left[1 + \frac{a(a + \zeta)}{R^2 + (a + \zeta)^2} \right], \qquad \text{(G.23a)}$$

$$\rho_N(R, z) = \frac{3b^2 M}{4\pi\zeta^3 \left[R^2 + (a + \zeta)^2\right]^{7/2}} \left[R^2(a^3 + \zeta^3) + (\zeta + a)^3(\zeta^2 + 4a\zeta + a^2) \right], \qquad \text{(G.23b)}$$

where $\zeta = \sqrt{z^2 + b^2}$. Using f defined by equation (G.6) in equations (G.4a)–(G.4e), we find that the components $T_z^R = T_R^z$ are non-zero. The physical
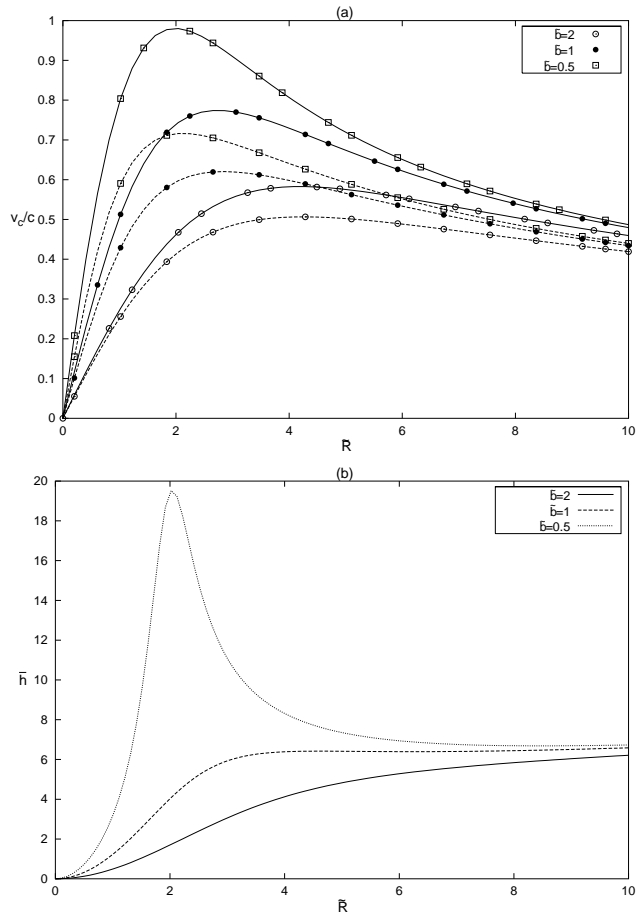
182

Figure G.5: (a) Relativistic rotation profile equation (G.19) and Newtonian rotation profile (dashed curves) with parameters $\tilde{a} = 1$ and $\tilde{b} = 2$, $\tilde{b} = 1$ and $\tilde{b} = 0.5$. (b) Specific angular momentum equation (G.20) for the same parameters.

variables of the matter distribution are obtained by solving the eigenvalue problem for T^a_b

$$T^a_b \Xi^b = \lambda \Xi^a. \tag{G.24}$$

We find that T^{ab} can be put in the form

$$T^{ab} = \sigma e^a_{(0)} e^b_{(0)} + p_+ e^a_{(1)} e^b_{(1)} + p_- e^a_{(2)} e^b_{(2)} + p_\varphi e^a_{(3)} e^b_{(3)}, \tag{G.25}$$

where

$$\sigma = \frac{T^t_t}{c^2}, \qquad e^a_{(0)} = \left(\frac{1+f}{1-f}, 0, 0, 0 \right),$$

$$p_\pm = -\frac{T^R_R + T^z_z}{2} \mp \frac{1}{2} \sqrt{(T^R_R - T^z_z)^2 + 4(T^R_z)^2}, \tag{G.26}$$

$$e^a_{(1)} = (0, e^R_{(1)}, e^z_{(1)}, 0), \qquad e^a_{(2)} = (0, e^R_{(2)}, e^z_{(2)}, 0),$$

$$p_\varphi = -T^\varphi_\varphi, \qquad e^a_{(3)} = \left(0, 0, 0, \frac{1}{R(1+f)^2} \right), \tag{G.27}$$

and

$$e^R_{(1)} = -\frac{T^R_z}{(1+f)^2 \sqrt{(T^R_z)^2 + (T^R_R + p_+)^2}}, \; e^z_{(1)} = \frac{T^R_R + p_+}{(1+f)^2 \sqrt{(T^R_z)^2 + (T^R_R + p_+)^2}},$$

$$e^R_{(2)} = -\frac{T^R_z}{(1+f)^2 \sqrt{(T^R_z)^2 + (T^R_R + p_-)^2}}, \; e^z_{(2)} = \frac{T^R_R + p_-}{(1+f)^2 \sqrt{(T^R_z)^2 + (T^R_R + p_-)^2}}.$$

$$\tag{G.28}$$

The effective Newtonian density reads $\rho = \sigma + p_+/c^2 + p_-/c^2 + p_\varphi/c^2 = \sigma - T^R_R/c^2 - T^z_z/c^2 + p_\varphi/c^2$. The explicit expressions for $\bar{\sigma}$, $\bar{\rho}$ and $\bar{p}_\varphi$ are

$$\bar{\sigma} = \frac{3\tilde{b}^2 \chi^4 \left[\tilde{R}^2 (\tilde{a}^3 + \xi^3) + (\tilde{a} + \xi)^3 (\tilde{a}^2 + \xi^2 + 4\tilde{a}\xi) \right]}{4\pi \xi^3 \left[\chi^{3/2} + \tilde{R}^2 + (\tilde{a} + \xi)(2\tilde{a} + \xi) \right]^5}, \tag{G.29}$$

$$\bar{\rho} = \frac{3\tilde{b}^2 \chi^{11/2} \left[\tilde{R}^2 (\tilde{a}^3 + \xi^3) + (\tilde{a} + \xi)^3 (\tilde{a}^2 + \xi^2 + 4\tilde{a}\xi) \right]}{4\pi \xi^3 \left[\chi^{3/2} + \tilde{R}^2 + (\tilde{a} + \xi)(2\tilde{a} + \xi) \right]^5 \left[\chi^{3/2} - \tilde{R}^2 - (\tilde{a} + \xi)(2\tilde{a} + \xi) \right]}, \tag{G.30}$$

$$\bar{p}_\varphi = \frac{\chi^4}{8\pi \xi^3 \left[\chi^{3/2} + \tilde{R}^2 + (\tilde{a} + \xi)(2\tilde{a} + \xi) \right]^5 \left[\chi^{3/2} - \tilde{R}^2 - (\tilde{a} + \xi)(2\tilde{a} + \xi) \right]} \times$$

$$\left\{ \tilde{R}^4 \left[\xi^3(\tilde{a}^2 + 2\tilde{b}^2) + 3\tilde{a}^3\tilde{b}^2 \right] + \tilde{R}^2(\tilde{a}+\xi)^2 \left[9\tilde{a}^3\tilde{b}^2 + 12\tilde{a}\tilde{b}^2\xi^2 + 4\tilde{b}^2\xi^3 \right. \right.$$
$$\left. \left. +2\tilde{a}^2(7\tilde{b}^2 + \tilde{z}^2)\xi \right] + (a+\xi)^4 \left[6\tilde{a}^3\tilde{b}^2 + 12\tilde{a}\tilde{b}^2\xi^2 + 2\tilde{b}^2\xi^3 + \tilde{a}^2(19\tilde{b}^2 + \tilde{z}^2)\xi \right] \right\}, \tag{G.31}$$

where $\xi = \sqrt{\tilde{z}^2 + \tilde{b}^2}$, $\chi = \tilde{R}^2 + (\tilde{a}+\xi)^2$ and the dimensionless variables were previously defined. The components T_R^R, T_z^R and T_z^z read

$$T_R^R = -\frac{Mc^2}{r_s^3} \frac{\chi^4}{8\pi\xi^3 \left[\chi^{3/2} + \tilde{r}^2 + (\tilde{a}+\xi)(2\tilde{a}+\xi) \right]^5 \left[\chi^{3/2} - \tilde{r}^2 - (\tilde{a}+\xi)(2\tilde{a}+\xi) \right]} \times$$
$$\left\{ \tilde{r}^4 \left[\xi^3(\tilde{a}^2 + 2\tilde{b}^2) + 3\tilde{a}^3\tilde{b}^2 \right] + \tilde{r}^2(\tilde{a}+\xi)^2 \left[9\tilde{a}^3\tilde{b}^2 + 12\tilde{a}\tilde{b}^2\xi^2 + 4\tilde{b}^2\xi^3 \right. \right.$$
$$\left. \left. +2\tilde{a}^2(\tilde{b}^2 - 5\tilde{z}^2)\xi \right] + (\tilde{a}+\xi)^4 \left[6\tilde{a}^3\tilde{b}^2 + 12\tilde{a}\tilde{b}^2\xi^2 + 2\tilde{b}^2\xi^3 + \tilde{a}^2(19\tilde{b}^2 + \tilde{z}^2)\xi \right] \right\}, \tag{G.32}$$

$$T_z^R = T_R^z = -\frac{Mc^2}{r_s^3} \times$$
$$\frac{3\tilde{a}^2\tilde{r}\tilde{z}(\tilde{a}+\xi)\chi^4 \left[\tilde{r}^2 - (a+\xi)^2 \right]}{4\pi\xi \left[\chi^{3/2} + \tilde{r}^2 + (\tilde{a}+\xi)(2\tilde{a}+\xi) \right]^5 \left[\chi^{3/2} - \tilde{r}^2 - (\tilde{a}+\xi)(2\tilde{a}+\xi) \right]}, \tag{G.33}$$

$$T_z^z = \frac{Mc^2}{r_s^3} \frac{\chi^4}{4\pi\xi^2 \left[\chi^{3/2} + \tilde{r}^2 + (\tilde{a}+\xi)(2\tilde{a}+\xi) \right]^5 \left[\chi^{3/2} - \tilde{r}^2 - (\tilde{a}+\xi)(2\tilde{a}+\xi) \right]} \times$$
$$\left\{ \tilde{r}^4\xi^2(\tilde{a}^2 - \tilde{b}^2) - 2\tilde{r}^2\xi(\tilde{a}+\xi)^2 \left[3\tilde{a}\tilde{b}^2 + \xi(2\tilde{a}^2 + \tilde{b}^2) \right] \right.$$
$$\left. +(\tilde{a}+\xi)^4 \left[\tilde{a}^2(\tilde{z}^2 - 8\tilde{b}^2) - \tilde{b}^2\xi(6\tilde{a}+\xi) \right] \right\}, \tag{G.34}$$

and $p_\pm$ is further adimensionalized as $p_\pm = \frac{Mc^2}{r_s^3}\bar{p}_\pm$.

The condition $(\tilde{a} + \tilde{b})^2 > (2\tilde{a} + \tilde{b})$ ensures positive densities and non-singular behaviour for the densities and pressures. The first-order expansion of equation (G.30) reads

$$\bar{\rho} \approx \frac{3\tilde{b}^2 \left[\tilde{R}^2(\tilde{a}^3 + \xi^3) + (\tilde{a}+\xi)^3(\tilde{a}^2 + \xi^2 + 4\tilde{a}\xi) \right]}{4\pi\xi^3[\tilde{R}^2 + (\tilde{a}+\xi)^2]^{7/2}} \times$$
$$\left\{ 1 - \frac{4[\tilde{R}^2 + (\tilde{a}+\xi)(2\tilde{a}+\xi)]}{[\tilde{R}^2 + (\tilde{a}+\xi)^2]^{3/2}} \right\}. \tag{G.35}$$

The surfaces and level curves of the densities equations (G.29) and (G.30) and pressures equation (G.26) are shown in Figs G.6 and G.7, respectively,
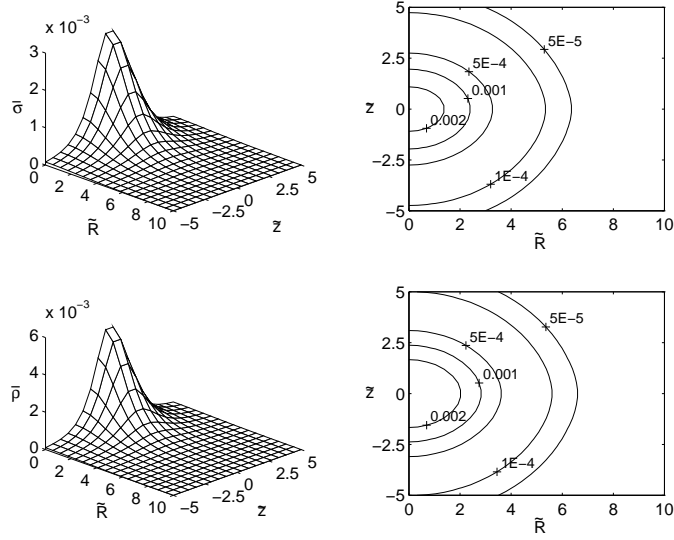
Figure G.6: Surface plot and level curves of the energy density $\bar{\sigma}$ equation (G.29) and 'effective Newtonian density' $\bar{\rho}$ equation (G.30) with parameters $\tilde{a} = 1$ and $\tilde{b} = 2$.
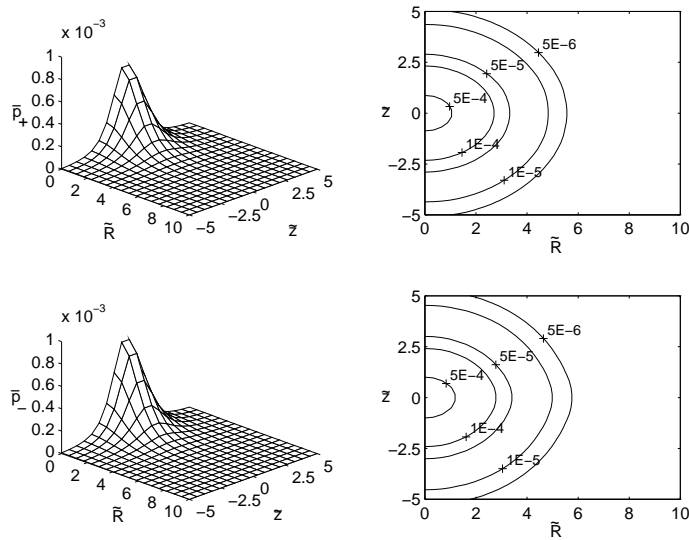

Figure G.7: Surface plot and level curves of the pressures $\bar{p}_{\pm}$ equation (G.26) with parameters $\tilde{a} = 1$ and $\tilde{b} = 2$.
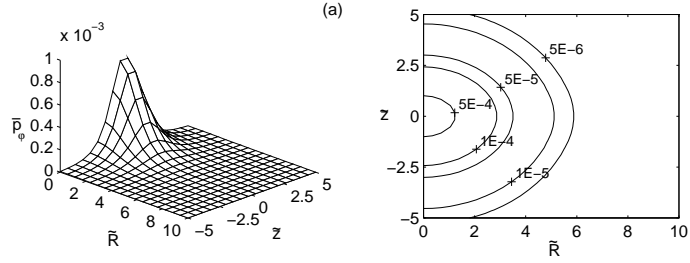
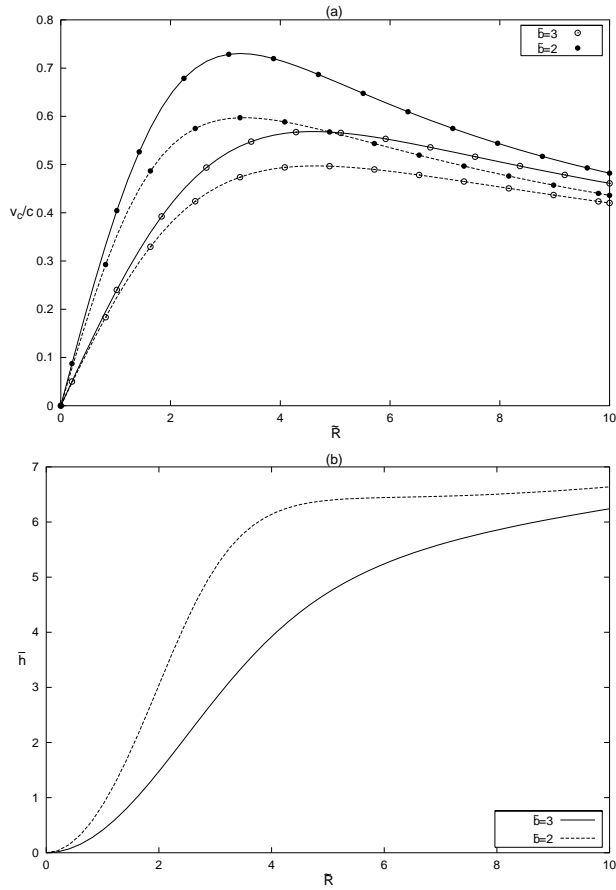Figure G.8: Surface plot and level curves of the azimuthal pressure $\bar{p}_\varphi$ equation (G.31) with parameters $\tilde{a} = 1$ and $\tilde{b} = 2$.

Figure G.9: (a) Relativistic rotation profile equation (G.36) and Newtonian rotation profile (dashed curves) with parameters $\tilde{a} = 1$ and $\tilde{b} = 3$, $\tilde{b} = 2$. (b) Specific angular momentum equation (G.37) for the same parameters.

for parameters $\tilde{a} = 1$, $\tilde{b} = 2$. Fig. G.8(a) displays the surface and level curves for the azimuthal pressure. For these parameters we have $\tilde{p}_\varphi/\tilde{\sigma} < 0.3$, $\tilde{p}_+/\tilde{\sigma} < 0.25$ and $\tilde{p}_-/\tilde{\sigma} < 0.3$.

The tangential circular velocity equation (G.11) and specific angular momentum equation (G.12) are given by

$$\left(\frac{v_c}{c}\right)^2 = \frac{2\tilde{R}^2\chi^{3/2}\left[\tilde{R}^2 + \eta(4\tilde{a} + \tilde{b})\right]}{\left[\chi^{3/2} - \tilde{R}^2 - \eta(2\tilde{a} + \tilde{b})\right]\left[\chi^{5/2} - \tilde{R}^4 - 5\tilde{a}\eta\tilde{R}^2 + \eta^3(2\tilde{a} + \tilde{b})\right]},$$
(G.36)

$$\bar{h} = \frac{\sqrt{2}\tilde{R}^2\left[\chi^{3/2} + \tilde{R}^2 + \eta(2\tilde{a} + \tilde{b})\right]^2\sqrt{\tilde{R}^2 + \eta(4\tilde{a} + \tilde{b})}}{\chi^{9/4}}\left\{\chi^4 + \right.$$
$$\left[\tilde{R}^2 + \eta(2\tilde{a} + \tilde{b})\right]\left[\tilde{R}^4 + 5\tilde{a}\eta\tilde{R}^2 - \eta^3(2\tilde{a} + \tilde{b})\right]$$
$$\left.-4\tilde{R}^2\chi^{3/2}\left[\tilde{R}^2 + \eta(4\tilde{a} + \tilde{b})\right]\right\}^{-1/2},$$
(G.37)

where $h = cr_s\bar{h}$, $\eta = \tilde{a} + \tilde{b}$ and $\chi = \tilde{R}^2 + \eta^2$. The first-order expansion of equation (G.36) reads

$$\frac{v_c}{c} = \frac{\sqrt{2}\tilde{R}\left[\tilde{R}^2 + (\tilde{a} + \tilde{b})(4\tilde{a} + \tilde{b})\right]^{1/2}}{\left[\tilde{R}^2 + (\tilde{a} + \tilde{b})^2\right]^{5/4}}\left\{1 + \frac{\tilde{R}^2\left[\tilde{R}^2 + (\tilde{a} + \tilde{b})(4\tilde{a} + \tilde{b})\right]}{\left[\tilde{R}^2 + (\tilde{a} + \tilde{b})^2\right]^{5/2}}\right\}.$$
(G.38)

In Figs G.9(a) and (b) we display the rotation profiles and curves of specific angular momentum for parameters $\tilde{a} = 1$, $\tilde{b} = 3$ and $\tilde{b} = 2$. As in the previous case, relativistic effects increase the tangential velocity. We also note that the orbits for $\tilde{b} = 3$ and $\tilde{b} = 2$ are all stable.

G.4   A General Relativistic Satoh Model

Satoh (1980) derived other pairs of three-dimensional potential and density functions by inflating the Plummer models of order n. In the limit when $n \to \infty$ the pair takes the simple form

$$\Phi(R, z) = -\frac{Gm}{\sqrt{R^2 + z^2 + a(a + 2\sqrt{z^2 + b^2})}},$$
(G.39a)

$$\rho_N(R,z) = \frac{ab^2 M}{4\pi} \frac{\left[R^2 + z^2 + (a + 2\sqrt{z^2 + b^2})(a + 3\sqrt{z^2 + b^2})\right]}{(z^2 + b^2)^{3/2}\left[R^2 + z^2 + a(a + 2\sqrt{z^2 + b^2})\right]^{5/2}}. \quad \text{(G.39b)}$$

Using the function $f(R,z)$ with Φ given by equation (G.39a), we obtain the following expressions for the non-zero components of the energy-momentum tensor equations (G.4a)–(G.4e)

$$\bar{\sigma} = \frac{\tilde{a}\tilde{b}^2\left[\tilde{R}^2 + \tilde{z}^2 + (\tilde{a} + 2\xi)(\tilde{a} + 3\xi)\right]}{8\pi\xi^3\left[1 + \sqrt{\tilde{R}^2 + \tilde{z}^2 + \tilde{a}(\tilde{a} + 2\xi)}\right]^5}, \quad \text{(G.40a)}$$

$$\bar{p}_R = \bar{p}_\varphi = \frac{\tilde{a}\tilde{b}^2\left[\tilde{R}^2 + \tilde{z}^2 + (\tilde{a} + 2\xi)^2\right]}{8\pi\xi^3\left[1 + \sqrt{\tilde{R}^2 + \tilde{z}^2 + \tilde{a}(\tilde{a} + 2\xi)}\right]^5\left[-1 + \sqrt{\tilde{R}^2 + \tilde{z}^2 + \tilde{a}(\tilde{a} + 2\xi)}\right]},$$
$$\text{(G.40b)}$$

$$\bar{p}_z = \frac{\tilde{a}\tilde{b}^2(\tilde{a} + 2\xi)}{4\pi\xi^2\left[1 + \sqrt{\tilde{R}^2 + \tilde{z}^2 + \tilde{a}(\tilde{a} + 2\xi)}\right]^5\left[-1 + \sqrt{\tilde{R}^2 + \tilde{z}^2 + \tilde{a}(\tilde{a} + 2\xi)}\right]},$$
$$\text{(G.40c)}$$

$$\bar{\rho} = \frac{\tilde{a}\tilde{b}^2\sqrt{\tilde{R}^2 + \tilde{z}^2 + \tilde{a}(\tilde{a} + 2\xi)}\left[\tilde{R}^2 + \tilde{z}^2 + (\tilde{a} + 2\xi)(\tilde{a} + 3\xi)\right]}{4\pi\xi^3\left[1 + \sqrt{\tilde{R}^2 + \tilde{z}^2 + \tilde{a}(\tilde{a} + 2\xi)}\right]^5\left[-1 + \sqrt{\tilde{R}^2 + \tilde{z}^2 + \tilde{a}(\tilde{a} + 2\xi)}\right]},$$
$$\text{(G.40d)}$$

where $\xi = \sqrt{\tilde{z}^2 + \tilde{b}^2}$ and the dimensionless variables were previously defined. As f has the form of equation (G.7), the energy-momentum tensor is diagonal and the radial and azimuthal stresses are equal. We have $\bar{\sigma} > 0$ and $\bar{\rho} > 0$ everywhere and pressures without singularities provided $\tilde{a}(\tilde{a} + 2\tilde{b}) > 1$. In the weak field limit, equation (G.40d) may be expanded as

$$\bar{\rho} \approx \frac{\tilde{a}\tilde{b}^2}{4\pi}\frac{\left[\tilde{R}^2 + \tilde{z}^2 + (\tilde{a} + 2\xi)(\tilde{a} + 3\xi)\right]}{\xi^3\left[\tilde{R}^2 + \tilde{z}^2 + \tilde{a}(\tilde{a} + 2\xi)\right]^{5/2}}\left[1 - \frac{4}{\sqrt{\tilde{R}^2 + \tilde{z}^2 + \tilde{a}(\tilde{a} + 2\xi)}}\right],$$
$$\text{(G.41)}$$

which introduces again a negative first-order relativistic correction to the Newtonian mass density.
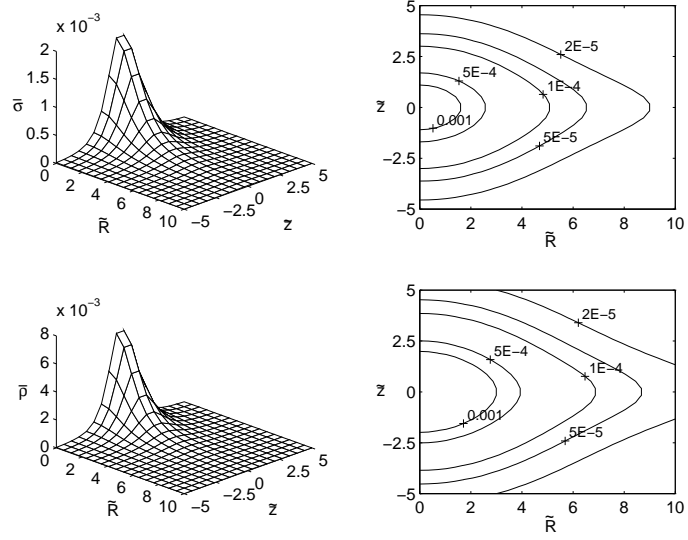
Figure G.10: Surface plot and level curves of the energy density $\bar{\sigma}$ equation (G.40a) and 'effective Newtonian density' $\bar{\rho}$ equation (G.40d) with parameters $\tilde{a} = 1$ and $\tilde{b} = 2$.
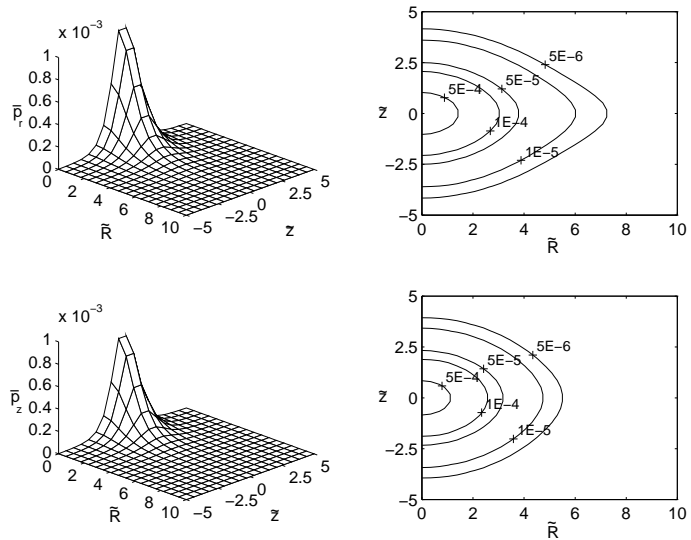

Figure G.11: Surface plot and level curves of the radial pressure $\bar{p}_R$ equation (G.40b) and vertical pressure $\bar{p}_z$ equation (G.40c) with parameters $\tilde{a} = 1$ and $\tilde{b} = 2$.

Expressions for the tangential velocity and angular momentum follow directly from equations (G.11) and (G.12)

$$\left(\frac{v_c}{c}\right)^2 = \frac{2\tilde{R}^2\sqrt{\tilde{R}^2 + \eta}}{\left[-\tilde{R}^2 + \eta + (\tilde{R}^2 + \eta)^{3/2}\right]\left(-1 + \sqrt{\tilde{R}^2 + \eta}\right)}, \quad \text{(G.42)}$$

$$\bar{h} = \frac{\sqrt{2}\tilde{R}^2\left(1 + \sqrt{\tilde{R}^2 + \eta}\right)^2}{(\tilde{R}^2 + \eta)^{3/4}\sqrt{(\tilde{R}^2 + \eta)^2 + \tilde{R}^2 - \eta - 4\tilde{R}^2\sqrt{\tilde{R}^2 + \eta}}}, \quad \text{(G.43)}$$

where $h = cr_s\bar{h}$ and $\eta = \tilde{a}(\tilde{a} + 2\tilde{b})$. The first-order expansion of equation (G.42) is given by

$$\frac{v_c}{c} = \frac{\tilde{R}\sqrt{2}}{\left[\tilde{R}^2 + \tilde{a}(\tilde{a} + 2\tilde{b})\right]^{3/4}}\left\{1 + \frac{\tilde{R}^2}{\left[\tilde{R}^2 + \tilde{a}(\tilde{a} + 2\tilde{b})\right]^{3/2}}\right\}. \quad \text{(G.44)}$$

The surfaces and level curves of the densities and pressures equations (G.40a)–(G.40d) for parameters $\tilde{a} = 1$, $\tilde{b} = 2$ are plotted in Figs G.10 and G.11. We have $\bar{p}_R/\bar{\sigma} < 0.6$ and $\bar{p}_z/\bar{\sigma} < 0.5$, so all energy conditions are satisfied. Rotation profiles and curves of specific angular momentum are displayed in Fig. G.12 for parameters $\tilde{a} = 1$, $\tilde{b} = 2$ and $\tilde{b} = 1$. We note that circular orbits are stable for $\tilde{b} = 2$.

G.5 Geodesic Orbits

An interesting application of the general relativistic galactic models is the study of geodesic orbits outside the galactic plane. As an example we calculate numerically two orbits for the first Miyamoto-Nagai model (Section G.3.1) and compare them with the Newtonian case.

We solve numerically the geodesic equations of motion

$$\ddot{x}^\mu + \Gamma^\mu_{\alpha\beta}\dot{x}^\alpha\dot{x}^\beta = 0, \quad \text{(G.45)}$$

for metric equation (G.2), where $\Gamma^\mu_{\alpha\beta}$ are the Christoffel symbols and the dot denote differentiation with respect to the proper time. With the orthonormal tetrad defined as

$$e^i_{(t)} = \frac{1 + f}{1 - f}(1, 0, 0, 0), \quad e^i_{(R)} = \frac{1}{(1 + f)^2}(0, 1, 0, 0),$$
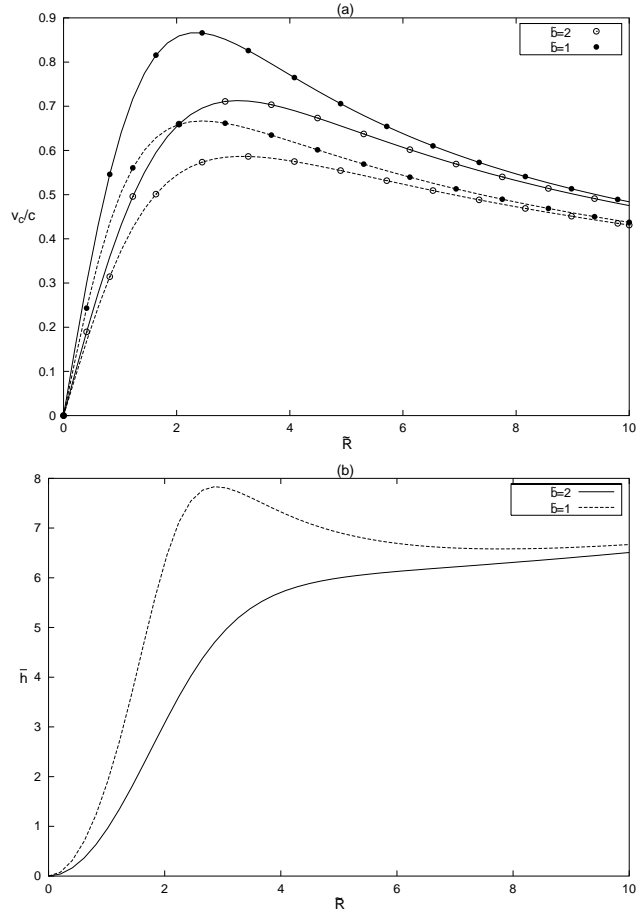
Figure G.12: (a) Relativistic rotation profile equation (G.42) and Newtonian rotation profile (dashed curves) with parameters $\tilde{a} = 1$ and $\tilde{b} = 2$, $\tilde{b} = 1$. (b) Specific angular momentum equation (G.43) for the same parameters.

$$e^i_{(z)} = \frac{1}{(1+f)^2}(0,0,1,0), \quad e^i_{(\varphi)} = \frac{1}{R(1+f)^2}(0,0,0,1), \qquad \text{(G.46)}$$

the tetrad components of the four-velocity v^i read

$$v^i = \gamma(1, v \sin\psi \cos\theta, v \sin\psi \sin\theta, v \cos\psi), \qquad \text{(G.47)}$$

with $\gamma = 1/\sqrt{1-v^2}$ (we have set $c = 1$). The specific energy and angular momentum of the test particle are

$$\mathcal{E} = \gamma \frac{1-f}{1+f}, \qquad \text{(G.48)}$$

$$h = r(1+f)^2 \gamma v \cos\psi. \qquad \text{(G.49)}$$

As initial conditions, we take a position at radius R_0 on the disc's plane and components of the four-velocity $v_0^i = \gamma(1, 0, v_0 \sin\psi, v_0 \cos\psi)$, where v_0 is equal to the tangential velocity of circular orbits at radius R_0. Similar initial conditions for the Newtonian case are chosen with the same angular momentum and energy $\mathcal{E} - 1$. Both the geodesic and Newtonian equations are solved with the fourth-fifth Runge-Kutta method with adaptive size step.

In Figs G.13–G.16 we compare both orbits for the first Miyamoto-Nagai model with parameters $\tilde{a} = 1$ and $\tilde{b} = 1$. For the orbits shown in Figs G.13 and G.14 large radii have been chosen as initial conditions. As expected, general relativistic effects are small. A noticeable difference is seen in a periodic variation of the amplitude of the $\tilde{R}$ coordinate as function of the azimuthal angle in the relativistic case. On the other hand, the orbits shown in Figs G.15 and G.16 have been computed near the center where the gravitational fields are strong, and the deviation between relativistic and Newtonian orbits are much more pronounced.

G.6 First-order Effects of Galactic Rotation on the Rotation Profiles

The galactic models presented in the last sections are all static. Astrophysical objects are expected to have angular momentum; thus, more realistic models should incorporate rotation. An exact stationary general relativistic galactic model could be constructed, for example, if one managed to find a closed form of the Kerr metric in terms of elementary functions in stationary isotropic coordinates, and then repeated the procedure outlined in the
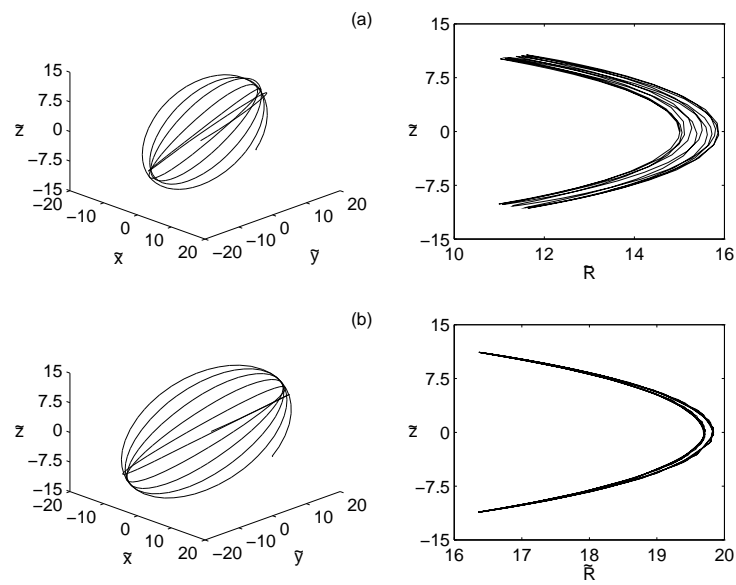
Figure G.13: (a) Geodesic orbits for the first Miyamoto-Nagai model with parameters $\tilde{a} = 1$, $\tilde{b} = 1$. Initial conditions: $\tilde{R}_0 = 15$, $\psi = 45^o$ with energy $\mathcal{E} \approx 0.901$ and angular momentum $\bar{h} \approx 5.03$. (b) Newtonian orbit with energy $\mathcal{E} - 1$ and same angular momentum. Initial conditions: $\tilde{R}_0 \approx 19.84$ and $\psi \approx 36.37^o$.
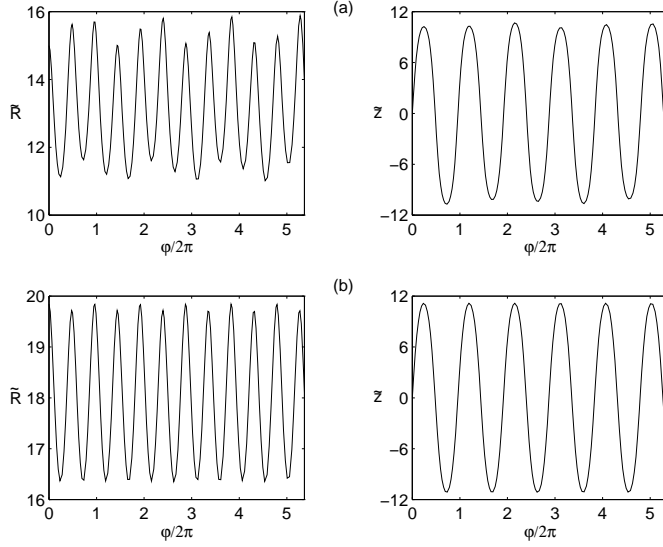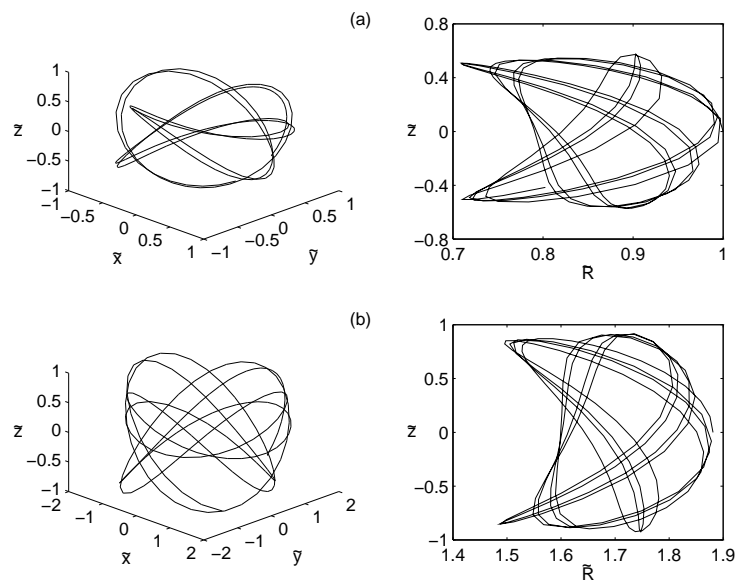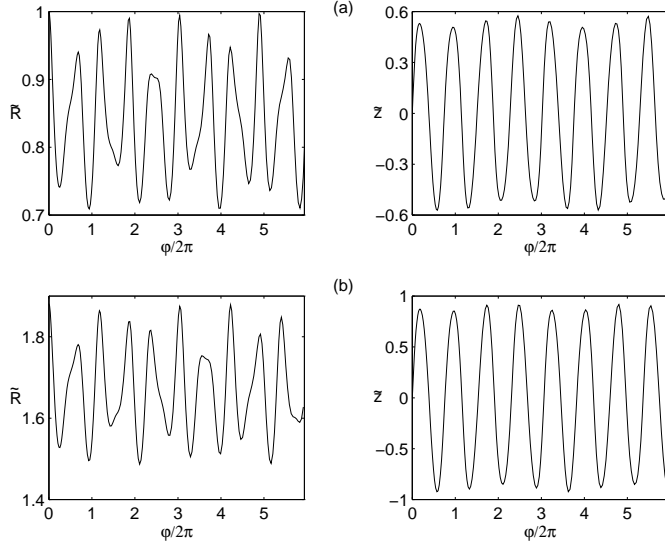
Figure G.14: The coordinates $\tilde{R}$ and $\tilde{z}$ as functions of the number of revolutions $\varphi/2\pi$ for the orbits shown in Fig. G.13. (a) Geodesic and (b) Newtonian orbit.

previous sections to calculate the matter properties. Although this cannot be done for the *exact* Kerr solution, the same is not true for the first-order expansion of the Kerr metric with respect to the rotation parameter. It reads

$$\mathrm{d}s^2 = \left(1 - \frac{2GM}{rc^2}\right)c^2\mathrm{d}t^2 - \frac{\mathrm{d}r^2}{1 - \frac{2GM}{rc^2}} - r^2(\mathrm{d}\theta^2 + \sin^2\theta\mathrm{d}\varphi^2)$$
$$+ \frac{4GM\alpha}{rc}\sin^2\theta\mathrm{d}t\mathrm{d}\varphi, \quad \text{(G.50)}$$

where α is the rotation parameter. If we transform metric equation (G.50) to cylindrical isotropic coordinates (t, R, z, φ) and express it in terms of the function f given by equation (G.3) we obtain

$$\mathrm{d}s^2 = \left(\frac{1-f}{1+f}\right)^2 c^2\mathrm{d}t^2 - (1+f)^4\left(\mathrm{d}R^2 + \mathrm{d}z^2 + R^2\mathrm{d}\varphi^2\right)$$
$$+ \frac{32\alpha R^2 f^3 c^5}{G^2 M^2 (1+f)^2}\mathrm{d}t\mathrm{d}\varphi. \quad \text{(G.51)}$$

Now the function f may be replaced by any of the forms presented in the previous sections to generate space-times with matter. However, a direct

195

Figure G.15: (a) Geodesic orbits for the first Miyamoto-Nagai model with parameters $\tilde{a} = 1$, $\tilde{b} = 1$. Initial conditions: $\tilde{R}_0 = 1$, $\psi = 45^o$ with energy $\mathcal{E} \approx 0.196$ and angular momentum $\bar{h} \approx 0.867$. (b) Newtonian orbit with energy $\mathcal{E} - 1$ and same angular momentum. Initial conditions: $\tilde{R}_0 \approx 1.88$ and $\psi \approx 38.01^o$.

Figure G.16: The coordinates $\tilde{R}$ and $\tilde{z}$ as functions of the number of revolutions $\varphi/2\pi$ for the orbits shown in Fig. G.15. (a) Geodesic and (b) Newtonian orbit.

calculation using the Einstein field equations and metric equation (G.51) shows that the influence of rotation on the physical variables of the matter is of at least $\mathcal{O}(\alpha^2)$. Thus, to have a consistent correction one should also start with metric form equation (G.51) corrected at least to $\mathcal{O}(\alpha^2)$; however, it does not seem possible to express this particular form of the metric with second-order corrections of the rotation parameter. Despite this, a consistent first-order correction of the rotation profiles can be calculated.

We rewrite equation (G.51) as

$$d\tau^2 = g_{tt}dt^2 - g_{RR}\left(dR^2 + dz^2 + R^2d\varphi^2\right) + 2g_{t\varphi}dtd\varphi, \qquad (G.52)$$

where for convenience we have set $c = 1$. Let $v^a = (\dot{t}, 0, 0, \dot{\varphi})$ be the velocity four-vector, where dots denote differentiation with respect to τ. The geodesic equation for circular orbits is

$$g_{tt,R}\dot{t}^2 + 2g_{t\varphi,R}\dot{t}\dot{\varphi} - (R^2 g_{RR}),_R\dot{\varphi}^2 = 0 \Rightarrow$$
$$\frac{\dot{\varphi}}{\dot{t}} = \frac{g_{t\varphi,R} \pm \sqrt{(g_{t\varphi,R})^2 + g_{tt,R}(R^2 g_{RR}),_R}}{(R^2 g_{RR}),_R}. \qquad (G.53)$$

Thus, the prograde and retrograde angular velocities are, in general, differ-

ent. We define an orthonormal tetrad $e_{(b)i}$ as

$$e_{(t)i} = \left(\frac{\sqrt{g_{t\varphi}^2 + R^2 g_{tt} g_{RR}}}{R\sqrt{g_{RR}}}, 0, 0, 0 \right),$$

$$e_{(R)i} = (0, -\sqrt{g_{RR}}, 0, 0), \quad e_{(z)i} = (0, 0, -\sqrt{g_{RR}}, 0),$$

$$e_{(\varphi)i} = \left(\frac{g_{t\varphi}}{R\sqrt{g_{RR}}}, 0, 0, -R\sqrt{g_{RR}} \right),$$
(G.54)

and project the components of v^a on the tetrad: $\mathsf{v}^{(a)} = e_i^{(a)} v^i = \eta^{(a)(b)} e_{(b)i} v^i$

$$\mathsf{v}^{(t)} = \frac{\sqrt{g_{t\varphi}^2 + R^2 g_{tt} g_{RR}}}{R\sqrt{g_{RR}}} \dot{t},$$
(G.55a)

$$\mathsf{v}^{(\varphi)} = -\frac{g_{t\varphi}}{R\sqrt{g_{RR}}} \dot{t} + R\sqrt{g_{RR}} \dot{\varphi}.$$
(G.55b)

Using equation (G.53) in equations (G.55a) and (G.55b) we obtain

$$\frac{\mathsf{v}^{(\varphi)}}{\mathsf{v}^{(t)}} = \frac{1}{\sqrt{g_{t\varphi}^2 + R^2 g_{tt} g_{RR}}} \left[-g_{t\varphi} + \frac{R^2 g_{RR}}{(R^2 g_{RR}),_R} \times \right.$$
$$\left. \left(g_{t\varphi,R} \pm \sqrt{(g_{t\varphi,R})^2 + g_{tt,R}(R^2 g_{RR}),_R} \right) \right].$$
(G.56)

The terms $g_{t\varphi}^2$ and $(g_{t\varphi,R})^2$ in equation (G.56) are of $\mathcal{O}(\alpha^2)$ and thus can be neglected. Using metric equation (G.51), equation (G.56) can be rearranged as

$$v_c = c\sqrt{\frac{-2Rf,_R}{(1-f)(1+f+2Rf,_R)}} \left[\pm 1 + \frac{24\alpha f^2 Rc^4}{G^2 M^2 (1+f)^3} \sqrt{\frac{-Rf,_R(1-f)}{2(1+f+2Rf,_R)}} \right],$$
(G.57)

where c has been reintroduced. The term outside brackets is the tangential velocity equation (G.11). The term with α is always positive, thus the first-order effect of rotation increases (decreases) the prograde (retrograde) tangential velocity.

Equation (G.57) calculated with the functions f used in Sections G.3

and G.4 results in

$$\frac{v_c}{c} = \frac{\sqrt{2}\tilde{R}(\tilde{R}^2+\xi)^{1/4}}{[-1+(\tilde{R}^2+\xi)^{1/2}]^{1/2}[-\tilde{R}^2+\xi+(\tilde{R}^2+\xi)^{3/2}]^{1/2}}\,[\pm 1$$

$$+\frac{3\tilde{\alpha}\tilde{R}^2(\tilde{R}^2+\xi)^{1/4}}{[1+(\tilde{R}^2+\xi)^{1/2}]^3}\sqrt{\frac{2[-1+(\tilde{R}^2+\xi)^{1/2}]}{-\tilde{R}^2+\xi+(\tilde{R}^2+\xi)^{3/2}}}\,\bigg], \qquad\qquad \text{(G.58)}$$

$$\frac{v_c}{c} =$$

$$\frac{\sqrt{2}\tilde{R}\zeta^{3/4}[\tilde{R}^2+(\tilde{a}+\tilde{b})(4\tilde{a}+\tilde{b})]^{1/2}}{\left[\zeta^{3/2}-\tilde{R}^2-(\tilde{a}+\tilde{b})(2\tilde{a}+\tilde{b})\right]^{1/2}\left[\zeta^{5/2}-\tilde{R}^4-5\tilde{a}(\tilde{a}+\tilde{b})\tilde{R}^2+(\tilde{a}+\tilde{b})^3(2\tilde{a}+\tilde{b})\right]^{1/2}}\times$$

$$\left[\pm 1+\frac{3\tilde{\alpha}\tilde{R}^2\zeta^{3/4}[\tilde{R}^2+(\tilde{a}+\tilde{b})(2\tilde{a}+\tilde{b})]^2}{[\zeta^{3/2}+\tilde{R}^2+(\tilde{a}+\tilde{b})(2\tilde{a}+\tilde{b})]^3}\times\right.$$

$$\left.\sqrt{\frac{2[\tilde{R}^2+(\tilde{a}+\tilde{b})(4\tilde{a}+\tilde{b})][\zeta^{3/2}-\tilde{R}^2-(\tilde{a}+\tilde{b})(2\tilde{a}+\tilde{b})]}{\zeta^{5/2}-\tilde{R}^4-5\tilde{a}(\tilde{a}+\tilde{b})\tilde{R}^2+(\tilde{a}+\tilde{b})^3(2\tilde{a}+\tilde{b})}}\,\right]. \qquad \text{(G.59)}$$

Here, in equation (G.58) $\xi = (\tilde{a}+\tilde{b})^2$ for the first Miyamoto-Nagai model (Section G.3.1), $\xi = \tilde{a}(\tilde{a}+2\tilde{b})$ for the Satoh model (Section G.4), and in equation (G.59) $\zeta = \tilde{R}^2 + (\tilde{a}+\tilde{b})^2$ for the second Miyamoto-Nagai model (Section G.3.2). The dimensionless variables were defined in Section G.3.1 and $\tilde{\alpha} = \alpha/r_s$.

In Figs G.17(a) and (b) we plot the curves of progade and retrogade tangential velocity for the first Miyamoto-Nagai model with parameters $\tilde{a} = 1$, $\tilde{b} = 2$ and $\tilde{a} = 1$, $\tilde{b} = 1$ with rotation parameter $\tilde{\alpha} = 0$, $\tilde{\alpha} = 0.2$ and $\tilde{\alpha} = 0.4$. The same curves for the second Miyamoto-Nagai model and for the Satoh model with parameters $\tilde{a} = 1$, $\tilde{b} = 2$ are shown in Figs G.18(a) and (b).

G.7 Discussion

Using a special form for the metric in cylindrical isotropic coordinates, we have constructed what may be interpreted as the general relativistic versions of some known Newtonian models for three-dimensional distributions of matter in galaxies, like those formulated by Miyamoto & Nagai (1975), Nagai & Miyamoto (1976) and Satoh (1980). For the first Miyamoto-Nagai potential and for one Satoh potential we obtained matter distributions that have similar properties: their energy-momentum tensor is diagonal with isotropy of pressure in the radial and azimuthal directions; energy density
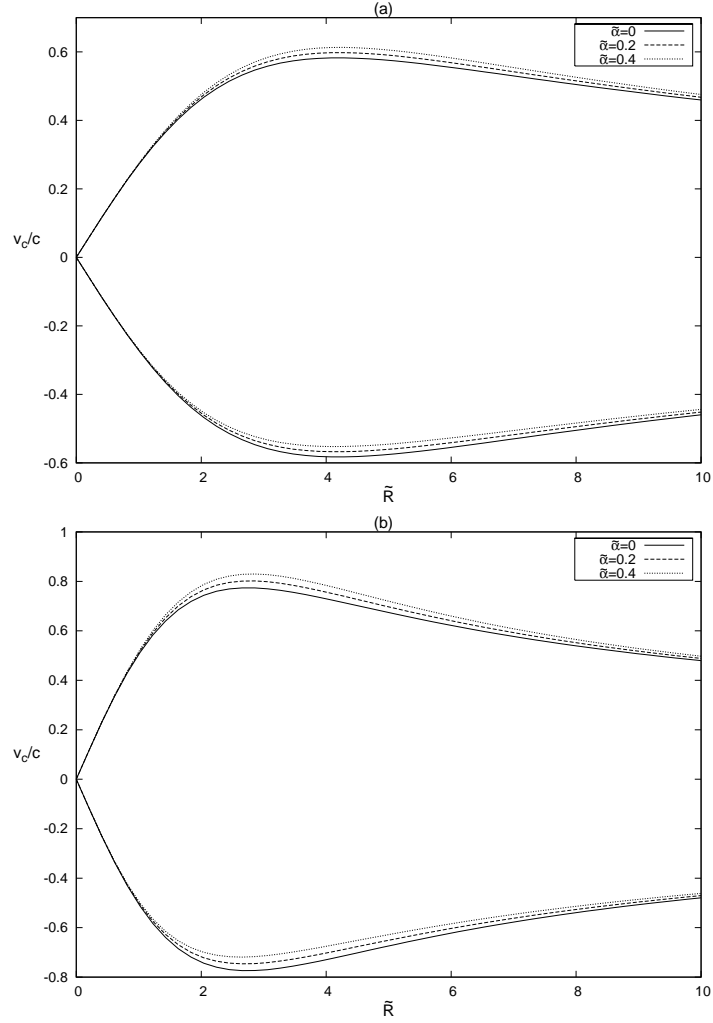
Figure G.17: Prograde (upper) curves and retrogade (lower) curves of tangential velocity equation (G.58) for the first Miyamoto-Nagai model with parameters (a) $\tilde{a} = 1$, $\tilde{b} = 2$ and (b) $\tilde{a} = 1$, $\tilde{b} = 1$. Rotation parameter: $\tilde{\alpha} = 0$ (solid line), $\tilde{\alpha} = 0.2$ and $\tilde{\alpha} = 0.4$.
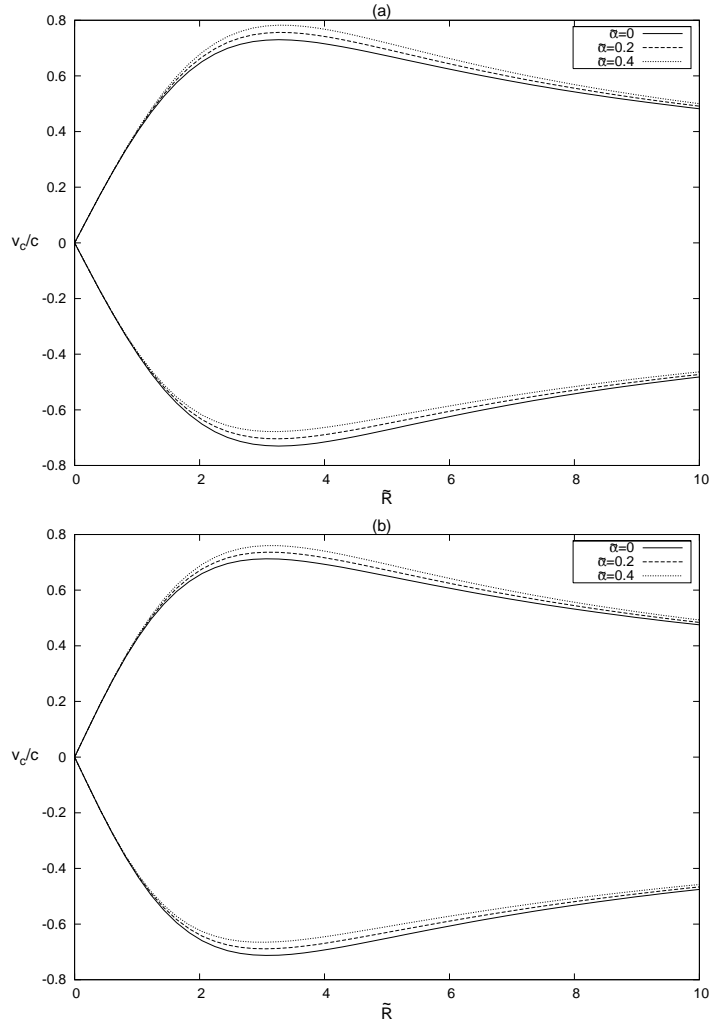
Figure G.18: Prograde (upper) curves and retrograde (lower) curves of tangential velocity for (a) the second Miyamoto-Nagai model equation (G.59) with parameters $\tilde{a} = 1$, $\tilde{b} = 2$ and (b) for the Satoh model equation (G.58) with parameters $\tilde{a} = 1$, $\tilde{b} = 2$. Rotation parameter: $\tilde{\alpha} = 0$ (solid line), $\tilde{\alpha} = 0.2$ and $\tilde{\alpha} = 0.4$.

and the 'effective Newtonian density' are positive everywhere as well as the stresses (pressures) in the vertical direction. For particular values of the free parameters, we found that the dominant energy condition is also satisfied. Stability analysis of the circular geodesic orbits on the galactic plane using an extension of the Rayleigh criteria of stability shows stable orbits for some combination of free parameters. The second Miyamoto-Nagai potential function, after diagonalization of the energy-momentum tensor, yields matter distributions with positive energy density and three different pressures. Also in this case, free parameters can be chosen so that all energy conditions are satisfied and circular orbits are stable on the galactic plane.

As an example of application of the models, we have numerically calculated some geodesic orbits for one of the potentials and compared them with the Newtonian orbits with the same energy and angular momentum. Near the central regions where the gravitational fields are strong, the motion of particles is considerably altered by general relativistic effects.

We also calculated the first-order effects of galactic rotation on the tangential velocity of circular orbits on the galactic plane using an approximate form of the Kerr metric expressed in cylindrical isotropic coordinates. In general, rotation increases the progade tangential velocity and has an opposite effect on the retrogade tangential velocity.

It should be mentioned that the stability study of the models presented based on the extension of Rayleigh criteria of stability is very limited. A more realistic stability analysis should rely on the first-order perturbed general relativistic fluid equations taking into account two spatial coordinates, which may be not a trivial task (see, for instance, Ujevic & Letelier 2004 for the one-dimensional case). This will be the subject of further investigation.

Acknowledgments

References

Bičák J., Ledvinka T.,1993, Phys. Rev. Lett., 71, 1669
Bičák J., Lynden-Bell D., Katz J., 1993a, Phys. Rev. D, 47, 4334
Bičák J., Lynden-Bell D., Pichon C., 1993b, MNRAS, 265, 126
Binney S., Tremaine S., 1987, Galactic Dynamics. Princeton Univ. Press, Princeton, NJ

Bonnor W. A., Sackfield A., 1968, Commun. Math. Phys., 8, 338

Frauendiener J., Klein C., 2001, Phys. Rev. D, 63, 084025

García G., González G., 2004, Phys. Rev. D, 69, 124002

González G., Espitia O. A., 2003, Phys. Rev. D, 68, 104028

González G., Letelier P. S., 1999, Class. Quantum Grav., 16, 479

González G., Letelier P. S., 2000, Phys. Rev. D, 62, 064025

González G., Letelier P. S., 2004, Phys. Rev. D, 69, 044013

Karas V., Huré J. M., Semerák O., 2004, Class. Quantum Grav., 21, R1

Katz J., Bičák J., Lynden-Bell D., 1999, Class. Quantum Grav., 16, 4023

King I. R., 1966, AJ, 71, 64

Klein C., 1997, Class. Quantum Grav., 14, 2267

Klein C., 2001, Phys. Rev. D, 63, 064033

Klein C., 2002, Phys. Rev. D, 65, 084029

Klein C., 2003a, Phys. Rev. D, 68, 027501

Klein C., 2003b, Ann. Phys., 12 (10), 599

Klein C., Richter O., 1999, Phys. Rev. Lett., 83, 2884

Kuzmin G. G., 1956, AZh, 33, 27

Landau L. D., Lifshitz E. M., 1987, Fluid Mechanics, 2nd edn. Pergamon Press, Oxford

Lemos J. P. S., 1989, Class. Quantum Grav., 6, 1219

Lemos J. P. S., Letelier P. S., 1993, Class. Quantum Grav., 10, L75

Lemos J. P. S., Letelier P. S., 1994, Phys. Rev. D, 49, 5135

Lemos J. P. S., Letelier P. S., 1996, Int. J. Mod. Phys. D, 5, 53

Letelier P. S., 1999, Phys. Rev. D, 60, 104042

Letelier P. S., 2003, Phys. Rev. D, 68, 104002 Letelier P. S., Oliveira S. R., 1987, J. Math. Phys., 28, 165

Lynden-Bell D., Pineault S., 1978, MNRAS, 185, 679

Miyamoto M., Nagai R., 1975, PASJ, 27, 533

Morgan T., Morgan L., 1969, Phys. Rev., 183, 1097

Morgan L., Morgan T., 1970, Phys. Rev. D, 2, 2756

Nagai R., Miyamoto M., 1976, PASJ, 28, 1

Neugebauer G., Meinel R., 1995, Phys. Rev. Lett., 75, 3046

Plummer H.C., 1911, MNRAS, 71, 460

Rayleigh J. W. S., 1917, Proc. R. Soc. London A, 93, 148

Satoh G., 1980, PASJ, 32, 41

Toomre A., 1963, ApJ, 138, 385

Ujevic M., Letelier P. S., 2004, Phys. Rev. D, 70, 084015

Vogt D., Letelier P. S., 2003, Phys. Rev. D, 68, 084010

Vogt D., Letelier P. S., 2004, Phys. Rev. D, 70, 064003

Apêndice H

On Multipolar Analytical
Potentials for Galaxies

Abstract

We present analytical potential–density pairs in three dimensions for the gravitational field of galaxies, obtained by thickening the multipolar expansion up to the quadrupole term. These may be interpreted as generalizations of the Miyamoto and Nagai potential–density pairs. With a suitable restriction on the possible values of the multipole moments, the density distributions are positive and monotone decreasing functions of the radial and axial coordinates.

Key Words: galaxies: kinematics and dynamics – galaxies: structure

H.1   Introduction

There are several three-dimensional analytical models in the literature for the gravitational field of different types of galaxies and galactic components. Jaffe (1983) and Hernquist (1990) discuss models for spherical galaxies and bulges. Three-dimensional models for flat galaxies were obtained by Miyamoto and Nagai (1975) and Satoh (1980). de Zeeuw and Pfenniger (1989) considered a set of ellipsoidal models appropriate to galactic bars. Long and Murali (1992) derived simple potential–density pairs for a

prolate and a triaxial bar by softening a thin needle with a spherical and a Miyamoto and Nagai potential, respectively. See Binney and Tremaine (1987) for a discussion of other galactic models. There also exist several general relativistic models of disks, e.g., Morgan and Morgan (1969, 1970), Bičák et al. (1993), Lemos and Letelier (1994), González and Letelier (2000, 2004), Vogt and Letelier (2003, 2005a). Recently, a general relativistic version of the Miyamoto and Nagai models was studied (Vogt and Letelier 2005b).

The potential–density pairs obtained by Miyamoto and Nagai (1975) are inflated versions of the thin-disk family first derived by Toomre (1963). In this work we consider a set of three-dimensional potential–density pairs obtained by using the same procedure of Miyamoto and Nagai on the multipolar expansion up to the quadrupole term. This generates a sequence of potential–density pairs that reduces to that of Miyamoto and Nagai for particular values of the multipole moments. This is done in subsection H.2.1 and subsection H.2.2. The thin-disk limit is investigated in subsection H.2.3 and corresponds to generalizations of Toomre's family of disks. Finally, the results are discussed in section H.3.

H.2 Multipolar Models for Flattened Galaxies

A general expression for a multipolar expansion in spherical coordinates can be cast as

$$\Phi = -\sum_{n=0}^{\infty} a_n \frac{P_n(\cos\theta)}{r^{n+1}}, \qquad (\text{H.1})$$

where P_n are the Legendre polynomials and a_n are coefficients related to the multipolar moments. We consider only the expansion up to the quadrupole term ($n = 2$). In cylindrical coordinates the explicit form reads

$$\Phi = -\frac{Gm}{\sqrt{R^2 + z^2}} - \frac{Dz}{(R^2 + z^2)^{3/2}} - \frac{Q(-R^2 + 2z^2)}{2(R^2 + z^2)^{5/2}}, \qquad (\text{H.2})$$

where D and Q are the dipole and quadrupole moments, respectively.

In the following three-dimensional models the mass-density distribution is obtained directly from Poisson equation,

$$\rho = \frac{1}{4\pi G}\left(\Phi_{,RR} + \frac{\Phi_{,R}}{R} + \Phi_{,zz}\right). \qquad (\text{H.3})$$

Other physical quantities of interest are the circular velocity, v_c of particles in the galactic plane, the epicyclic frequency, κ, and the vertical frequency, ν, of small oscillations about the equilibrium circular orbit in the galactic plane. They are calculated with the expressions (Binney and Tremaine 1987):

$$v_c^2 = R\Phi_{,R}, \tag{H.4}$$

$$\kappa^2 = \Phi_{,RR} + \frac{3}{R}\Phi_{,R}, \tag{H.5}$$

$$\nu^2 = \Phi_{,zz}, \tag{H.6}$$

where all quantities are evaluated on $z = 0$. The stability conditions are set by $\kappa^2 \geq 0$ and $\nu^2 \geq 0$.

H.2.1   Generalized Miyamoto and Nagai Model 2

We first consider $Q = 0$, and apply the transformation $z \to a + \sqrt{z^2 + b^2}$ on the multipolar expansion equation (H.2), where a, b are non-negative constants. Using equation (H.3), we obtain

$$\tilde{\rho} = \frac{\tilde{b}^2}{4\pi\xi^3 \left[\tilde{R}^2 + (1+\xi)^2\right]^{7/2}} \left\{ \tilde{R}^4(1-\tilde{D}) + \tilde{R}^2(1+\xi)\left[\tilde{D}(1-8\xi)\right.\right.$$
$$\left.\left. +(1+\xi)(2+3\xi)\right] + (1+\xi)^3\left[2\tilde{D}(1+4\xi) + (1+\xi)(1+3\xi)\right]\right\}, \tag{H.7}$$

where the variables and parameters were rescaled in terms of a: $\tilde{R} = R/a$, $\tilde{z} = z/a$, $\tilde{b} = b/a$, $\tilde{D} = D/(Gma)$, $\rho = m\tilde{\rho}/a^3$, and $\xi = \sqrt{\tilde{z}^2 + \tilde{b}^2}$. For the particular value $\tilde{D} = 1$, equation (H.7) reduces to the mass density of the Miyamoto–Nagai model 2.

Unfortunately the density distribution, equation (H.7), has some defects. For certain ranges of the parameters $\tilde{b}$ and $\tilde{D}$ it is not a monotone decreasing function of the radial and axial coordinates, and even has domains with negative densities. To overcome this, we impose a reasonable restriction that the derivative of the density distribution with respect to the $\tilde{R}$ coordinate along $\tilde{z} = 0$ should have only one critical point at $(\tilde{R}, \tilde{z}) = (0,0)$ as well as the derivative with respect to $\tilde{z}$ along $\tilde{R} = 0$. A graphical study of the resulting equations is displayed in figures H.1a–b. In figure H.1a the curves of $\tilde{\rho}_{,\tilde{R}} = 0$ are plotted as functions of the radial coordinate and the parameter $\tilde{D}$ for some values of $\tilde{b}$. In this case decreasing $\tilde{b}$ narrows the interval of $\tilde{D}$ for which there are no other critical points, as on $\tilde{R} = 0$. Figure H.1b shows

the curve of $\tilde{\rho}_{,\tilde{z}} = 0$ as functions of $\tilde{z}$ and $\tilde{D}$ for the same values of $\tilde{b}$. One can see from both graphs that the allowed interval for the parameter $\tilde{D}$ for a fixed value of $\tilde{b}$ in the case (a) is contained in the allowed interval in case (b).

The expressions for the circular velocity, epicyclic frequency and vertical frequency follow from equations (H.4)–(H.6)

$$\tilde{v}_c^2 = \frac{\tilde{R}^2 \left[\tilde{R}^2 + (1+\tilde{b})(1+\tilde{b}+3\tilde{D}) \right]}{\left[\tilde{R}^2 + (1+\tilde{b})^2 \right]^{5/2}}, \tag{H.8}$$

$$\tilde{\kappa}^2 = \frac{1}{\left[\tilde{R}^2 + (1+\tilde{b})^2 \right]^{7/2}} \left\{ \tilde{R}^4 + \tilde{R}^2(1+\tilde{b}) \left[5(1+\tilde{b}) - 3\tilde{D} \right] \right.$$

$$\left. +4(1+\tilde{b})^3(1+\tilde{b}+3\tilde{D}) \right\}, \tag{H.9}$$

$$\tilde{\nu}^2 = \frac{\tilde{R}^2(1+\tilde{b}-\tilde{D}) + (1+\tilde{b})^2(1+\tilde{b}+2\tilde{D})}{\tilde{b} \left[\tilde{R}^2 + (1+\tilde{b})^2 \right]^{5/2}}, \tag{H.10}$$

where $v_c^2 = Gm\tilde{v}_c^2/a$, $\kappa^2 = Gm\tilde{\kappa}^2/a^3$, and $\nu^2 = Gm\tilde{\nu}^2/a^3$. The condition $\tilde{v}_c^2 \geq 0$ and the stability conditions $\kappa^2 \geq 0$ and $\nu^2 \geq 0$ also impose restrictions on the possible values of $\tilde{D}$ and $\tilde{b}$. We find that $\tilde{D} \geq -(1+\tilde{b})/3$ ensures the positivity of the circular velocity and of the square of the epicyclic frequency, whereas the square of the vertical frequency is always non-negative if $\tilde{D} \geq -(1+\tilde{b})/2$.

In figures H.2a–c we plot some isodensity curves of the density function, equation (H.7), with parameter $\tilde{b} = 0.5$ and (a) $\tilde{D} = 1$, (b) $\tilde{D} = 0.5$, and (c) $\tilde{D} = -0.1$. For these values the density is a monotone decreasing function, as can be checked from figure H.1. It is clearly seen that as the parameter $\tilde{D}$ decreases, the density distribution becomes more flattened. Figure H.2d and figures H.3a–b show, respectively, curves of the velocity profile, equation (H.8), the epicyclic frequency, equation (H.9), and of the vertical frequency, equation (H.10), for the same parameters as in figures H.2a–c. With decreasing $\tilde{D}$ the radius where the highest circular velocity occurs is increased and the epicyclic frequency is lowered. The vertical frequency becomes lower near the center, but for $\tilde{R} \gtrsim 2$ it is increased.
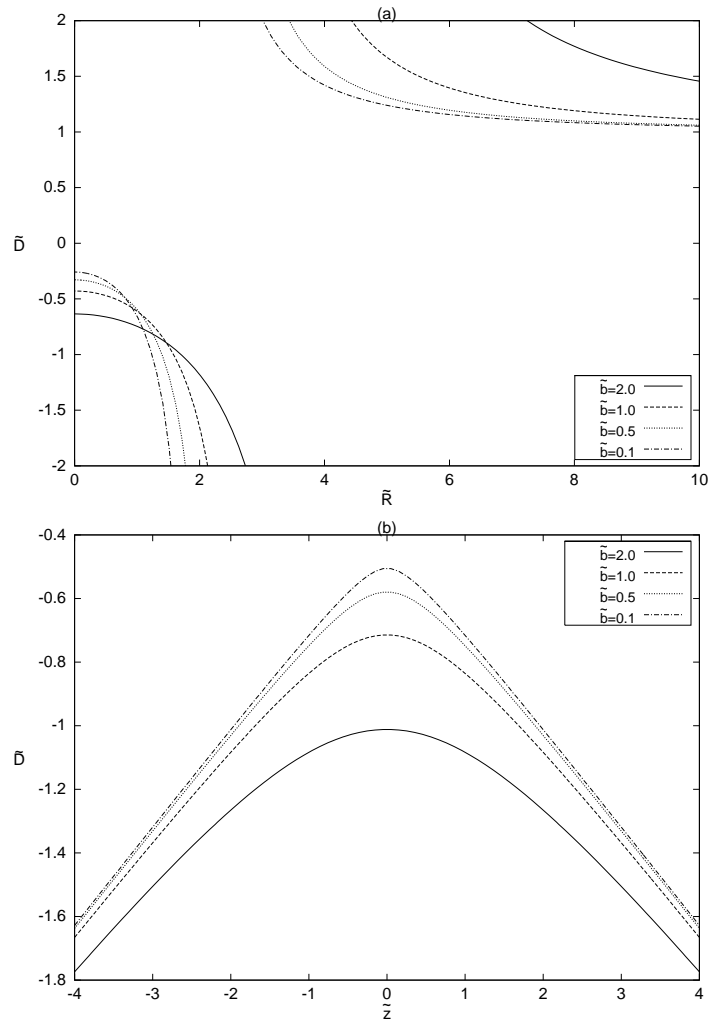
Figure H.1: (a) Curves of $\tilde{\rho}_{,\tilde{R}} = 0$ as functions of $\tilde{R}$ and $\tilde{D}$ for $\tilde{b} = 2$, 1, 0.5, and 0.1. (b) $\tilde{\rho}_{,\tilde{z}} = 0$ as functions of $\tilde{z}$ and $\tilde{D}$ for $\tilde{b} = 2$, 1, 0.5, and 0.1.
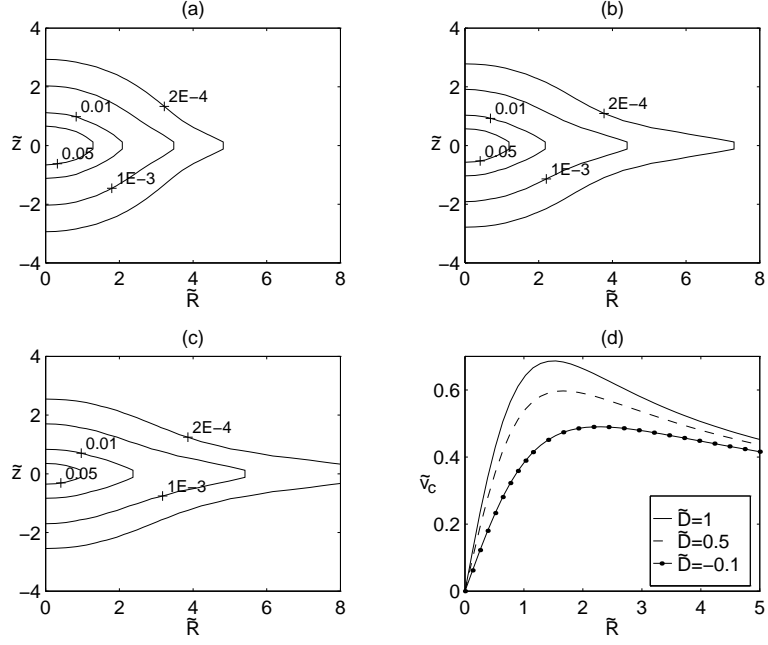
Figure H.2: Constant-density curves of equation (H.7) with parameters $\tilde{b} = 0.5$ and (a) $\tilde{D} = 1$, (b) $\tilde{D} = 0.5$, and (c) $\tilde{D} = -0.1$. (d) The circular velocity $\tilde{v}_\mathrm{c}$ (equation (H.8)), in the galactic plane for cases (a)–(c).
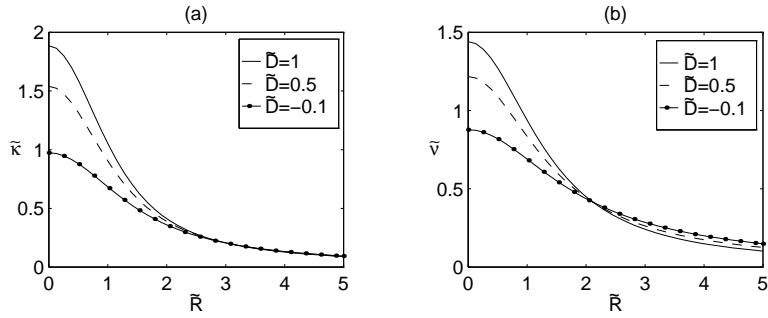
Figure H.3: Curves of (a) the epicyclic frequency, $\tilde{\kappa}$ (equation (H.9)), and (b) the vertical frequency, $\tilde{\nu}$ (equation (H.10)), for the same parameters as in figure H.2.

H.2.2 Generalized Miyamoto and Nagai Model 3

We now consider the full expression equation (H.2) and apply the transformation $z \to a + \sqrt{z^2 + b^2}$. The resulting mass density distribution reads

$$\tilde{\rho} = \frac{\tilde{b}^2}{8\pi\xi^3 \left[\tilde{R}^2 + (1+\xi)^2\right]^{9/2}} \left\{ 2\tilde{R}^6(1-\tilde{D}) + 3\tilde{R}^4 \left[2(1+\xi)^3 - 6\tilde{D}\xi(1+\xi) \right. \right.$$

$$\left. -3\tilde{Q} \right] + 3\tilde{R}^2(1+\xi)^2 \left[2(1+\xi)^2(1+2\xi) + 2\tilde{D}(1+\xi) - \tilde{Q}(1+25\xi) \right]$$

$$\left. +2(1+\xi)^4 \left[(1+\xi)^2(1+3\xi) + 2\tilde{D}(1+\xi)(1+4\xi) + 3\tilde{Q}(1+5\xi) \right] \right\}, \quad \text{(H.11)}$$

where the variables and parameters have been rescaled, as in subsection H.2.1 and $\tilde{Q} = Q/(Gma^2)$. For particular values $\tilde{D} = 1$, $\tilde{Q} = 2/3$ we recover the Miyamoto and Nagai model 3.

Also here the range of the parameters must be restricted to produce physically acceptable density distributions. In figures H.4a–b we show, respectively, some curves of $\tilde{\rho}_{,\tilde{R}} = 0$ along $\tilde{z} = 0$ and $\tilde{\rho}_{,\tilde{z}} = 0$ along $\tilde{R} = 0$ as functions of $\tilde{Q}$ for some sets of values of $\tilde{D}$ and $\tilde{b}$. The expressions for the circular velocity, epicyclic frequency and vertical frequency follow from equations (H.4)–(H.6)

$$\tilde{v}_c^2 = \frac{\tilde{R}^2}{2\left[\tilde{R}^2 + (1+\tilde{b})^2\right]^{7/2}} \left\{ 2\tilde{R}^4 + \tilde{R}^2 \left[4(1+\tilde{b})^2 + 6\tilde{D}(1+\tilde{b}) - 3\tilde{Q} \right] \right.$$

$$\left. +2(1+\tilde{b})^2 \left[(1+\tilde{b})^2 + 3\tilde{D}(1+\tilde{b}) + 6\tilde{Q} \right] \right\}, \quad \text{(H.12)}$$

$$\tilde{\kappa}^2 = \frac{1}{2\left[\tilde{R}^2 + (1+\tilde{b})^2\right]^{9/2}} \left\{ 2\tilde{R}^6 + 3\tilde{R}^4 \left[4(1+\tilde{b})^2 - 2\tilde{D}(1+\tilde{b}) + \tilde{Q} \right] \right.$$

$$+18\tilde{R}^2(1+\tilde{b})^2 \left[(1+\tilde{b})^2 + \tilde{D}(1+\tilde{b}) - 3\tilde{Q} \right]$$

$$\left. +8(1+\tilde{b})^4 \left[(1+\tilde{b})^2 + 3\tilde{D}(1+\tilde{b}) + 6\tilde{Q} \right] \right\}, \quad \text{(H.13)}$$

$$\tilde{\nu}^2 = \frac{1}{2\tilde{b}\left[\tilde{R}^2 + (1+\tilde{b})^2\right]^{7/2}} \left\{ 2\tilde{R}^4(1+\tilde{b}-\tilde{D}) + \tilde{R}^2(1+\tilde{b}) \left[4(1+\tilde{b})^2 \right. \right.$$

$$\left. +2\tilde{D}(1+\tilde{b}) - 9\tilde{Q} \right] + 2(1+\tilde{b})^3 \left[(1+\tilde{b})^2 + 2\tilde{D}(1+\tilde{b}) + 3\tilde{Q} \right] \right\}, \quad \text{(H.14)}$$

A graphical analysis of the constraints on the parameters imposed by $\tilde{v}_c^2 \geq 0$, $\kappa^2 \geq 0$ and $\nu^2 \geq 0$ shows that they are contained in the restrictions imposed by the gradient of the mass density.
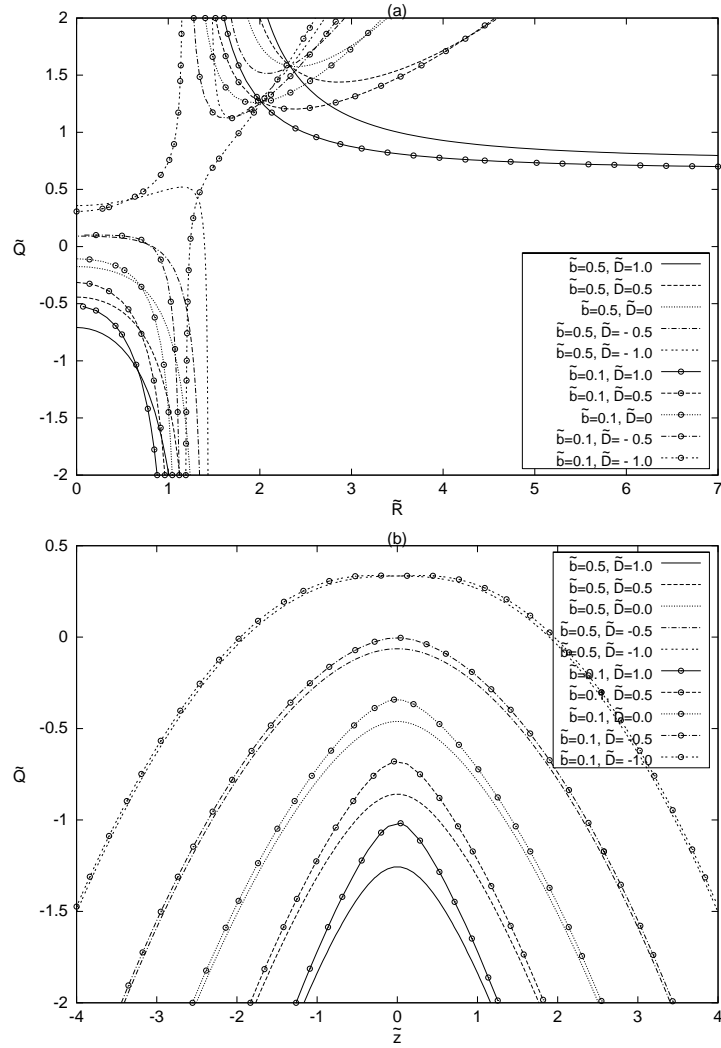
Figure H.4: (a) Curves of $\tilde{\rho}_{,\tilde{R}} = 0$ as functions of $\tilde{R}$ and $\tilde{Q}$ for some values of the parameters $\tilde{b}$ and $\tilde{D}$. (b) Curves of $\tilde{\rho}_{,\tilde{z}} = 0$ as functions of $\tilde{z}$ and $\tilde{Q}$ for some values of the parameters $\tilde{b}$ and $\tilde{D}$.
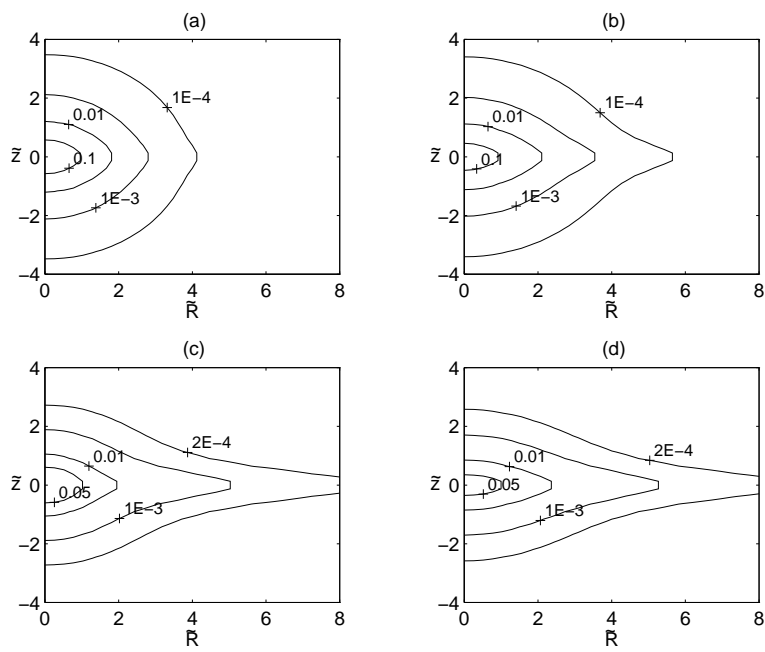
Figure H.5: Constant density curves of equation (H.11) with parameters $\tilde{b} = 0.5$ and (a) $\tilde{D} = 1$, $\tilde{Q} = 2/3$, (b) $\tilde{D} = 1$, $\tilde{Q} = -0.1$, (c) $\tilde{D} = 0$, $\tilde{Q} = 2/3$, and (d) $\tilde{D} = 0$, $\tilde{Q} = -0.1$.
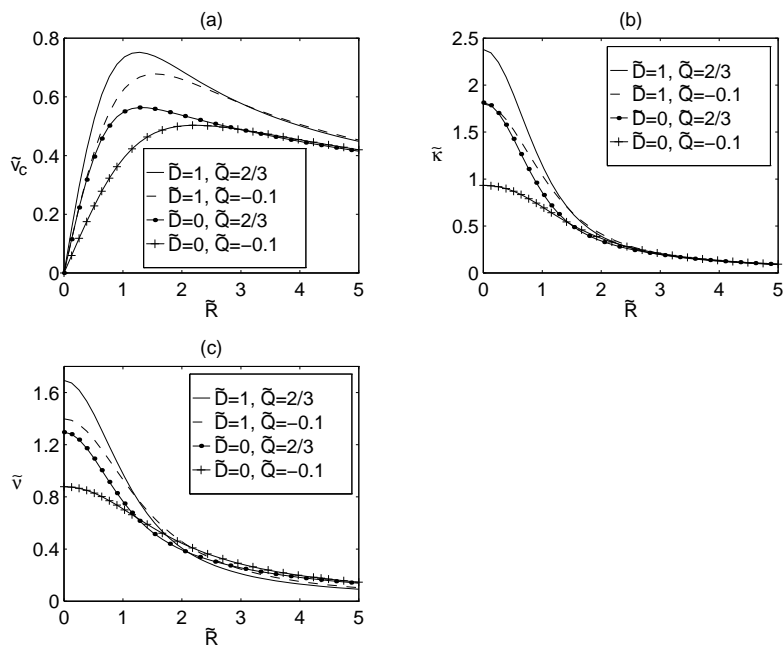
Figure H.6: Curves of (a) the circular velocity $\tilde{v}_c$ equation (H.12) in the galactic plane, (b) the epicyclic frequency $\tilde{\kappa}$ equation (H.13) and (c) the vertical frequency $\tilde{\nu}$ equation (H.14) for the same parameters as in figure H.5.

Some level curves of the mass density, equation (H.11), are displayed in figures H.5a–d. In general, as $\tilde{D}$ and $\tilde{Q}$ are lowered for a fixed $\tilde{b}$, the mass distribution profile becomes flatter. We also note from figures H.6a–c that the maximum of the circular velocity is shifted to larger radii, and the epicyclic frequencies and vertical frequencies are lowered near the center.

H.2.3   Thin Disk Limit

To investigate the thin limit of the potential–density pairs deduced in the previous sections, it is more convenient to rederive an expression for the surface density, σ, by applying the transformation $z \to a + |z|$ on the multipolar expansion, equation (H.2) and using the well-known relation (Binney and Tremaine 1987),

$$\sigma = \frac{1}{2\pi G}\Phi_{,z}, \tag{H.15}$$

214

where the right-hand side is evaluated at $z \to 0^+$. We obtain

$$\tilde{\sigma} = \frac{1}{4\pi(\tilde{R}^2 + 1)^{7/2}} \left[2(\tilde{R}^2 + 1)^2(1 - \tilde{D}) + 6\tilde{D}(\tilde{R}^2 + 1) - 3\tilde{Q}(3\tilde{R}^2 - 2) \right]. \tag{H.16}$$

The variables and parameters were rescaled as in subsection H.2.2, and $\sigma = m\tilde{\sigma}/a^2$. In particular cases with $\tilde{D} = 1$, $\tilde{Q} = 0$ and $\tilde{D} = 1$, $\tilde{Q} = 2/3$ we obtain Toomre's models 2 and 3, respectively (Toomre 1963). Expressions for the circular velocity and epicyclic frequency are given by equation (H.12) and equation (H.13) with $\tilde{b} = 0$, and the vertical frequency is calculated from equation (H.6) evaluated at $z \to 0^+$:

$$\tilde{\nu}^2 = \frac{1}{2(\tilde{R}^2 + 1)^{9/2}} \left[2\tilde{R}^6 + 9\tilde{R}^4(2\tilde{D} - \tilde{Q}) \right.$$
$$\left. + 6\tilde{R}^2(-1 + \tilde{D} + 12\tilde{Q}) - 4(1 + 3\tilde{D} + 6\tilde{Q}) \right]. \tag{H.17}$$

Figure H.7 shows curves of $\tilde{\sigma}_{,\tilde{R}} = 0$ (lines without circles) and $\tilde{\nu} = 0$ (lines with circles) as functions of $\tilde{Q}$ and $\tilde{R}$ for some values of the parameter $\tilde{D}$. In the thin limit, the disks always have regions of vertical instability. The Kuzmin disk ($\tilde{D} = \tilde{Q} = 0$) is stable for $\tilde{R} \geq \sqrt{2}$; Toomre's model 2 ($\tilde{D} = 1$, $\tilde{Q} = 0$) is stable for $\tilde{R} \geq \sqrt{2}\sqrt{-2 + \sqrt{6}}$; if $\tilde{Q} = 0$ the disk is stable for

$$\tilde{R} \geq \frac{\sqrt{2}}{2} \left[1 - 9\tilde{D} + \sqrt{3(27\tilde{D}^2 + 2\tilde{D} + 3)} \right]^{1/2} \tag{H.18}$$

if $\tilde{D} \geq -1/3$; and

$$0 \leq \tilde{R} \leq \frac{\sqrt{2}}{2} \left[1 - 9\tilde{D} - \sqrt{3(27\tilde{D}^2 + 2\tilde{D} + 3)} \right]^{1/2}, \tag{H.19}$$

$$\text{and } \tilde{R} \geq \frac{\sqrt{2}}{2} \left[1 - 9\tilde{D} + \sqrt{3(27\tilde{D}^2 + 2\tilde{D} + 3)} \right]^{1/2} \tag{H.20}$$

if $\tilde{D} < -1/3$.

In figure H.8 we plot some curves of the surface density equation (H.16), the circular frequency equation (H.12) with $\tilde{b} = 0$, the epicyclic frequency equation (H.13) also with $\tilde{b} = 0$ and the vertical frequency equation (H.17) for some values of $\tilde{D}$ and $\tilde{Q}$. The behaviour of the three first physical quantities, displayed as the multipole parameters are decreased, is very similar to those of the thick-disk model of the previous section.
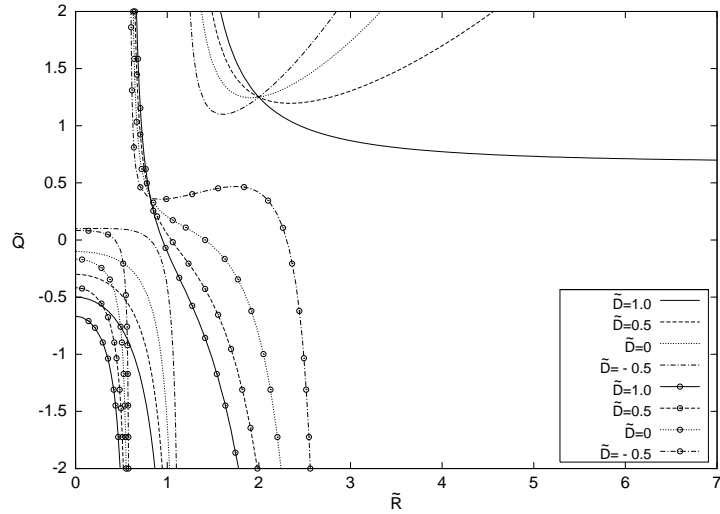
Figure H.7: Curves of $\tilde{\sigma}_{,\tilde{R}} = 0$ (lines without circles) and of $\tilde{\nu} = 0$ (lines with circles) as functions of $\tilde{Q}$ and $\tilde{R}$ for $\tilde{D} = 1$, 0.5, 0, and -0.5.

H.3   Discussion

A Miyamoto and Nagai-like transformation was applied on the multipolar expansion up to the quadrupole term to produce potential–density pairs for flattened galaxies. These models, the first without the quadrupole term and the second with the quadrupole term, may be viewed as generalizations of the Miyamoto and Nagai models 2 and 3, respectively. The thin disk limit was also investigated and corresponds to generalizations of Toomre's models 2 and 3. For each model we also calculated the velocity profile in the galactic plane and the epicyclic and vertical frequencies of oscillation of perturbed circular orbits.

The major drawback of our models is that the density distribution is not a monotone decreasing function of the radial and axial coordinates for arbitrary values of the free parameters. Thus we imposed the condition that the derivatives of the density distributions with respect to R and z do not have critical points, except at the origin. These imposed restrictions on the possible ranges of the multipole moments. We found that, except in the thin case limit, those restrictions were also suficient to ensure non-negative circular velocities and also non-negative epicyclic and vertical frequencies (disk stability on the $z = 0$ plane).
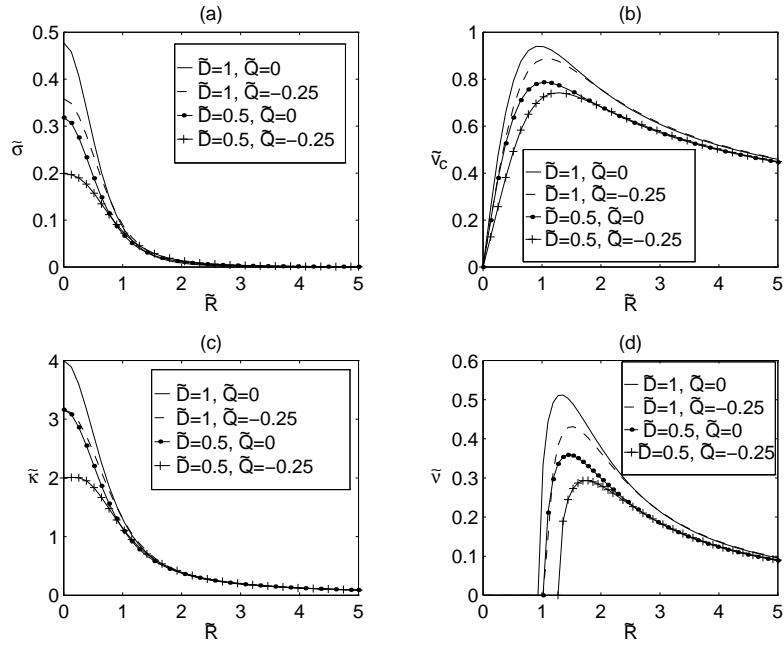
Figure H.8: (a) Curves of the surface density equation (H.16), (b) the circular velocity equation (H.12) with $\tilde{b} = 0$, (c) the epicyclic frequency equation (H.13) with $\tilde{b} = 0$ and the vertical frequency equation (H.17). Parameters: $\tilde{D} = 1$, $\tilde{Q} = 0$ (solid lines); $\tilde{D} = 1$, $\tilde{Q} = -0.25$ (dashed lines); $\tilde{D} = 0.5$, $\tilde{Q} = 0$ (lines with points); $\tilde{D} = 0.5$, $\tilde{Q} = -0.25$ (lines with +).

References

Bičák, J., Lynden-Bell, D., & Katz, J. 1993, Phys. Rev. D, 47, 4334
Binney, S., & Tremaine, S. 1987, Galactic Dynamics (Princeton, Princeton University Press), p. 121
de Zeeuw, T., & Pfenniger, D. 1988, MNRAS, 235, 949
González, G. A., & Letelier, P. S. 2000, Phys. Rev. D, 62, 064025
González, G. A., & Letelier, P. S. 2004, Phys. Rev. D, 69, 044013
Hernquist, L. 1990, ApJ, 356, 359
Jaffe, W. 1983, MNRAS, 202, 995
Lemos, J. P. S., & Letelier, P. S. 1994, Phys. Rev. D, 49, 5135
Long, K., & Murali, C. 1992, ApJ, 397, 44
Miyamoto, M., & Nagai, R. 1975, PASJ 27, 533
Morgan, L., & Morgan, T. 1970, Phys. Rev. D, 2, 2756
Morgan, T., & Morgan, L. 1969, Phys. Rev., 183, 1097
Satoh, C. 1980, PASJ, 32, 41
Toomre, A. 1963, ApJ, 138, 385
Vogt, D., & Letelier, P. S. 2003, Phys. Rev. D, 68, 084010
Vogt, D., & Letelier, P. S. 2005a, Phys. Rev. D, 71, 084030
Vogt, D., & Letelier, P. S. 2005b, MNRAS, 363, 268

Livros Grátis

(http://www.livrosgratis.com.br)

Milhares de Livros para Download:

Baixar livros de Administração
Baixar livros de Agronomia
Baixar livros de Arquitetura
Baixar livros de Artes
Baixar livros de Astronomia
Baixar livros de Biologia Geral
Baixar livros de Ciência da Computação
Baixar livros de Ciência da Informação
Baixar livros de Ciência Política
Baixar livros de Ciências da Saúde
Baixar livros de Comunicação
Baixar livros do Conselho Nacional de Educação - CNE
Baixar livros de Defesa civil
Baixar livros de Direito
Baixar livros de Direitos humanos
Baixar livros de Economia
Baixar livros de Economia Doméstica
Baixar livros de Educação
Baixar livros de Educação - Trânsito
Baixar livros de Educação Física
Baixar livros de Engenharia Aeroespacial
Baixar livros de Farmácia
Baixar livros de Filosofia
Baixar livros de Física
Baixar livros de Geociências
Baixar livros de Geografia
Baixar livros de História
Baixar livros de Línguas